Padeye engineering tool development

Load capacity of an asymmetrical padeye welded to a jacket structure

Mitchel Oorebeek

Technische Universiteit Delft

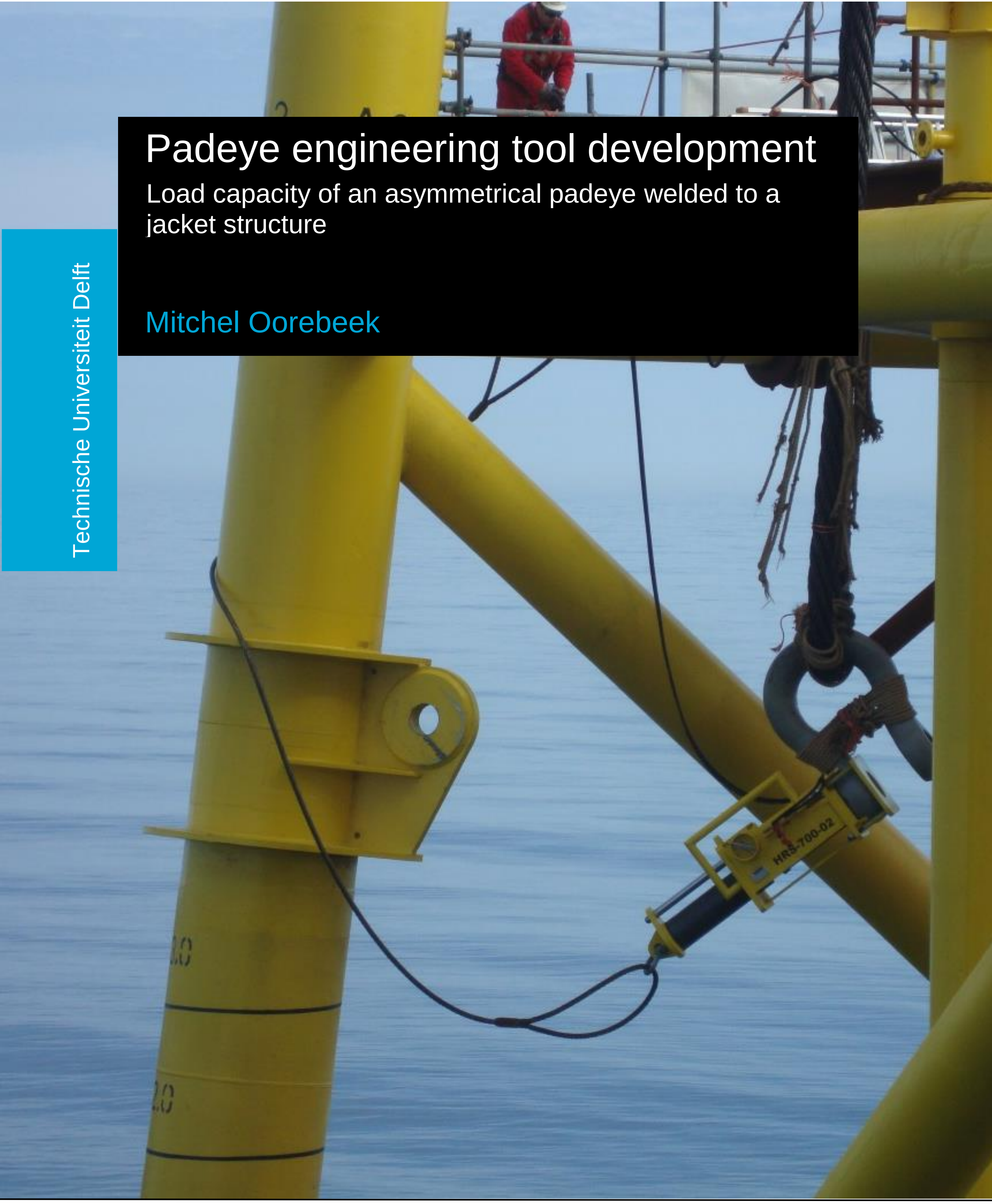

TU Delft Delft University of Technology

Seaway Heavy Lifting

Challenge the future

Padeye engineering tool development

Load capacity of an asymmetrical padeye welded to a jacket structure

MASTER THESIS

by

MITCHEL OOREBEEK

Submitted in partial fulfilment of the requirements for the degree of

MASTER OF SCIENCE

in

CIVIL ENGINEERING - STRUCTURAL ENGINEERING TRACK

Thesis committee:

• Prof.ir. F.S.K. Bijlaard (Chairman)	TU Delft, Steel and Timber Constructions
• Ir. R. Abspoel	TU Delft, Steel and Timber Constructions
• Dr. Ir. P.C.J Hoogenboom	TU Delft, Structural Mechanics
• W. van Dalen, MSc.	Seaway Heavy Lifting B.V.
• M. Kwa, MSc.	Seaway Heavy Lifting B.V.
• Ir. L.J.M. Houben	TU Delft, Road and Railway Engineering

TU Delft Delft University of Technology

Seaway Heavy Lifting

Acknowledgements

This thesis is the finalisation of my master study Structural Engineering at Delft University of Technology, faculty of Civil Engineering and Geoscience. The work is performed from May 2015 until January 2016 at the office of Seaway Heavy Lifting in Zoetermeer. In this thesis an padeye engineering tool is developed, which is used to improve the calculations on padeye-to-CHS connections used within Seaway Heavy Lifting.

The objective of this thesis would not have been reached without the help of others. First of all I want to thank my graduation committee members for their helpful feedback, criticism and shared knowledge during this master thesis.

Secondly I would like to thank Seaway Heavy Lifting for offering the opportunity to graduate within the company. Furthermore I'd like to thank all Seaway heavy Lifting employees and my fellow graduates who contributed to my thesis, for their interest and advice on the topic. In particular I would like to thank Martijn Lenting for his help with the use of the FEM program Ansys.

Finally I want to thank my friends and family for their believe and support during this master thesis and the rest of the study.

Mitchel Oorebeek

Zoetermeer, January 2016

Abstract

Seaway Heavy Lifting (SHL) is an offshore contractor offering Transport and Installation (T&I) and Engineering, Procurement, Construction and Installation (EPCI) solutions for the offshore industry. Offshore structures often consist of Circular Hollow Sections (CHS). During installation the structure is loaded when lifted at multiple lift points, which each consist of a padeye welded to the CHS. The padeye-to-CHS connection is denoted as the padeye load case. Within Seaway Heavy Lifting, the stresses in the CHS cross-section are calculated using the Roark equations and Finite Element Modelling (FEM). From the Roark equations a quick but conservative solution is obtained for the load capacity using a two-dimensional model, while from a FEM program an accurate solution is obtained using a three-dimensional model. However, the use of a FEM program is time-consuming and therefore expensive to use for every padeye-to-CHS connection.

The objective of this thesis is to determine an engineering tool which will be an advanced method of the Roark equations, providing a quick and accurate solution of the load capacity in the padeye load case.

In order to obtain better understanding of the structural behaviour of the padeye load case at first, a simplified model is assumed. In this simplified model a plate-to-CHS connection is considered, denoted as the plate load case. A numerical three-dimensional model is constructed for both the plate and padeye load case using the FEM program Ansys. Because little plastic strain is allowed in this connection, the average linearized plastic strain is limited to 0.04. Besides the numerical models, an analytic two-dimensional ring model is derived for both the padeye load case and the plate load case using the Euler Bernoulli curved beam theory. This ring model is similar to the model used in the derivation of the load case from Roark. From the ring model it follows that the CHS will deform due to loading of the padeye, mainly causing bending moment stresses in the cross-section. The governing stresses in the CHS cross-section occur at the connection between the padeye and the CHS.

A parametric study of the FEM models is performed using multiple variable dimensions, in which the plastic strain criterion is used. From the finite element analysis (FEA) the relation between the ultimate load and the geometry is obtained, which is similar in both the plate and the padeye load case. Varying the geometry of the CHS cross-section results in a variable stiffness of the CHS. When varying the (padeye) main plate geometry, the force is distributed over a varying surface of the main plate-to-CHS connection and bending moments occur in the main plate.

Using the equation from the analytical ring model and a curve fitting tool, the data from the FEA is fitted. By fitting the data an engineering tool is derived for the padeye load case. The engineering tool is validated by comparing the load capacity results with Roark and the FEA results for padeye geometries used in projects performed by Seaway Heavy Lifting. From this comparison it is concluded that the derived tool gives an accurate load capacity for padeye geometries within a specific range. Within this range, the derived engineering tool predicts the load capacity with a deviation that meets the convergence criterion of 5%, while the results from Roark have a large deviation of around 70%. Therefore it is concluded that the engineering tool is an advanced method of the Roark method in the load capacity calculation of the padeye load case.

Outside the considered range the results from the engineering tool have a smaller deviation from the FEA results relative to the Roark equations. However, the results from the engineering tool are unknown outside this range. Therefore it is recommended to expand the range in which the engineering tool is valid.

List of symbols

D	= shackle pin diameter
F_{Lp}	= sling force
F_x F_y F_z	= longitudinal, lateral and radial force component respectively
LT_M, LT_N, LT_V	= Load terms belonging to the various load cases in Roark
M, M_{Lat}	= padeye in-plane and out-of-plane bending moment respectively
$M_{end,i}$	= end moment at the CHS boundary
M_i	= internal moment at i
N_i	= internal normal force at i
R	= $d_0/2$ = radius of the CHS
R_0, R_m	= Radius of the pinhole and the main plate respectively
R^2	= Coefficient of determination
U	= total elastic energy of the system
V_i	= internal shear force at i
W	= force acting on the two-dimensional ring model
b_m	= base width of the padeye main plate
b_{eff}	= effective width
d_0	= diameter of the CHS
d_{sc}	= width between bottom and centre stiffener
$d_{sc,0}$	= width between pinhole and centre stiffener
f_y	= yield stress
h_0	= height of the pinhole centre
h_{si}	= height of front, back and centre stiffener
k_2	= hoop-stress deformation factor
l_0	= length of the CHS chord
t_0	= thickness of the CHS chord
t_m	= main plate thickness
t_c	= cheek plate thickness
t_{si}	= thickness of the stiffener plates
u_i	= displacement in the direction of the i-axis
Δ	= Displacement of the centroid segment in Roark
Δ_x, Δ_y	= Nodal displacement components in x and y direction respectively
Δ_H, Δ_V	= Changes is horizontal and vertical diameters of the ring respectively
α	= $2L/d_0$ = chord length parameter of the hollow section
α_{ip}, α_{op}	= in-plane and out-of-plane sling angle respectively
β	= t_1/d_0 = plate thickness over diameter ratio
γ	= $d_0/2t_0$= radius to thickness ratio of the hollow section
ε_{ii}	= normal strain in the i-plane in direction of the i-plane
ε_p	= plastic strain
η	= b_m/d_0= effective width ratio between the chord and the padeye main plate
θ	= rotational angle in the CHS cross-section
ξ	= ratio between extensional stiffness and total stiffness of the cross-section
σ_{eqv}	= Von Mises equivalent stress
σ_i	= normal stress in the i-plane in direction of the i-plane
σ_{ij}	= shear stress in the i-plane in direction of the j-plane
σ_y	= yield stress
τ_{ij}	= shear stress in the i-plane direction of the j-plane
φ	= rotation of the element cross-section

List of abbreviations

CHS	= Circular Hollow Section
DOF	= Degree Of Freedom
ELT	= External Lifting Tool
EPCI	= Engineering, Procurement, Construction and Installation
FEA	= Finite Element Analysis
FEM	= Finite Element Modelling
ILT	= Internal Lifting Tool
RMD	= Relative Mean Deviation
RMSD	= Root Mean Squared Deviation
RMSE	= Root Mean Squared Error
SHL	= Seaway Heavy Lifting
SPAR	= Single Point Anchor Reservoir
T&I	= Transport and Installation
TLP	= Tension Leg Platform
WTG	= Wind Turbine Generator

Contents

1 Introduction

1.1 Seaway Heavy Lifting

Seaway Heavy Lifting (SHL) is an offshore contractor established in the 1990s and active in the Oil & Gas and Renewable industry. The activity of SHL in the renewables industry has increased in recent years. Within both markets, SHL offers Transport and Installation (T&I) and Engineering, Procurement, Construction and Installation (EPCI) solutions for offshore constructions. While executing these services, safety, efficiency and quality have a high priority in the process.

SHL operates in the North Sea, Mediterranean, America, Africa, Asia Pacific and Middle East. With the operational spread expanding internationally, SHL has multiple offices across Europe. These offices are located in Aberdeen, Cyprus, Glasgow, Paris and Zoetermeer. This latter office is the head office at which most of the engineering work is performed.

The transport and installation solutions are delivered using the two vessels Oleg Strashnov and Stanislav Yudin. The Oleg Strashnov has a fully revolving crane with a lifting capacity of 5000 tonnes. The Stanislav Yudin is also equipped with a fully revolving crane, which has a lifting capacity of 2500 tonnes. In addition to these two vessels, SHL owns a wide range of equipment which is used to operate in a safe and efficient manner. This equipment includes rigging, hammers and a variety of pile handling tools.

SHL has installed over 150 platforms and hundreds of wind energy foundations. The installation projects in the oil and gas industry cover platform, module and deepwater installations. In the renewables industry the projects consist of Wind Turbine Generator (WTG) and substation installations.

Figure 1: Installation of a topside by Seaway Heavy Lifting vessel Stanislav Yudin [1]

Many of the offshore constructions, such as floating SPAR platforms, Tension Leg Platform (TLP) constructions and deepwater templates, consist of Circular Hollow Sections (CHS). Besides these constructions there is also equipment, such as spreaderbars, that consist of CHS. These CHS are steel sections with a circular hollow cross-section, shown in Figure 2. During installation and transportation, forces will be applied on the structures causing stresses. These stresses in the cross-section are called ring stresses.

When the stresses in the cross-section exceed a certain stress limit, the CHS cross-section will deform and possibly fail. Therefore the ring stresses have to be examined. These calculations are performed within Seaway Heavy Lifting by using the Roark equation for stresses and strains. The Roark equations consist of hand calculations that are based on analytical derivation and experimental data, assuming that the CHS cross-section fails if the maximum stress in the ring exceeds the yield stress. Because of this assumption the Roark equations give a conservative stress distribution.

As an alternative method, Finite Element Modelling (FEM) is used in the ring stress calculations. A FEM program translates the physical system into a mathematical model of the system, which is able to simulate and predict aspects of behaviour of a system. In a FEM program the model is split up in a finite number of elements. In order to determine the stress distribution a numerical analysis of the model is performed, called the Finite Element Analysis (FEA). Despite the fact that the use of a FEM program gives an accurate representation of reality, the program and the implementation of the results can be misunderstood by inexperienced users. Besides this the program is time-consuming and only available on a computer, making it expensive to use for every CHS connection appearing in a project.

Finally, there are alternative calculation methods to determine the load capacity of a similar load case. This load case is the plate-to-CHS connection, in which a rectangular plate is welded to a circular hollow section and loaded in-plane by a distributed force. The equations that describe the load capacity of the plate-to-CHS load case are derived by, amongst others, Wardenier et al. [2] and Voth [3]. These calculations are based on plastic theory, numerical analysis and experiments. However, the padeye geometry used within projects performed by Seaway Heavy Lifting is beyond the range used in the equations of Wardenier et al. and Voth.

Figure 2: Steel Circular Hollow Sections (CHS) [4]

1.2 Objective

The objective of this thesis is to determine an engineering tool which is an advanced method of the Roark equations, giving a more accurate solution of the CHS load capacity. This engineering tool will be based on the finite element model in which plastic material behaviour is taken into account.

1.3 Approach

In order to reach the proposed objective, the appropriate background is determined first in chapter 2. The background contains the different possible load cases to which the CHS can be subjected during the transport and installation. Besides this the available calculation methods of the ring stresses, and hence the load capacity, in the CHS are obtained. Finally the elastic and plastic material behaviour is described with the corresponding failure criteria.

In chapter 3 the boundaries are determined. In order to obtain an engineering tool for the load capacity that is suitable for the projects performed by Seaway Heavy Lifting, the proper boundaries have to be determined. These boundaries are obtained by comparing the load case geometries that are used in present practice, resulting in a range of the geometry.

In order to derive an engineering tool, a numerical model must be constructed using the FEM program Ansys. This model is constructed in chapter 4, in which the appropriate boundaries from chapter 3 are applied. Next, the proper element type, element size and analysis type will be determined for the numerical model.

The analysis results from the analytical model and the FEM model have to be compared in order to obtain an engineering tool. Therefore the analytical model has to be derived, which is achieved in chapter 5. In the analytical derivation a two-dimensional ring model is assumed for the CHS cross-section. From this model the analytical equation for the load capacity can be determined. This equation will not only be used to compare the results from both types of analysis, but also to obtain the influence of the different dimensions in the load case.

The results from the FEA with the model derived in chapter 4 are described in chapter 6. The proper limit criterion is determined in order to describe the load capacity of the load case from the numerical analysis. These analysis are performed for each geometry within the range obtained in chapter 3, which will result in a load capacity of the entire load case. The load capacities will be evaluated and the influence of the different dimensions are obtained.

Finally, the engineering tool is derived in chapter 7, using the results from the FEA from chapter 6 and the analytical equation from chapter 5. The influences of the dimension on the load capacities are compared for both the analytical and the numerical analysis. The analytical equation will then be adapted to describe the results from the numerical analysis. This will lead to an engineering tool which described the load capacities of the CHS load case present in projects performed by Seaway Heavy Lifting, which is an advanced version of the Roark method.

2 Background

2.1 Load cases

During installation of an offshore construction, the circular hollow sections (CHS) can be loaded by multiple types of loading. These different types of loading are called load cases which cause ring stresses in the cross-section. These ring stresses could lead to failure of the CHS. Several load cases which cause ring stresses in the CHS cross-section are the use of a padeye, pipe trunnion, pile catcher and Internal- and External Lifting Tools (ILT and ELT respectively). These load cases are shortly described below:

- Padeyes and pipe trunnions (Figure 3) are welded to the structure and connect the structure to the crane by use of slings. The construction is then lifted from the deck onto the seabed or onto a substructure. In the case of a padeye a shackle is put through the pinhole to connect the sling with the structure, while in the case of a trunnion the slings are put around the trunnion. Both cases cause radial loading of the CHS.

Figure 3: Padeye on a jacket member and a pipe trunnion on an offshore structure [5]

- Pile catchers are used to guide the foundation pile through the jacket during installation. The pile catcher is welded to the top of the jacket leg. When the foundation pile is guided via the pile catcher, this causes a radial distributed load over the circumference of the jacket leg.
- The internal and external lifting tools (Figure 4) are used to lift piles off the deck of a vessel or barge. In case of an ILT the load is evenly distributed over the CHS circumference, where for an ELT the load is applied in two points of the CHS. This causes distributed axial load in case of an ILT and radial point loads in case of an ELT.

Figure 4: ELT clamped to a monopile [6] and an ILT lifting a monopile [7]

2.2 Padeye load case

Because there's limited time and the analysis is expected to be time-consuming, the scope of this study is narrowed. This is done by choosing a single load case. From this point onwards, only the padeye load case is considered.

2.2.1 Load case description

Padeyes are used to connect the to-be-lifted offshore construction and the crane by use of slings. The padeyes that are used in practice have various geometries, depending on the type of load. In case of a solely vertical force the geometry is symmetrical. However in the case of a force under an in-plane angle α_{ip}, the geometry is asymmetrical due to the different force components. When looking at the padeye load case, the asymmetric geometry is used in most lifts performed by Seaway Heavy Lifting, because the force is acting under an angle.

In many cases an intermediate spreaderbar is used between the crane and the lift point. The spreaderbar is used to ensure that the slings are acting under an angle within the allowed range. Each lift point consists of a padeye which is welded to the structure and connected to the sling by a shackle. The lifting force (F_{Lp}) acting on the padeye is caused by the weight of the structure and the equipment used. This lifting force is transferred to the sling by a shackle put through the padeye pinhole, creating a pinned connection. In this pinned connection the force has its origin at the centre of the shackle pin cross-section, which is acting in the centre of the pinhole (Figure 5).

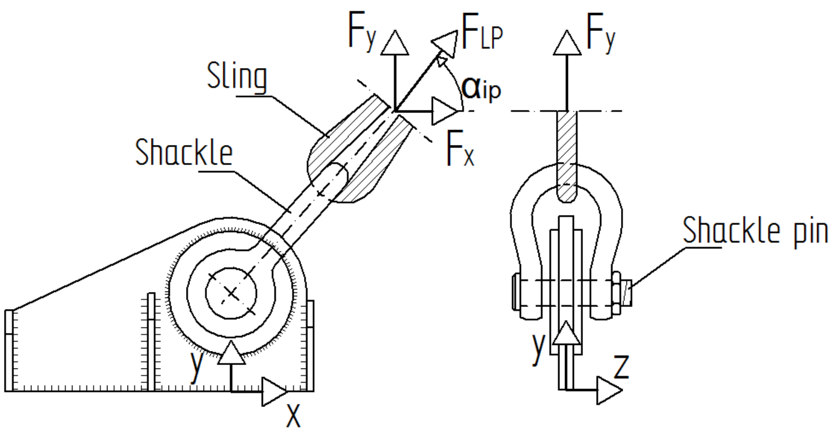

Figure 5: Shackle connecting the padeye and sling, working under an angle α_{ip}

The pinhole centre lies at a height h_0 above the bottom of the main plate. Because the sling is acting under an angle α_{ip} in the plane of the main plate, the force at the pinhole will be under the same angle (α_{ip}). Due to this angle of the force α_{ip}, the force can be divided into a vertical component F_y and a horizontal component F_x. Because the horizontal force components is acting at a height h_0, this will result in an in-plane bending moment M_{ip}.

2.2.2 Load resistance

To withstand these loads during operation, a padeye consists of a main plate and occasional ring stiffeners (Figure 6). The main plate is conducted with a pair of cheek plates to stiffen the pinned connection and to prevent the main plate from failing due to bearing stress. The ring stiffeners are attached to the main plate to take on the radial and lateral forces and prevent excessive deformation of the CHS.

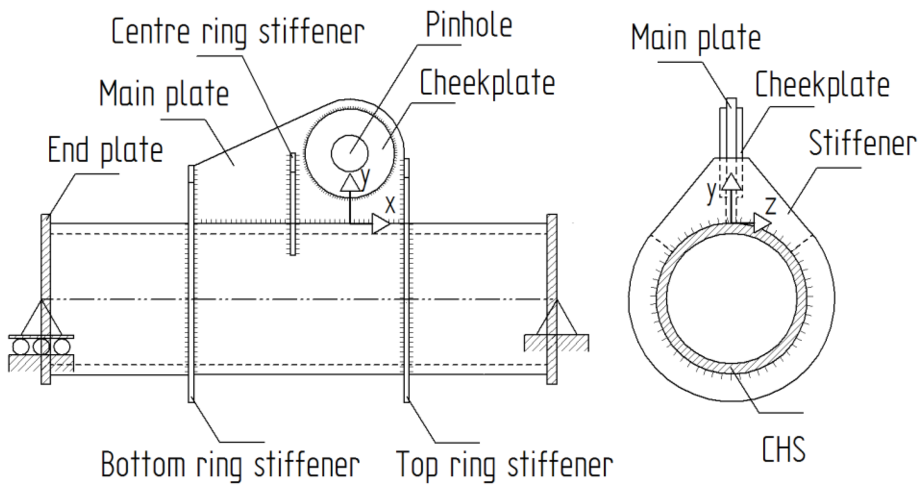

Figure 6: Description of the components in the padeye load case

In the padeye load case with ring stiffeners applied, the load is transferred from the padeye pinhole to the main plate. The load on the main plate is then distributed over the ring stiffener to the CHS. From the connecting face, the load is transferred via the circumference of the CHS to the supports. The different force components are transferred from the main plate to the CHS as described below:

- The horizontal force component F_x is taken by the weld between the padeye main plate and the CHS
- The vertical force component F_y is taken by the top and centre ring stiffener
- The in-plane bending moment M_{ip} is taken by the top and bottom ring stiffener

The force distributions in the padeye load case with additional ring stiffeners is shown in Figure 7. These ring stiffeners are not always present in the padeye load case. The force distribution in the case of a padeye without additional ring stiffeners is also shown in Figure 7 and is described below.

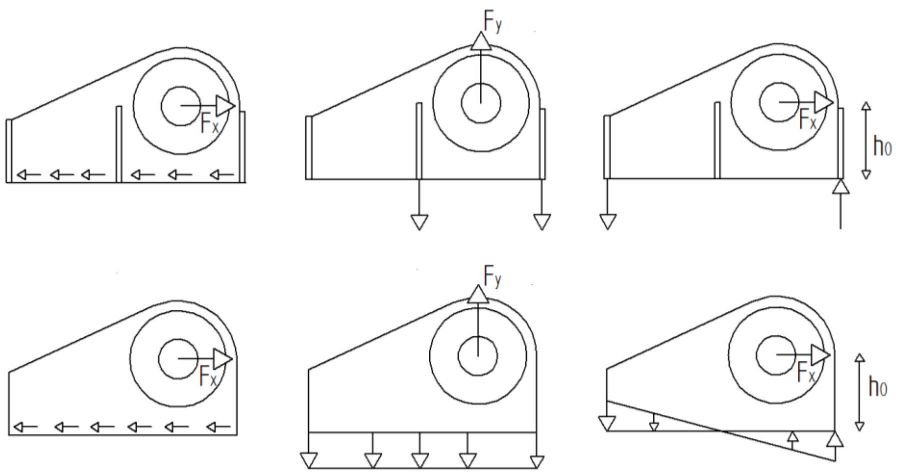

Figure 7: Force distribution in the padeye load case with ring stiffeners (top) and without ring stiffeners (bottom)

In the case that there are no ring stiffeners present, the horizontal and vertical force components will be distributed over the total main plate-to-CHS connection interface. In this case the load is transferred from the padeye pinhole through the padeye main plate to the CHS. From the connecting face, the force flows to the supports in the same manner as in the case with ring stiffeners. The force components are transferred from the main plate to the CHS as described below:

- The horizontal force component F_x is taken by the weld between the padeye main plate and the CHS
- The vertical force component F_y is distributed over the base of the main plate
- The in-plane bending moment M_{ip} is distributed over the base of the main plate

In order to narrow down the scope of this study, only the padeye load case without ring stiffeners is considered from this point onwards.

2.2.3 Padeye failure modes

Due to the loads and hence the stresses that pass through the structure, multiple padeye failure modes can occur. The location at which failure could occur can be determined by looking at the load path. The load path is the manner in which the load is transferred to the supports. This load path is already described in 2.2.2 for the padeye load case without additional ring stiffeners. From this it can be obtained that the possible failure modes are failure of the cheek plate and the main plate and failure of the welds. The conditions and the effects of the possible failure modes can be obtained from the General criteria for lift points [8].

In case the main plate has a low thickness-to-width ratio ($\gamma = d_0/t$) and the plate has sufficient ductility, the yield capacity of the plate can be governing. This could lead to the following failure modes shown in Figure 8 and described below:

- Bearing stress can occur at the contact area with the shackle pin. This is a local phenomenon caused by the compressive loading of the shackle pin at the pinhole.
- Tear-out stress can occur at section α-α, due to the shear stresses.
- Yielding at section β-β and section γ-γ can occur, due to the tension stress.

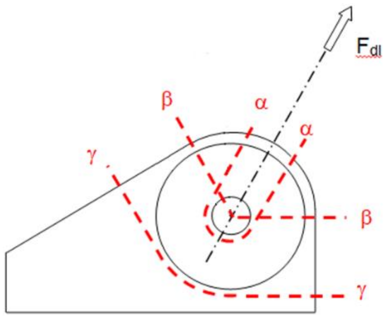

Figure 8: Possible failure of the padeye main plate and cheek plate due to loading

If the strength of the weld is lower than the strength of the main plate, the weld may yield and eventually crack. This could occur at the weld between the main plate and the cheek plate and the weld between the main plate and the CHS. In the case of plastic deformation due to yielding of the weld this will result in little rotational capacity of the joint, which is not allowed.

The goal of this thesis is to describe the ring stresses in the CHS due to padeye loading. In many cases standard padeye dimensions are used, which are designed to resist the applied load. Because of these reasons, it is assumed that the padeye and the welds are adequately designed and are non-critical.

2.3 CHS ring stresses

Due to loading of the padeye, the CHS will experience deformations. These deformations will be bigger in circumferential direction than in the longitudinal direction, due to the low circumferential rigidity. Because the deformation and curvature correspond with the stresses, it can be expected that the stresses in circumferential direction are governing. The allowable stresses in the structure depend on the type of material behaviour. If the stress-strain relation is based on linear elastic material behaviour, it is assumed that the material will fail when the maximum stress in the cross-section reaches the yield stress (σ_y). If the stress-strain relation is based on nonlinear plastic material behaviour, the material will fail due to cracking when the strain is reached which coincides with the ultimate strength (Figure 9).

When the nonlinear plastic material behaviour is taken into account, the stress becomes constant (σ_{PL}) when the maximum stress in the cross-section exceeds the yield stress (σ_{EL} in Figure 9). When the load is increased, only the strain (ε) will increase and adjacent material will start to yield. This will continue until the strain hardening part of the stress-strain curve is reached, causing both the stress and the strain to increase. Finally, when the stress reaches the ultimate stress (σ_U), the material will begin to crack. Due to these cracks the material will no longer be able to take any stresses or strains, causing the adjacent material to take the load. Because the remaining area has to take a relatively higher load, crack prolongation will occur in the cross-section. By increasing the load this crack prolongation will eventually lead to failure of the cross-section.

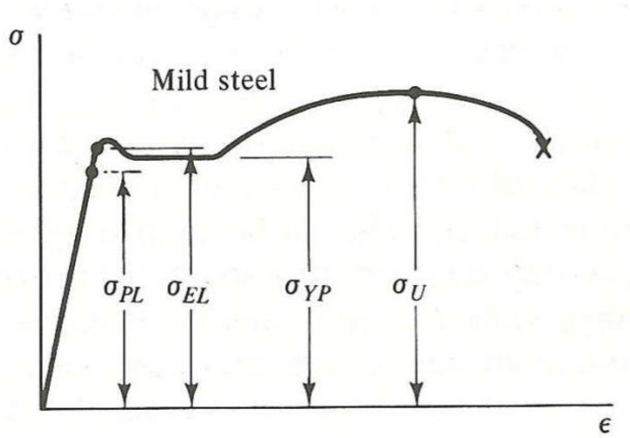

$\sigma_{PL} \Rightarrow$ **Proportional Limit** - Stress above which stress is not longer proportional to strain.

$\sigma_{EL} \Rightarrow$ **Elastic Limit** - The maximum stress that can be applied without resulting in permanent deformation when unloaded.

$\sigma_{YP} \Rightarrow$ **Yield Point** - Stress at which there are large increases in strain with little or no increase in stress. Among common structural materials, only steel exhibits this type of response.

$\sigma_{YS} \Rightarrow$ **Yield Strength** - The maximum stress that can be applied without exceeding a specified value of permanent strain (typically .2% = .002 in/in).

Figure 9: Stress-strain curve for mild steel [9]

2.3.1 CHS failure modes

The forces acting on the padeye are transferred to the supports via the CHS. Both the vertical force component F_y and the in-plane bending moment M_{ip} result in radial tension load on the CHS cross-section. Due to this radial loading of the CHS, local concentrated yielding will occur introducing plastic strains. These plastic strains can lead to failure of the cross-section. Different modes of failure are possible in CHS under padeye loading.

Chord plastification can develop due to high stresses in the chord. In the case of plastification, the chord experiences large plastic deformations while the connecting member will remain intact. Due to these large deformations at the connection, a practical deformation limit is reached before the ultimate stress is reached. The deformations can also cause secondary moments due to, for instance, plastic rotation of the joint. In order to prevent this the connection must have sufficient rotational capacity.

In many cases the padeye is connected to the leg of a jacket structure, which consist of a circular hollow section (CHS). When this jacket structure is installed, a foundation pile is driven through the legs of the structure in order to maintain its position during the structural lifetime. When the jacket leg experiences large deformations during the installation, the foundation pile will no longer fit. Therefore the deformations of the structure must be limited in order to avoid loss of serviceability.

When the plastic strains in the CHS reach the ultimate strain, cracks can develop in the chord. By increasing the loads, the cracks will propagate which will lead to brittle failure of the connection. This brittle failure can have different causes. Due to high localized shear stresses in the chord connection face, chord punching shear could occur. Punching shear occurs when a crack is initiated at a point of high stress concentration in the chord. When the load on the connection increases, the crack could propagate around the weld perimeter, causing punching shear failure. Besides punching shear failure, the padeye-to-CHS connection can encounter lamellar tearing. This is cracking due to manganese-sulphide inclusions (M_nS), which result in a weakened cross-section. These inclusions can be present if the thickness of the CHS is very large.

Finally the plastic strain can affect the low cycle fatigue lifetime. Low cycle fatigue is a progressive and localised damage due to repeated plastic strain in the material under tensile stress. The padeye loading only takes place during the installation, therefore it won't cause fatigue damage. However, in most cases the padeye is connected to the CHS member at a joint of multiple braces. These joints are subjected to high stresses and hence stress variations during the lifetime of the structure. If the CHS locally experiences large plastic strains due to the padeye loading, the fatigue lifetime of the CHS joint could be affected. Because this could affect the fatigue lifetime of the total structure, the plastic strain due to the padeye loading must be limited.

In most cases the CHS will be stiffened by using a larger thickness of the CHS at the location of the padeye connection. The padeye is also located near a joint at the top of the structure, causing the member to be rigid and relatively free of wave forces. Due to these facts the plastic deformation in the CHS due to padeye loading will not cause fatigue failure, as long as the plastic strain remains small.

2.4 Limit state criteria

In order to prevent failure of the padeye-to-CHS connection, the yielding and therefore the plastic strain must be limited. Several limit state criteria are present for the elastic and plastic strains. Some of these criteria applicable on the padeye load case are given in this paragraph.

To check if the stresses in the cross-section do not exceed the yield stress, the Von Mises criterion is used. This criterion determines an equivalent one-dimensional stress for the multi-dimensional stress state of an element. This equivalent stress is the stress performed on a tensile test and is stated in (2.1). In the three-dimensional model, all six stress components shown in Figure 10 in are considered. When using a two-dimensional ring model, only three stress components are considered. These stress components are the normal and shear stresses in the yz-plane (σ_y, σ_z, τ_{yz}).

$$\begin{aligned} \sigma_{eqv} &= \frac{1}{\sqrt{2}}\sqrt{\left[\left(\sigma_x-\sigma_y\right)^2+\left(\sigma_y-\sigma_z\right)^2+\left(\sigma_z-\sigma_x\right)^2+6\tau_{xy}^2+6\tau_{yz}^2+6\tau_{zx}^2\right]} \\ \sigma_{eqv} &= \sqrt{\left[\left(\sigma_y\right)^2+\left(\sigma_z\right)^2+3\tau_{yz}^2\right]}=\sqrt{\left[\left(\sigma_\theta\right)^2+\left(\sigma_r\right)^2+3\tau_{r\theta}^2\right]} \end{aligned} \tag{2.1}$$

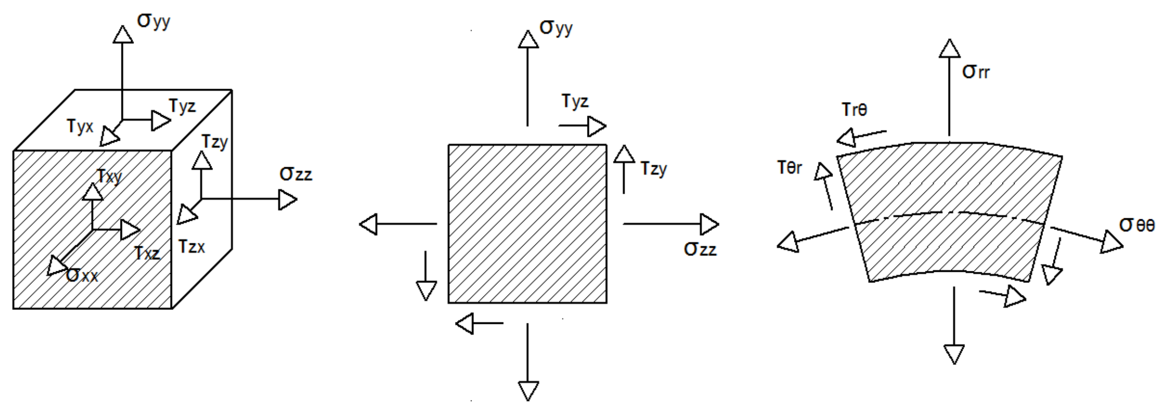

Figure 10: Stress components in a three-dimensional cartesian coordinate system and in a two-dimensional cartesian and polar coordinate system

When taking into account nonlinear material behaviour, plastic stresses and strain can develop in the model. The DNV-RP-C208 report [10] describes the strain limit for tensile failure due to gross yielding of plane plates. Because the CHS is a curved plate with large diameter and thus a small curvature, these strain limits are used as the limit state criteria. These strain limits state that for steel S355, the structure may experience a principal plastic linearized strain with a maximum value of 0.04 (4%). This principal plastic linearized strain is the average plastic strain over a rectangular prismatic volume at the location with the largest strain.

For out-of-plane bending of the plate, the length, width and thickness of the prismatic volume are equal to the thickness (t_0) of the plate. In case of local cut outs in the tensile part of the cross-section, the ratio between the net area and the gross area (net section ratio) must be at least 0.95. The net area is the cross-sectional area in which cut outs are subtracted. In case the net section ratio is less than 0.95, the influence of the cut outs have to be taken into account. However, in the padeye load case there are no cut outs present and this criterion will not be used.

Critical strain and net area ratio for uniaxial stress state 1), 2)				
	Maximum principal plastic linearized strain 1)			
	S235	*S355*	*S420*	*S460*
Critical gross yield strain	0.05	0.04	0.03	0.03
Net section ratio	0.94	0.95	0.96	0.97
1) The strain can be calculated as average values over a length (in the direction of the principal strain) equal to the thickness for in-plane bending and up to 5 times the thickness for pure membrane strains. 2) Any strain due to cold-forming should be added to the calculated plastic strain considering the direction of the plastic strain due to cold forming				

Critical local maximum principal plastic strain for uniaxial stress states 1)				
	Maximum principal plastic critical strain			
	S235	*S355*	*S420*	*S460*
Critical local yield strain	0.15	0.12	0.10	0.09
1) Any strain due to cold-forming should be added to the calculated plastic strain considering the direction of the plastic strain due to cold forming				

Figure 11: Tables from DNV-RP-C208 [10] giving the limit state criteria for the maximum principal plastic linearized strain and the maximum plastic critical strain

To prevent tensile failure due to cracking at local strain concentrations, a critical plastic strain limit is given in the DNV-RP-C208 report [10]. This critical plastic strain is the largest locally occurring plastic strain in the governing volume, and has a maximum value of 0.12 (12%). The governing volume in which the strain occurs is the same volume as used for the principal plastic linearized strain.

In the Eurocode EN 1993-1-5 [11] a limit state criterion is presented for the plastic strain. This limit state criterion is similar to the criterion stated in the DNV report for the principal plastic linearized strain. The limit state criterion given by the Eurocode states that for a connection loaded in tension, a maximal plastic principal strain of 5% is recommended. The governing plastic strain is a local strain, and does not need to be averaged over a certain volume.

Another criteria which assumes ductile failure after reaching a maximum plastic strain is derived by Lemaitre. In this criteria the maximum strain is dependent of the Poisson's ratio, the isotropic stress and the Von Mises stress. The isotropic stress occurs when a material is under equal compression/tension in all directions. The stress in this case is directed perpendicular to the surface, independent of the surface's orientation. By introducing the ratio between the isotropic stress and the Von Mises stress (the triaxiality ratio), triaxiality is taken into account. In case of triaxial stress, a combination of different types of stress are active on an element. This causes different stresses in different directions which are nonzero. The equation of the maximal plastic strain derived by Lemaitre is stated below for $\nu = 0.3$:

$$\varepsilon_f = \frac{\varepsilon_0}{\frac{9}{2}\frac{1-2\nu}{1+\nu}\left(\frac{\sigma_h}{\sigma_{eqv}}\right)^2+1} = \frac{\varepsilon_0}{1.38\left(\frac{\sigma_h}{\sigma_{eqv}}\right)^2+1} \qquad (2.2)$$

$$\sigma_h = \frac{1}{3}\left(\sigma_1+\sigma_2+\sigma_3\right)$$

By rewriting this equation the equivalent plastic strain $\varepsilon_{eq,p}$ (= $\varepsilon_f/\varepsilon_0$) can be obtained, which is a function of the triaxiality. Failure of the material according to the Lemaitre strain criterion is shown in Figure 12 for the Poisson's ratio ν equal to 0.3.

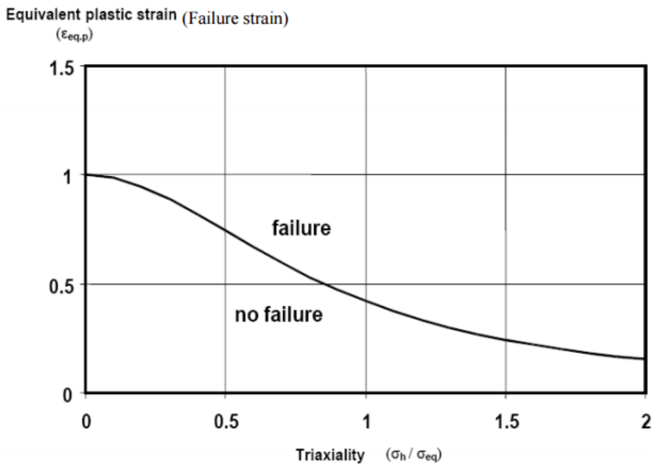

Figure 12: Master curve of Lemaitre failure criterion for v=0.3

As described before, yielding of the material causes large deformations. Therefore there are also limit state criteria for the deformation instead of the plastic strain. In Wardenier [2] and Voth [3] a deformation limit is used, which is determined by Lu et al. [12]. This criterion states that the CHS cross-section may not experience a deformation that is larger than 3% of the CHS diameter d_0.

2.5 Load capacity calculation methods

Multiple calculation methods are present to determine the stress distribution in the padeye load case. Within SHL, Roark's formulas for stress and strain [13] and Finite Element Modelling (FEM) are used. Besides these two methods, different calculation methods are available that describe the load capacity of a similar load case. This load case is the plate load case, which consists of a T-type plate-to-CHS connection shown in Figure 15.

2.5.1 Roark's formulas for stress and strains [13]

Roark's formulas describe the stress distribution in a large number of cross-sections due to different load cases. It is intended as a reference book consisting of three parts, which can help in the design and strength check of a diversity of structures. The first part describes the terminology, properties and units used. The second part describes the stress-strain relationship of materials, the behaviour of bodies under stress and the methods of stress analysis used. Finally the third part describes the stress, strain and strength calculations of structural elements under multiple loading conditions.

The formulas given in the third part are stated in tables and are based upon analytical and experimental stress analysis of structural components. The formulas give a quick calculation method which determines the linear elastic stress distribution. In case multiple loads are active on the system, the stress distributions can be superimposed. The maximum stress from Roark's formulas is checked on exceedance of the yield stress, allowing only linear elastic material behaviour.

For the stresses in the CHS in the padeye load case, Roark's formulas for bending of curved beams are used. In these formulas the ring is assumed as a curved beam with wide flanges. In the case of ring stiffeners the cross-section is considered to be a T-section (Figure 13 right), in which the CHS is acting as the flange and the stiffener is acting as the web. The width of the CHS cross-section, which is contributing to the stiffness, is called the effective width b_{eff} and is used to account for the stiffness of the cross-section in longitudinal direction. This effective width is a function of the diameter (d_0 = 2R) and the thickness (t_0) of the CHS, and is stated below:

$$b_{eff} = 1,56\sqrt{d_0 t_0} \tag{2.3}$$

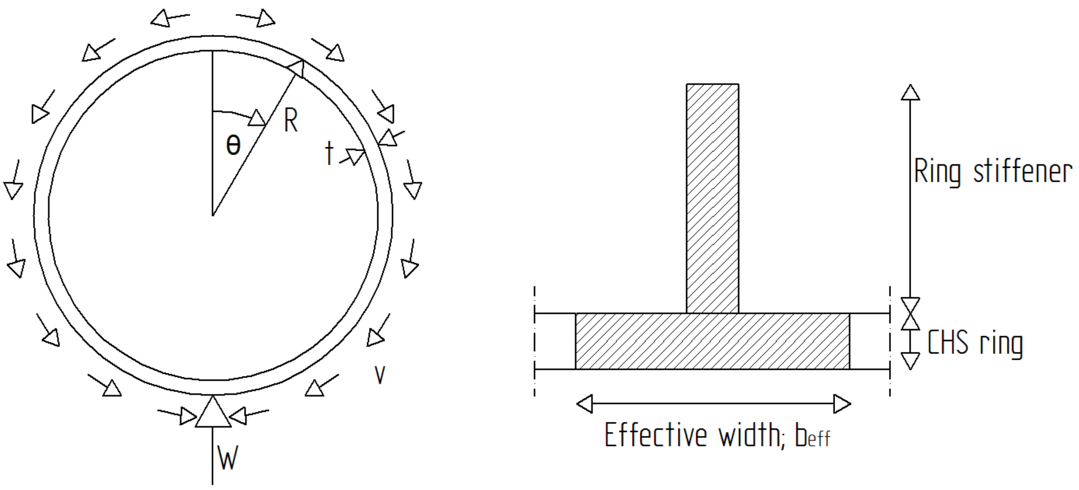

Figure 13: Two dimensional ring model of load case 20 from Roark [13] (left) and its effective width (right)

To determine the stress distribution in the two-dimensional model the forces acting in this cross section have to be calculated. For the padeye load case, Roark's load case 20 can be used (Figure 13 left). This load case consists of a ring under a point load, which is supported by transverse shear. The point load represents the padeye load onto the CHS, while the transverse shear represents the shear resistance of the adjacent rings onto the considered ring. The transverse shear stress in Roark's load case 20 is described below:

$$v = \frac{W}{\pi R}\sin(\theta) = \frac{2W}{\pi d_0}\sin(\theta) \tag{2.4}$$

The general formulas for the moment (M), hoop load (N) and radial load (V) given by Roark (2.5) are derived from the curved beam theory. With the formulas for the ring loads the stress distribution along the ring can be determined for different load cases.

$$\begin{aligned} M &= \frac{WR}{2\pi}\left(\frac{1}{2}\cos(\theta) + \theta\sin(\theta) + \frac{I}{AR^2} - 1\right) \\ N &= \frac{W}{\pi}\left(\frac{3}{4}\cos(\theta) - \frac{\theta}{2}\sin(\theta)\right) \\ V &= \frac{W}{2\pi}\left(\theta\cos(\theta) + \frac{1}{2}\sin(\theta)\right) \end{aligned} \tag{2.5}$$

With the force and moment distributions known, the stresses are calculated using the theory for straight beams. With these stresses the Von Mises equivalent stress can be calculated, with which the maximum stress is checked for exceedance of the yield stress.

$$\begin{aligned} &\sigma_{\theta,N} = \frac{N}{A}; \quad \tau_{r\theta} = \frac{V}{A}; \quad \sigma_{\theta,M} = \frac{M}{\frac{1}{6}bt^2} \\ &\sigma_{eqv} = \sqrt{\left(\left(\sigma_{\theta,N} + \sigma_{\theta,M}\right)^2 + 3\tau_{r\theta}^2\right)} \end{aligned} \tag{2.6}$$

2.5.2 Finite Element Analysis

Besides the use of Roark's method, the stresses can be calculated using a numerical computer based Finite Element Modelling (FEM) program. Within Seaway Heavy Lifting the FEM program Ansys is used.

As described before, in a FEM model the physical system is translated into a mathematical model of the system, which simulates and predicts the behaviour of the system. The model is split up in a finite number of elements, hence the name Finite Element Modelling, in which the behaviour is determined. This subdivision of the model into a number of elements is called meshing. A fine mesh means that the model contains many elements which are analysed, and thus gives an accurate solution. However, an increase in the number of elements also means an increase in computation time. This means that an optimum number of elements have to be determined which gives an accurate solution of the model.

To obtain the stresses from the Finite Element Model, an analysis has to be performed. A distinction can be made between the linear and nonlinear analysis types. In the linear elastic analysis the displacements are assumed small, the strain is proportional to the stress, the loads are independent on displacements and the supports remain unchanged during loading.

The nonlinear analysis can be subdivided in geometrical nonlinearities, material nonlinearities and boundary nonlinearities. The geometrical nonlinearities take into account the effect of large displacements on the overall geometric configuration of the structure. Because of these large displacements the angle of the force on the structure will change during loading, causing the force to change. The material nonlinearities take into account the fact that the material behaviour is not linear. The material models that can be used in this analysis are nonlinear elastic, elastoplastic, viscoelastic and viscoplastic. Finally for the boundary nonlinearities, displacement dependant boundary conditions are taken into account. These nonlinearities are usually found in contact problems, in which a force is modelled that can only have influence on a structure when it has a contact area.

The numerical analysis of the model is an iterative process, which is shown in Figure 14. In the analysis, the stiffness of each element is stored in an element stiffness matrix. These element stiffness matrices are used to solve the displacements for a given external load on the structure, applied at each load step. With the displacement known, the strains and therefore the stresses are determined at each element using Gaussian co-ordinates or Gauss points. When more Gauss points are used in an element, both the accuracy of the solution and the computation time will increase. By using the stresses at each element, the internal load on the structure can be determined. The internal load is compared with the applied external load on the structure. If the internal load is equal to the external load, the calculated deformations, stresses and strains are correct and the next load step can be applied. If the internal load is not equal to the external load, a new iteration has to be performed.

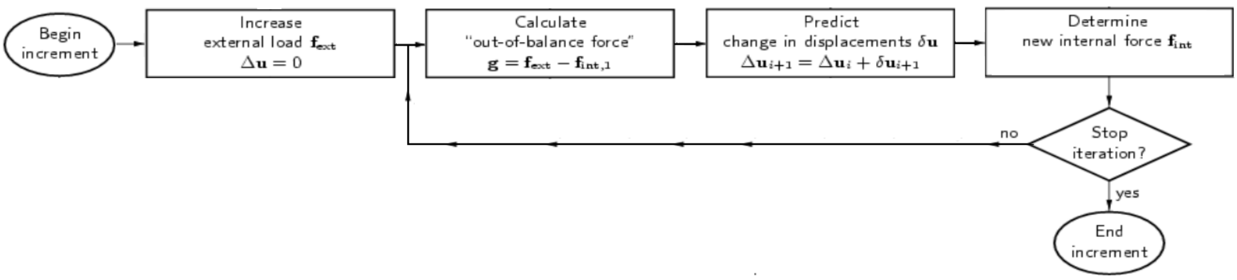

Figure 14: Iterative procedure Finite Element Analysis (FEA) [14]

2.5.3 Comparative calculation methods

In the design guide for CHS by Wardenier et al. [2] and in the study by Voth [3], the load capacity of a similar load case, a T-type plate-to-CHS connection (Figure 15), is determined. For this case the boundaries of the connection strength are given, which are the two possible failure mechanisms. These failure mechanisms are chord plastification and chord punching shear, and are dependent on many of the geometry parameters. Chord plastification is a ductile failure due to excessive plastic deformation of the joint interface, while chord punching shear is a brittle failure under local loads due to formation of diagonal tension cracks. Both failure mechanisms are dependent on the connection geometry.

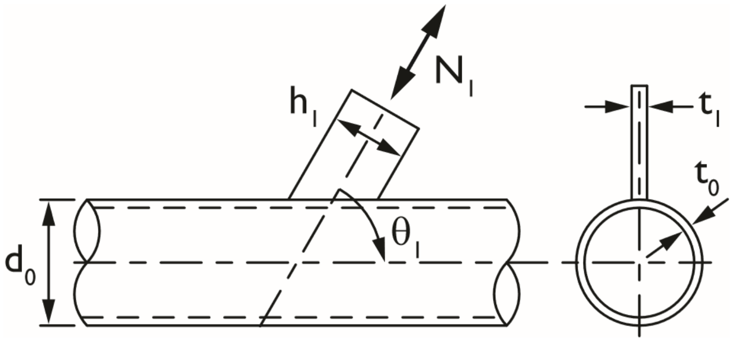

Figure 15: Longitudinal T-type branch plate-to-CHS connection, described in Wardenier [2] et al. and Voth [3]

For punching shear failure, it is assumed that local stresses at a surface through the chord wall limits the joint strength. These local stresses may not exceed the punching shear stresses.
In the case of chord plastification, several plastic hinges are formed due to the exceeding of the yield stress, forming a mechanism. When a mechanism is formed, the CHS experiences large deformations. In order to determine the ultimate capacity of the joint, a deformation limit is used. The out-of-plane deformation of the connecting CHS face is limited to 3% of the CHS diameter d_0. The ultimate load is reached when the deformation in the CHS exceeds this deformation limit.

The equations of the load capacity due to plasticity are derived using the ring model by Togo for a CHS-to-CHS connection, and is described by van der Vegte [15]. By using symmetry, the three-dimensional T-type CHS-to-CHS connection configuration can be translated into a two-dimensional half ring model representing the CHS chord. Brace forces are applied on the model as a line load, acting over a certain length. By using plasticity theory, the locations of possible plastic hinges are assumed and an analytical equation is derived. This model is shown in Figure 16.

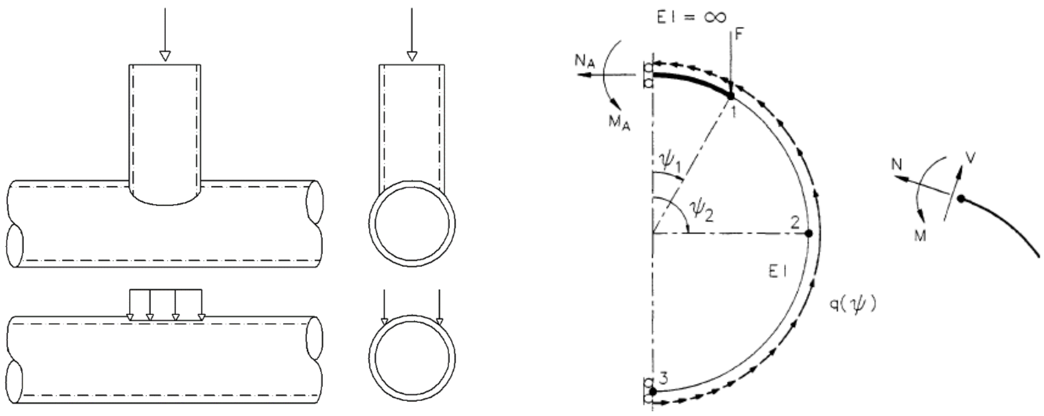

Figure 16: Three-dimensional CHS-to-CHS T-joint translated into a two-dimensional ring model with plastic hinges

The two-dimensional ring model is loaded by a point load at an angle φ_1 and a transverse shear stress $q(\varphi)$, which is similar to ring model used in Roark. The transverse shear stress is equal to:

$$q(\varphi) = \frac{4F}{\pi d_0}\sin(\varphi) \tag{2.7}$$

Due to the applied load on the joint the stresses in the ring will increase. When somewhere in the structure the bending moment reaches the plastic moment, a plastic hinge develops. When the load is increased, multiple plastic hinges will develop until a mechanism is formed. When the structure becomes a mechanism it can deform unlimitedly without the load being increased. The number of plastic hinges that is needed to create a mechanism is equal to the degree of static indeterminacy of the structure. In the considered ring model there are three plastic hinges needed in order to create a mechanism. Hinge 1 is located at an angle φ_1 at which the brace is connected to the chord. Hinge 3 is located at the bottom of the CHS cross-section at an angle φ_3. The angle φ_2 at which plastic hinge 3 is located is unknown. This location can be determined by looking at the minimal force to create a mechanism.

In order to determine the load capacity of a T-joint plate-to-CHS connection, the model used for the CHS-to-CHS connection is adapted. The plate-to-CHS ring connection can be simplified to a CHS-to-CHS connection with a very small diameter ratio β (d_1/d_0), and therefore a small angle φ_1. Due to the small plate diameter, hinge 1 will be located near the upper support of the ring. With this assumption, an analytical equation is obtained that is used to describe the numerical and experimental results.

This equation of the capacity of the T-type plate-to-CHS connection is derived by Wardenier et al. [2] (2008, 2009). This equation is given in (2.8). One of the most significant changes is the way the axial load is taken into account. The influence of the axial load is based on numerical analysis and is presented in the chord stress function Q_f. In this function the value C_1 is equal to 0.25 for chord compressive stress ($n < 0$) and equal to 0.20 for chord tension stress ($n \geq 0$).

$$N_1 = 5(1+0.4\eta)Q_f \frac{f_{y0}t_0^2}{\sin(\theta)} \tag{2.8}$$

$$Q_f = (1-|n|)^{C_1} \quad with:\ n = \frac{N_0}{N_{pl,0}} + \frac{M_0}{M_{pl,0}}$$

Recently Voth [3] (2010) conducted a research using numerous experimental connections and finite element models, in order to gain a better understanding of branch plate-to-CHS connections and determine the influence of different geometries and loads on the connection capacity. In contrast to the research by Wardenier et al., Voth conducts that the plate thickness is significant for the connection capacity. Therefore the influence of the plate thickness is included in the calculations by Voth. The proposed calculation for chord face plastification is given in (2.9).

$$N_1 = 7.6\xi\left(1+\left(\frac{b_1}{d_0}\right)^2\right)\left(1+0.6\frac{h_1}{d_0}\right)\left(\frac{d_0}{2t_0}\right)^{0.1} Q_f \frac{f_{y0}t_0^2}{\sin(\theta_1)} \quad \xi = 0.9 \tag{2.9}$$

$$Q_f = (1-|n|)^{C_1} \quad with:\ n = \frac{N_0}{N_{pl,0}} + \frac{M_0}{M_{pl,0}}$$

Besides plastification of the chord, punching shear could also lead to an ultimate load due to failure of the chord. By using the numerical and experimental data, the load capacity can be determined using the limit state criteria that the local maximum stress cannot exceed the punching shear stress. The equation for punching shear failure described by both Wardenier and Voth is given in (2.10). In this equation the normal force and both in-plane and out-of-plane bending moments are taken into account. In case only a normal force under an angle θ_1 is present in the model, the equation can be simplified into equation (2.11).

$$\frac{N_1}{A_1}+\frac{M_{ip,1}}{W_{el,ip,1}}\frac{M_{op,1}}{W_{el,op,1}}\leq 1.16 f_{y0}\frac{t_0}{t_1} \tag{2.10}$$

$$N_1 \leq 1.16 h_1 \frac{f_{y0}t_0}{\sin^2\left(\theta_1\right)} \tag{2.11}$$

The equations given for the failure modes plastification and punching shear are valid within a certain range. The range in which the equations of both Wardenier et al. and Voth are valid, are given in Table 1.

Table 1: Range for load capacity equations derived by Wardenier et al. and Voth

	Wardenier et al.		Voth	
	Minimum	Maximum	Minimum	Maximum
$\beta = t_1/d_0$	0.2	1.0	0.09	0.27
$\gamma = d_0/t_0$	0	50	14	50
$\eta = h_1/d_0$	1.0	4.0	0.2	4.5

2.6 Conclusion

A lot of research is performed for branch plate-to-CHS connections, similar to the studies by Wardenier et al. [2] and Voth [3]. However, in the application of a padeye to CHS connection there is little research to be found. The present method of using Roark's formulas of stress and strain only assumes linear elastic material behaviour, which makes this method very conservative. Besides the material behaviour, the model is based on a two-dimensional ring model which assumes the resistance of the adjacent cross-sections to be influenced by an effective width and a distributed shear force. This is however a simplification of reality, in which some influencing factors are lost with respect to the three-dimensional model.

In order to obtain a three-dimensional model which includes the non-linear plastic material behaviour, a Finite Element Modelling (FEM) program is used. When using non-linear plastic material behaviour in the Finite Element Analysis (FEA), multiple failure criteria can be used to determine the load capacity. The disadvantages of performing a FEA is that the use of such programs require thorough understanding, are not always available and are time-consuming.

It is desired to gain an engineering tool that describes the load capacity of the padeye load case, using one of these failure criteria. This engineering tool will be similar to the equations from Wardenier et al. [2] and Voth [3], and must be an advanced method of the Roark equations. This means that the engineering tool must give a load capacity that is less conservative than the Roark equations, which can be obtained using non-linear material behaviour. The tool can be obtained by using multiple Finite Element Analysis (FEA) of the padeye load case.

3 Padeye model

3.1 Model

In order to describe the ring stresses in the CHS cross-section in the padeye load case, the load case is translated into a three-dimensional model. The load case can be modelled as a simply supported CHS with a padeye at midspan, subjected to a tensile point load at the pinhole. The CHS has a length L on either side of the padeye. Due to the vertical component of the load (F_y) on the padeye and the length of the CHS, a bending moment will be present in the CHS. This bending moment causes normal stresses in the cross-section, which are tensile at the top and compressive at the bottom. The maximum moment occurs at midspan and is described below:

$$M_{Max} = \frac{1}{4} F_y L \tag{3.1}$$

To determine the influence of padeye loading on the ring stresses in the CHS cross-section, the normal stresses due to the bending moment must be removed. With the bending moment at midspan due to the length being equal to zero, the tension and compression in the cross-sections of the connecting CHS face will be independent of the length L. In the study performed by Voth [3], a similar model is used in which end moments are used to remove the bending moment at midspan. By applying end moments that are opposite to the maximum moment, the bending moment and hence the normal forces due to the length become equal to zero at the padeye (Figure 17**Fout! Verwijzingsbron niet gevonden.**).

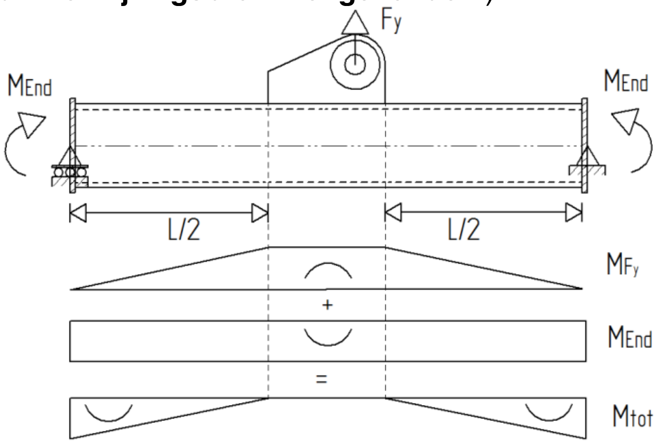

Figure 17: Moment distribution in case of end moments applied equal to the bending moment at midspan

Besides the bending moment due to the length of the CHS, the influence of the rigid end plates is also considered. Due to these rigid end plates, the circumferential deformation of the cross-section is restrained over an unknown length. This restraint deformation influences the stress distribution in the CHS cross-section.

In the literature, the chord length is described as the ratio between the length and the radius ($R = d_0/2$) of the CHS. This ratio is the chord length parameter $\alpha = 2L_0/d_0$. The value α for which the end plates no longer have influence on the deformation of the CHS at the padeye connection, is the so called ''effective chord length parameter''. For values of α larger than the effective chord length parameter, the restrained deformation is no longer present at the padeye.

In the book on Tubular Structures by Packer and Willibald [16] an effective chord length parameter $\alpha_{eff} = 20$ ($L_{eff} = 10d_0$) is given for a CHS-to-CHS T-joint, with end moments applied at both chord end supports. A similar study is performed by Voth [3] for a longitudinal plate-to-CHS X-type connection. For this connection the effective chord length parameter $\alpha_{eff} = 12$ ($L = 6d_0$) for $\gamma = 19.7$ and $\gamma = 27.6$. The effective chord length parameter for the padeye load case without ring stiffeners is studied in the Finite Element Modelling in chapter 4. From this study an α_{eff} will be determined, at which the end plates have no effect on the deformation at the padeye.

3.2 Geometry

The model of a padeye load case must be a representation of the load case occurring in projects performed by Seaway Heavy Lifting. Therefore a proper geometry has to be chosen. Because failure of the padeye is beyond the scope of this thesis, it is assumed that the padeye is adequately designed and non-critical. It is also assumed that the welded connections are stronger than the main plate, therefore the welds are non-critical, and have sufficient rotational capacity.

Full penetration welds are used in present practice to connect the main plate to the CHS. For this type of weld, shown in Figure 18, the excess weld thickness Δt_w on either side of the plate is limited to a thickness of 3 mm [17]. From comparison of padeyes used in practice (Appendix B) it can be determined that the commonly used main plate thickness t_m is equal to 70 mm. This causes the width of the welded plate-to-CHS connection ($t_m+2\Delta t_w$) to be roughly the same as the cross-sectional width of the main plate (t_m). Therefore the weld will not have significant influence on the stress distribution in the CHS cross section, and will not be taken into account.

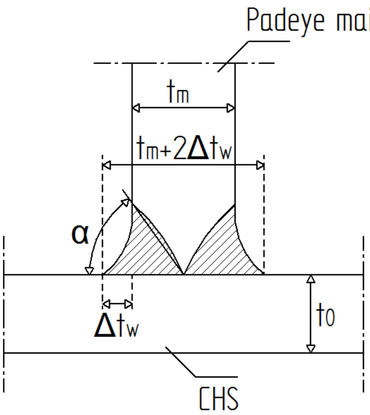

Figure 18: Full penetration weld with angle α, plate thickness T and additional weld thickness Δtw

The remaining geometry of the padeye load case can be subdivided into the padeye geometry and the CHS geometry, both consisting of multiple dimensions. These dimensions can be determined by considering several projects performed by Seaway Heavy Lifting, in which padeyes are used to lift the offshore structure. The dimensions of these different padeye connections are compared and stored in a project comparison table, Table 11 in Appendix B. In this table a minimum, maximum and mean value is determined for each dimension. The individual padeye dimensions are compared with the mean value from the comparison table, and the relative deviation from the mean value is obtained using equation (3.2).

$$D_{mean,\mathrm{rel}} = \frac{1}{n}\Sigma D_{rel} = \frac{1}{n}\Sigma\left(\frac{d_i - d_{mean}}{d_{mean}}\right) \tag{3.2}$$

With these relative deviations, a mean relative deviation is determined for the individual geometries. This mean relative deviation is given in Table 12, Appendix B. It is assumed that the padeye geometry with the least mean relative deviation gives the best representation of a padeye used in practice by Seaway Heavy Lifting. From this table it is concluded that the geometry used in project 27.1726 meets this criterion. Therefore the geometry from project 27.1726 is assumed to be the mean padeye geometry. The dimensional values from this project are given in Table 2, and an impression is shown in Figure 19.

The dimensions used in the padeye load case can be compared with the range in which the equations of Wardenier et al. [2] and Voth [3] are valid. In Table 11 it can be seen that the β ratio between the main plate and the CHS diameter ($\beta = t_1/d_0$) is ranging from 0.05 till 0.09. This is smaller than the ratio for which both the equations are valid. Therefore a new engineering tool must be determined which is valid for the geometric range considered in this thesis.

When only considering the mean geometry, the load capacity study will have no significant value. Therefore a parametric study will be performed within the geometrical boundaries from the padeye comparison table. In order to obtain a limited number of variable parameters, the dimensions of the padeye model will be subdivided into constant and variable dimensions. The constant dimensions are the padeye dimensions that are assumed to have little influence on the ring stress distribution. The variable dimensions on the other hand are the dimensions that are assumed to have a significant influence on the ring stress distribution.

Table 2: Constant padeye dimensions from project 27.1726 by Seaway Heavy Lifting

Division	Subdivision	Sign	Unity	Value
CHS	Diameter jacket/leg	d_0	[mm]	1219.2
	Thickness jacket/leg	t_0	[mm]	57.15
Padeye	Main plate base width	b_m	[mm]	1300
	Main plate radius	R_m	[mm]	375
	Pinhole radius	R_0	[mm]	111
	Cheek plate radius	R_c	[mm]	325
	Height pinhole centre	h_0	[mm]	425
	Main plate thickness	t_m	[mm]	70
	Cheek plate thickness	t_c	[mm]	50
	Height of padeye bottom	h_2	[mm]	490

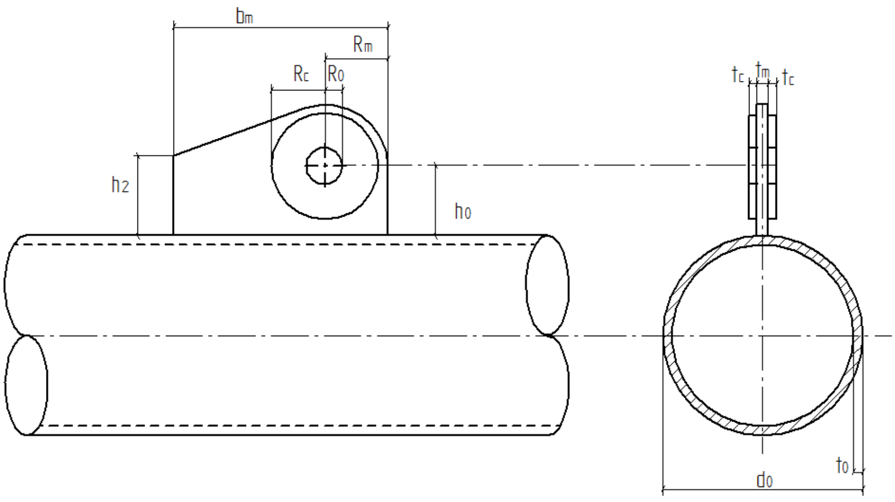

Figure 19: Geometry of the padeye load case, consisting of a padeye-to-CHS connection

3.2.1 Variable dimensions

The variable dimensions are determined from reference studies performed by Wardenier et al. [2] and Voth [3], in which the following variable dimensions are used:

- Base width of the main plate (b_m)
- Diameter of the circular hollow section member (d_0)
- Thickness of the circular hollow section member (t_0)

These dimension can be varied in different ways. First of all the padeye dimensions can be taken as a function of the plate width. When increasing the plate width, the total geometry of the padeye will increase linear (Figure 20 left padeye geometry). Second, the plate width can be varied while the height of the padeye remains constant (Figure 20 right padeye geometry). In the latter case a ratio between the padeye plate width and height is present, which is stated as $\lambda = b_m/(R_m + h_0)$.

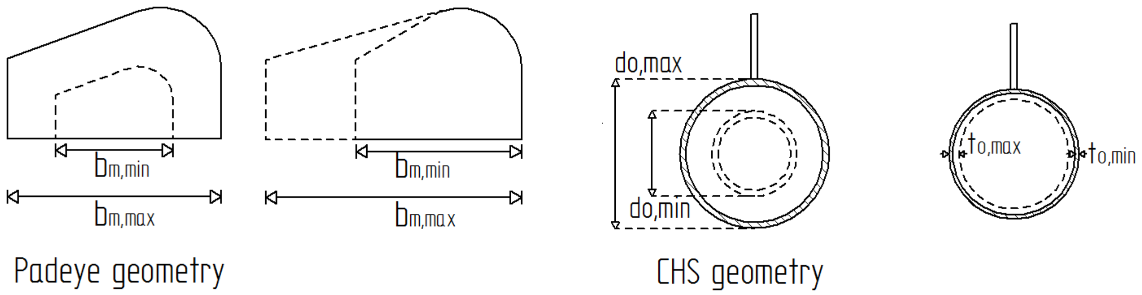

Figure 20: Variable dimensions in the padeye load case; plate width b_m (left), CHS diameter d_0 (middle) and CHS thickness t_0 (right)

The boundaries for the base width of the main plate (b_m) and the diameter and thickness of the circular hollow section (d_0 and t_0) are given by the minimum and maximum dimensional values from the comparison of padeyes used in practice (Table 3). In order to reduce the number of variable dimensions, the following two dimensionless ratios are determined:

- Nominal plate depth ratio, $\eta = b_m/d$
- Half diameter to thickness ratio, $\gamma = d_0/2t_0$

These dimensionless ratios are obtained from the reference studies of Wardenier et al and Voth. The values of the present ratios are given in Table 3.

Table 3: Boundary values of the variable dimensions:

Variable	**Unit**	**Mean**	**Min**	**Max**
d_0	[mm]	1219.2	800	1397
t_0	[mm]	57.2	35	64
b_m	[mm]	1300	1100	2000
$\eta = b_m/d_0$	[-]	1.07	0.92	1.64
$\gamma = d_0/2t$	[-]	10.67	9.33	13.50
$\lambda = b_m/(R_0+h_0)$	[-]	1.63	1.38	2.50

3.2.2 Constant dimensions

The values of the constant dimensions are equal to those used in the governing geometry from project 27.1726. These values are given in Table 4. As described in 3.2.1, the variable padeye plate width is varied in two different ways. In the first case the constant dimensions are assumed to be a function of the plate width. The ratios in which these constant dimensions are present, are equal to those found in the mean geometry and given in Table 4.

In the second case, the variable plate width is varied while the height of the padeye remains constant. This means that the height of the pinhole centre (h_0) and the radii of the main plate (R_m), cheek plate (R_c) and pinhole (R_0) will obtain the constant values stated in Table 4.

Table 4: Constant padeye dimensions from project 27.1726 by Seaway Heavy Lifting

Division	**Subdivision**	**Sign**	**Unity**	**Value**	**Ratio**
Main plate	Main plate radius	R_m	[mm]	375	$b_m/3.5$
	Pinhole radius	R_0	[mm]	111	$b_m/11.7$
	Cheek plate radius	R_c	[mm]	325	$b_m/4.0$
	Height pinhole centre	h_0	[mm]	425	$b_m/3.1$
	Height padeye bottom	h_2	[mm]	490	$b_m/2.7$
	Thickness main plate	t_m	[mm]	70	$b_m/18.6$
	Thickness cheek plate	t_c	[mm]	50	$b_m/26.0$

3.3 Simplified geometry

The padeye load case consist of many different parameters, both constant and variable. Many of these parameters influence the stiffness of the main plate. The stress distribution in the padeye, and hence the stress distribution in the CHS, is dependent of this main plate stiffness. In order to obtain a good understanding of the load path active in the load case, the load case has to be simplified. This can be achieved by narrowing down the number of dimensions that is used.

The influence on the padeye stiffness is due to the presence of cheek plates and the variation between the height at top and bottom of the padeye main plate. By neglecting these influencing factors, the remaining geometry is equal to that of a plate-to-CHS model shown in Figure 21.

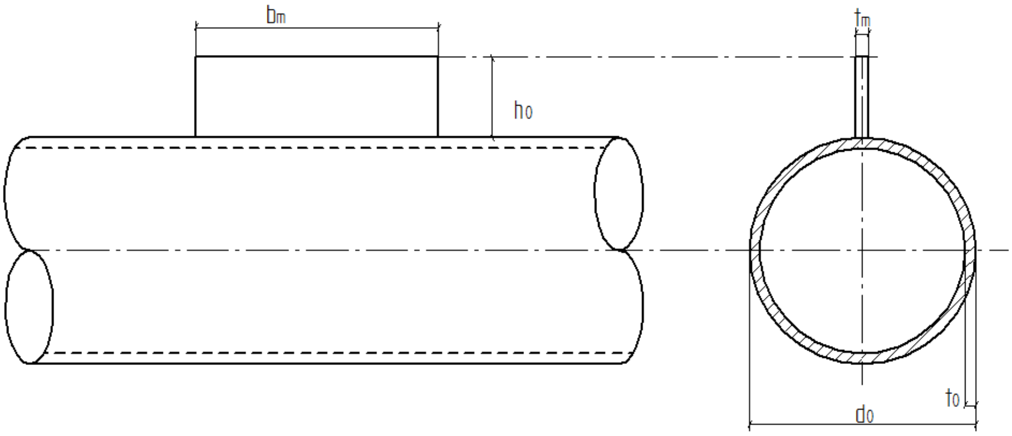

Figure 21: Geometry of the plate load case, consisting of a plate-to-CHS connection

The plate model consists of an rectangular plate with a height h_0, a plate width of b_m and a plate thickness t_m. The CHS geometry remains equal to the padeye model, in which it consists of a diameter d_0 and a thickness t_0. The variable dimensions in the plate model are the same as in the padeye model (d_0, t_0, b_m). These dimensions will vary between the same minimal and maximal values and are shown in Figure 22.The constant dimensions in the model are the plate height h_0 and plate thickness t_m, which will be the function of the plate width b_m as stated in Table 4.

With a reduction of dimensions in the plate model with respect to the padeye model, the padeye model is simplified significant. The plate model is used to gain a good understanding of the load case behaviour for the variable dimensions.

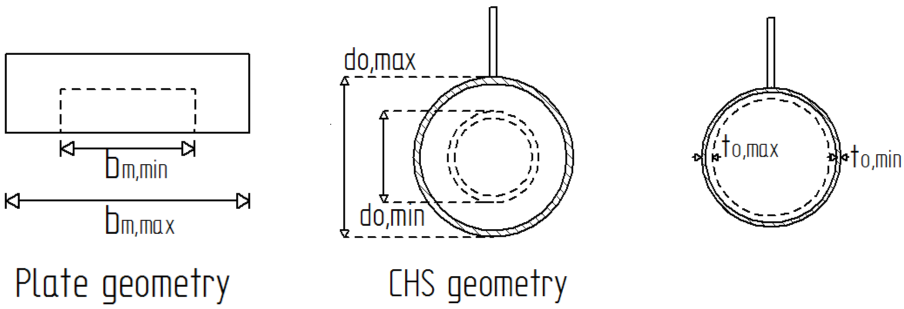

Figure 22: Variable dimensions in the plate load case: plate width b_m (left), CHS diameter d_0 (middle) and CHS thickness t_0 (right)

3.4 Conclusion

In order to obtain a geometry for the padeye load case which is a representation of the padeyes used in practice within Seaway Heavy Lifting, several projects performed by Seaway Heavy Lifting are compared. From this comparison, a governing padeye geometry is chosen. The padeye geometry assumed to be governing is used in project number 27.1726. This geometry is subdivided into constant and variable dimension. The variable dimensions are the dimensions which have a large influence on the stress distribution and hence the load capacity, while the constant dimensions are those with little influence on the stress distribution.

Besides the padeye load case, a simplified plate load case is modelled with a reduced amount of dimension as in the padeye load case model. Because the plate model has less dimension influencing the stress distribution, it will be used to gain a good understanding of the variable dimension on the load case behaviour. By using the similarities in the two load cases, the load capacity in the padeye load case can be determined. The constant and variable dimensions used in the plate load case are equal to those used in the padeye load case.

Finally it must be noted that the padeye geometry is beyond the range used in the equations of Wardenier et al. and Voth. Therefore an engineering tool must be determined which is valid for the geometric range of the padeye load case.

4 FEM Modelling

To gain a thorough understanding of the behaviour of the padeye load case, a finite element analysis (FEA) will be performed. To perform a finite element analysis, the structure is turned into a mathematical model of the system. In this model the structure is divided into a finite number of elements, hence the name finite element model. The model, consisting of many elements, is able to simulate and predict the behaviour of the structure.

Because the solution from the finite element method heavily relies on the factors and parameters that are used, the validity of the model has to be investigated. Without a thorough understanding of the solution method, input needed and the correct functions, a correct behaviour of the response cannot be gained. As they say: “garbage in, garbage out”. The validity of the models can be investigated using the theory of finite element modelling by Wells [18]. The several factors that have to be validated are the boundary conditions, the elements type, the element size and the type of analysis. These factors will be discussed in the following paragraphs.

4.1 Geometry

As described in chapter 2.6, two simplified three-dimensional models will be used: a plate-to-CHS connection and the padeye-to-CHS connection (Figure 23). The first model will be used to gain a good understanding of the behaviour of the CHS under radial loading by a plate, and will be denoted as the plate load case. With this knowledge the behaviour of the CHS under radial loading by a padeye can be studied, which is in fact a more complex plate-to-CHS connection. This model will be denoted as the padeye load case from this point onwards.

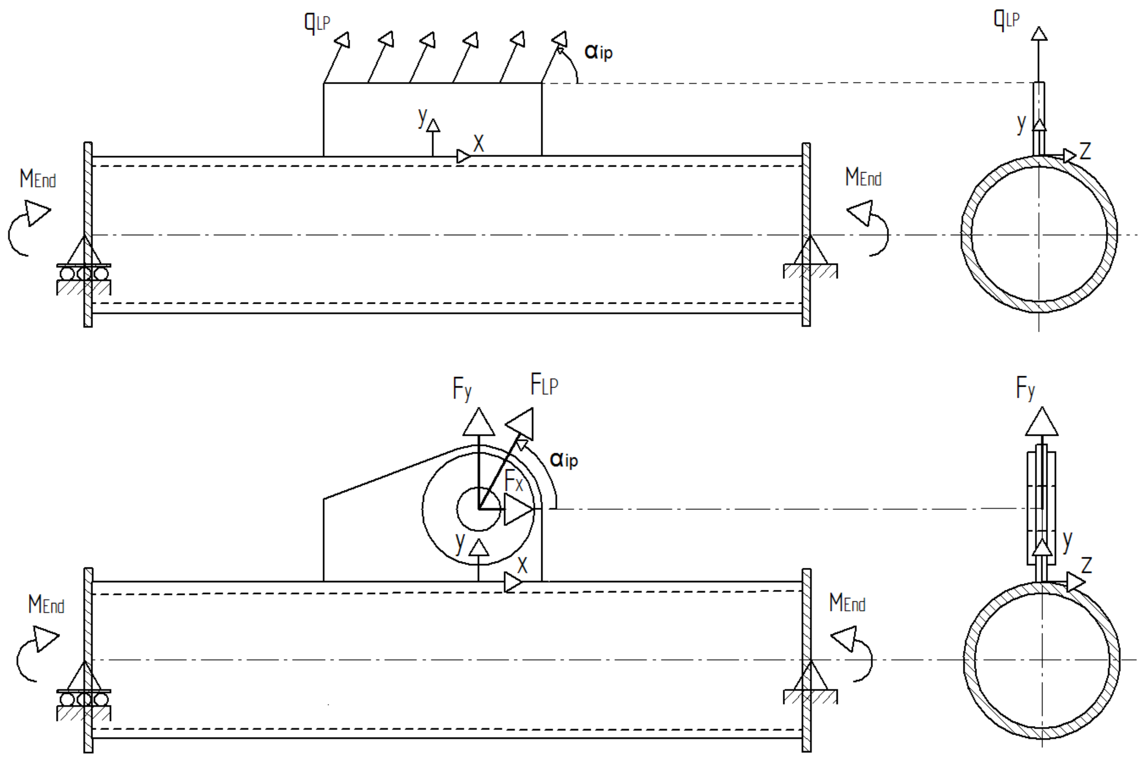

Figure 23: Three-dimensional plate-to-CHS connection model (top) and padeye-to-CHS model (bottom)

4.1.1 Boundary conditions

The boundary conditions which are used in both the padeye and the plate load case can be divided into essential and natural boundary conditions. The essential boundary conditions involve conditions with respect to displacements, whereas the natural boundary conditions involve conditions with respect to forces.

The essential boundary conditions contain several types of displacement conditions, which can be used to provide a better prediction of the system or to gain a shorter computational time. Support constraints are applied such that the construction is statically determined, preventing rigid body motion of the structure. The degrees of freedom, according to the active coordinate system, which have to be constrained are the following:

- u_x, u_y, u_z = translations in the direction of the x,y and z axis respectively
- θ_x, θ_y, θ_z = rotations around the x,y and z axis respectively

In the models a rigid end plate is attached at the CHS at the supports, which means that a rigid cross section is assumed. This can be obtained by using the CERIG command in Ansys, generating constraint equations needed for defining rigid links between a master and slave node (Figure 24). The boundary conditions are applied at the master node and then translated to the slave nodes. For both boundaries the master node lies in the origin of the CHS cross-section and is defined as a ''Mass 21 elements''. The slave nodes are defined as the nodes in the CHS cross-section. The end moments which are active in the model are applied on the master nodes at both boundaries and act on the origin of the CHS. The master nodes translate the bending moment to normal forces working on the CHS cross-section.

Besides the support constraints, symmetry conditions can be applied in the model using solid elements. These conditions impose symmetry at the vertical y-axis, along the z = 0 plane in longitudinal direction of the CHS. By applying these symmetry conditions, the computation time is reduced. The essential conditions used are shown in Figure 24 and described below:

- Left support:
  - Translation: $u_x = 0$, $u_y = 0$, $u_z = 0$
  - Rotation: $\theta_x = 0$, $\theta_y = 0$
- Right support:
  - Translation $u_y = 0$, $u_z = 0$
  - Rotation: $\theta_x = 0$, $\theta_y = 0$
- Along plane z = 0
  - Translation: $u_z = 0$
  - Rotation: $\theta_x = 0$, $\theta_y = 0$

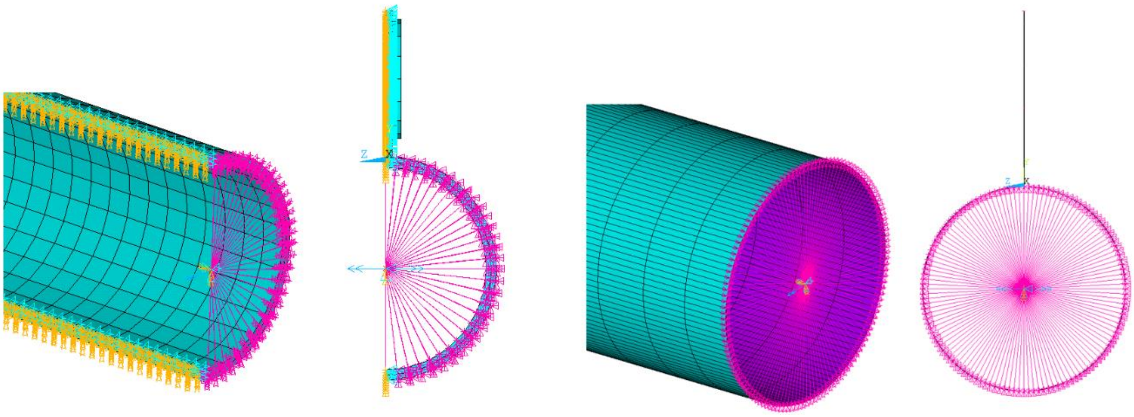

Figure 24: Support constraints and symmetry conditions in the case of solid elements (left) and shell elements (right)

The natural boundary conditions contain the applied forces, which can be applied as concentrated point loads and distributed line, area or volume loads. Distributed loads are more commonly used than concentrated point loads, because a point load isn't a very good representation of reality. The distributed line, area and volume loads are measured in force per unit length, area or volume respectively.

In the plate load case, a distributed load is applied on the top of the plate. This is done in both the model consisting of shell and solid elements. In the case of solid elements, only half the force is applied due to the applied symmetry conditions.

The force acting on the padeye is applied at the centre of the pinhole. Two different methods are used to model the force for both the model using shell elements and the model using solid elements. In the model using shells elements the force is modelled similar to the boundary condition. This model is called the cartwheel model, which is used within Seaway Heavy Lifting. Link 10 elements are created between a node at the pinhole centre and the nodes on the interior of the pinhole. The link elements only transfer force when in compression. The force is applied on the node in pinhole centre as a component in x- and y-direction (Figure 25).

In the model using solid elements a bearing load is derived from Ansys Workbench. This bearing load uses "Surface 154 elements" which are applied on the interior area of the pinhole. The load is transferred from the surface elements to the connecting nodes. The force is applied on the surface elements and only transfers load if the normal of the surface elements is negative with respect to x-axis in the local coordinate system. This local coordinate system has its origin in the pinhole centre and is applied under an angle α_{iP}, having its positive x-axis in the direction of the force. Similar to the plate load case using solid elements, only half the load is applied due to the use of symmetry.

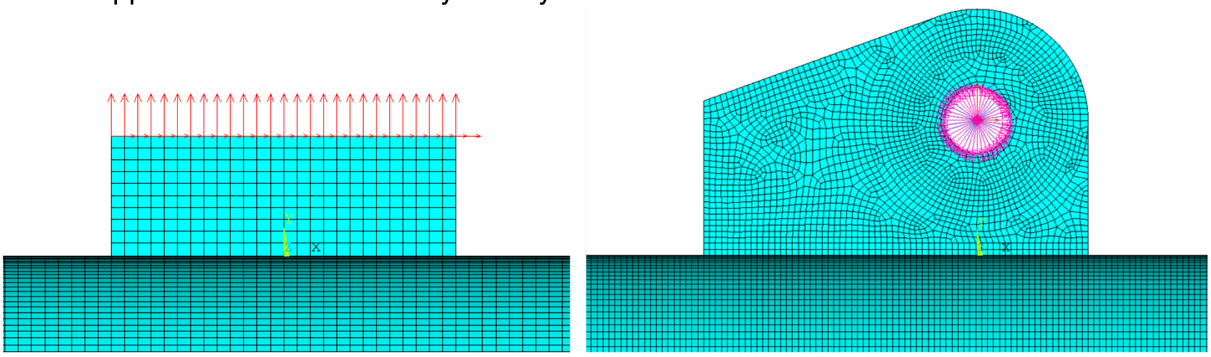

Figure 25: Natural boundary conditions in the plate load case using distributed loading (left) and the padeye load case using the cartwheel model (right)

4.2 Mesh

Meshing gives a discrete representation of the system geometry. Meshing divides areas or volumes of the finite element model into small elements over which the equations are numerically approximated. By using a finer mesh, the model consists of more elements than it would in a coarse mesh. By approximating the equations for many elements, a good representation is given of the stress/strain distribution over the area/volume. If the mesh is for instance coarse, the model consists of fewer elements and thus a rough representation of the stress/strain distribution is given. A representation of a fine and a coarse mesh is shown in Figure 26. Because a fine mesh results in a longer computation time, an optimal mesh should be determined. As an alternative of choosing a fine mesh for the total model, the mesh can also be refined at certain locations. The locations at which mesh refinement may be necessary are regions where a high stress/strain ratio is expected such as near entrance corners, at concentrated (point) loads, at abrupt changes in geometry and at abrupt changes in material properties.

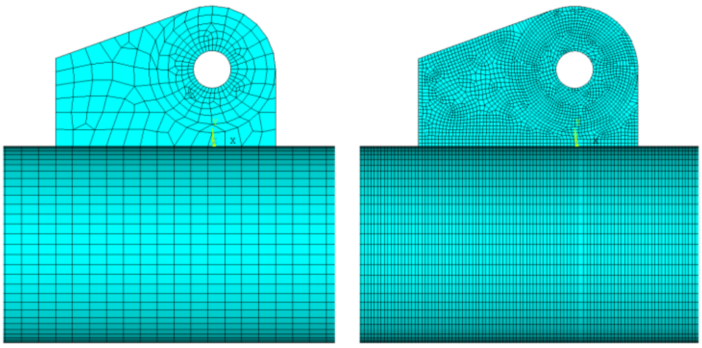

Figure 26: Model element size; Coarse mesh (left) versus a fine mesh (right)

The mesh can be made out of several element shapes. Because both the padeye and the plate load case are three-dimensional, only the three-dimensional shapes are considered, these are:

- Tetrahedron
- Pyramid
- Triangular prism
- Hexahedron

The accuracy of the mesh is, besides the density, also depending on some other factors. These factors are the skewness (indicator of the mesh quality and suitability), smoothness (change in size should be smooth) and aspect ratio (ratio of shortest and longest side of the cell) of the different mesh elements. Improving these factors would improve the quality of the outcomes of the FEM analysis.

4.2.1 Element type

Each element has multiple degrees of freedom (DOF's), representing the translations and rotations of the element in which the response is expressed. The number of degrees of freedom used is dependent on the element dimensions. The elements can have one, two or three dimensions. Each element also consists of a number of nodal points or nodes. These nodes define the element geometry and are the points at which the DOF's of the element are applied. The element shape is defined between these nodes and the accuracy of each element depends on the number of nodes that is used, which is depending on the order of the element used. Multiple element geometries are shown in Figure 27.

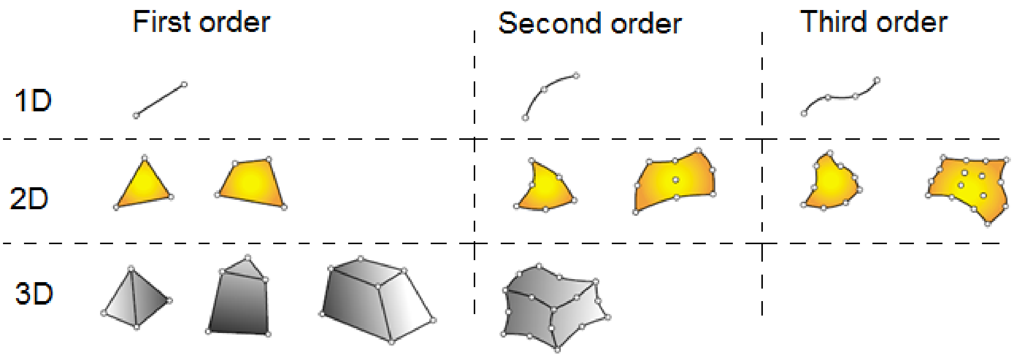

Figure 27: Dimension and order of elements, depending on the number of nodes active in the element

The different types of structural elements (beams, plates, shells etc.) rely on different theories. Therefore different types of element are applicable. The different types of elements are link, beam, pipe, solid, shell and solid-shell elements. In the case of both the padeye and plate load case, a three-dimensional model is considered. These models consist of a circular hollow section (CHS) and a plate, therefore the following element types are considered:

- Shell elements are used to model structural elements in which two dimensions are much greater than the third one and when the change of the analysed stresses/strains in this third direction can be neglected. This is applicable for static analysis of elements such as plates, slabs and thin-walled shells. The advantages of the use of shell elements results mainly in time-saving due to reduced number of finite elements (and thus the number of equations to solve).
- Solid elements are used if the change of the analysed stresses/strains is significant in all directions of the analysed element. This will be the case if the thickness of the CHS is large with respect to the diameter.
- Solid-shell elements are used in case of shell structures with a wide range of thickness. This type of elements can be used for multi-layered materials such as composites in which thickness, material and orientation differ through the thickness. However, both the padeye and the plate load case consist of steel which is an isotropic material. Therefore the solid-shell elements is not used to create the finite element model.

The analysis is performed using the Shell 181, Shell 281, Solid 185 and Solid 186 elements. The applied elements are shown in Figure 28. Both Shell 181 and Solid 185 use only nodes on the edges, whereas Shell 281 and Solid 185 elements use additional mid-side nodes. Using mid-side nodes makes the element more accurate. However, it is possible mid-side nodes get linked to edge nodes in a connection. This causes numerical inaccuracy of the solution obtained from the analysis.

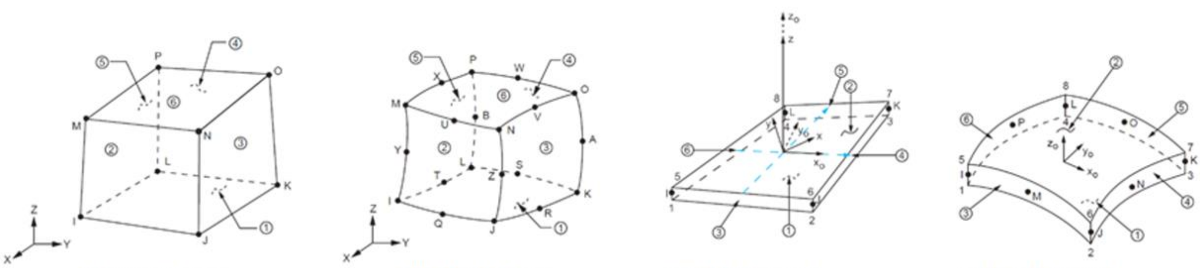

Figure 28: Elements used in the padeye/plate load case: Solid 185, Solid 186, Shell 181 and Shell 281 elements

4.2.2 Element size

The size of the elements that is used in the model, determines if the mesh is coarse or fine. With smaller element sizes, the mesh becomes finer. Because a smaller element size means a more accurate solution but also a longer computation time, an optimal element size is determined. In order to obtain such optimal element size, the results from the finite element analysis using different element sizes have to be compared.

The accuracy of the model is defined as the difference of the displacement and stress in a certain point of the structure, for varying element sizes. Using different element sizes, a difference in the results that is less than 5% is considered sufficient [18]. This would mean that for smaller element size results will converge to a single solution.

Because the padeye load case is governing, the results are considered for this load case only. From the finite element model the displacement vector (u_{sum}) and the Von Mises equivalent stress (σ_{eqv}) are obtained. These results are taken from a node at a significant location in the model, where there are no abrupt changes in geometry which could lead to inaccuracy due to peak stresses. The goal of this thesis is to determine the governing ring stresses at the padeye, therefore the results are taken from the CHS cross-section at bottom of the padeye. Because peak stresses occur at the intersection of the main plate and the CHS, the results will be obtained from the location of node 1 in Figure 29. This node is located in the CHS cross-section at the padeye main plate bottom, at half the diameter in y- and z-direction.

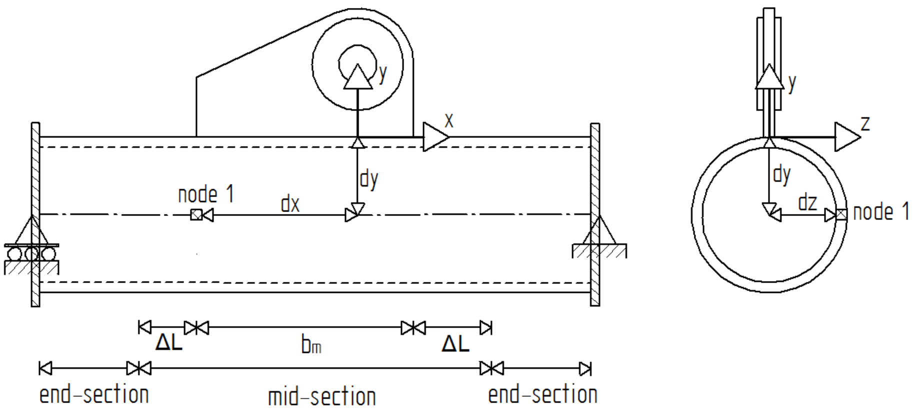

Figure 29: Location of node 1 in which the output from the Finite Element Analsysis (FEA) is obtained

The analysis is performed using the Shell 181, Shell 281, Solid 185 and Solid 186 elements. When using the solid elements, the CHS thickness (t_0) is divided into 2, 4 and 8 elements to determine the accuracy. For all types of element the element sizes 150 mm, 100 mm, 50 mm and 20 mm are used in the analysis.

The displacement (u_{sum}) and stress (σ_{eqv}) obtained from node 1 in the padeye load case, are plotted against the corresponding element size (Appendix C). For both solid elements the governing number of elements over the thickness is determined, which can be compared with the use of shell elements. In Figure 30 the resulting Von Mises stress and the displacement vector are compared. From these graphs it is obtained that for all element types, the results converge to a single solution for element sizes smaller than 50 mm. The Shell 281 and the Solid 185 elements converge rather quickly with respect to the Shell 181 and Solid 185 elements, due to the use of mid-side nodes. The computation time of these element using mid-side nodes is however much longer. Besides this, it can also be noted that both shell elements converge to a single solution, where the solid elements each converge to a separate solution. From these results the optimal element type is assumed to be the Shell 181 elements with an element size of 20 mm.

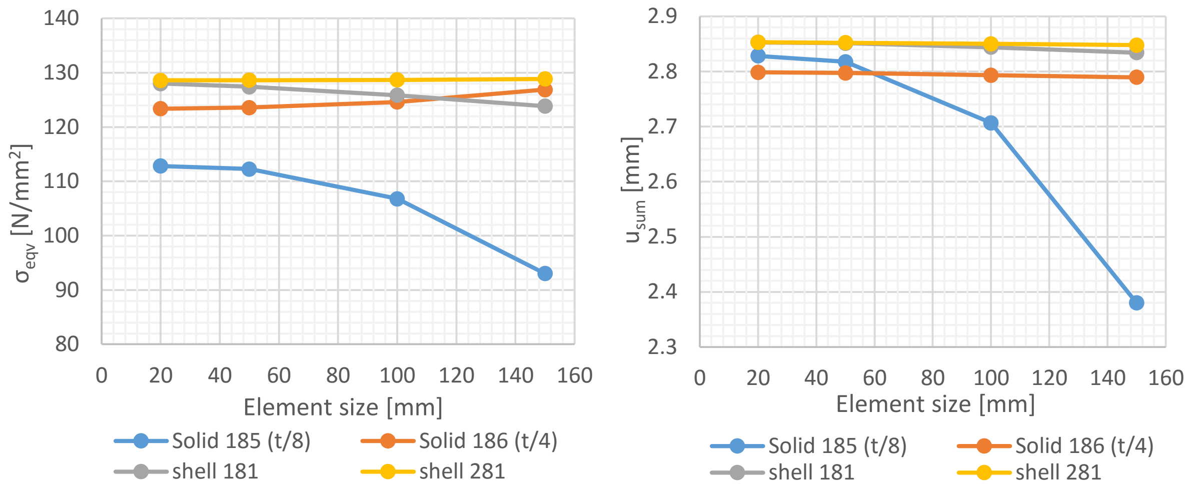

Figure 30: Von Mises equivalent stress at location of node 1 for different element type and size

In order to reduce the computation time of the model using "Shell 181 elements", the element size will be changed for locations with uniform cross-section. The cross-section is uniform for the CHS with no added padeye or plate. The model can be divided into a non-uniform mid-section and two uniform end-sections, shown in Figure 29. In order to maintain the accuracy at the location of the padeye/plate, the mid-section spans beyond the main plate with a length ΔL. The mid-section will have element size N_1 = 20 mm, while the end-sections will have a different element size N_2 to reduce computation time. In order to determine the element size N_2 and the length ΔL, both will be varied while element size N_1 will remain unchanged. By comparing the displacement vector and the Von Mises stress in node 1 for the different element size N_2 and the length ΔL, a final model can be assumed.

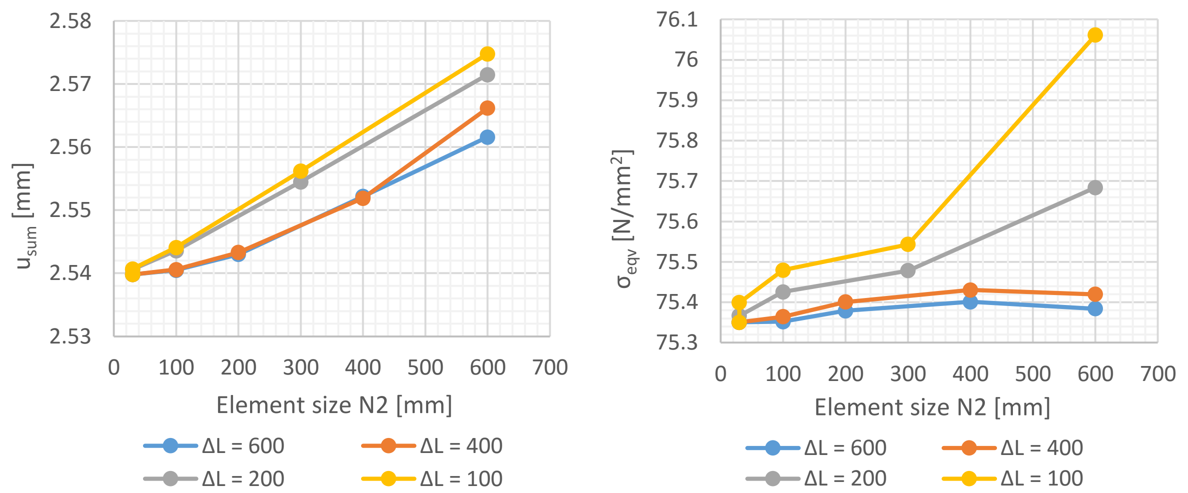

Figure 31: Displacement vector and Von Mises stress at the location of node 1 for different length ΔL and element size N_2

The displacements and stresses from these analysis are given in Appendix C, and are shown in Figure 31. In these graphs the case of element size N_2 = 20 mm is equal to the case of uniform element size N_1 = 20 mm. At the transition from mid-section to the edge-section the element size N_1 and N_2 are active. Due to this, the elements in the edge-section will have a height equal to N_1 and a width equal to N_2, creating elements with an aspect ratio may not exceed a value of 20. If the aspect ratio exceeds this value, the solution could contain numerical errors. In order to obtain an accurate model with low computation time, an element size N_2 is assumed to be 300 mm and a length ΔL equal to 400 mm.

4.3 CHS length

By using the end moments at the support, the bending at mid-span due to the chord length is balanced. The length of the chord does however still influence the stress distribution in the CHS cross-section. Because end plates are used at the supports, the deformations in the CHS cross-section are restrained. This restrained deformation of the cross-section occurs over a certain length of the CHS, influenced by the end plates. Because the stresses are related to the displacements, the stress distribution over this length is also influenced by the end plates.

The chord length is chosen in such a manner that the influence of this chord length on the stresses and displacements at the padeye can be neglected. The chord length can be expressed as the ratio between the length and the diameter of the CHS, which is known as the chord length parameter $\alpha = 2L_0/d_0$. The parameter for which the stresses and displacements are no longer influenced is called the effective chord length parameter. To determine the effective chord length parameter, the displacement of the CHS in radial direction is obtained for different chord lengths. The results are obtained for node 1 (Figure 29) in the CHS at the location of the padeye, in which the radial displacements are assumed to be large.

A linear elastic analysis is performed with chord length parameters α for the minimal, maximal and mean ratios of γ_0. The results are plotted in Figure 32 for the padeye load case and the plate load case. From these graphs it can be seen that the radial displacement meet the 5% convergence criterion at an effective chord length parameter of $\alpha = 12$. This constant value will be used from this point onwards.

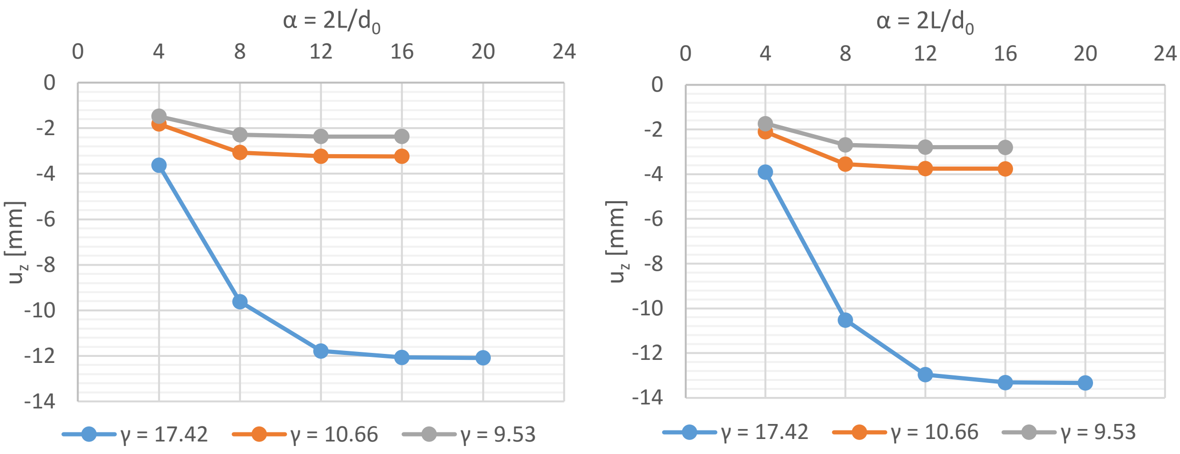

Figure 32: Effective chord length for the padeye load case (left) and the plate load case (right), with β = 0.94

4.4 Reinforced band

With a length parameter α of 12, both the padeye model and the plate model consist of a slender CHS with a bending moment at the supports. These bending moments cause normal forces in the CHS cross-section. In case of a small CHS diameter d_0 these normal forces will be high, resulting in local yielding of the CHS at the support. Due to this local yielding, failure of the CHS can occur at the support before failure at the plate-to-CHS connection. This failure mode, shown in Figure 33, is however not the considered failure mode of this study.

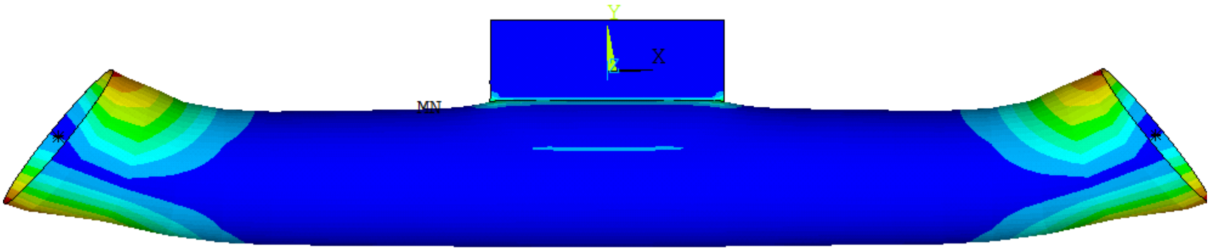

Figure 33: Local plastic yielding in the plate model due to bending moments at supports

The local failure due to the bending moment can be prevented by using a cross-section with a higher strength at the supports. This cross-section can be seen as a reinforced band of the CHS. The reinforced band may not influence the deformation and stresses of the padeye to CHS connection. Therefore it must have the same stiffness and geometry as the rest of the CHS, but a higher yield stress. This is obtained by applying the same Young's modulus and a higher yield stress of σ_y = 500 N/mm^2 at the reinforced band.

By varying the length of the reinforced band, the optimal length can be determined at which an increase of the length does not lead to variations in the deformations of the CHS cross section at the location of the padeye. In Appendix C, a feasible length of 800 mm is determined.

4.5 Analysis

To obtain the stresses from the Finite Element Model, an analysis is performed. A distinction can be made between the linear and nonlinear analysis type. In the linear elastic analysis the displacements are assumed small, the strain is proportional to the stress, the loads are independent of displacements and the supports remain unchanged during loading.

The nonlinear analysis can be subdivided in geometrical nonlinearities, material nonlinearities and boundary nonlinearities. These nonlinearities are briefly described below:

- The geometrical nonlinearities take into account the effect of large displacements on the overall geometric configuration. Because of these large displacements the applied force angle will change during loading, causing the force to change.
- The material nonlinearities take into account the fact that the material behaviour is not linear. The material models that can be used in this analysis are nonlinear elastic, elastoplastic, viscoelastic and viscoplastic.
- The boundary nonlinearities takes into account the displacement dependant boundary conditions. These nonlinearities are usually found in contact problems, in which a force is modelled that can only have influence on a structure when it has a contact area.

With the limited displacements in the padeye load case in order to maintain the serviceability, geometrical nonlinearity is not applied. Because peak stresses occur in both the padeye and the plate load case, the yield stress is reached at a relatively low load. Therefore plasticity is wanted in the model in order to allow redistribution of the stress. In order to allow plasticity to occur, a nonlinear analysis is performed using material nonlinearity.

In the padeye used in projects performed by Seaway Heavy Lifting, S355 steel is mainly used. During this plastic behaviour of this type of steel, some of the stiffness is regained, which is called strain hardening. The material properties of S355 steel are obtained from DNV [10] and are shown in Table 5. The plastic behaviour can be described using simplified multi-linear plastic stress-strain curve with a yield plateau and strain hardening (Figure 34).

Table 5: Proposed non-linear properties for S355 steels (Engineering stress-strain) from DNV RP-C208 [10]

	S355		
Thickness [mm]	$t \leq 16$	$16 < t \leq 40$	$40 < t \leq 63$
E [MPa]	210000		
$\sigma_{prop}/\sigma_{yield}$	0.9		
E_{p1}/E	0.001		
σ_{prop} [MPa]	319.5	310.5	301.5
σ_{yield} [MPa]	355	345	335
σ_{yield2} [MPa]	358.4	348.4	338.4
σ_{ult} [MPa]	470	470	450
ε_{p_y1}	0.004		
ε_{p_y2}	0.02		
ε_{p_ult}	0.15		
E_{p2}/E	0.0041	0.0045	0.0041

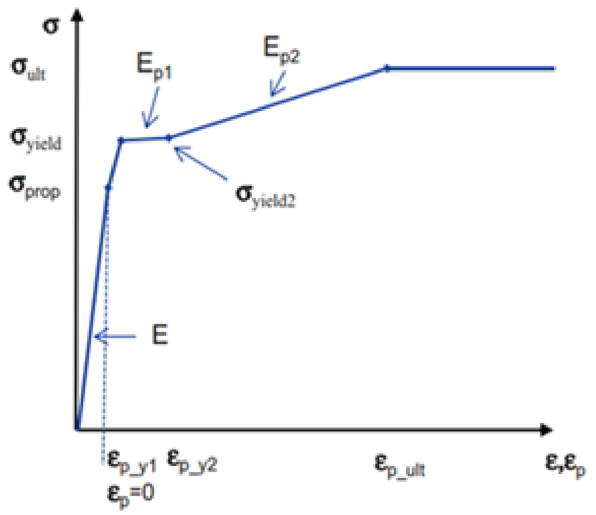

Figure 34: Multi-linear stress-strain curve with strain hardening from DNV [10] for steel S355;

4.6 Conclusion

By using Ansys Mechanical, the padeye load case can be translated into a finite element model. In this numerical model of the padeye load case, the load capacity can be determined by performing a non-linear plastic analysis.

In order to properly use the model, a number of assumptions are made. These assumptions are given below:

- The length of the CHS is taken equal to 6 times the CHS diameter d_0. By doing this the stiff end plates have little influence on the deformation of the CHS cross-section at the location of the padeye.
- The element size is assumed to be 20 mm in order to obtain an accurate solution for the stresses and deformations in the load cases.
- To reduce computation time without losing accuracy of the solution, the element size at both end spans of the CHS is chosen to be 300 mm, gaining a coarser mesh. This end span is the length of the CHS from the support onto a point 400 mm from the padeye/plate.
- At both sides of the CHS end span, a reinforced band of 800 mm is applied, with a yield stress of 500 N/mm^2 instead of the 335 N/mm^2 used for the rest of the construction. The reinforced band prevents the CHS to yield due the applied end moments. If no reinforced band will be applied, the CHS at the support could fail before the padeye-to-CHS connection fails due to plastic yielding.

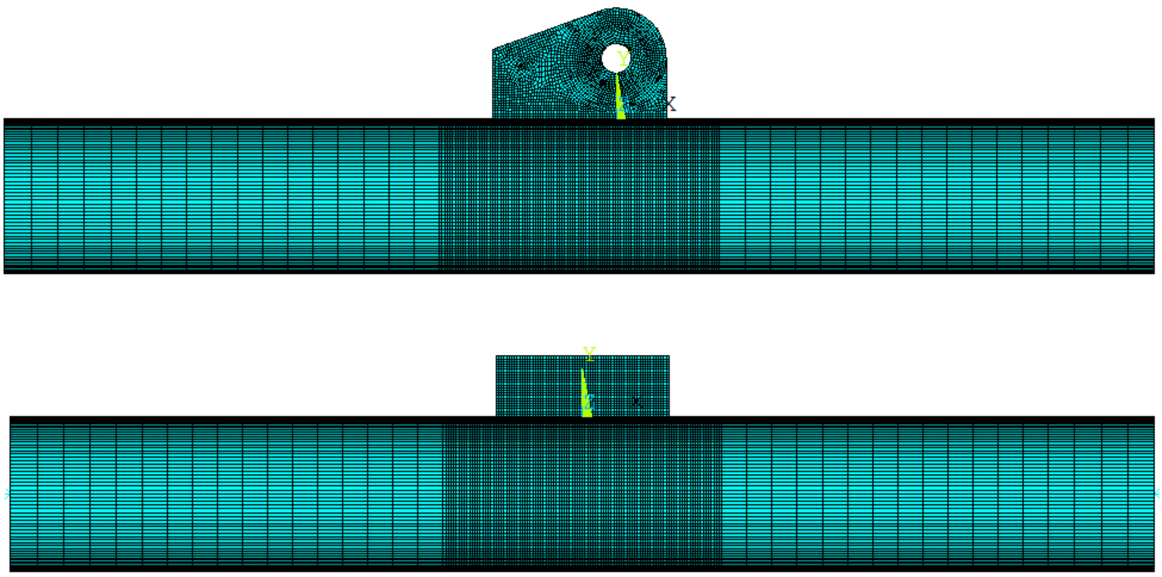

Figure 35: Finite Element Model of the padeye and plate load case

5 Analytical model

Beside the use of a finite element method, the padeye load case is described analytical. For the derivation of the analytical two-dimensional ring model, the Euler-Bernoulli curved beam theory is used. In this theory it is assumed that the thickness of the ring is relatively thin, causing little variation in shear stress over the height of the beam cross-section. In contrast to the use of a FEM model, the Euler-Bernoulli theory assumes a linear stress-strain relation, meaning that there is no plastic material behaviour. Therefore the analytical model will only be used to describe the data, which follow from the model using a FEM program.

5.1 Euler-Bernoulli curved beam theory

In order to derive a ring model which describes the padeye load case, the load case is simplified. In present practice within Seaway Heavy Lifting, Roark load case 20 (Figure 36) is used to calculate the load capacity of the padeye load case. Therefore the model geometry is assumed that be identical to the geometry used in Roark load case 20. Because the ring geometry is symmetrical, only half of the model will be considered. In this model half a ring is subjected to a point load W/2, which is balanced by a uniform distributed transverse shear force v. The transverse shear force in the ring model is representing the resistance of the adjacent cross-sections against displacement due to applied force. This shear force is assumed constant and is given below:

$$v = \frac{W}{4Rb} \tag{5.1}$$

The direction of the force in the Euler-Bernoulli model is however different from the force used in the Roark load case. In the Euler-Bernoulli model the applied force W/2 is working as a tensile force on the structure, whereas in the model used in Roark the force is applied as a compressive force. Besides this it must be noted that the Roark load case model and the model using Euler-Bernoulli have a different orientation of the axis. To compare the results between both models, the shear force and bending moment values f from Roark have to be multiplied by -1.

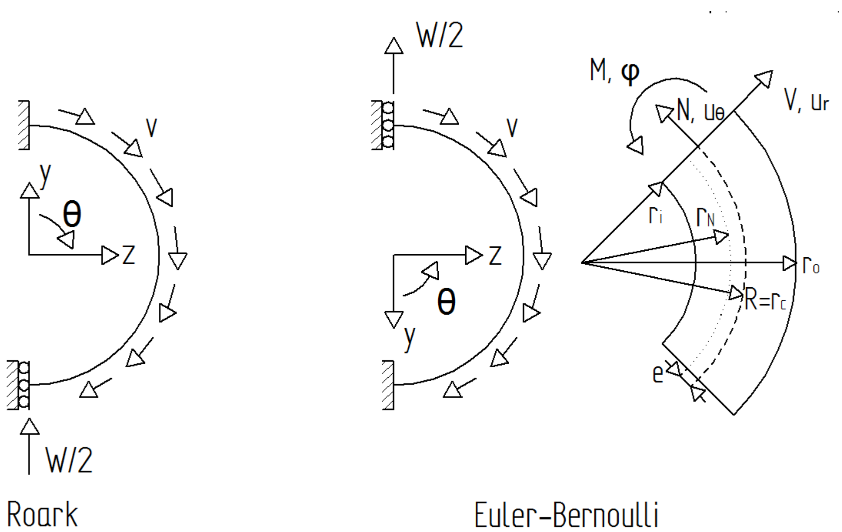

Figure 36: Roark load case 20 [13] (left) and the Euler-Bernoulli curved beam model (right), including notation

Using the model geometry described above, the decoupled differential equations given in (5.2) can be solved. In these differential equation there are two unknowns, which are the transverse displacement (u_θ) and the radial displacement (u_r). The strains, stresses and forces are related to the displacements. Thus by solving the equations for the displacements, the stress distribution is known.

$$\frac{d^5u_r}{d\theta^5}+2\frac{d^3u_r}{d\theta^3}+\frac{du_r}{d\theta}=\frac{R^4b}{EI}v-\frac{R^2b}{EA}\frac{d^2v}{d\theta^2}$$
$$\frac{du_\theta}{d\theta}=-Q\left(\frac{d^4u_r}{d\theta^4}+\frac{d^2u_r}{d\theta^2}\right)-u_r-\frac{QR^2b}{EA}\frac{dv}{d\theta} \tag{5.2}$$

$$in\ \ which:\quad Q=\frac{EI}{EI+R^2EA}$$

In order to solve the equations, boundary conditions have to be applied. Just like in the FEM model, essential and natural boundary conditions are used. The essential boundary conditions are expressed in symmetry conditions at the top and bottom of the ring. At the top of the ring ($\theta = \pi$) the transverse displacement and rotation are restrained, while the radial displacement is free. At the bottom of the ring ($\theta = 0$) the model is fixed, meaning that all displacements and rotations are restrained. Beside the essential conditions only one natural boundary condition is used in the model. This condition is the force which is the applied at the top of the ring ($\theta=\pi$). All the boundary conditions used in the padeye load case model are shown in (5.3).

$$\theta_i=0\begin{cases}u_r(0)=0\\u_{\theta0}(0)=0\\\phi(0)=0\end{cases}\qquad \theta_i=\pi\begin{cases}u_{\theta0}(\pi)=0\\\phi(\pi)=0\\V(\pi)=\dfrac{W}{2}\end{cases} \tag{5.3}$$

Both differential equations stated in (5.2) are solved in Appendix D with the boundary conditions stated above, obtaining the equations for the displacements. With these displacement equations, the solution for the normal force, shear force and the bending moment are obtained. The results from the model using the Euler-Bernoulli curved beam theory are stated in (5.4) and can be compared with those from Roark load case 20 (5.5). Due to the difference in directions in both the coordinate systems, the shear force and the bending moment have to be multiplied with -1 in order to be compared, as denoted before.

It can be seen that both methods give similar equations for normal force, shear force and bending moment. All equations consist of sine and cosine functions, whereas in the equations of the bending moments and additional constant is applied. In the bending moment equation from Roark, this constant factor is called the hoop stress deformation factor k_2. This factor is a ratio between the bending stiffness and the extensional stiffness.

A similar factor is used in equations from the Euler-Bernoulli model. This factor ξ is a ratio between the extensional stiffness and the sum of both the rotational and extensional stiffness. Where the factor k_2 is only used in the bending moment equation, the factor ξ is present in the equations of the normal force, shear force and the bending moment.

$$
\begin{aligned}
N(\theta) &= \frac{W}{\pi}\left(\frac{\pi}{4}\sin(\theta) - \xi\cos(\theta)\right) \\
V(\theta) &= \frac{W}{2\pi}\left(\frac{\pi}{2}\left(\cos(\theta)-1\right) + 2\xi\sin(\theta)\right) \\
M(\theta) &= \frac{WR}{2\pi}\left(\frac{1}{2}\pi\left(\theta - \sin(\theta)\right) + 2\xi\cos(\theta) + 1 - \frac{\pi^2}{4}\right) \quad with: \quad \xi = \frac{AR^2}{AR^2 + I}
\end{aligned}
\tag{5.4}
$$

$$
\begin{aligned}
N(\theta) &= \frac{W}{\pi}\left(\frac{3}{4}\cos(\theta) - \frac{\theta}{2}\sin(\theta)\right) \\
V(\theta) &= -\frac{W}{2\pi}\left(\theta\cos(\theta) + \frac{1}{2}\sin(\theta)\right) \\
M(\theta) &= -\frac{WR}{2\pi}\left(\frac{1}{2}\cos(\theta) + \theta\sin(\theta) - k_2\right) \qquad with: \quad k_2 = 1 - \frac{I}{AR^2}
\end{aligned}
\tag{5.5}
$$

Because there is an interaction between the normal force, shear force and bending moment, the Von Mises equivalent stresses is considered. In order to calculate the Von Mises stress distribution in the ring model, the transverse and radial stress must be determined. The transverse stress consist of the stress due to bending moment and normal force in the beam, while the radial stress consists of stress due to shear force. The Von Mises equivalent stress in the ring is obtained with the equations stated in (5.6).

$$
\sigma_{eqv} = \sqrt{\left(\sigma_\theta{}^2 + \sigma_r{}^2 + 3\tau_{r\theta}^2\right)} = \sqrt{\left(\left(\sigma_{\theta,N} + \sigma_{\theta,M}\right)^2 + 3\tau_{r\theta}^2\right)} \tag{5.6}
$$

The transverse and radial stress distributions in the ring can be derived using the forces and bending moment from equations (5.4). The transverse stress due to normal force and the radial stress can be determined in a similar manner as for straight beams. This is not the case for the transverse stress due to the bending moment. Because a curved beam is considered, the length on the inside of the ring is shorter than the length on the outside of the ring. The difference in length result in an unequal elongation on both sides of the ring, when loaded by a bending moment. This difference in elongation cause the bending moment stress to be influenced by the eccentricity between the neutral axis and the centroid axis [19]. Therefore an eccentricity factor (e) is used to determine the transverse stress due to the bending moment. This factor derived in Appendix D and is stated below:

$$
e = 3\frac{d_0}{2t_0} - 1
$$

When substituting the diameter and the thickness of the CHS in the cross-sectional area and the second moment of inertia, the factor ξ is determined. With the diameter of the ring being about 10 times larger than the thickness of the ring, it can be seen in (5.7) that $(d_0\text{-}t)^2/t^2$ is much larger than 1/3. By assuming that this constant 1/3 can be neglected, ξ becomes equal to 1.

$$
\xi = \frac{\left(d_o - t_0\right)^2}{t_0{}^2\left(\frac{\left(d_o - t_0\right)^2}{t_0{}^2} + \frac{1}{3}\right)} \approx 1 \tag{5.7}
$$

With the assumption of the factor ξ equal to 1, the transverse and radial stresses can be determined and are stated in (5.8). The stresses are dependent of the load W, the diameter d_0, the thickness t_0, the effective width b_{eff} and the location θ.

$$\begin{aligned} \sigma_{\theta,N}(\theta) &= \frac{N}{bt_0} = \frac{W}{\pi b_{eff} t_0} \frac{\pi}{4} \sin(\theta) \\ \tau_{r\theta}(\theta) &= \frac{V}{bt_0} = -\frac{W}{\pi b_{eff} t_0} \frac{\pi}{4} \left(\cos(\theta) - 1\right) \\ \sigma_{\theta,M}(\theta) &= \frac{Me}{\frac{1}{4} bt_0 d_0} = \frac{W}{2\pi b_{eff} t_0} \left(3\frac{d_0}{2t_0} - 1\right)\left(\pi\left(\theta - \sin(\theta)\right) + 2 - \frac{\pi^2}{2}\right) \end{aligned} \tag{5.8}$$

Using the equations derived above, the stress distributions from the Euler-Bernoulli curved beam model is compared with Roark's formulas of load case 20. In both the Roark load case equation and the padeye model equations, sated in equations (2.6) and (5.8) respectively, the mean CHS geometry is applied. Both Von Mises equivalent stress (σ_{eqv}) distributions are given in Figure 37, together with the contribution of the normal force, shear force and bending moment. From this graph is can be noticed that the stress is mainly dependent of the bending moment stress. This bending moment stress cause tension at the top and bottom of the CHS, and compression at the mid-surface.

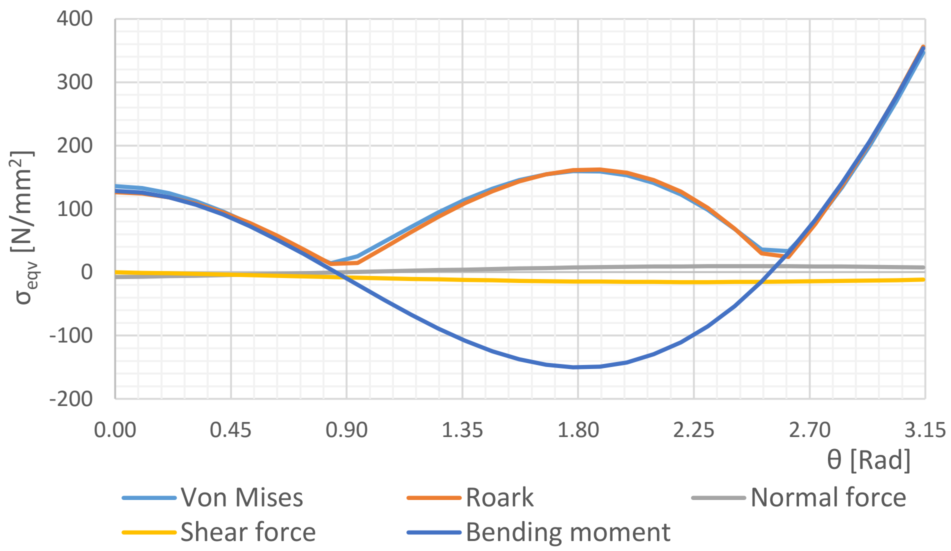

Figure 37:Comparison of Von Mises equivalent stress with Euler-Bernoulli curved beam theory and Roark's formulas for load case 20

In Figure 37 it can also be seen that the governing stress in the cross-section occurs at the top of the ring, θ = π, where the force is applied. Because the Von Mises equivalent stress is mainly influenced by the transverse stresses due to the bending moment, it is assumed that the bending moment stress at the top of the ring is governing. With these assumptions, the Von Mises stress becomes equal to the following:

$$\sigma_{eqv} = \sqrt{\sigma_{\theta,M}{}^2} = \frac{W}{\pi b_{eff} t_0}\left(3\frac{d_0}{2t_0} - 1\right)\left(\frac{\pi^2}{4} + 1\right) \tag{5.9}$$

The load W on the ring consists of two parts, the force due to the vertical component F_y and the in-plane bending moment M_{ip} (Figure 38). The bending moment is a function of the horizontal force component F_x and the pinhole height, which is equal to $b_m/3.05$. This leads to the equation for load W given below:

$$W = \left(\frac{N_1 \sin(\alpha_{ip})}{b_m} + \frac{h_0 N_1 \cos(\alpha_{ip})}{\frac{1}{6} b_m^{\ 2}} \right) b_{eff} = \frac{N_1 b_{eff}}{b_m} \left(\sin(\alpha_{ip}) + 1.96 \cos(\alpha_{ip}) \right) \tag{5.10}$$

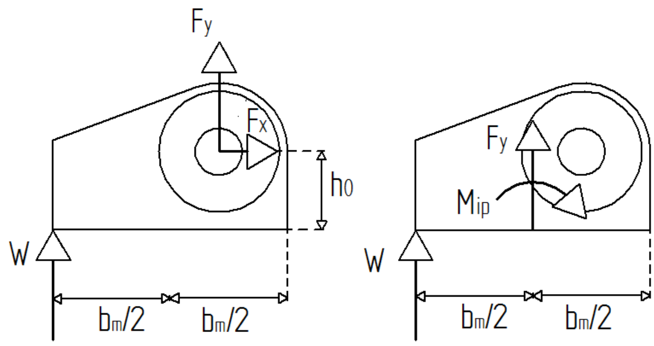

Figure 38: Influence of the force components on the force W on the ring model

By rewriting equation (5.9) and substituting the expression for the load W (5.10), an equation is determined that describes the load capacity of the ring. Because the Euler-Bernoulli curved beam theory assumes linear elastic material behaviour, the maximum load capacity is reached for the Von Mises equivalent stress σ_{eqv} equal to the yield stress σ_y. This result in an equation for the linear elastic load capacity, given in (5.11), which is a function of the CHS diameter d_0, CHS thickness t_0, the plate width b_m and the angle of the force α_{ip}.

$$N_1 = \frac{\pi}{\left(\frac{\pi^2}{4} + 1 \right)} \frac{b_m}{\left(3 \frac{d_0}{2t_0} - 1 \right)} \frac{f_{y0} t_0}{\sin(\alpha_{ip}) + 1.96 \cos(\alpha_{ip})} \tag{5.11}$$

The present dimensions in the equation can be rewritten into dimensionless ratios. By using the dimensionless ratios, two non-dimensionalised engineering tools are obtained, stated in (5.12). These capacity are obtained by dividing the load by $f_{0y}t_0^2$ or $f_{0y}t_0d_0$. The governing equation of the two will be determined by using the FEA results.

$$\begin{aligned} \frac{N_1}{f_{y0} t_0^{\ 2}} &= \frac{\eta \gamma}{(3\gamma - 1)} \frac{1.81}{\sin(\alpha_{ip}) + 1.96 \cos(\alpha_{ip})} \\ \frac{N_1}{f_{y0} t_0 d_0} &= \frac{\eta}{(3\gamma - 1)} \frac{0.91}{\sin(\alpha_{ip}) + 1.96 \cos(\alpha_{ip})} \end{aligned} \tag{5.12}$$

Besides using Euler-Bernoulli curved beam theory to create the ring model, the ring model can be derived using other theories. Plastic theory is used in the ring model derived by Togo (Figure 39), which describes the load capacity of a T-type plate-to-CHS connection. In this model it is assumed that plastic hinges are formed in the ring in case the plastic moment is reached at this location. The locations of the plastic hinges are unknown. In order to determine the load capacity of the model, the locations of the plastic hinges have to be determined at which the lowest load capacity is reached. This leads to a load capacity equation given in (5.13).

$$N_1 = 5.7 \frac{B_e}{d_0} \frac{\gamma^2}{1.64\gamma^2 + 1} f_{y,0} {t_0}^2 \tag{5.13}$$

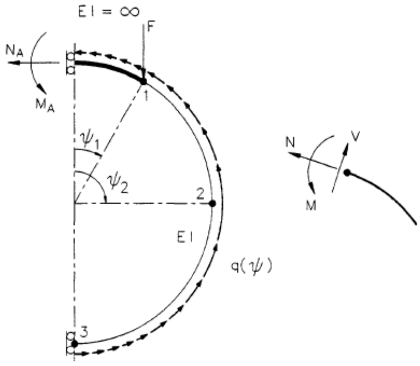

Figure 39: Ring model derived by Togo using plastic theory

In this equation B_e is the effective connection length of the CHS. In case the effective length is equal to the plate length, B_e/d_0 becomes equal to $b_m/d_0 = \eta$. The equation can be rewritten into equation (5.14). When comparing the equation from both the model using Euler-Bernoulli curved beam theory and the plastic ring model derived by Togo, it can be seen that both equations are dependent of the yield stress, CHS thickness and dimensionless ratio's η and γ.

$$N_1 = 5.7 \frac{\eta\gamma^2}{1.64\gamma^2 + 1} f_{y,0} {t_0}^2 \tag{5.14}$$

5.2 Conclusion

By using the Euler-Bernoulli curved beam theory, a ring model can be made which is similar to Roark's formulas, and give a similar stress distribution along the ring. The model consist of a point load applied on half a ring, which is compensated by a distributed transverse shear force. Linear elastic material behaviour is assumed in the model, allowing only stresses which are lower than the yield stress.

Because there is interaction between the normal force, shear force and bending moment, the stresses are expressed in the Von Mises equivalent stress. It is found that the Von Mises mainly consist of stress due to the bending moment. Because of this the Von Mises equivalent stress is assumed equal to the absolute transverse stress due to the bending moment.

From the ring stress distribution it is found that the maximum stress occurs at top of the ring, at the location where the load is applied. In order to obtain an equation which determines the load capacity of the ring, the stress at the top of the ring is considered. With these assumptions the load capacity of the ring model is determined by the bending moment at the top of the ring. The equation for the load capacity is described in (5.15) and is a function of CHS thickness t_0, the CHS diameter d_0, the main plate width b_m and the force angle α_{ip}.

$$N_1 = 1.81\frac{\eta\gamma}{(3\gamma-1)}\frac{f_{y0}t_0^{\ 2}}{\sin(\alpha_{ip})+1.96\cos(\alpha_{ip})} \tag{5.15}$$

The equation for the load capacity can be rewritten into a non-dimensionalised load. This normalised load can be obtained by dividing the force N_1 by $f_{y0}t_0^2$ or $f_{y0}d_0t_0$. Both normalised loads are given in equation (5.16).

$$\begin{gathered}\frac{N_1}{f_{y0}t_0^{\ 2}} = \frac{\eta\gamma}{(3\gamma-1)}\frac{1.81}{\sin(\alpha_{ip})+1.96\cos(\alpha_{ip})} \\ \frac{N_1}{f_{y0}t_0d_0} = \frac{\eta}{(3\gamma-1)}\frac{0.91}{\sin(\alpha_{ip})+1.96\cos(\alpha_{ip})}\end{gathered} \tag{5.16}$$

6 FEM Analysis

The goal of this thesis is to derive an engineering tool that describes the relation between the load case geometry and the load capacity. In order to obtain the behaviour of the padeye and plate load case during loading, the FEM model derived in chapter 4 will be analysed. In these analysis, the influence of the variable dimensions will be determined by varying their values. To determine the load capacity, the results from the FEM analysis will be examined using a limit state criteria stated in 2.3.1. This limit state criteria will be discussed in this chapter for the plate- and padeye load case.

6.1 Location governing strain

In order to apply the limit state criteria on the plate and padeye load case, the location at which the governing plastic strain occurs has to be determined. From theory it is obtained in chapter 5 that largest stresses, and thus strains, occur at the intersection of the CHS and the main plate. Because of the sudden change of geometry at the top and bottom of the main plate, it can be assumed that peak stresses will be active at these locations. By analysing the padeye model for the mean geometry, it can be noted from Figure 40 that this is correct. Therefore the location of the governing plastic strain can be assumed at the edge of the plate-to-CHS connection.

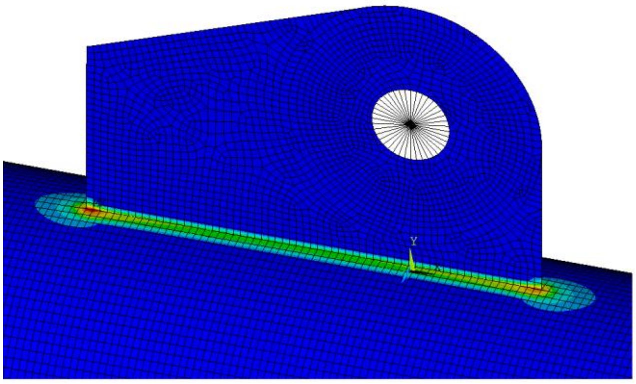

Figure 40: Von Mises plastic strain in the padeye load case with mean geometry

From the finite element analysis it is noticed that the location of the governing plastic strain shifts when varying the diameter to thickness ratio γ. For a low ratio γ, the governing plastic strain lies on the inside of the plate-to-CHS connection edge, while for a large ratio γ the plastic region lies just outside the connection edge. This shifting of the plastic region is shown in Figure 41, and is caused by the influence of the thickness on the stiffness of the CHS.

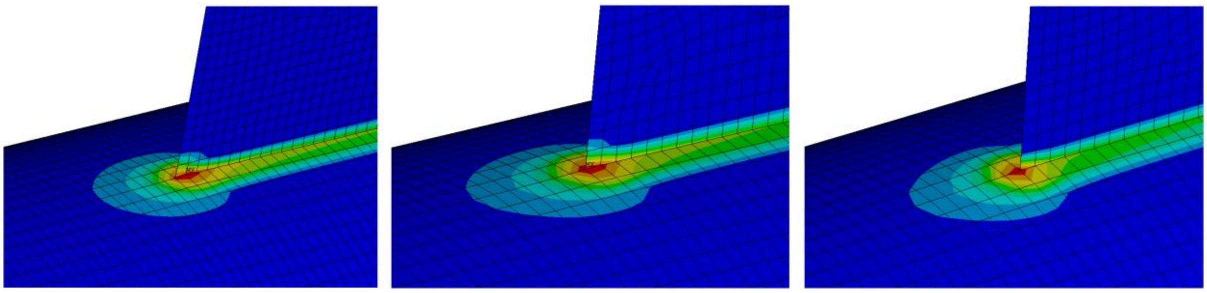

Figure 41: Von Mises plastic strain at the plate-to-CHS connection edge, for varying γ ratio. Left to right: $\gamma = 9.25, 12.19, 17.42$.

The CHS cross-section has a high rigidity in the longitudinal direction, causing mainly bending deformation in the circumferential direction (Figure 42 left). Due to this deformation, plastic strains occur in the cross-section at the location where the force is applied. Besides this, the deformation in circumferential direction causes a variation in deformation with respect to the adjacent cross-sections. This variation cause a bending moment in longitudinal direction, which lead to stresses. The combination of the stresses in circumferential and longitudinal direction, together with the abrupt change in geometry, result in high stresses in the edge of the plate-to-CHS connection. At this location plastic strains occur due to these stresses.

In case of a small γ ratio, the rigidity of the CHS is quite large. This causes a small variation in bending deformation between the adjacent cross-sections in the longitudinal direction of the CHS. Therefore the stresses, and thus plastic strains, are mainly caused by the circumferential deformation. In this case the plastic region will be on the inside of the plate edge. When the γ ratio of the CHS becomes larger, the rigidity decreases. Due to the decrease in rigidity, a larger variation of bending deformation between the adjacent cross-sections occurs (Figure 42 left). This will result in stresses caused by a combination of circumferential and longitudinal deformation. In this case the plastic region appears on the outside of the plate edge.

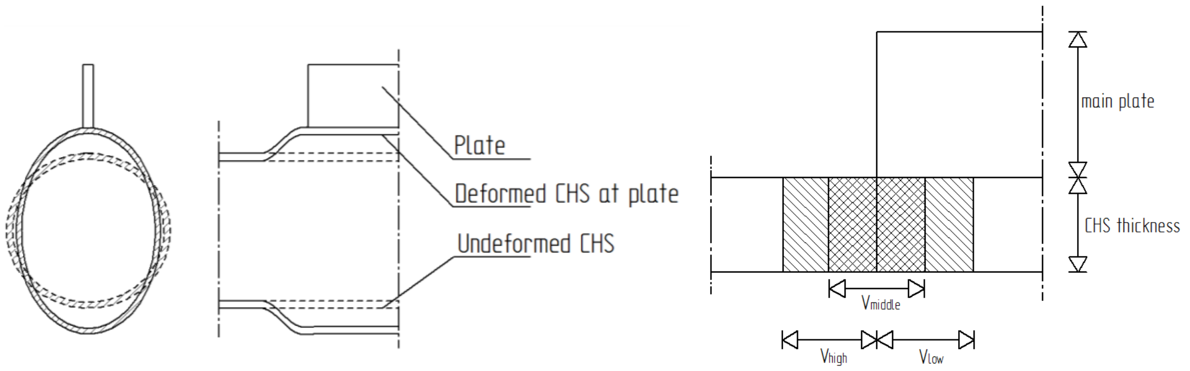

Figure 42: Circumferential and longitudinal deformation of the CHS cross-section at the plate connection (left); Location of the volume over which the average plastic strain is determined (right)

Because of the shifting of the location of the governing plastic strain, the volume over which the principal plastic linearized strain is obtained will also shift. In order to process the results correctly, three volumes are considered over which the average plastic strain is determined. The volume which gives the highest average strain will be governing and the related load will be the ultimate load. The locations of the volume are shown in Figure 42 (right) and are stated below:

- High: Middle of the volume on the outside of the plate-to-CHS intersection
- Middle: Middle of the volume at the edge of the plate-to-CHS intersection
- Low: Middle of the volume on the inside of the plate-to-CHS intersection

6.2 Limit state criteria

These failure criterion are compared in the force-displacement graph and the force-strain graph. These are shown in Figure 43 for the mean geometry of the padeye load case. Because the 4% principal plastic linearized strain and the 5% principal plastic strain are very similar, only the first one is shown. The different failure criteria are denoted below:

- Yield stress (ε_y, u_y)
- 4% principal plastic linearized strain ($\varepsilon_{4\%}$, $u_{4\%}$)
- 5% principal plastic strain
- 12% principal plastic strain ($\varepsilon_{12\%}$, $u_{12\%}$)
- Lemaitre strain criterion (ε_f, u_f)
- 3%d_0 displacement ($\varepsilon_{3\%d}$, $u_{3\%d}$)

In Figure 43 it can be seen the lowest limit state is given by the yield stress. This criterion assumes that no plastic stresses and strains are allowed. The smallest limit state using plastic material behaviour is given by the 4% principal plastic linearized strain, leading to an ultimate load that is roughly double the load from the yield stress criterion. The 12% principal plastic strain occurs at the point from which both the displacement and the strain will increase linear with the force. This limit state leads to a ultimate load that is roughly triple the yield stress criterion. The displacement criterion of 3%d_0 gives an ultimate load which is slightly larger than the ultimate load from the 12% plastic strain criterion. Finally the largest load capacity is obtained from the Lemaitre strain criterion, which occurs at very high strain with respect to the other limit state criteria. Because of the low slope of the graphs at this point, the load capacity due to the Lemaitre criterion is only 10% larger than the load from the displacement criterion.

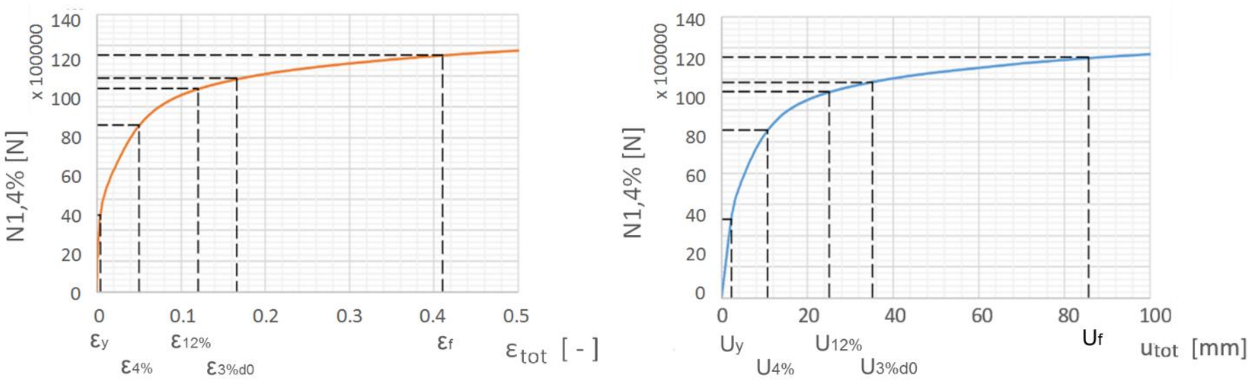

Figure 43: Comparison of limit state criteria, plotted in a force-strain diagram and a force-displacement diagram (right)

In practice the padeye is connected to a CHS member, like a jacket leg or a similar structure, at a joint in which several braces coincide. Multiple forces are active in such a joint, causing stresses and therefore stress variations during the lifetime of the structure. This means that the joint is subjected to fatigue loading. Because of this the plastic deformation due to the padeye loading must be limited. Besides this, a foundation pile has to be driven through the jacket leg in order to secure the structure to the bottom. This also will dictate a deformation limit of the connection due to padeye loading.

Because the plastic strains correspond with the plastic deformation, this plastic deformation has to be limited. In order to obtain a solution which is less conservative than the use of the yield stress criterion and limits the plastic deformation, the 4% plastic strain criterion from the DNV [10] is assumed to be the governing criterion.

6.3 Parametric numerical study

In order to determine the influence of the variable dimensions on the behaviour of the plate and padeye load case, a numerical parametric study is performed. This parametric study takes into account the variable dimensions, determined in 3.2.1 and used in the model geometry. The minimal, maximal and mean values of these dimensions are given in Table 6 and shown in Figure 44: Visualisation of the variable dimensions in the padeye model and the plate model. In the parametric study, these values will be varied independent from each other, in which a single variable dimension is varied between the minimal and maximal value. In this case the other variable dimensions will adopt the mean value.

Table 6: Variable dimensions for the padeye load case with the corresponding mean, minimum and maximum values

Variable	Unit	Mean	Min	Max
d_0	[mm]	1219.2	800	1397
t_0	[mm]	57.2	35	64
b_m	[mm]	1300	1100	2000
$\eta = b_m/d_0$	[-]	1.07	0.92	1.64
$\gamma = d_0/2t$	[-]	10.67	9.33	13.50

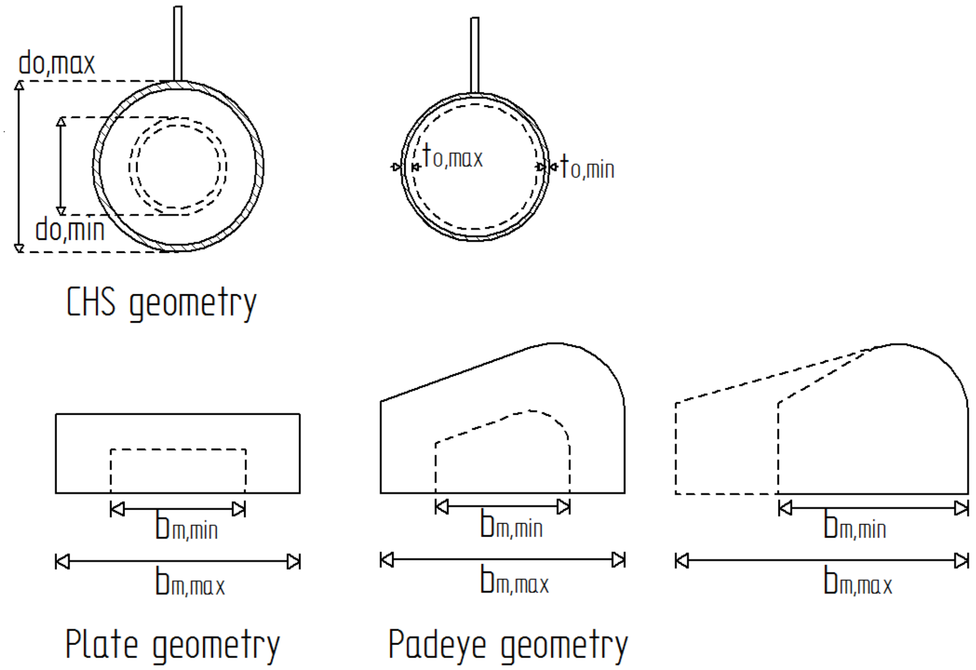

Figure 44: Visualisation of the variable dimensions in the padeye model and the plate model

Because the padeye model consist of many dimensions which could influence the load capacity, the plate model will be considered at first. In this model less variable dimensions are used with respect to the padeye model. By using the plate model, a conception can be made about the influence of each variable dimension. The plate model will be analysed with a force under an angle of 90 degrees, in order to except the influence of the bending moment due to the horizontal force component. This analysis is followed by an analysis of the force under an angle of 60 degrees, which includes the influence of the bending moment. Finally the padeye model is analysed, in which the force angle is variable. For both the plate model and the padeye model, the 4% plastic strain limit is used to determine the ultimate load capacity.

6.4 Plate load case

6.4.1 Force angle α_{ip} = 90˚

The plate model is subjected to an equally distributed load at the top of the plate. By analysing the model using the FEM program Ansys the distribution of the resulting stresses, strains and deformations can be obtained. These results are shown in Figure 45, in which the overall and local Von Mises stress and the local Von Mises plastic strain are given.

From the overall stress distribution it can be noticed that the stresses in the CHS are highest in the cross-sections at the connection with the plate and at the supports. In the local stress distribution, the stress distribution shows a constant stress distribution in the middle of the plate-to-CHS connection. At the edges of the plate, the region with high stress is larger than in the middle of the plate. The high stresses at the plate-to-CHS connection cause the plastic strains, shown in the local strain distribution.

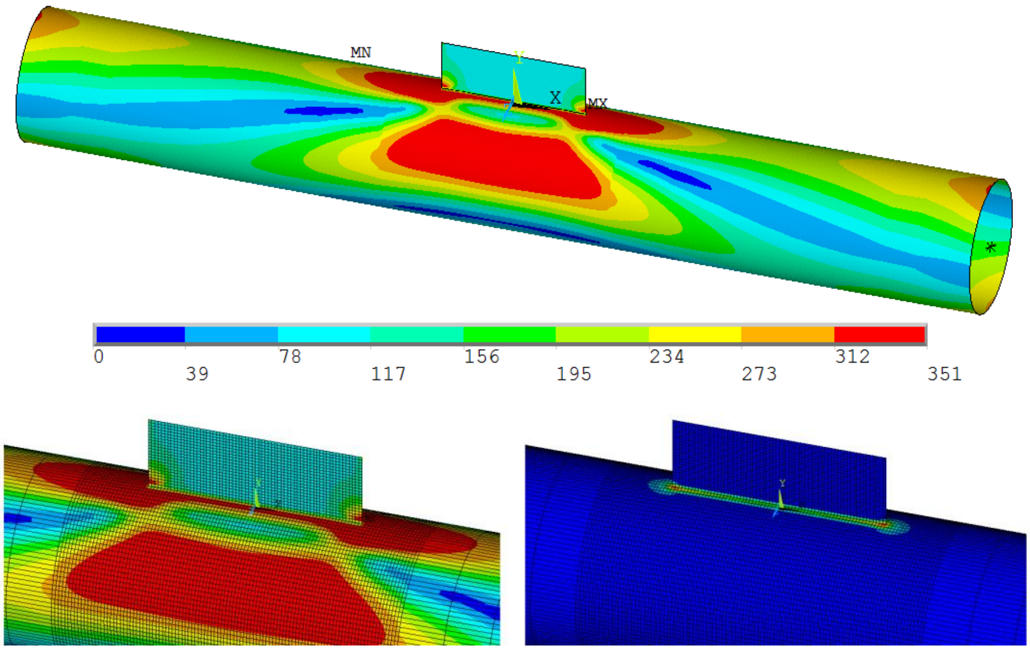

Figure 45: Plate load case, angle α_{ip} = 90˚, at 4% strain limit state $N_{1,4\%}$ .Overall (top) and local (bottom) Von Mises stress and plastic strain distribution

The high stresses in the CHS at the supports are caused by the applied end moments. The end moments can be dissolved as two normal forces, working on the top and bottom of the CHS. By doing this the stress at the middle of the cross-section becomes very low, which is the case.

When looking at the plate-to-CHS connection in circumferential direction, the stresses in the cross-section are highest at the plate intersection and at the sides of the CHS. The stresses shown in Figure 45 from the FEM analysis can be described using the stress distribution obtained from the Euler-Bernoulli curved beam theory in chapter 5. The force on the plate causes circumferential deformation in the CHS. The deformation, mentioned earlier as ovalisation, causes mainly bending moments which lead to stresses. Similar to Figure 37, these stresses are highest at the plate-to-CHS intersection and at the height of the CHS normal line.

When looking at the plate-to-CHS connection in longitudinal direction, the stresses are highest on both sides of the plate edge. These stresses are due to the variation in deformation of the adjacent cross-sections, causing bending moment in longitudinal direction. This effect is also described in 6.1.

As a result of the stresses caused by the deformations and the abrupt change in geometry, peak stresses occur at the top and bottom of the plate-to-CHS connection. When the load on the plate increases, the stresses reach the yield stress and the plate-to-CHS connection will experience plastic strain. When increasing the load even further, the plastic strain will reach the plastic limit strain. The load at which the plastic limit strain is reached is called the ultimate load $N_{1,4\%}$. For each geometry the ultimate load $N_{1,4\%}$ is obtained.

The resulting load capacities of the plate load case, obtained from the FEM analysis, are shown in Figure 46 for the mean diameter d_0. For the remaining diameters the results are given in Appendix E. These results from the FEM analysis are expressed as a function of the radius-to-thickness ratio γ ($=d_0/2t_0$) and the nominal depth ratio η ($=b_m/d_0$). In these graphs is can be seen that the load capacity is linearly dependent of the ratio η and inverse dependent of the ratio γ. Because in this case the diameter is constant, the only variables will be the CHS thickness t_0 and the plate width b_m. The stress distribution for some corresponding geometries and loads from Figure 46 are shown in Figure 47.

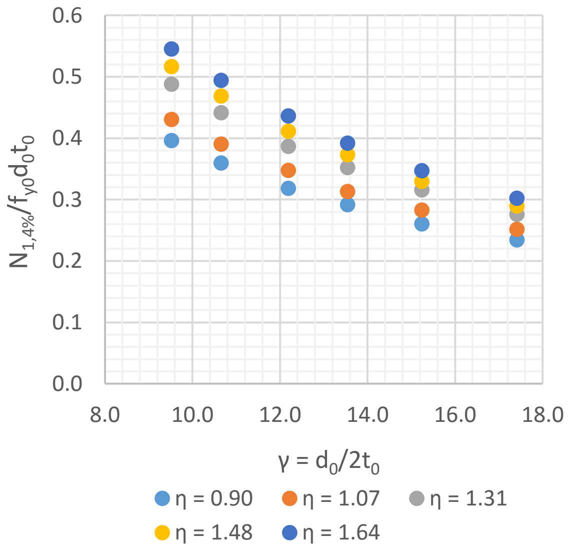

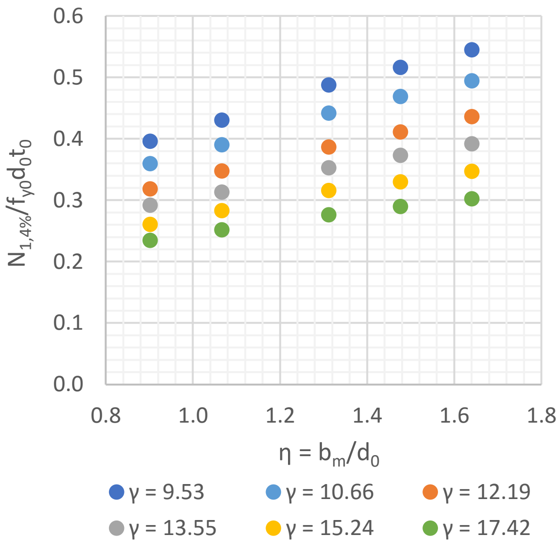

Figure 46: Load capacity of the plate load case for the mean diameter d_0, with variable ratios γ and η

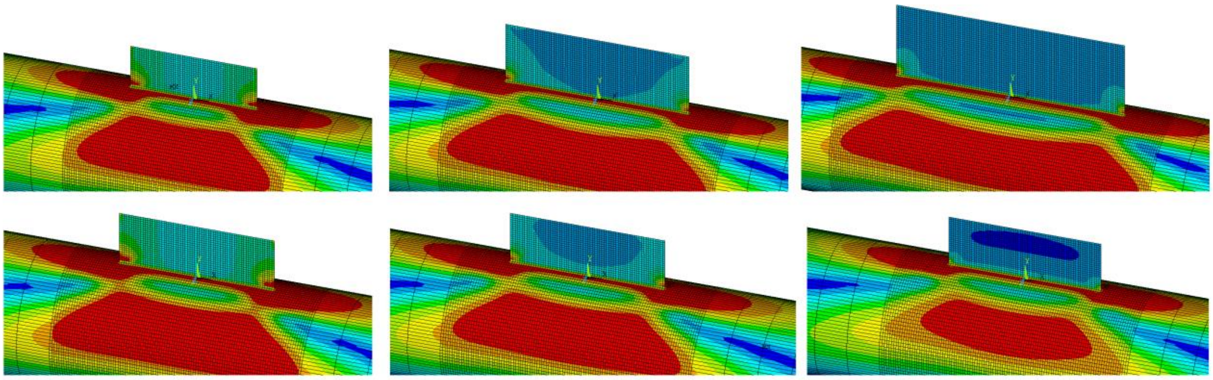

Figure 47: Plate load case with variable η and γ (top left to right η = 0.90, 1.07, 1.64; bottom left to right: γ = 9.5, 12.2, 17.4) and mean diameter d0 = 1219.2 mm

From the results (Figure 47) it can be obtained that for an increasing plate width b_m (and thus an increasing ratio η), the stress distribution at the plate-to-CHS connection is linearly expanding with the plate width. For a small plate width the in-plane bending stiffness of the plate is small, causing relatively large deformations in the plate. When increasing the plate width, the in-plane bending stiffness also increases. This leads to a small deformation of the plate and a stress distribution that is almost constant. Because the force on the plate is evenly distributed over the plate width, the distributed load on the CHS becomes smaller when the same load is applied on an increasing plate width. Due to this behaviour of the plate-to-CHS connection, the ultimate load is linearly dependent on the plate width and therefore on η.

In the case of an increasing CHS decreasing t_0 (and thus an increasing ratio γ), the stiffness of the CHS will also decrease. For a small CHS stiffness the deformations due to loading are large. Because large deformations result in large strains, the plastic strain limit is reached at a relatively low load in the plate load case with small stiffness. Due to this behaviour ultimate load is inverse dependent on the thickness of the CHS, and therefore on γ.

The load capacity can be expressed as a dimensionless parameter. This can be done by dividing the ultimate load $N_{1,4\%}$ by $f_y t_0^2$ or $f_y d_0 t_0$, as stated in equation (5.12) in 5.1. For both cases the non-dimensionalised parameter, called the normalised load, is plotted as function of the ratios γ and η in Figure 48 and Figure 49 for different diameters d_0.

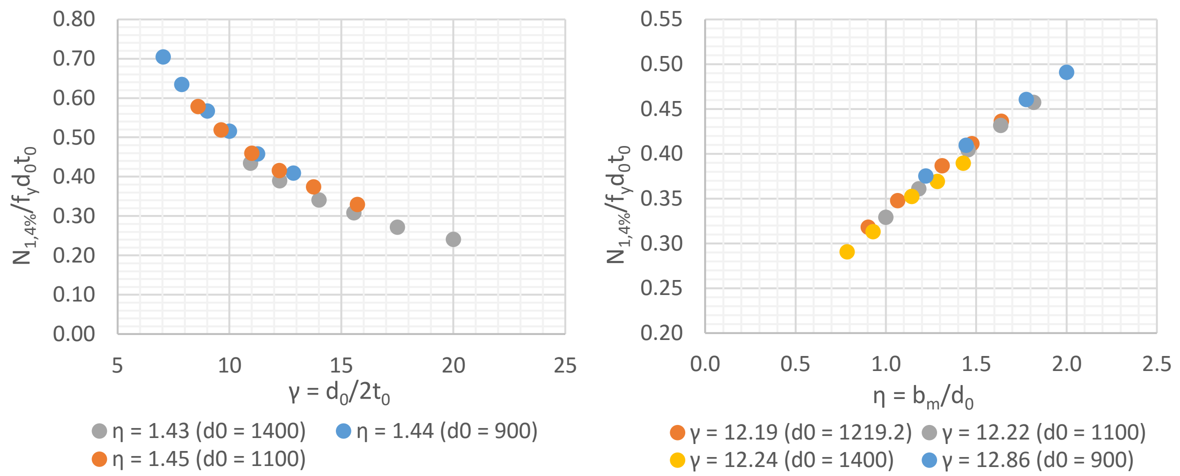

Figure 48: Dimensionless load capacity $N_{1,4\%}/f_y d_0 t_0$ for similar ratios γ and η with varying diameter d_0

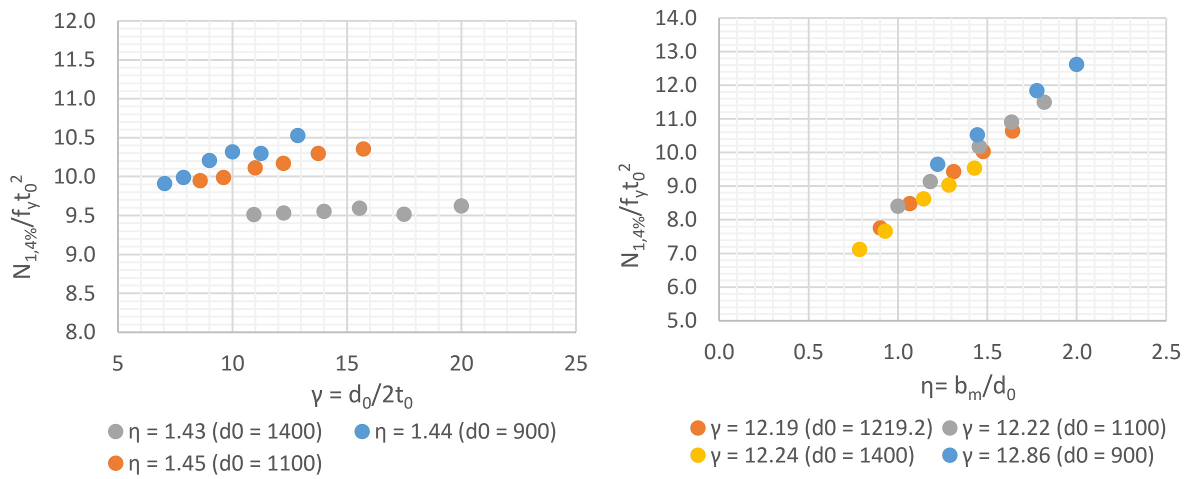

Figure 49: Dimensionless load capacity $N_{1,4\%}/f_y t_0^2$ for similar ratios γ and η with varying diameter d_0

In the results a large influence of the diameter d_0 can be denoted, which is present in both the ratio γ and η. When dividing the ultimate load by $f_y d_0 t_0$ (Figure 48), there is little scatter in the result for similar ratios γ and η with a different diameter d_0. However, when looking at the ultimate load divided by $f_y t_0^2$ (Figure 49), a lot of scatter is obtained for similar ratios γ with different diameter d_0. Due to the small scatter between the results in case the normalised load is equal to $N_{1,4\%}/f_{y0}d_0t_0$, this notation for the normalised load will be used from this point onwards.

As mentioned before, the stresses at the support are large because of the applied bending moments. In case of a small diameter d_0, these stresses will exceed the yield stress and plastic strain will occur. For ratios $\eta = b_m/d_0$ larger than 2.0, the plastic strain at the supports will reach the strain limit at before the plastic strain at the plate-to-CHS connection will. By applying reinforced band with a larger stiffness and length in these cases, the circumferential displacement of CHS at the plate will change. This will cause the stress distribution to differ from the models used for other geometries. Therefore the load capacity of the geometry in which η is larger than 2.0 is much higher with respect to the other geometries (Figure 50). Because of this, geometries for which the ratios η is larger than 2.0 will be neglected.

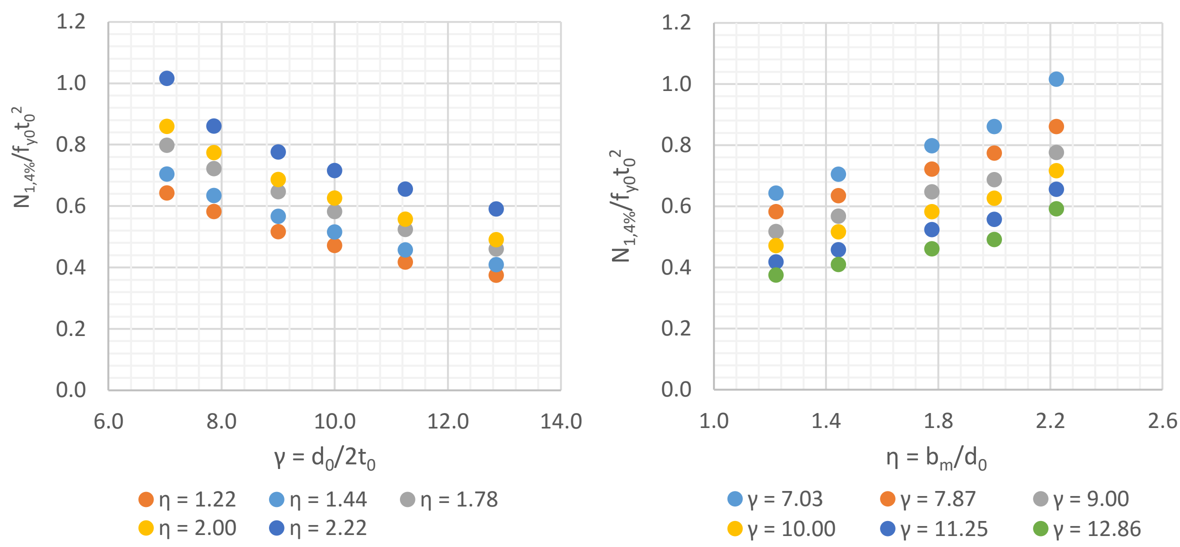

Figure 50: Dimensionless load capacity N1,4%/fyd0t0 for diameter d0 = 900 mm and variable ratios γ and η, showing relatively large load for η > 2.0

6.4.2 Force angle $\alpha_{ip} = 60^\circ$

By applying the force on the plate under an angle of 60 degrees, a bending moment is introduced in the plate due to the horizontal force component. This bending moment causes compressive load in one end of the plate and tensile load in the other. Due to the compressive load, the existing tensile stresses due to the vertical force component are reduced. On the other end of the plate, the tensile load will increase the existing tensile stresses. This will cause the strains at the latter location to reach the plastic limit strain at a lower force than in the case of a force angle of 90 degrees.

The Von Mises stress and plastic strain distribution, for the mean geometry at the ultimate load $N_{1,4\%}$, are given in Figure 51. In these figure the effects of the bending moment, described above, is visible. In the overall Von Mises equivalent stress distribution it can be seen that the high stresses over the CHS cross-section are only present at one side of the plate. This is due to the large deformations and the variation in deformation with respect to the adjacent cross-section. On the other side of the plate however, the stresses will be low due to small deformations. The stresses in the CHS will reach the yield stress, and therefore the plastic strain limit, on one side of the plate only.

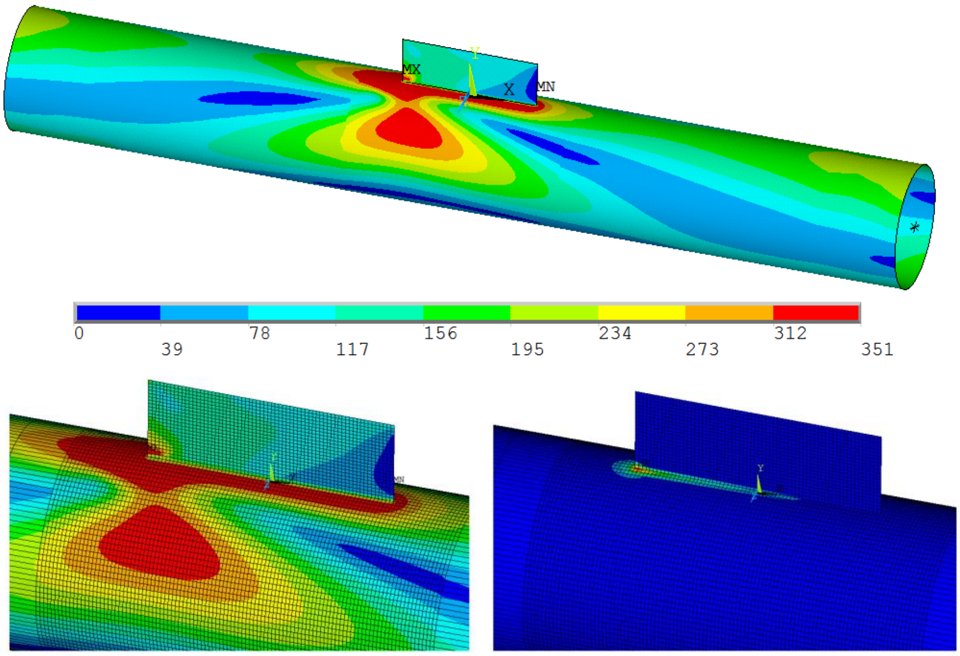

Figure 51: Plate load case, angle $\alpha_{ip} = 60^\circ$, at 4% strain limit state N1,4% .Overall (top) and local (bottom) Von Mises stress and plastic strain distribution

The load capacity of the different plate load case geometries, with a force angle of 60 degrees, will be determined. This is done in a similar manner as the load case with the force angle of 90 degrees, by varying the ratios η and γ. The results from the finite element analysis are shown in Figure 52 for the mean diameter d_0. The analysis results for the other geometries are given in Appendix E. From Figure 52 it can be seen the normalised load capacity is inversely dependent on the ratio γ, and linearly dependent on the ratio η. This is the same loading behaviour as for the plate load case under an angle of 90 degrees.

The Von Mises stress distribution in the plate-to-CHS connections corresponding with the geometry and load from Figure 52 are shown in Figure 53. These stress distributions are given for a geometry with a minimal, maximal and intermediate value of the ratios γ and η. In these geometries the diameter d_0 is constant and equal to 1219.2 mm, therefore the only variables will be the CHS thickness t_0 and the plate width b_m.

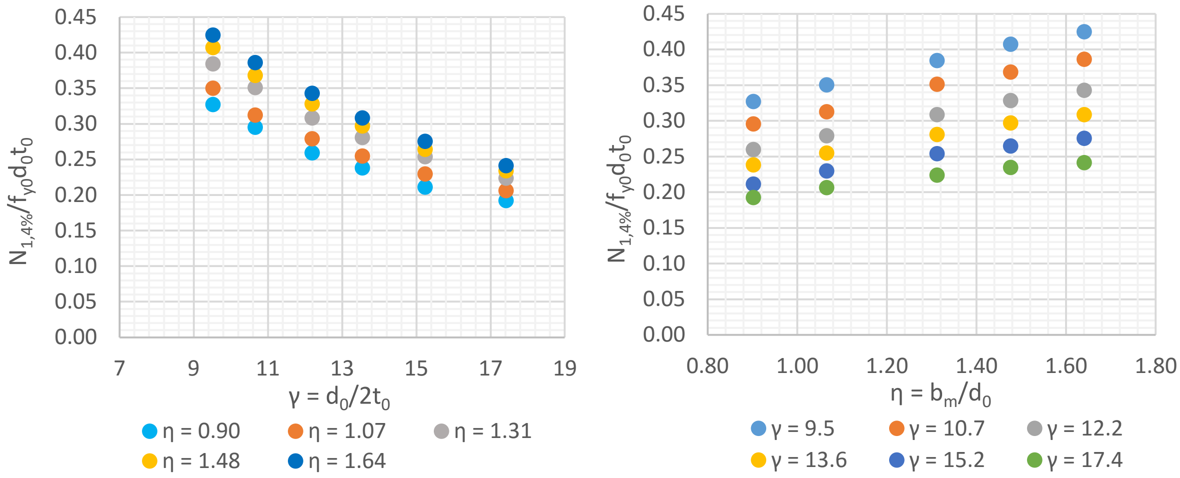

Figure 52: Load capacity of the plate load case (α_{ip} = 60˚) for mean diameter d_0 and variable ratios γ and η

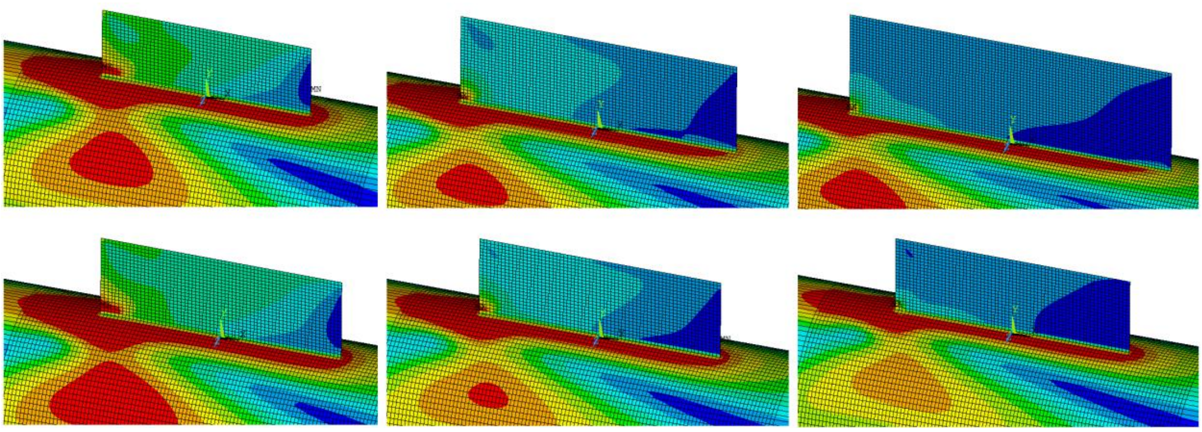

Figure 53: Plate load case with variable η and γ (top left to right η = 0.90, 1.07, 1.64; bottom left to right: γ = 9.5, 12.2, 17.4) and mean diameter d_0 = 1219.2 mm

From Figure 52 and Figure 53 it can be seen that an linear increasing plate width (and thus an increasing η) leads to a linear increasing normalised load. When applying the same force on the load case with increasing plate width, the distributed load on the CHS will decrease. This is also true for the bending moment due to the horizontal force component, which will a have small resulting vertical load when applied over a large length.

Besides the decrease in distributed load, the in-plane bending stiffness of the plate becomes larger for increasing plate width. This causes less deformation, and hence stresses, in the plate. Due to this rigid plate behaviour and the applied bending moment, there will be little deformation in the CHS on one side of the plate and large deformation on the other. For large plate width this will result in the end with large deformations to behave like the plate load case with a force angle of 90 degrees, while at the other end the plate will act as if there is no load applied. The behaviour of the plate-to-CHS connection described above due to an increasing ratio η, causes the normalised load to increase linearly with this ratio.

When varying the thickness t_0 (and thus the ratio γ) of the CHS, an inverse relation with the ultimate load can be obtained. Decreasing the thickness (therefore increasing η) will result in an decreasing stiffness of the CHS, causing larger deformation of the cross-section when the load remains the same. These large deformations will lead to large strains and therefore large stresses. Due to this behaviour the ultimate strain limit is reached at a relatively low load for small CHS thickness, causing a decrease in normalised load capacity for increasing ratio γ.

6.5 Padeye load case

6.5.1 Constant geometry

The Von Mises stress and plastic strain distribution are given in Figure 54 for the mean padeye geometry at reaching the ultimate load $N_{1,4\%}$. In these figures it can be seen that, despite the fact that the force is acting under an angle of 60 degrees, the stress distribution in the CHS is similar to the plate load case with a force angle of 90 degrees. This causes a plastic strain distribution over the total length of the connection between the padeye and the CHS, which is also similar to the plate load case.

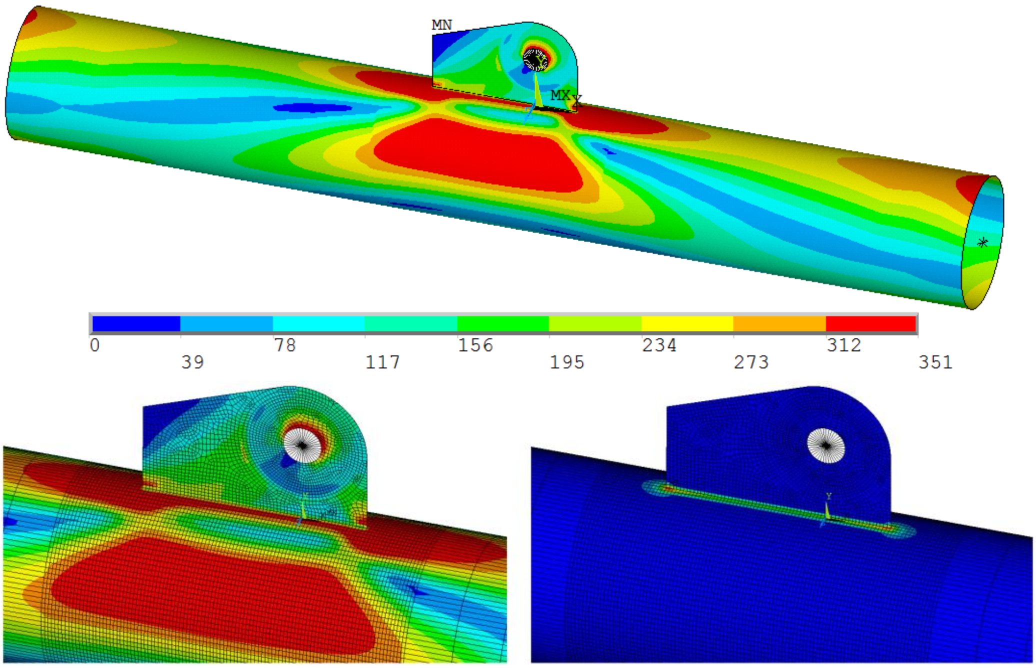

Figure 54: Overall (top) and local (bottom) Von Mises stress and plastic strain distribution in the padeye load case, with force under angle α_{ip} = 60˚

This similar stress distribution between the padeye and the plate load case (α_{ip} = 90˚) is due to the fact that the line of the force coincides with the main plate centre, shown in Figure 55. Therefore no bending moment is active in the main plate and the stress distribution is caused by bending as a result of the vertical force component. In case the line of the force doesn't coincide with the main plate centre, a bending moment will occur due to the eccentricity Δb_m of the of the force with respect to the plate centre.

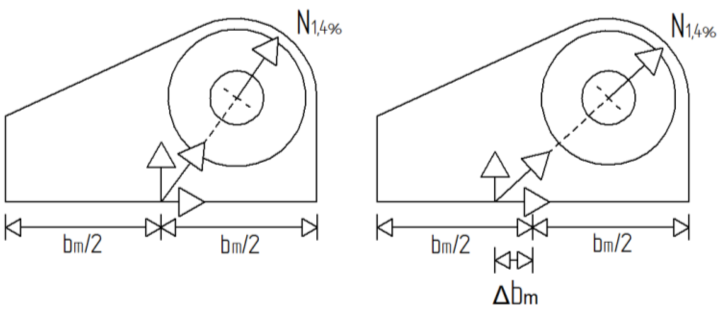

Figure 55: Force distribution in the main plate with bending (right) and without bending (left) due to eccentricity Δb_m

The force is applied at the pinhole and transferred to the plate-to-CHS connection by induced strain in the main plate. Relatively high stresses are present due to the contact force at the pinhole. Because the cheek plates are relatively stiff, it is assumed that these will experience little strain. Therefore the force at the pinhole is assumed evenly distributed over the cheek plate cross-section, causing strains in the main plate. The largest strains occur in line with the force (normal force) and perpendicular to the force (shear force). Strain that is not in line with the force will be lower due to the triangulation, which causes the force to be divided into three principal direction.

In this case it means that the strain between the cheek plates and the bottom and top edge of the main plate will be largest, due to the tensile and shear force respectively. The strain underneath the cheek plates will be lower, because these are not in line with the force. Because the strains correspond with the stresses, high stresses will occur at both edges of the plate-to-CHS connection. This stress distribution in the main plate is shown in Figure 56.

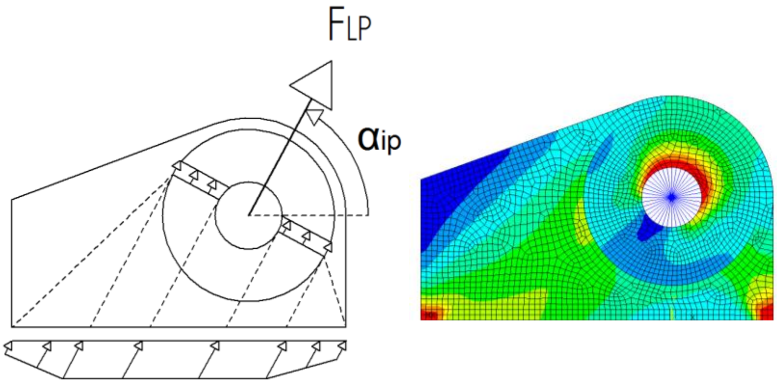

Figure 56: Theoretical stress distribution in the padeye (left) versus Von Mises stress distribution following the Finite Element Analysis (right) .

The load capacity of the padeye load case can be determined for different geometries of the padeye and the CHS. Similar to the plate load case, these different geometries are obtained by varying the ratios γ and η in the model used in the finite element analysis. The results of the analysis are given in Appendix E for all geometries, and is shown in Figure 57 and Figure 58. In these figure the ratios γ and η are varied with mean diameter d_0, resulting in a varying thickness t_0 and plate width b_m respectively. The relations between the normalised load and the variable ratios γ and η are similar to those in the plate load case. The ratio γ is inverse related to the normalised load, while the ratio η is linear related to the normalised load.

As described in chapter 3, the other dimensions of the padeye will vary proportional to the width b_m, preserving constant geometrical ratios. When increasing the plate width b_m, and therefore the ratio η, the distance between the cheek plates and the plate-to-CHS connection will increase. This causes the strains, and therefore the stresses, in the main plate directly beneath the cheek plates to become significantly smaller with respect to the plate edges. Because the force on the padeye is distributed over a larger length, the distributed load becomes smaller. Therefore the force at which the plastic limit strain is reached increases with the increasing plate width. Due to this behaviour, the stress distribution in the CHS becomes similar to the plate load case with a force angle of 90 degrees.

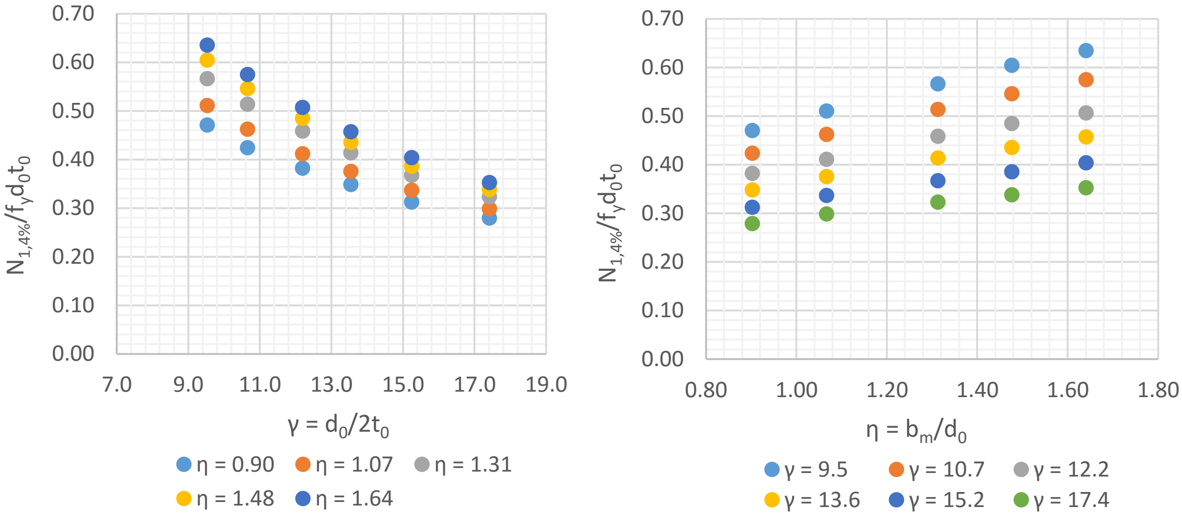

Figure 57: Load capacity of the padeye load case for mean diameter d_0 and variable ratios γ and η

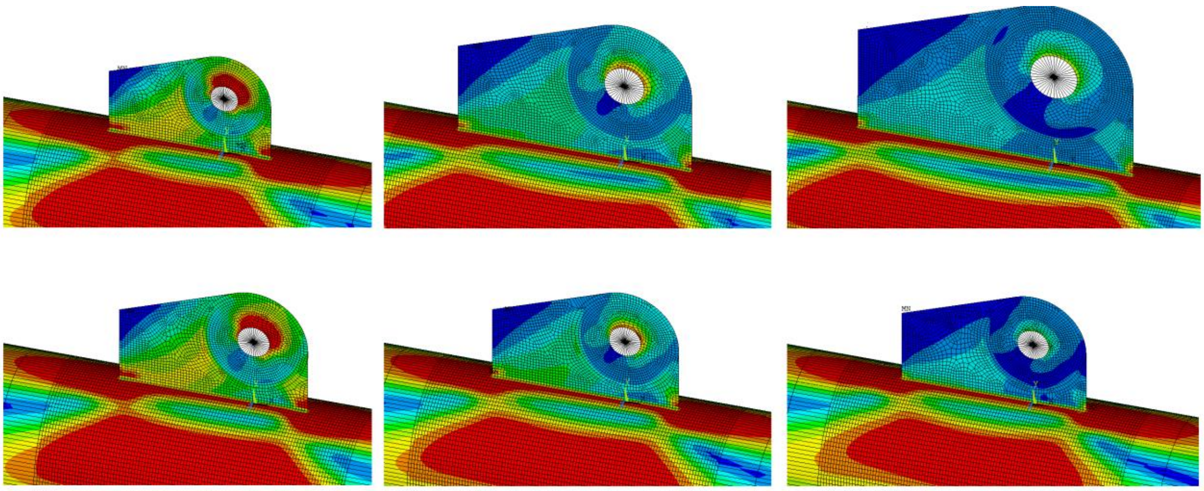

Figure 58: Padeye load case with variable η and γ (top left to right η = 0.90, 1.07, 1.64; bottom left to right: γ = 9.5, 12.2, 17.4) and mean diameter d0 = 1219.2 mm

When decreasing the thickness t_0 of the CHS, hence increasing the ratio γ, the stiffness of the CHS cross-section is reduced. This will result in larger deformations of the CHS cross-section at an equal load. These large deformations cause large strains at the intersection of the plate and the CHS. This will result in an inverse relation between the load capacity of the padeye load case and the ratio γ.

In case of a small ratio γ and η (γ ≤ 7.0 and η ≤ 1.38), the stiffness of the CHS cross-section is large and the padeye geometry is small. This causes high contact stresses at the pinhole due to the high load capacity of the CHS. Due to these stresses, the cheek plates will start to yield at the contact area with the force (Figure 59). This behaviour of the padeye only occurs in two lower bound geometries within the considered range. These lower bound geometries are in the case of a plate width b_m = 1100 mm, a thickness t_0 = 64 mm and a diameter d_0 = 800 and 900 mm (γ = 6.3, η ≤ 1.38 and γ = 7.0, η = 1.22). Because only these two geometries experience plastic strains at the cheek plates, this behaviour will not be taken into account.

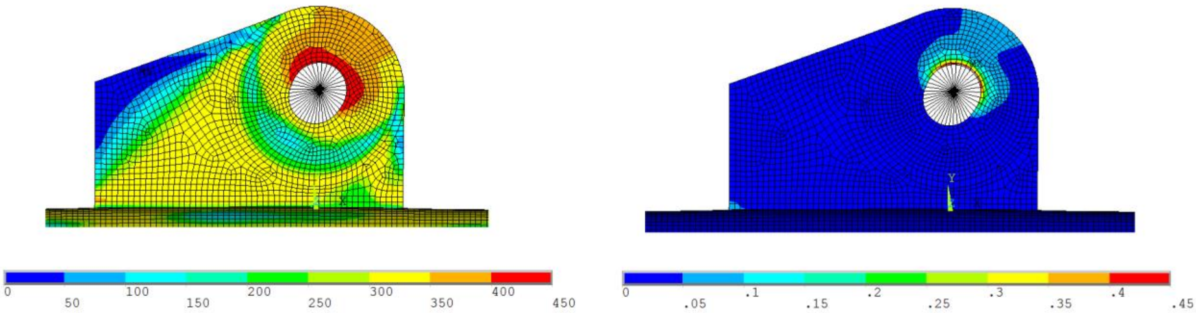

Figure 59: Von Mises stress (left) and plastic strain (right) distribution for small ratios of γ and η

In case of a large ratio η ($\eta > 2.22$), the load capacity will be high. This will cause high stresses in the CHS at the support due to the applied bending moments. Similar to the plate load case, this will result in large plastic strains of the CHS at the support, despite the applied reinforced band. Because of this structural behaviour the load capacities of padeye geometries in which η is larger than 2.22 will not be taken into account.

6.5.2 Variable geometry

By assuming the padeye dimensions as a function of the main plate width, the connection behaviour is determined for geometries equal to the mean geometry only. In order to obtain the behaviour of multiple padeye geometries, the main plate width is varied while the height of the padeye remains constant. This results in the use of an additional ratio λ, which is stated as the ratio between the padeye width and the height ($\lambda = b_m/(R_m + h_0)$).

By varying the ratios γ and λ, the relation between the ratios and the normalised load is obtained. The connection behaviour is shown in Figure 60 and Figure 61. In Figure 60 the Von Mises stress distribution is shown for a variable ratio λ and mean diameter d_0. The stress distribution for variable ratio γ is already given in Figure 58. In the stress distributions in Figure 58 it is obtained that for geometries other than the mean geometry, the highest stresses are present on only one side of the main plate. This behaviour is similar to the plate load case with a force angle of 60 degrees, and is caused by the presence of a bending moment. The bending moment occurs when the line of the force doesn't coincide with the centre of the main plate, as described in 6.5.1.

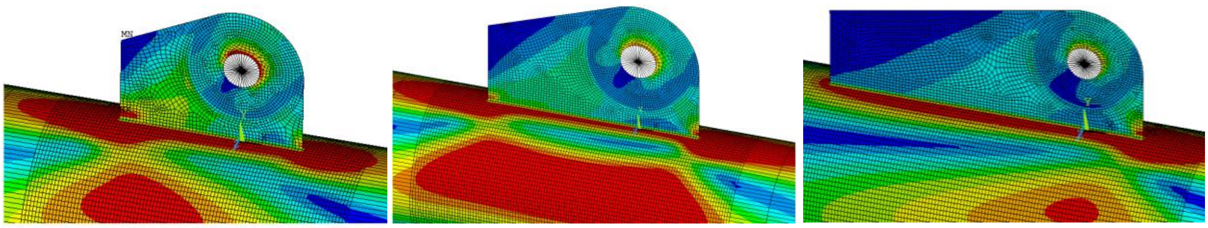

Figure 60: Padeye load case with variable ratio λ (left to right η = 1.38, 1.63, 2.50) and mean diameter d0 = 1219.2 mm

From Figure 61 it can be noted that the relation between the normalised load and the ratio γ remains the same as in the case of a constant padeye geometry. When looking at the normalised load as a function of the ratio λ, it can be noted that two different relations are present. The ratio λ equal to 1.63 represents the mean padeye geometry which is used in 6.5.1.

The first relation, ranging between λ = 1.38 and λ = 1.63, between the normalised load and λ is linear. In this case a relatively small plate width is used, which is shown in the left geometry given in Figure 60. This results in an eccentricity of the load with respect to the plate centre and hence a clockwise bending moment. Therefore the largest stresses occur at the left side of the main plate.

The second relation, ranging between λ = 1.63 and λ = 250, between the normalised load and λ is inverse. A relatively large plate width is used, shown in the geometry stated at the right side of Figure 60. The eccentricity of the load with respect to the plate centre causes a anticlockwise bending moment, resulting in large stresses at the right side of the main plate.

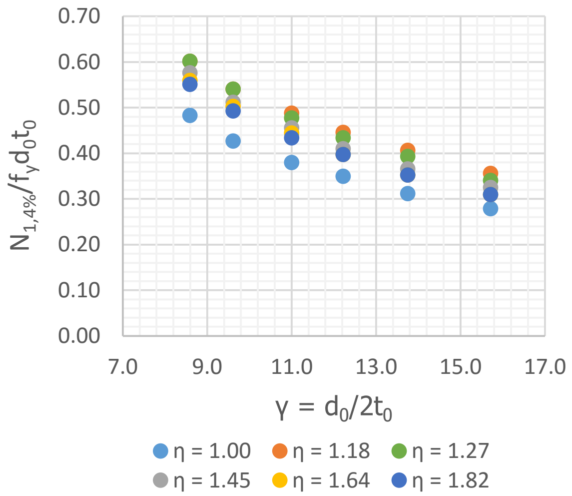

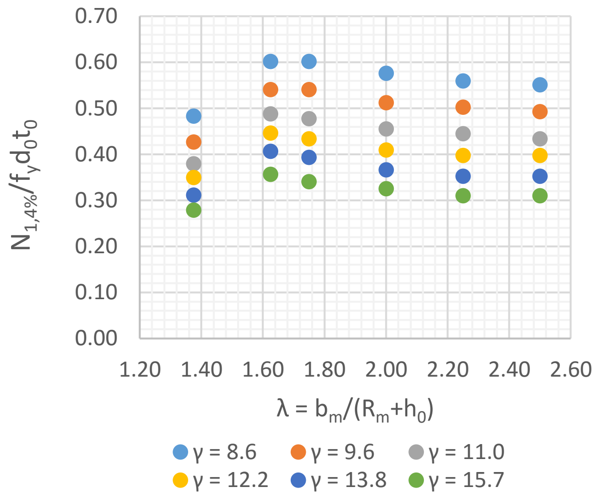

Figure 61: Load capacity of the padeye load case for mean diameter d_0 and variable ratios γ and λ

6.6 Conclusion

In the plate load case with a force angle of 90 degrees, a vertical force is uniformly distributed over the plate width. This causes a uniform deformation of the plate. In the plate load case with a force angle of 60 degrees, both a vertical and a horizontal force component are uniformly distributed over the plate width. The horizontal force component causes a bending moment in the plate, resulting in a variation of the plate deformation in the longitudinal direction. The resulting deformations of the CHS cause bending moments in the cross-section. These bending moments, and the abrupt change in geometry at the edges of the plate-to-CHS connection, cause governing peak stresses.

When looking at the padeye load case, the force is applied at the pinhole. Cheek plates are applied at the pinhole to stiffen the cross-section and prevent the main plate from bearing load failure. Due to the relatively high stiffness, the load is distributed over the cheek plate cross-section. The largest strains, and therefore stresses, are active in line with and perpendicular to the force angle. These stresses are therefore caused by normal and shear force.

In the mean padeye geometry, the line of the force coincides with the main plate centre. Therefore no bending moments are active in the main plate, causing a stress distribution which is similar to the stress distribution in plate load case with a force of angle 90 degrees. With the geometry remain constant, this stress distribution remains similar when varying the variable dimensions. However, when varying the geometry of the padeye the stress distribution will change. Because the line of the force does no longer coincide with the main plate centre in padeye geometries other than the mean geometry, bending moments will occur in the main plate.

Due to these stresses, plastic strains will develop in the cross-section. The load at which the plastic strain criterion is reached is denoted as the ultimate load $N_{1,4\%}$. In Figure 62 the relations between the normalised load and the variable ratios γ and η is given for the mean geometry. In Figure 61 the relation between the normalised load and the variable ratio λ is shown.

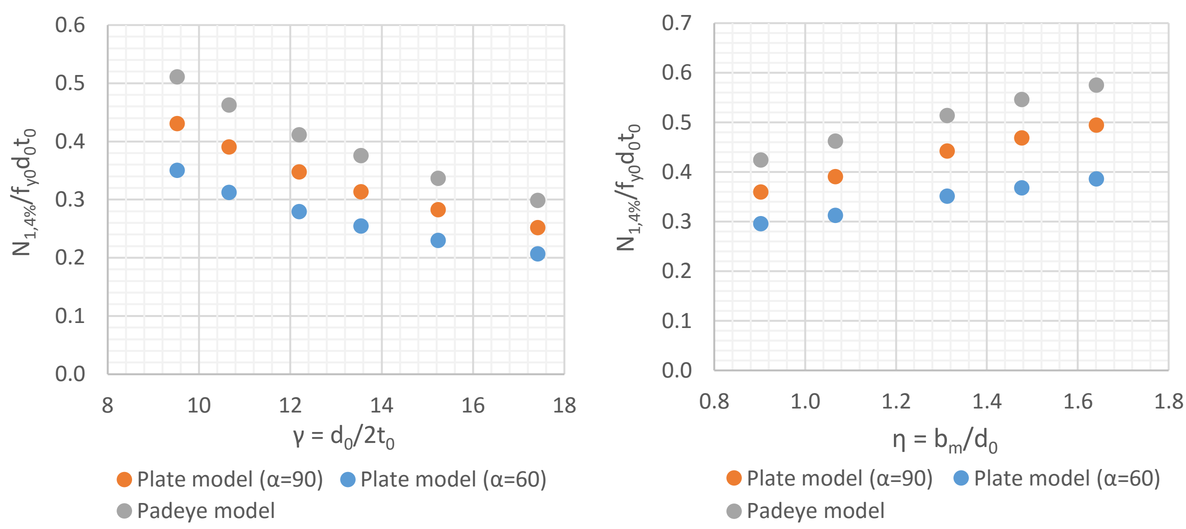

Figure 62: Load capacity comparison for the mean geometry in the plate load case (α_{ip} = 90 and α_{ip} = 60) and the padeye load case

From Figure 61 and Figure 62 it can be noticed that the relations of both the plate load case and the padeye load case are similar, when loaded in radial direction. These relations between the ultimate load and the ratios are stated below:

- Ultimate load $N_{1,4\%}$ - γ = inverse relation
- Ultimate load $N_{1,4\%}$ - η = linear relation
- Ultimate load $N_{1,4\%}$ - λ = linear relation for $1.38 \leq \lambda \leq 1.63$
- Ultimate load $N_{1,4\%}$ - λ = inverse relation for $1.63 \leq \lambda \leq 2.50$

In case of a small CHS diameter, large plastic strains can occur at the support due to the applied bending moments. Because this type of failure is not considered in this study, boundaries are applied. Within these boundaries, the load cases will be subjected to failure due to exceeding of the plastic limit strain at the plate-to-CHS connection. The applied boundaries are described in Table 7.

Table 7: Boundaries of the plate load case (α_{ip} =90˚ and α_{ip} =60˚) and the padeye load case (constant and variable geometry)

Load case	**$\gamma = d_0/2t_0$ [-]**	**$\eta = b_m/d_0$ [-]**	**$\lambda = b_m/(R_m+h_0)$ [-]**	**α_{ip} [deg]**
Plate (α_{ip} = 90˚)	$6.3 \leq \gamma \leq 20.0$	$0.79 \leq \eta \leq 2.00$	-	90˚
Plate (α_{ip} = 60˚)	$6.3 \leq \gamma \leq 20.0$	$0.79 \leq \eta \leq 2.50$	-	60˚
Padeye const. geom.	$6.3 \leq \gamma \leq 20.0$	$0.79 \leq \eta \leq 2.22$	$\lambda = 1.63$	60˚
Padeye var. geom.	$6.3 \leq \gamma \leq 20.0$	$0.79 \leq \eta \leq 2.22$	$1.38 \leq \lambda \leq 2.50$	60˚

7 Post processing FEM results

The results following the FEA are processed to obtain an engineering model that describes the load capacity of the padeye load case. These FEA results are processed using the curve fitting tool from Matlab, in which it is possible to fit a curve or surface onto the gained data from the FEA. An custom equation is applied in the curve fitting tool, containing the variable dimensions and a number of constants. Matlab will fit the equation to the data by determining the constant values for which the error is as little as possible.

7.1 Curve fitting

7.1.1 Matlab curve fitting tool

In order to determine the accuracy of the prediction with respect to the data obtained from the FEA, the Matlab curve fitting tool uses the coefficient of determination. This coefficient, denoted as R^2, is a number that indicates how well the applied equation fits the data. The value of R^2 varies between 0 and 1, where 0 indicates that the data is not fit at all and 1 indicates that the data is fit perfectly. In order to calculate R^2, the total sum of squares and the residual sum of squares is needed. The total sum of squares is the variance of the data and the residual sum of squares is the deviation between the prediction and the FEA data.

The mean deviation of the curve with respect to the data is denoted as the Root Mean Squared Error (RMSE) or the Root Mean Squared Deviation (RMSD). This RMSE represents the standard deviation of the differences between the FEA data and the predicted load capacity. The individual differences for each data point are called residuals. Low residuals, and therefore a low RMSE, mean that there is little variation between the data and the prediction.

7.1.2 Analytic equation

To find an equation that fits the data from the FEM models, the equation of the normalised load capacity from the Euler-Bernoulli curved beam theory (5.16) is used. From chapter 6 it is obtained that the normalised load $N_1/f_{y0}d_0t_0$ is governing, because of the large variation of the ultimate load for variable diameter d_0. Therefore the equation derived in chapter 5 is used as a first estimation of the curve predicting the load capacity. This equation is described below:

$$\frac{N_{1,4\%}}{f_{y0}t_0d_0} = 0.91\frac{\eta}{(3\gamma-1)}\frac{1}{\sin(\alpha)+1.96\cos(\alpha)} \tag{7.1}$$

To use the formula as a first estimation, the constant factors are replaced by constants C_i, shown in (7.2). By doing this, Matlab can find the appropriate constants needed to fit the data found in the FEA. Because of the similarities in both the plate load case and the padeye load case, the equation will be used to curve-fit the FEA data for both load cases.

$$\frac{N_{1,4\%}}{f_{y0}t_0d_0} = C_1\frac{\eta}{(C_2\gamma-1)}\frac{1}{\sin(\alpha)+C_3\cos(\alpha)} \tag{7.2}$$

7.2 Plate load case

7.2.1 Force angle α_{ip} = 90˚

When using a force angle α_{ip} of 90 degrees, the is no reduction due to the force angle. When substituting α_{ip} into equation (7.2) the reduction factor becomes equal to 1.0 and is therefore not present in the equation. From this the following equation is obtained for the load capacity in the plate load case:

$$\frac{N_{1,4\%}}{f_{y0}t_0d_0} = C_1 \frac{\eta}{(C_2\gamma - 1)} \tag{7.3}$$

From 6.4, the relations between the variable ratios and the normalised load is obtained. This relation is inverse for the γ ratio and linear for the η ratio. From the equation stated in (7.3), it can be seen that these relations are already present. When applying this equation in the Matlab curve fitting tool, the accuracy of the resulting curve is determined. In Figure 63, the dots are the data obtained from the FEA and the curve is a three-dimensional plot of equation (7.3). At the left figure the curve is compared with the data, where at the right figure the deviation between the curve and the data is shown.

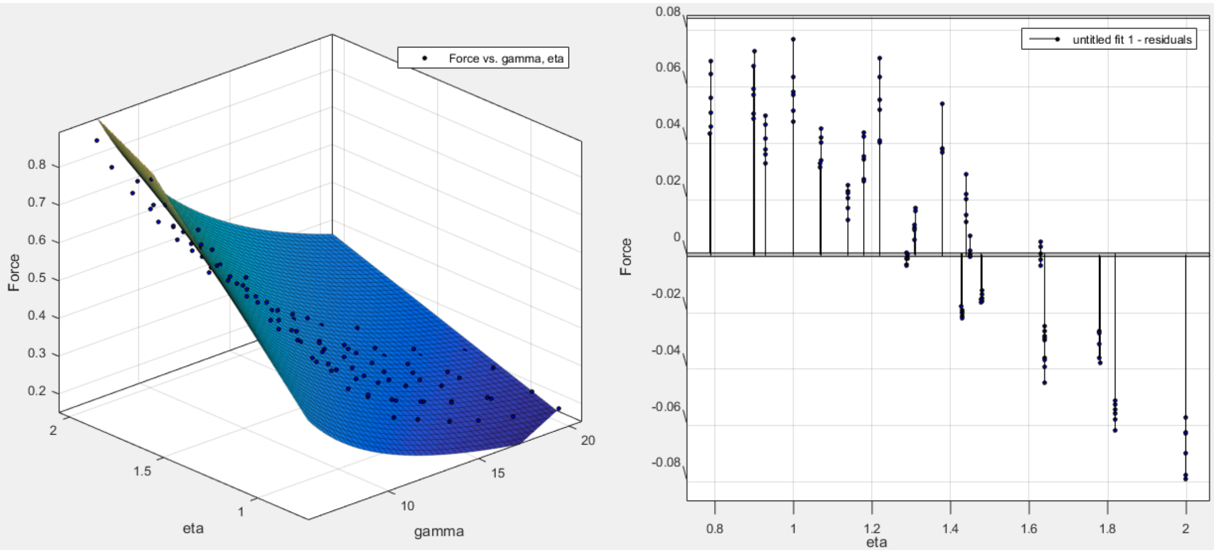

Figure 63: Curve fitting the data for the plate load case using Matlab curve fitting tool; Main plot (left) and residuals plot (right)

From Figure 63 it can be seen that that the use of equation (7.3) gives a poor fit over the variable ratio η. The deviation between the normalised load obtained from the FEA and the equation is quite large and has an inverse relation with the ratio η. This results in a R^2 of 0.927 and a RMSE of 0.04 (±8%). Because the curve does not coincide well with the data along the η axis, the η ratio has to be altered in the equation. This is done by applying an additional constant C_3 to the ratio η, which is determined in the curve fitting tool. The equation becomes the following:

$$\frac{N_{1,4\%}}{f_{y0}t_0d_0} = C_1 \frac{C_3\eta + 1}{(C_2\gamma - 1)} \tag{7.4}$$

By using equation (7.4), the deviation between the FEA data and the analytical equation is small with respect to the use of equation (7.3). However, the constant values that are obtained from the Matlab curve fitting tool, given in Table 8, are very large. These large constant values can be solved by changing the -1 in the denominator to +1. Because the function 1/(γ+1) has a gradient that is less steep than the function 1/(γ-1), the constant values will be lower. These constant values are also given in Table 8. The resulting engineering model for the ultimate load in the plate load case (α_{ip} = 90˚) is the equation stated below:

$$N_{1,4\%} = 17.1 \frac{\eta + 1}{(8.4\gamma + 1)} f_{y0} t_0 d_0 \tag{7.5}$$

The ultimate loads according to the FEA data and the acquired engineering model are plotted in Figure 64 and Figure 65, from which it can be noted that there is still little deviation in the case of a CHS diameter of 900 mm. For a CHS diameter of 1400 mm the largest deviation appears at the lowest γ, and thus the largest CHS thickness t_0. However, the mean deviation is 2.3% and therefore meets the convergence criterion. This convergence criterion states that the deviation must be smaller than 5%.

Table 8: Constant values, R^2 and RMSE following the Matlab curve fitting tool

Denominator	C_1	C_2	C_3	R^2	RMSE
$C_2\gamma - 1$	$1.5E^{+4}$	3672	0.59	0.995	0.011
$C_2\gamma + 1$	17.1	8.4	1.0	0.995	0.011

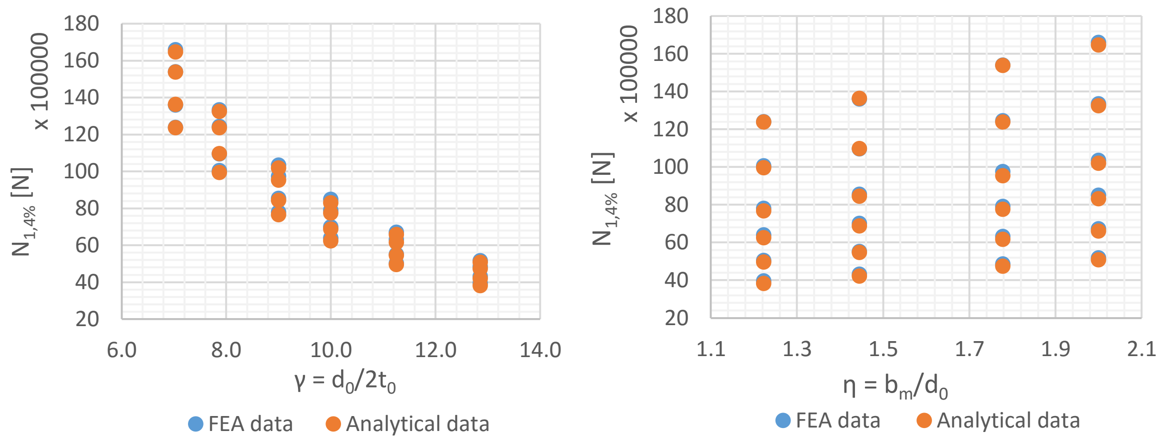

Figure 64: Comparison of FEA and analytical data for variable η, with diameter d_0 = 900 mm

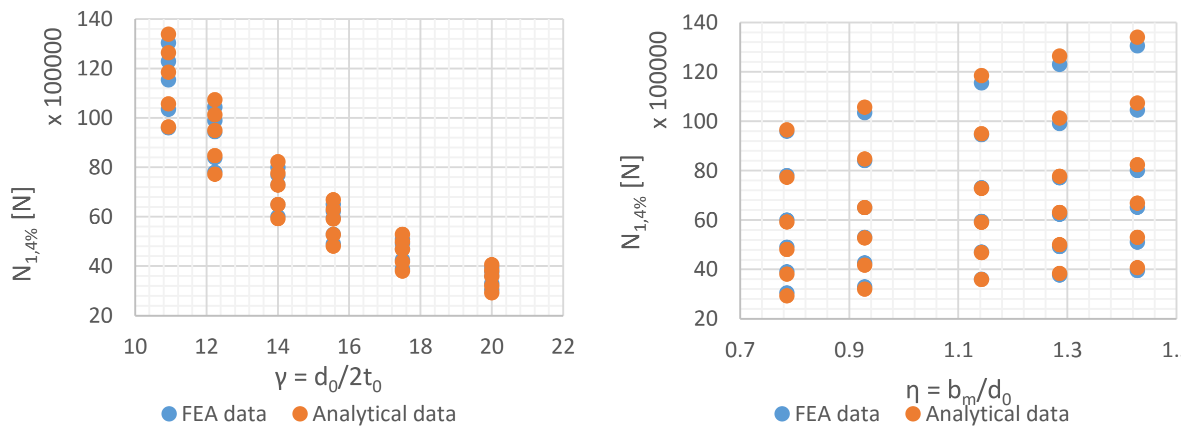

Figure 65: Comparison of FEA and analytical data for variable η, with diameter d_0 = 1400 mm

7.2.2 *Force angle $\alpha_{ip} = 60^{\circ}$*

When considering the plate load case with a force angle α_{ip} of 60 degrees, the reduction factor caused by the force angle is taken into account. Therefore the equation stated in (7.2) is used, with the constants determined in 7.2.1. When substituting both the angle α_{ip} and the constants C_1, C_2 and C_3 into this equation, the following equation is obtained for the load capacity:

$$\frac{N_{1,4\%}}{f_{y0}t_0d_0} = 17.1\frac{\eta+1}{(8.4\gamma+1)}\frac{1}{\sin(60)+C_4\cos(60)} \tag{7.6}$$

In this equation only one constant value C_4 is present, which is solved by curve fitting the data from the FEA. By applying equation (7.6) in the curve fitting tool, a constant value C_4 of 0.75 is obtained. By substituting this constant value into (7.6), equation (7.7) is determined. When using this equation, the coefficient of determination (R^2) is equal to 0.991 and the mean deviation (RMSE) is equal to 0.015. This corresponds with a mean deviation of 2.8%, which meets the convergence criterion. Therefore equation (7.7) is assumed to be a proper engineering model for the plate load case under an force angle of 60 degrees. The ultimate load prediction is plotted in Figure 66 and Figure 67 for a CHS diameter d_0 of 800 mm and 1400 mm, along with the data following the FEA. For the other diameters, similar plots are given in 0.

$$N_{1,4\%} = 17.1\frac{\eta+1}{(8.4\gamma+1)}\frac{f_{y0}t_0d_0}{\sin(60)+0.75\cos(60)} \tag{7.7}$$

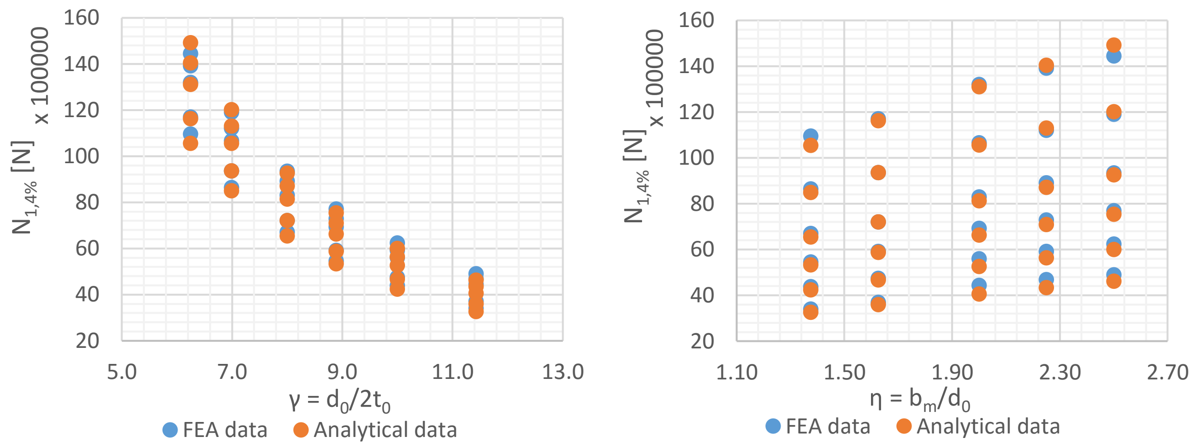

Figure 66: Comparison of FEA and analytical data in the plate load case for variable η, with diameter d0 = 800 mm

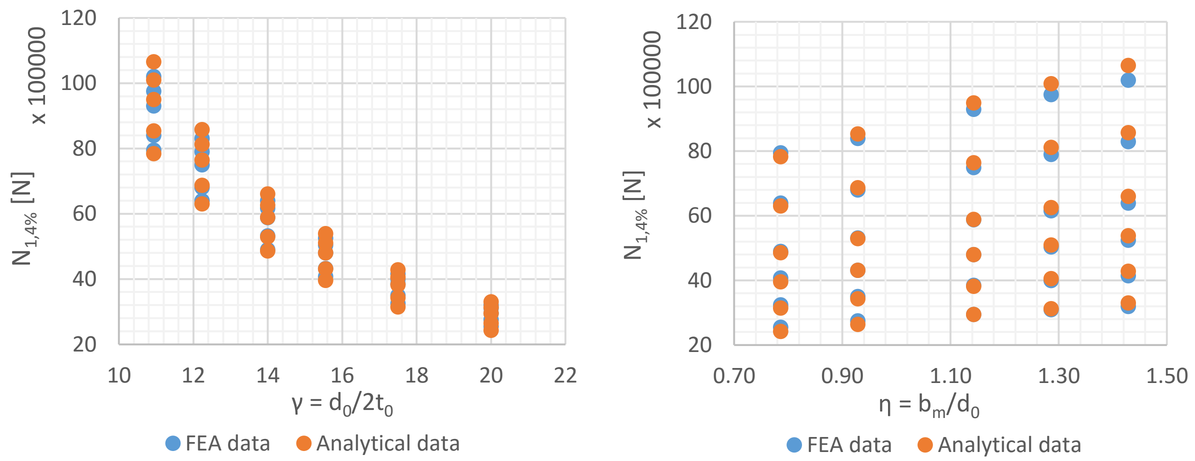

Figure 67: Comparison of FEA and analytical data in the plate load case for variable η, with diameter d0 = 1400 mm

7.3 Padeye load case

7.3.1 Constant padeye geometry

In 6.5, the relation between the ultimate load and the variable ratios is obtained for the padeye load case with a constant geometry. These relations are similar to those in the plate load case (α_{ip} = 90˚). Besides the similarities in connection behaviour, the stress distribution in the CHS in the both load case is also similar. Therefore the ultimate load in the padeye load case is derived by using the same engineering model as for this plate load case (α_{ip} = 90˚). In this engineering model, the constants are assumed to be unknown, giving the equation stated below:

$$\frac{N_{1,4\%}}{f_{y0}t_0d_0} = C_1\frac{C_2\eta+1}{\left(C_3\gamma+1\right)} \tag{7.8}$$

By applying equation (7.8) in the Matlab curve fitting tool (Figure 68), the constant values are obtained. By substituting these constant the resulting engineering tool for the padeye load case is described in (7.9). For this engineering tool the coefficient of determination (R^2) is 0.992 and the mean deviation (RMSE) is 0.017. This corresponds with a mean deviation of 2.7%, which meets the convergence criterion. The ultimate load prediction from the engineering tool is plotted in Figure 69 and Figure 70 for the variable dimension in the padeye load case, along with the data following the FEA. In Figure 69 the plot contains the data for a diameter equal to 800 mm, while in Figure 70 the plot contains data for a diameter of 1400 mm. For the other diameters, similar plots are given in 0.

$$N_{1,4\%} = 8.5\frac{\eta+1}{\left(3.5\gamma+1\right)}f_{y0}t_0d_0 \tag{7.9}$$

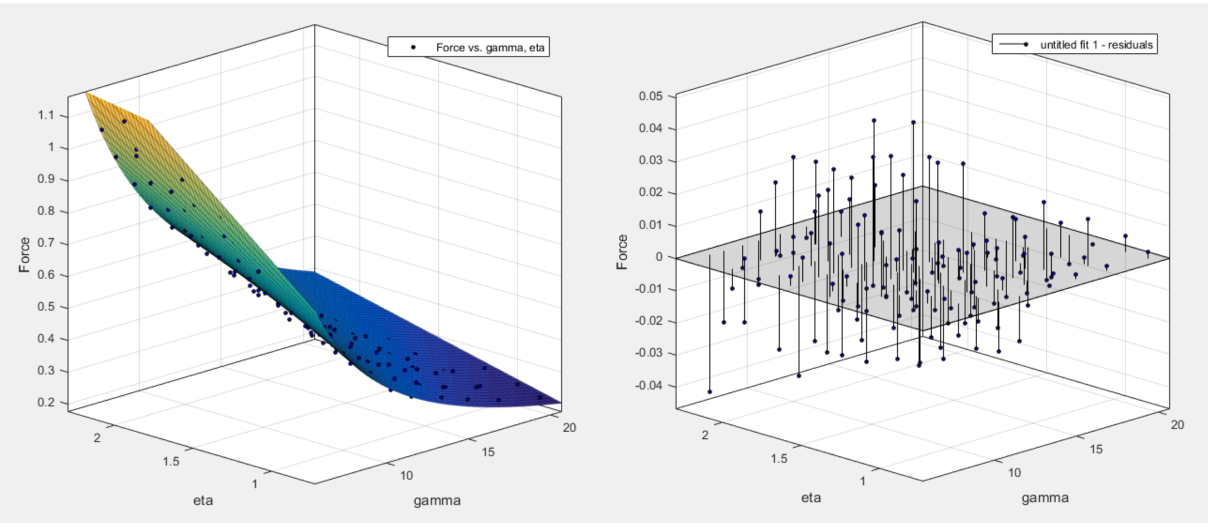

Figure 68: Curve fitting the data for the padeye load case using Matlab curve fitting tool; Main plot (left) and residuals plot (right)

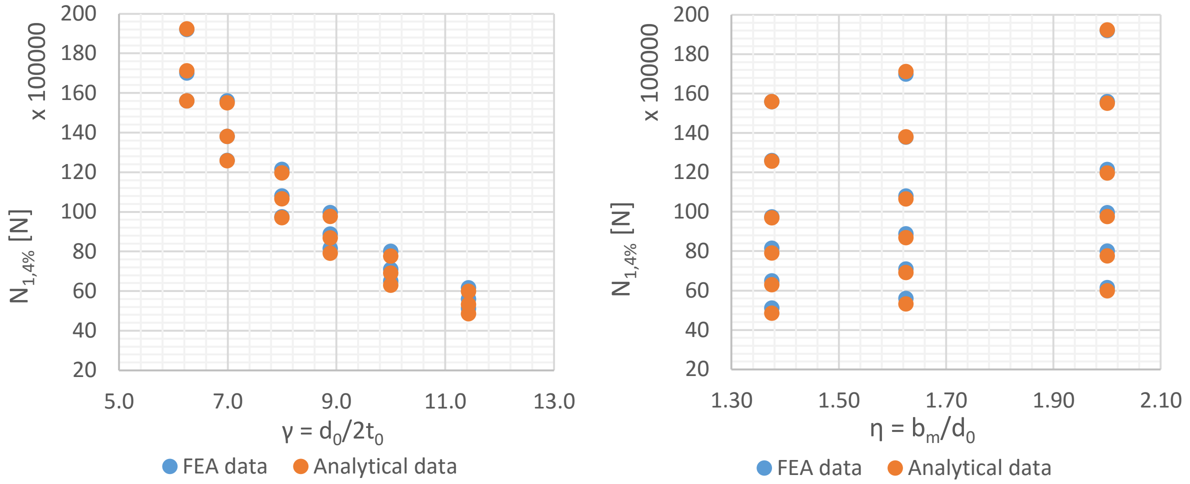

Figure 69: Comparison of FEA and analytical data in the padeye load case for variable η, with diameter d0 = 800 mm

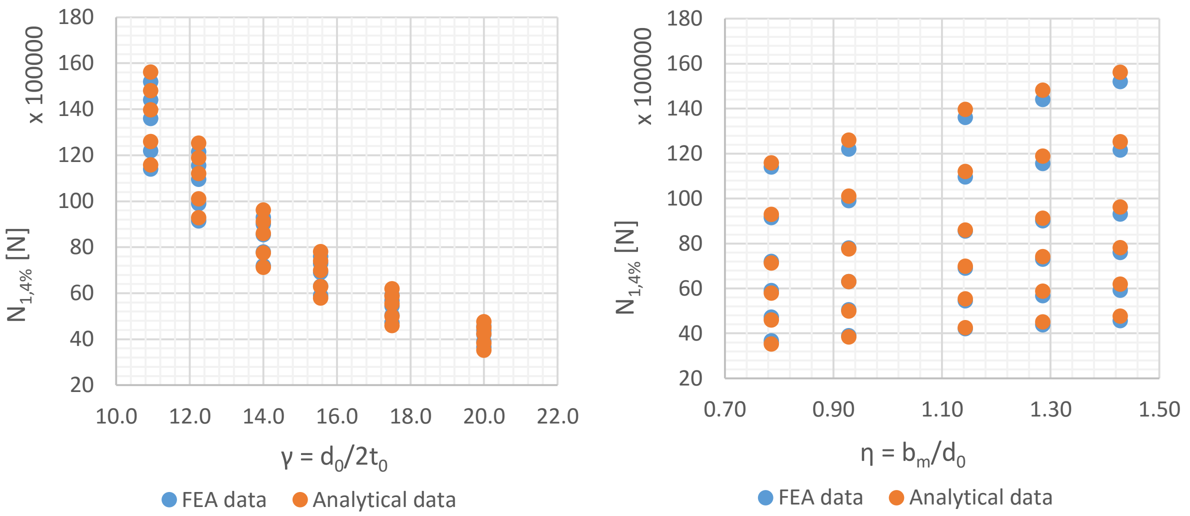

Figure 70: Comparison of FEA and analytical data in the padeye load case for variable η, with diameter d0 = 1400 mm

7.3.2 Variable padeye geometry

Besides the assumption of a constant geometry described in 6.5, the structural behaviour of the padeye is also determined for the use of a variable geometry. In the latter case, the structural behaviour is dependent of an additional plate width over height ratio ($\lambda=b_m/(R_m+h_0)$). The relation between the normalised load capacity and the λ ratio is divided over two ranges. The λ ratio is implied in the present engineering tool for the padeye load capacity, derived in 7.3.1.

For a ratio λ equal to the ratio used in the mean geometry (λ = 1.63), the present engineering tool stated in (7.9) is applied. When the ratio λ is lower than this mean value, the relation between the normalised load and λ is linear. Therefore the ratio λ is added as a linear factor in the engineering tool. For values of λ larger than the mean value used in the mean geometry, the relation between the normalised load and λ is inverse. In this case the ratio λ is added to (7.9) as an inverse factor instead of linear. Because the ratios γ and η must remain as derived in (7.9), the λ ratio is applied instead of the constant C_1. Both equations are shown in (7.10) below for λ larger and smaller than the mean value.

$$
\begin{aligned}
N_{1,4\%} &= \left(1+C_5\lambda\right)\frac{\eta+1}{\left(3.5\gamma+1\right)} f_{y0}t_0d_0 \quad 1.38\le\lambda\le1.63 \\
N_{1,4\%} &= \left(1+\frac{C_5}{\lambda}\right)\frac{\eta+1}{\left(3.5\gamma+1\right)} f_{y0}t_0d_0 \quad 1.63\le\lambda\le2.50
\end{aligned}
\tag{7.10}
$$

With this equation equal to (7.9) for the mean λ, the unknown constant C_5 can be solved in both cases. This is done in (7.11). By substituting this value into (7.10), the equation is used to determine an engineering tool that describes the load capacity in the padeye load case with variable geometry and λ.

$$
\begin{aligned}
C_1 &= \left(1+C_5\lambda\right)\rightarrow 8.5=\left(1+C_5 1.63\right)\rightarrow C_5=4.6 \\
C_1 &= \left(1+\frac{C_5}{\lambda}\right)\rightarrow 8.5=\left(1+\frac{C_5}{1.63}\right)\rightarrow C_5=12.2
\end{aligned}
\tag{7.11}
$$

When varying the constant values of C_5 from their determined values, an optimal solution can be obtained for the engineering tool of the padeye load case with variable geometry. This optimal solution is stated in , for which a coefficient of determination (R^2) of 0.996 and a mean deviation (MRSE) of 0.016 are determined. This corresponds with a mean deviation of 2.3%, which is well within the boundary of the convergence criterion.

$$
\begin{aligned}
N_{1,4\%} &= \left(1+4.65\lambda\right)\frac{\eta+1}{\left(3.5\gamma+1\right)} f_{y0}t_0d_0 \quad 1.38\le\lambda\le1.63 \\
N_{1,4\%} &= \left(1+\frac{12.5}{\lambda}\right)\frac{\eta+1}{\left(3.5\gamma+1\right)} f_{y0}t_0d_0 \quad 1.63\le\lambda\le2.50
\end{aligned}
\tag{7.12}
$$

The comparison between the ultimate load prediction from the engineering tool and the FEA data is plotted in Figure 71 and Figure 72 for the variable dimension in the padeye load case. In Figure 71 the plot contains the data for a diameter equal to 800 mm. In Figure 72 the data for a diameter of 1400 mm is plotted. Similar plots are given in 0 for the other diameters.

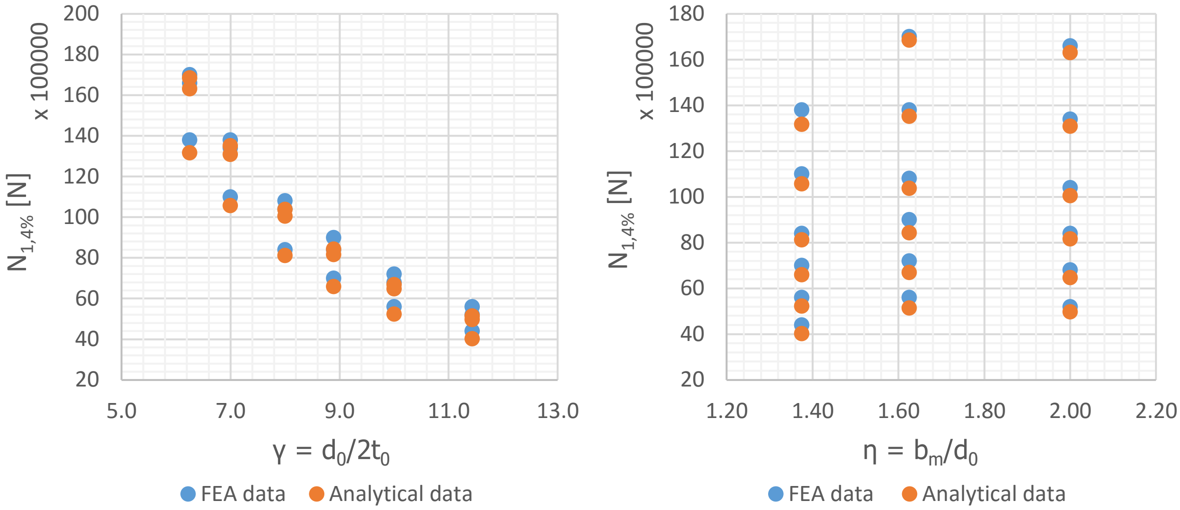

Figure 71: Comparison of FEA and analytical data in the padeye load case for variable η, with diameter d0 = 800 mm

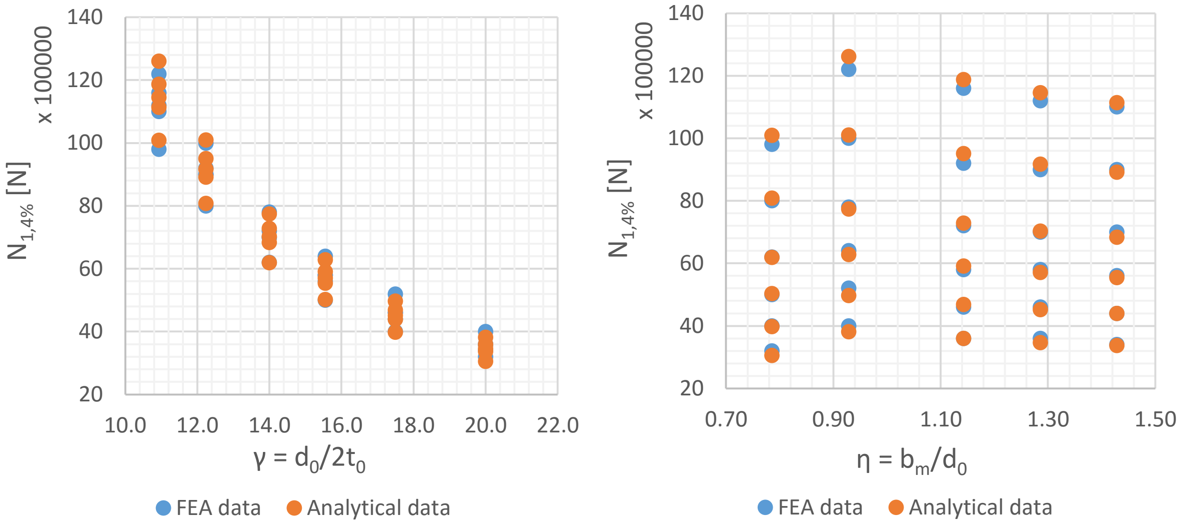

Figure 72: Comparison of FEA and analytical data in the padeye load case for variable η, with diameter d0 = 1400 mm

7.4 Validation

In order to validate the obtained engineering tool for the load capacity in the padeye load case, the tool is used on the geometries used in the padeye comparison. For each padeye geometry in this comparison, the ultimate load is determined using FEA and the engineering tools of the plate and padeye load case. Besides the load capacity calculation of the engineering tools, the capacity is also determined by using the Roark method and the equations by Wardenier et al. and Voth. The deviation between the FEA data and the different calculation methods is described in (7.13). The resulting deviations from the FEA data are given in Table 9, in which a positive value corresponds with an underestimation and a negative value corresponds with an overestimation.

$$\Delta N_{1,4\%} = \left(1 - \frac{N_{1,4\%,Analytic}}{N_{1,4\%,\mathrm{FEA}}}\right)100 \tag{7.13}$$

In this figure it can be noted that the Roark method gives an underestimation of 60% to 70%. The deviation confirms that the Roark method is very conservative in the calculation of the load capacity in the padeye load case. This is due to the use of the linear elastic material behaviour and therefore the yield stress criterion.

The equation derived by Wardenier et al. gives a load prediction that deviates 3% to 20% from the FEA results. Despite the fact that the equation describes the load capacity of a plate-to-CHS connection, it still gives a ultimate load prediction which is more accurate than using the Roark method. However, the equation derived by Wardenier et al. is based upon a different load case and a different failure criterion. Therefore it this equation is not a good prediction of the ultimate load in the padeye load case.

Voth adjusted the equation by Wardenier et al, such that it includes the influence of the plate thickness. The same load case and failure criteria are used as in the derivation by Wardenier. The equation by Voth gives an overestimation of the load capacity, which deviation between 60% and 100% from the FEA data. From this it is concluded that the equation by Voth cannot be used to describe the load capacity in the padeye load case.

Table 9: Comparison of the deviations between the FEA data and Engineering tool calculations

Project	FEA results		Deviation						
	Row	$N_{1,4\%}$ [N]	Roark	Wardenier	Voth	Plate (α_{ip}=90˚)	Plate (α_{ip}=60˚)	Padeye Const.	Padeye Var.
Wintershall Noordzee bv	1	1.10E+07	61.0	4.7	-97.8	-5.9	14.6	-24.5	-6.2
	2	1.12E+07	61.7	6.4	-94.3	-4.0	16.2	-22.2	-8.3
GFD Suez		7.80E+06	71.7	11.7	-78.1	12.9	29.8	-2.7	-0.4
	A1	1.18E+07	74.2	19.6	-60.3	16.1	32.4	1.6	3.1
	A2	1.08E+07	74.2	16.4	-66.5	15.6	32.0	0.8	-0.8
Chevron A18	A	1.04E+07	70.2	10.3	-80.5	7.3	25.3	-8.9	-2.6
	C	9.60E+06	72.1	7.0	-84.5	6.9	25.0	-9.4	0.7
Ika-JZ		4.80E+06	70.9	23.5	-57.2	18.2	34.1	3.8	8.5
Cardon-Perla		1.04E+07	70.9	2.7	-102.7	-0.7	18.9	-18.3	2.1

Deviation ≤ 5%
5% ≤ Deviation ≤ 10%
Deviation > 10%

When considering the engineering tool derived for the plate load case with a force angle of 90 degrees, it is noted that the deviation is similar to that from the equation by Wardenier et al. From the engineering tool a load capacity is obtained that deviates between 1% and 18% from the FEA data. Although this is a rather rough ultimate load prediction for the padeye load case, it is still more accurate than using the Roark method.

By including the reduction factor for the force angle, the engineering tool of the plate load case with a force angle of 60 degrees can be considered. Because a reduction factor is applied, the resulting load capacity gives a underestimation of the load capacity. The deviation between the engineering tool and the FEA data range from 15% to 35%.

Finally the engineering tool for padeye load case is considered. By using this tool, the ultimate load prediction deviates between 1% and 25% from the FEA data. In four of the compared padeye geometries the engineering tool gives a prediction for which the deviation meets the convergence criteria of 5%. However, in three cases an overestimation is obtained for which the deviation is around 20%. This is due to the fact that only the mean geometry is considered in the determination of the engineering tool. Therefore the load prediction is inaccurate for geometries other than the mean geometry.

Due to the difference in geometry for the padeyes used in the padeye comparison, the engineering tool geometries is developed for variable. By using this engineering tool, the deviations between the ultimate load prediction and the FEA data range from 0.5% to 8.5%. The three largest deviations, from the projects of Wintershall Noordzee B.V. and Ika-JZ, are due to the different height over main plate radius ratio that is present in these geometries. In the mean geometry, this ratio is 1.1, while in the geometries with a large deviation this ratio is around 1.4. These different geometrical ratios are shown in Figure 73.

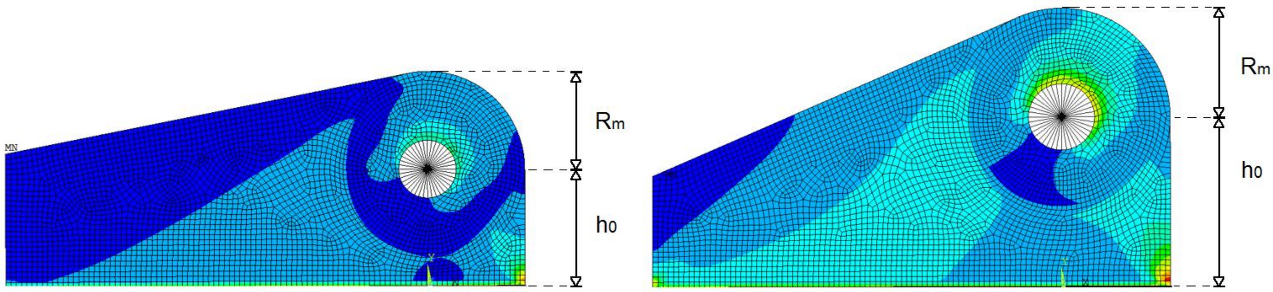

Figure 73: Comparison between the mean geometry with variable plate width (left) and the padeye geometry used in the project of Wintershall Noordzee B.V.

Due to this influencing factor, the range in which the derived engineering tools are valid has to be narrowed. This is done by including the ratio between the height of the pinhole centre and the radius of the main plate. Including this factor leads to a range stated in Table 10.

Table 10: Range for which the different engineering tools are valid

Load case	**$\gamma = d_0/2t_0$ [-]**	**$\eta = b_m/d_0$ [-]**	**$\lambda = b_m/(R_m+h_0)$ [-]**	**α_{ip} [deg]**	**h_0/R_m [-]**
Plate ($\alpha_{ip} = 90^\circ$)	$6.3 \leq \gamma \leq 20.0$	$0.79 \leq \eta \leq 2.00$	-	90˚	-
Plate ($\alpha_{ip} = 60^\circ$)	$6.3 \leq \gamma \leq 20.0$	$0.79 \leq \eta \leq 2.50$	-	60˚	-
Padeye const. geom.	$6.3 \leq \gamma \leq 20.0$	$0.79 \leq \eta \leq 2.22$	$\lambda = 1.63$	60˚	1.1
Padeye var. geom.	$6.3 \leq \gamma \leq 20.0$	$0.79 \leq \eta \leq 2.22$	$1.38 \leq \lambda \leq 2.50$	60˚	1.1

7.5 Conclusion

From the load capacities obtained from the FEA data in chapter 6, engineering tools are derived that describe the load capacity for the corresponding load case. This is done by using the Matlab curve fitting tool to describe the data with the input of a custom equation. The engineering tools from this curve fitting tool are described below. In the first case the equation of the plate load case with α_{ip} = 90˚ is described in order to obtain a the proper behaviour of the variable dimensions in the CHS. The obtained equation is stated below:

$$N_{1,4\%} = 17.1\frac{\eta+1}{\left(8.4\gamma+1\right)} f_{y0}t_0d_0 \tag{7.14}$$

Because the force in the padeye load case is predominantly under an angle of 60 degrees, this force angle is applied in the plate load case. Because of this force angle, a reduction term is added to the plate load case with α_{ip} = 90˚ that takes into account the load reduction due to the bending moment. This load case contains the force angle α_{ip}. Including this reduction factor does result in the equation of the plate load case with α_{ip} = 60˚, which is stated below:

$$N_{1,4\%} = 17.1\frac{\eta+1}{\left(8.4\gamma+1\right)} \frac{f_{y0}t_0d_0}{\sin\left(60\right)+0.75\cos\left(60\right)} \tag{7.15}$$

Finally the engineering tool of the load capacity in the padeye load case is determined. This tool is similar to that of the plate load case with α_{ip} = 90˚. However, by varying the plate width while the height of the padeye remains constant, a bending moment is included in the main plate. To take the influence of the bending moment into account, an additional ratio λ is used. Because the force angle does not vary, the reduction factor due to the angle is not included in this engineering tool. The obtained equation for the load capacity in the padeye load case is stated below:

$$\begin{aligned} N_{1,4\%} &= \left(1+4.65\lambda\right)\frac{\eta+1}{\left(3.5\gamma+1\right)} f_{y0}t_0d_0 \qquad 1.38 \le \lambda \le 1.63 \\ N_{1,4\%} &= \left(1+\frac{12.5}{\lambda}\right)\frac{\eta+1}{\left(3.5\gamma+1\right)} f_{y0}t_0d_0 \qquad 1.63 \le \lambda \le 2.50 \end{aligned} \tag{7.16}$$

In order to validate the equation of the padeye load case, the padeye geometries used in the padeye comparison in chapter 3 are analysed using FEA. The ultimate load of these geometries is determined using both the derived engineering tools and the available calculation methods, stated in 2.5. By comparing these results it is obtained that the engineering tool for the padeye load case gives an accurate prediction of the ultimate load for padeye geometries equal within the range given in Table 10.

8 Conclusions and recommendations

8.1 Conclusions

The objective of this thesis is to determine an engineering tool which is an advanced method of the Roark equations, giving a more accurate solution of the load capacity of a padeye connected to a circular hollow section (CHS). This load case is denoted as the padeye load case. The engineering tool is based on the finite element model (FEM) in which plastic material behaviour is taken into account.

Present methods of calculating the load capacity in the padeye load case are determined in chapter 2. The available methods are the Roark method and finite element modelling (FEM). The Roark method is a quick but conservative calculation method, while FEM software is accurate but also very time consuming and therefore expensive to use. For a plate load case, which is a simplified model of the padeye load case, multiple calculation methods are available. Two of these are the method derived by Wardenier et al. and Voth. In contrast to the Roark method, these methods allow plastic material behaviour.

Subsequently the considered models are determined in chapter 3. The padeye load case model consists of a padeye connected to a simply supported CHS section. Besides this model, the plate load case is used as a simplified model of the padeye load case. In both load cases end plates and bending moments are applied at the supports. The considered geometries are obtained by comparing the geometries used in projects performed by Seaway Heavy Lifting. From this comparison a mean geometry is determined, in which the dimensions are divided into constant and variable dimensions.

The variable dimensional have a large influence on the load capacity in the corresponding load case, while the constant dimension are assumed to have little influence. In order to reduce the number of variables, the ratios of these variable dimensions are used. These are the radius to thickness ratio of the CHS ($\gamma_0 = d_0/2t_0$), the effective width ratio between the chord and the padeye main plate ($\eta = b_m/d_0$) and the ratio between the plate width and height ($\lambda = b_m/(R_m+h_0)$). The constant dimensions are varied as a function of the plate width b_m, while in the padeye load case the plate width is also varied while the height remains constant. The range of the variable dimensions is obtained from the comparison of padeye geometries used in projects. This range is stated below:

- CHS diameter: d_0 = 800 - 1400 mm
- CHS thickness: t_0 = 35 – 64 mm
- Padeye plate width: b_m = 1100 – 2000 mm

In order to derive an engineering tool, the numerical model is constructed in chapter 4 using the FEM program Ansys. In this model the appropriate boundaries from chapter 3 are applied. The three-dimensional model consists of four-node shell elements with a fine mesh at the plate-to-CHS connection. At the end sections of the CHS the mesh is chosen relatively coarse. In order to exclude the influence of the stiff end plates at the main plate, the chord length of the CHS is determined to be 6 times the diameter d_0.

An analytical, two-dimensional ring model is derived in chapter 5 for both the padeye load case and the plate load case. In this model the CHS is represented as a ring with a point load, which is balanced by a distributed transverse shear force. A similar model is used to determine the equations used in Roark, Wardenier et al. and Voth. The deformation of the CHS mainly causes bending moments in the cross-section. The governing stresses in the CHS are due to these bending moments and occur at the location of the applied point load.

The results following the FEA of the FEM model derived in chapter 4 are described in chapter 6. By allowing plastic material behaviour in the FEM model, a limit state criterion must be determined. The governing failure criterion is assumed to be the average linearized plastic strain of 4%. This linearized strain is the mean plastic strain at the governing section of the CHS, over a volume with dimensions equal to the CHS thickness. When using the failure criterion in the finite element analysis (FEA) of the padeye load case, the load capacities of the considered geometries are obtained. When processing the results from the FEA, a dimensionless normalised force $N_{1,4\%}/f_y d_0 t_0$ is used. The relation between the ratios η, γ and λ and the ultimate load is obtained by varying these ratios in the FEA. The relations are stated below:

- $N_{1,4\%}/f_y d_0 t_0 - \gamma$: inverse relation
- $N_{1,4\%}/f_y d_0 t_0 - \eta$: linear relation
- $N_{1,4\%}/f_y d_0 t_0 - \lambda$: linear relation for $1.38 \leq \lambda \leq 1.63$
- $N_{1,4\%}/f_y d_0 t_0 - \lambda$: inverse relation for $1.63 \leq \lambda \leq 2.50$

The value of γ is inversely related to the stiffness of the CHS. As the stiffness decreases the load capacity will decrease as well. For an increasing value of η the area over which the force is distributed increases, resulting in a lower distributed load and therefore an increasing load capacity. The mean value of λ causes the line of the force to coincide with the centre of the main plate, causing only normal and shear force in the main plate-to-CHS connection. When varying the ratio λ an eccentricity will be present between the line of the force and the main plate centre, causing a bending moment in the main plate. Due to this reason the relation is divided over two ranges, for both a positive and negative bending moment.

Finally, the engineering tools are derived in chapter 7 for the different load cases, using the results from the FEA from chapter 6 and the analytical equation from chapter 5. The relation between the variable ratios and the normalised load are similar for both the FEA results and the derived analytical equation. This equation is fit to the FEA data with the Matlab curve fitting tool. From this an engineering tool is derived for both the plate load case and the padeye load case.

When validating the engineering tool by comparing the ultimate loads of other padeye geometries, it is concluded that the derived method is only valid for padeye geometries within a specific range. Within this range the derived engineering tool predicts the load capacity with a deviation that meets the convergence criteria. This results in a engineering tool that is an advanced method of the Roark method.

8.2 Recommendations

This study resulted in an engineering tool for the padeye load case. Because the developed engineering tool is valid within a specific range, it is recommended to expand this range for different geometries. This can be done by:

- Expanding the present variable ratios γ, η and λ.
- Studying the influence of the ratio between the height of the pinhole centre and the main plate radius (h_0/R_m).
- Varying the angle of the applied force. Within projects performed by Seaway Heavy Lifting the force is applied under an angle of 60 degrees, with a deviation of 7.5 degrees. Therefore it is desired to obtain the influence of the variable force angle.
- Applying ring stiffeners. These ring stiffeners are neglected in this study, but are present in most projects performed by Seaway Heavy Lifting. These ring stiffeners have significant influence on the stress distribution in the CHS and therefore on the load capacity.

The padeye load case is only one of many load cases in which CHS cross-section are present. These load cases have some similarities, but also many differences. When it is desired to obtain the load capacity of other load cases containing CHS, these load cases can be considered separately or in relation with the padeye load case.

9 Bibliography

[1] Seaway Heavy Lifting, Seaway Heavy Lifting, 2015. [Online]. Available: https://www.seawayheavylifting.com.cy/. [Accessed 04 November 2015].

[2] J. Wardenier, Y. Kurobane, J. Packer, G. van der Vegte and X.-L. Zhao, Design guide for circular hollow sections (CHS) joints under predominantly static loading, CIDECT, 2008.

[3] A. Voth, “Branch Plate-to-Circular Hollow Structural Section Connections,” Toronto, 2010.

[4] Tata steel, “Current issues within the UK steel supply chain for the offshore wind industry,” Tata steel, 24 May 2012. [Online]. Available: http://www.all-energy.co.uk/__novadocuments/14893. [Accessed 13 January 2016].

[5] Seaway Heavy Lifting, “General criteria for liftpoints,” Seaway Heavy Lifting, Zoetermeer, 2015.

[6] Abuco, “Upending tool for IHC HS,” Abuco construct and repair, 8 June 2015. [Online]. Available: https://www.abuco.nl. [Accessed 6 August 2015].

[7] Large Diameter Drilling (LDD), “ILT: Interla Lift Tool,” Large Diameter Drilling (LDD), 2014. [Online]. Available: http://www.lddrill.com. [Accessed 6 August 2015].

[8] Seaway Heavy Lifting, “General criteria for liftpoints,” Zoetermeer, 2013.

[9] Mechanical Design in Optical Engineering, “Stress-Strain Relationships,” [Online]. Available: http://fp.optics.arizona.edu/optomech/references/OPTI_222/OPTI_222_W4.pdf. [Accessed 20 january 2016].

[10] DNV-RP-C208, Determination of Structural Capacity by Non-linear FE analysis Methods, Det Norske Veritas AS, june 2013.

[11] The European Union Per Regulation, “Eurocode 3 - Design of steel structures - Part 1-5: Plates structural elements,” European Committee for Standardization, 2006.

[12] L. Lu, G. d. Winkel, Y. Yu and J. Wardenier, “Deformation limit for the ultimate strength of hollow section joints,” Melbourne, Australia, 1994.

[13] W. Young and R. Budynas, Roark's Formulas for Stress and Strain, United States of America: McGraw-Hill, 2002.

[14] C. C. M. o. Structures, Artist, [Art]. TU Delft, 2013.

[15] G. J. van der Vegte, “The static strength of uniplanar and multiplanar tubular T- and X-joints,” Delft University Press, Delft, 1995.

[16] J. A. Packer and S. Willibald, "The ultimate strength of axially loaded CHS uniplanar T-joints," in *Tubular Structures XI*, CRC Press, 2006, pp. 115-120.

[17] Nederlands Instituur voor Lastechniek, "Laskenning opgefrist (nr. 56): Geometrische afwijkingen - deel 1," 2008. [Online]. Available: http://www.nil.nl/public/cms/lists/upload/56_geometrie_1.pdf. [Accessed 19 10 2015].

[18] D. G. N. Wells, The Finite Element Method: An Introduction, University of Cambridge and Delft University of Technology, 2009.

[19] R. J. Schmidt, A. P. Boresi and O. M. Sidebottom, Advanced mechanics of materials, Wiley, January 1993.

[20] H. Welleman, "Arbeidstheorema's van Castigliano," in *CT3109 Constructiemechanica 4: Inleiding Arbeid en Energie*, Delft, Faculteit CITG, Technische Universiteit Delft, 2011, pp. 28-37.

[21] J. Alexiou, "Deflection of a Ring using Energy Methods," Koyo Bearings USA, LLC., Greenville USA, 2011.

[22] C. J. Dekker and J. Cuperus, "Local load stresses in cylindrical shells at plate clips," *In. J. Pres. Ves. & Piping,* no. 67, 1995.

[23] A. -K. Soh and C. -K. Soh, "Design and Analysis of Offshore Lifting Padeyes," *J. Construct. Steel Research ,* vol. 1989, no. 14, 1989.

[24] Y. S. Choo, K. H. Lee and W. H. Lee, "Stresses and Strength of Padeye to Circular Pipe Connection," Los Angeles, 1996.

[25] A. C. Ugural and S. K. Fenster, Advanced Mechanics of Materials and Applied Elasticity, United States of America: Pearson Education, Inc., 2012.

[26] A. Gasmi, P. F. Joseph, T. B. Rhyne and S. M. Cron, "Closed-form solution of a shear deformable, extensional ring in contact between to rigid surfaces," *International Journal of Solids and Structures,* no. 48, 2010.

[27] Ansys, Inc., "Ansys Mechanical APDL Element Reference," Ansys, Inc., Canonsburg, October 2012.

[28] E. Q. Sun, "Shear locking and hourglassing in MSC Nastran, ABAQUS and ANSYS," in *MSC Software Users Meeting*, 2006.

[29] P. C. Hoogenboom, "CIE4143 Shell Analysis, Theory and Application," 2014/2015. [Online]. Available: http://homepage.tudelft.nl/p3r3s/CT4143_schedule.html. [Accessed 11 Juni 2015].

[30] W. Yi and C. Basavaraju, "Cylindrical Shells Under Partially Distributed Radial Loading," *J. Pressure Vessel Technol.,* p. 5, 1996.

[31] J. Morshedian , "Stress Analysis in Elastic Bending Beams and Thick Hollow Cylinders," *Polymer Research Center of Iran,* p. 6, Teheran.

[32] M. Serati, H. Alehossein and D. J. Williams, “Elastic stress analysis of partially loaded hollow disks,” no. 53, 2012.

[33] ESAB, “Template for giant offshore platform,” ESAB Welding & Cutting, 8 June 2015. [Online]. Available: http://www.esab.com. [Accessed 6 August 2015].

[34] R. S. Puthli and S. Herion, “Sensitivity study,” in *Tubular structures IX*, Lisse, Swets & Zeitlinger B.V., 2001, pp. 175-180.

[35] B. Wieland and U. Simon, *Handout: Plasticity and Hardening,* Ulm.

[36] “Deformation (engineering),” Wikipedia, 14 June 2015. [Online]. Available: https://en.wikipedia.org/wiki/Deformation_(engineering). [Accessed 04 November 2015].

Appendix A Literature study

A.1 Padeye design criteria

In order to design a padeye, the general criteria for lift points [8] have to be met. These criteria which the lift points have to fulfil are criteria prepared by Seaway Heavy Lifting, which form a part of the Seaway Heavy Lifting Quality System. These criteria are based on the codes AISC 2010 for the checks of lift points, API 2007 for the checks on jackets and topsides during installation and the Eurocode for the design of welded and bolted connections.

In the lift point criteria it is stated that the padeye should be strong enough and be easy to reach in order to install and remove the shackle. Besides its strength, the padeye should have a low impact on the module structure. In order to determine if the strength of the padeye is sufficient, the design criteria have to be checked. These criteria can be divided into three groups, which are criteria of the main plate, the stiffener plates and the welds. The strength of the welds is however beyond the scope of this thesis, and will therefore not be taken into account.

A.1.1 Force distribution

The lifting force (F_{Lp}) acting on the padeye is caused by the weight of the structure and the equipment used. This lifting force is transferred to the sling by a shackle through the padeye pinhole and has its origin at the centre of the shackle cross-section, which is acting in the centre of the pinhole (Figure 74). This pinhole centre lies at a height h_0 above the bottom of the main plate. Because the sling is acting under an in-plane angle α_{ip} with the main plate, the force at the pinhole will be under the same angle (α_{ip}). The in-plane sling angle β_{ip} is given in the criteria from the SHL Quality System [8] and is assumed to be 60 degrees with a variation of 7.5 degrees.

Due to this angle of the force α_{ip}, the force can be divided into a transverse component F_y and a longitudinal component F_x. Because the force is acting at a height h_0 the longitudinal component causes an in-plane bending moment M_{ip}.

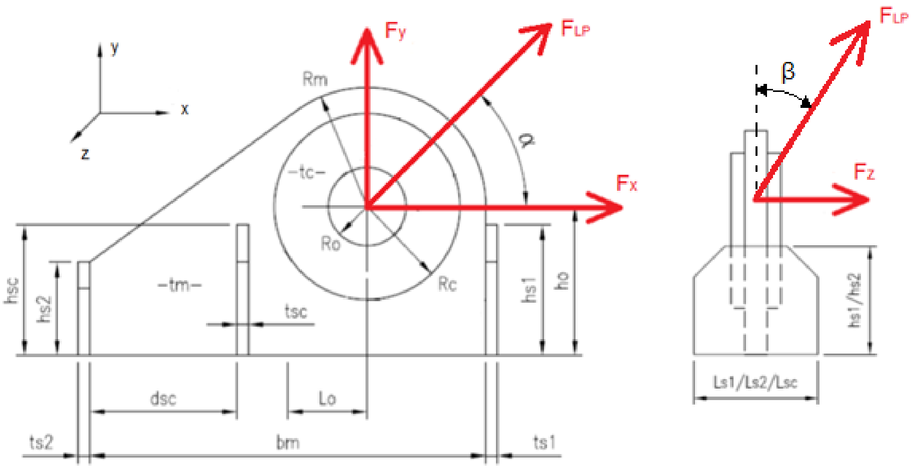

Figure 74: Padeye geometry, as given in the Seaway Heavy Lifting Quality System [8]

Besides these force components a lateral force (F_z) can occur as a result of any misalignment, causing the sling to act under an out-of-plane angle (β), perpendicular to the plain of the padeye main plate (Figure 74). This lateral force also causes a bending moment (M_{Lat}). The lateral load will be 5% of the total load for misalignments smaller than 1˚. For misalignments larger than 1˚, the lateral load will be and 5% of the total load, plus an additional factor tan(β).

$$\begin{aligned} &for: \beta < 1^{\circ} \rightarrow F_z = 0.05 F_{Lp} \\ &for: \beta \geq 1^{\circ} \rightarrow F_z = (0,05 + \tan(\beta)) F_{Lp} \end{aligned} \tag{9.1}$$

A.1.2 Main plate design

Following the criteria from the Quality System prepared by Seaway Heavy Lifting, a number of design considerations applicable on this load case are given. First the main plate should have an outer radius (R_m) of 1.75 times the diameter of the shackle pin (D) and should not have more than one cheek plate at each side. This cheek plate thickness (t_c) should not exceed the thickness of the main plate (t_m) and its radius (R_c) will be taken as 1.5 times the diameter of the shackle pin. Besides these design consideration some standard dimensions are given in the criteria, shown below.

$$\begin{aligned} R_0 &= 1.1D \\ R_m &= 1.75D \\ R_c &= 1.50D \\ t_m &= 0.25 \text{ } to \text{ } 0.40D \\ t_c &= 0.15 \text{ } to \text{ } 0.30D \end{aligned} \tag{9.2}$$

Beside these dimensional criteria in relation to the shackle pin, the main plate should be strong enough to withstand stresses due to the load. The stresses in the main plate could lead to multiple failure mechanisms, which can be obtained from the General criteria for liftpoints [8]. These failure mechanisms, shown in Figure 75, are:

- Bearing stress at contact area with shackle pin (f_p)
- Shear stress at section α-α (f_S)
- Shear stress at weld between the main plate and the cheek plate (f_c)
- Tension stress at section β-β (f_T)
- Tear-out stress at section γ-γ (f_S)

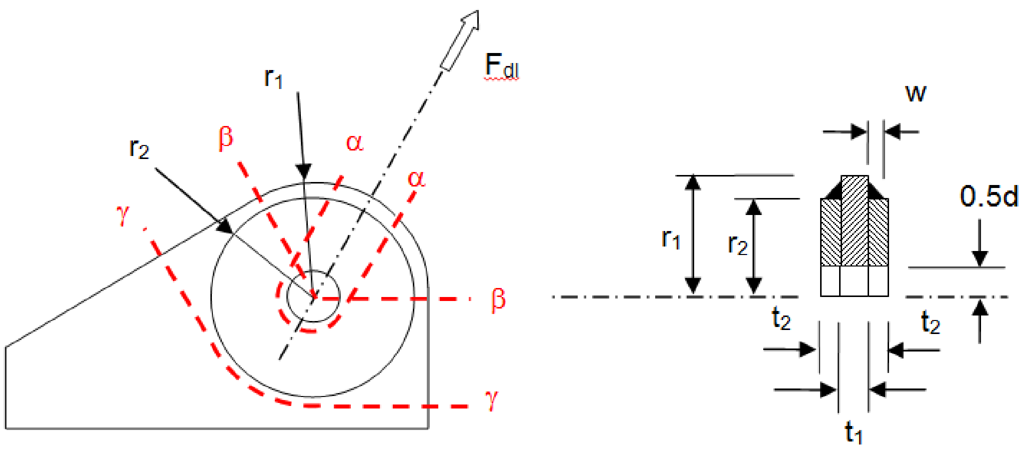

Figure 75: Padeye main plate failure mechanism, from Seaway Heavy Lifting general criteria for liftpoints [8]

A.1.3 Stiffener plate design

The geometry of the ring stiffeners is depending on the load distribution. The forces are distributed over the different stiffeners, depending on the geometry.

- The longitudinal force (F_x) is taken by the padeye main plate to CHS connection (Figure 76 a). Because the weld is assumed non-critical, the cross-section of the main plate has to take the stresses caused by this force.
- The bending moment (M) is taken by the top and bottom stiffener (Figure 76 b).
- The radial force (F_y), the lateral force (F_z) and the lateral bending moment (M_{Lat}) are distributed over the top and centre stiffener (Figure 76c and d).

With the force distribution known, the stiffener geometry is designed such that the stiffener plates can withstand the stresses due to the load. This means that the stiffeners plates and the main plate must have sufficient intersecting cross-section to transfer the stresses.

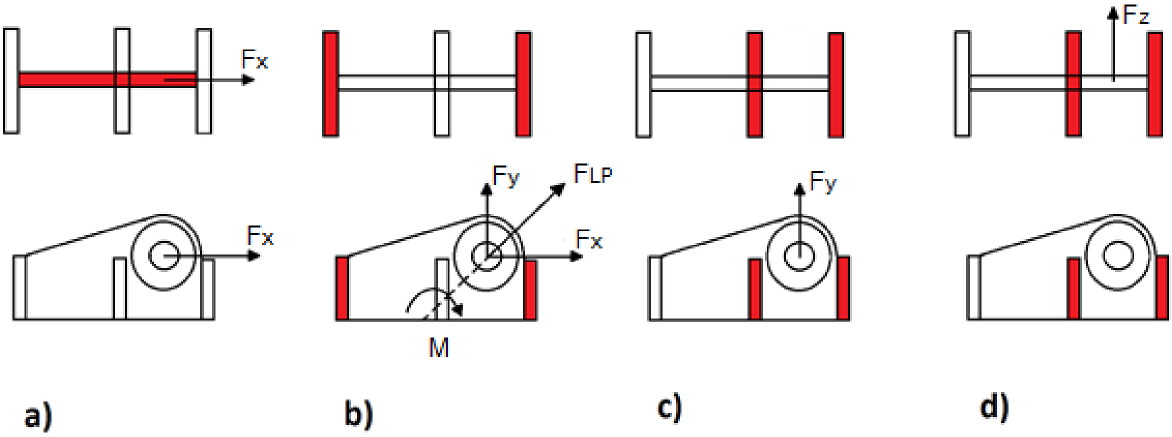

Figure 76: Force distribution over the padeye with ring stiffeners

A.2 Roark [13]

In Roark's approach a two dimensional model is considered in which multiple formulas are used to determine the stress distribution in the cross section due to different types of loading. Roark's formulas for stress and strain are based upon analytical, numerical and experimental stress analysis of structural components. It was meant for the purpose of making available a compact, adequate summary of the formulas, facts and principles on determining these stress distributions.

With Roark's formulas the solutions and data for the ring stresses can be approximated with the use of tables. This can be done for problems which otherwise have to be solved with a Finite Element Analysis. In the formulas two basic systems of unit are used: SI units and USCU units. The SI units are mass-based units using kilogram (kg), meter (m), second (s) and Kelvin (K) or degree Celsius (°C). The USCU units are force-based units using the pound force (lbf), inch (in), foot (ft), second (s) and degree Fahrenheit (°F).

For the use of the Roark formulas on circular rings and arches some assumptions are made, because the equations used to derive the Roark formulas are for general use of curved beams. First of all the closed ring is regarded as a statically indeterminate beam and analysed as such by the use of Castigliano's second theorem (9.3) described in Welleman [20]), which is a method to calculating displacements. This theorem states that a deformation is the summation of individual parts contribution to this deformation, better known as superposition, using the total elastic energy of the system (U).

$$\begin{aligned} \delta u &= \frac{\delta U}{\delta F} = \frac{R}{EI}\int_0^{\pi} M(\theta)\frac{dM(\theta)}{dF}d\theta \\ \delta\phi &= \frac{\delta U}{\delta T} = \frac{R}{EI}\int_0^{\pi} M(\theta)\frac{dM(\theta)}{dT}d\theta \end{aligned} \tag{9.3}$$

A.2.1 Castigliano's theorem

As an example from Alexiou [21], Castigliano's second theorem is used to solve the internal force distribution for a thin circular ring subjected to a point load, shown in Figure 77, only half of the ring can be considered using the accompanying boundary conditions.

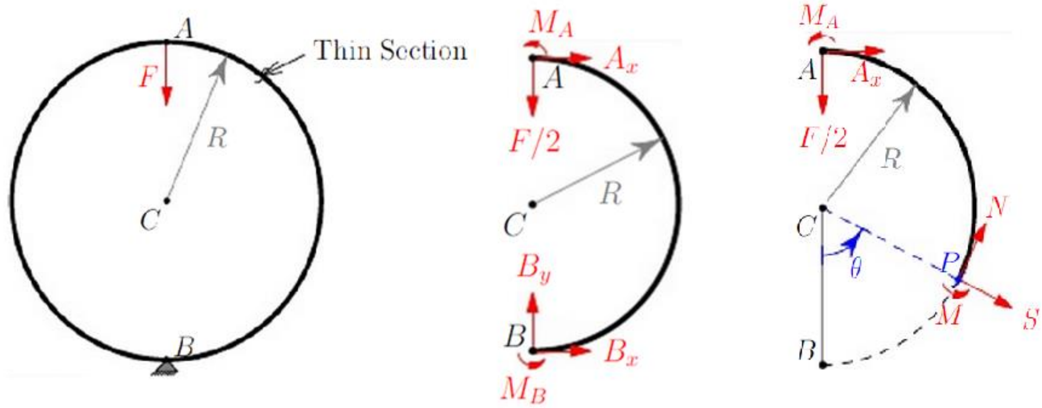

Figure 77: Thin ring subjected to a point load on a hinged support [10]

In this problem there are six unknowns: two horizontal forces (A_x, B_x), two vertical forces (A_y, B_y) and two bending moments (M_A, M_B). By using horizontal, vertical and moment equilibrium and the fact that the vertical force A_y is equal to the force F/2, these unknowns can be expressed in a constant, unknown, horizontal force (A_x) and bending moment (M_A). The equations of the internal forces, as a function of the angle (θ), can be determined, containing these two unknown constants (9.4).

$$\begin{aligned} N(\theta) &= \frac{F}{2}\sin\theta - A_x\cos\theta \\ S(\theta) &= -\frac{F}{2}\cos\theta - A_x\sin\theta \\ M(\theta) &= R\left(A_x(1+\cos\theta) - \frac{F}{2}\sin\theta\right) - M_A \end{aligned} \tag{9.4}$$

The equations of the internal forces can be solved with the boundary conditions, using elastic energy as described in (9.3). It is assumed that, because of symmetry the rotation and the horizontal displacement at A are zero, leading to the conditions stated in (9.5). By substituting the moment distribution from (9.4) in (9.5), the two unknown constants can be found. The values for the constants A_x and M_A can then be substituted back into equations (9.4), giving the internal force distributions for the ring under a point load.

$$\partial u_{Ax} = \frac{\partial U}{\partial A_x} = 0; \quad \partial\phi_A = \frac{\partial U}{\partial M_A} = 0 \tag{9.5}$$

A.2.2 Assumptions

In the formulas of Roark the ring formulas are based upon the following assumptions:

- The ring is of uniform cross section and has a symmetry about the plane of curvature. An exception is made if moment restraints are provided to prevent rotation of each cross section out of its plane of curvature.
- All loadings are applied at the radial position of the centroid of the cross section.
- It is nowhere stressed beyond the elastic limit.
- It is not severely deformed as to lose its original cylindrical shape.
- It's deflection is primarily due to bending. For thicker rings the deflection due to deformation by axial tension or compression and/or by transverse shear stresses in the ring may be included. This is included by the axial stress deformation factor α and the transverse shear deformation factor β.
- In the case of pipes acting as beams between widely spaced supports, the distribution of shear stresses across the section is in accordance with the theory of straight beams (Figure 78):

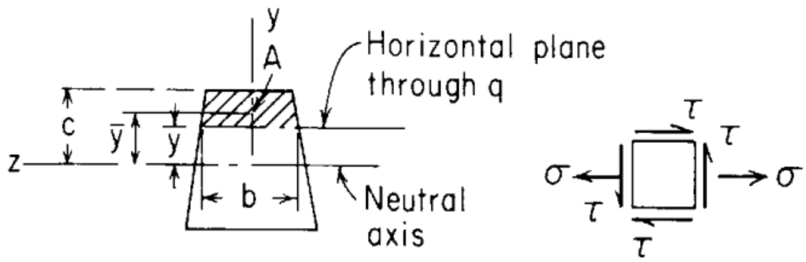

Figure 78: Cross-section of a curved beam described as a straight beam [13]

Due to the use of ring stiffeners, the stiffness of the two-dimensional ring model changes. The combination of a curved sheet and attached stiffeners forms a curved beam with wide flanges. In the flanged sections with thin webs the radial stress may be larger at the junction of the flange and the web. At this position the circumferential stress is also large, which can lead to excessive shear stress and possible yielding if the radial and circumferential stresses are of opposite sign. If there is a large compressive radial stress in a cross section with a thin web, buckling of the web can occur.

A.2.3 Ring stresses

With the ring assumed as a curved beam with wide flanges, the stiffness of this cross section can be determined. This stiffness is translated to the width of a T-section, at which the tubular section is acting as the flange is and the stiffener is acting as the web, and used as the width of the two dimensional ring model. This so called ‘’effective width’’ (Figure 79 right) is given in equation (9.6).

$$b_{eff} = 1,56\sqrt{d_0 t_0} \tag{9.6}$$

For the determination of the ring stress distribution in the padeye load case, load case 20 is used (Figure 79 left). Load case 20 is a ring subjected to a point load, which is compensated by a distributed transverse shear load. By using Roark’s formulas the stress distribution in the ring can be determined, from which the maximum stress is checked in a unity-check. To determine the stress distribution in the two dimensional model, the forces acting in this cross section have to be calculated. The general formulas for the moment (M), hoop load (N) and radial load (V) from the curved beam theory and the assumptions, are given in equation (9.7).

$$\begin{aligned} M &= M_A - N_A R(1-u) + V_A R z + LT_M \\ N &= N_A u + V_A z + LT_N \\ V &= -N_A z + V_A u + LT_V \end{aligned} \tag{9.7}$$

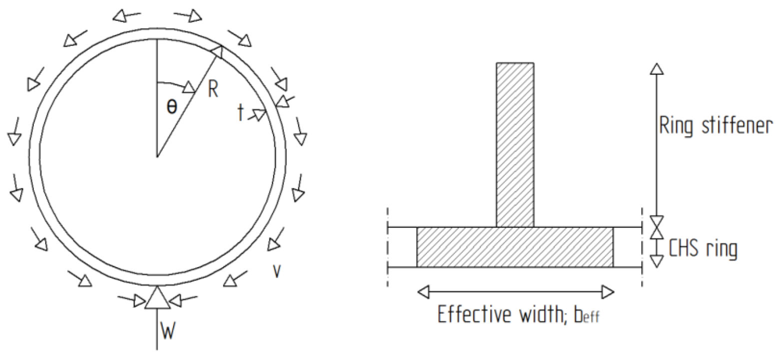

Figure 79: Ring load case 20 and effective width from Roark [13]

With these equations the ring stress distribution along the ring circumference can be determined for different load cases. This can be done by using the load term (LT_M, LT_N, LT_V) corresponding to the considered load case. For load case 20, these load terms are given in equation (9.8).

$$\begin{aligned} LT_M &= \frac{WR}{\pi}\left(1-\cos(\theta)-\frac{\theta}{2}\sin(\theta)\right) \\ LT_N &= -\frac{W}{2\pi}\theta\sin(\theta) \\ LT_V &= \frac{W}{2\pi}\left(\sin(\theta)-\theta\cos(\theta)\right) \end{aligned} \tag{9.8}$$

The normal force, shear force and bending moment distribution in the ring is, beside load terms, depending on the forces and bending moment in point A. These forces and bending moment in point A are given in (9.9).

$$\begin{aligned} M_A &= \frac{WR}{2\pi}\left(k_2 - 0.5\right) \\ N_A &= 0.75\frac{W}{\pi} \\ V_A &= 0 \end{aligned} \tag{9.9}$$

In the function of the bending moment in point A, the factor k_2 is present, given in equation (9.10). This factor takes into account the hoop-stress, using the hoop-stress deformation factor α. This hoop-stress factor is a ratio between the bending moment stiffness and the extension stiffness.

$$\mathrm{k}_2 = 1 - \alpha = 1 - \frac{I}{AR^2} \tag{9.10}$$

Finally (9.8), (9.9) and (9.10) can be substituted into equation (9.7), obtaining the equation for the stress distribution of the ring in load case 20. This equation is given below.

$$\begin{aligned} M &= -\frac{WR}{2\pi}\left(\frac{1}{2}\cos(\theta) + \theta\sin(\theta) + \frac{I}{AR^2} - 1\right) \\ N &= \frac{W}{\pi}\left(\frac{3}{4}\cos(\theta) - \frac{\theta}{2}\sin(\theta)\right) \\ V &= -\frac{W}{2\pi}\left(\theta\cos(\theta) + \frac{1}{2}\sin(\theta)\right) \end{aligned} \tag{9.11}$$

The distribution of elastic stress across the section of a member can have a great stress increase over a short distance, due to the local irregularities in the geometry. The condition is called stress concentration, and the irregularities causing this are called stress raisers. The maximum intensity of elastic stress is expressed by the stress concentration factor (K_t). This stress concentration factor is the ratio between the true maximum stress and the nominal stress calculated by use of ordinary formulas of mechanics. These nominal stress calculations are based on the net section properties at the location of the stress raiser, ignoring the redistribution of stress caused by the form irregularities.

A.3 Reference studies

A.3.1 Branch plate-to-circular hollow structural section connections

In the design guide for CHS by Wardenier et al. [2] and in the study by Voth [3], the load capacity of a similar load case, a T-type plate-to-CHS connection, is determined. For this case the boundaries of the connection strength are given, which are the two possible failure mechanisms. These failure mechanisms are chord plastification and chord punching shear, and are dependent on many of the geometry parameters. Chord plastification is an ductile failure due to excessive plastic deformation of the joint interface, while chord punching shear is a brittle failure under local loads due to formation of diagonal tension cracks. Both failure mechanisms are dependent on the connection geometry.

In the equations describing the load capacity due to punching shear failure, it is assumed that local stresses at a surface through the chord wall limit the joint strength. These local stresses may not exceed the punching shear stresses.

In the case of chord plastification, several plastic hinges are formed due to the exceeding of the yield stress, forming a mechanism. When a mechanism is formed, the CHS experiences large deformations. In order to determine the ultimate capacity of the joint, a deformation limit is used. The out-of-plane deformation of the connecting CHS face is limited to 3% of the CHS diameter d_0. The force at which the deformation in the CHS reaches this limit deformation is denoted a the ultimate load.

The equations of the load capacity due to plasticity are derived using the ring model by Togo for a CHS-to-CHS connection, and is described by van der Vegte [15]. By using symmetry, the three-dimensional T-type CHS-to-CHS connection configuration can be translated into a two-dimensional half ring model representing the CHS chord. Brace forces are applied on the model as a line load, acting over a certain length. By using plasticity theory, the locations of possible plastic hinges are assumed and an analytical equation is derived. This model is shown in Figure 80.

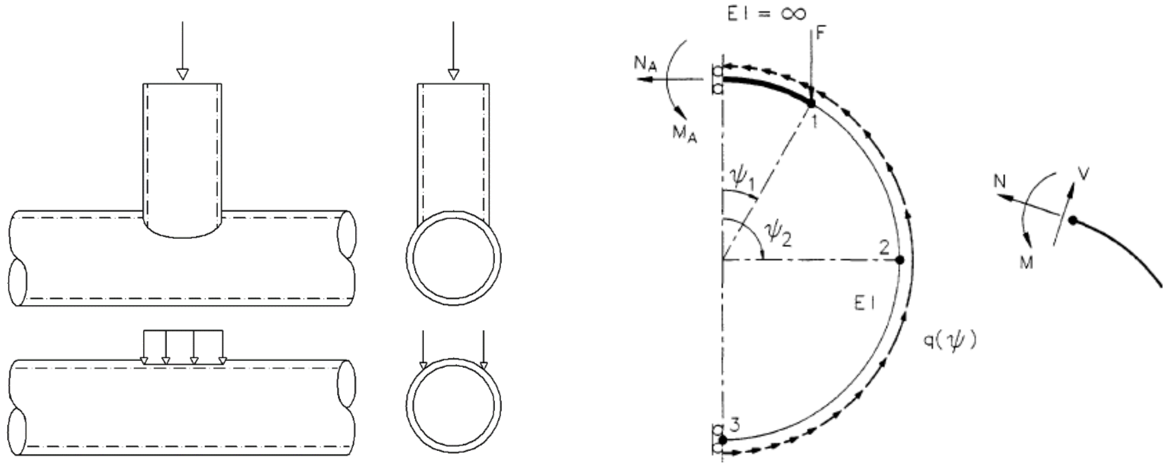

Figure 80: Three-dimensional CHS-to-CHS T-joint translated into a two-dimensional ring model with plastic hinges

The two-dimensional ring model is loaded by a point load at an angle φ_1 and a transverse shear stress $q(\varphi)$, which is similar to ring model used in Roark. The transverse shear stress is equal to:

$$q(\varphi) = \frac{4F}{\pi d_0} \sin(\varphi) \tag{9.12}$$

Due to the applied load on the joint the stresses in the ring will increase. When somewhere in the structure the bending moment reaches the plastic moment, a plastic hinge develops. When the load is increased, multiple plastic hinges will develop untill a mechanism is formed. When the structure becomes a mechanism it can deform unlimitedly without the load being increased. The number of plastic hinges that is needed to create a mechanism is equal to the degree of static indeterminacy of the structure. In the considered ring model there are three plastic hinges needed in order to create a mechanism. Hinge 1 is located at an angle φ_1 at which the brace is connected to the chord. Hinge 3 is located at the bottom of the CHS cross-section at an angle φ_3. Both angles are given in equation (9.13). The angle φ_2 at which plastic hinge 3 is located is unknown. This location can be determined by looking at the minimal force to create a mechanism.

$$\begin{aligned} \varphi_1 &= \arcsin(\beta) \\ \varphi_3 &= \pi \end{aligned} \tag{9.13}$$

By using moment equilibrium at the location of all three hinges, the bending moment M_A, normal force N_A and force F can be obtained. This will lead to a basic ring model approach, in which only the plastic moment are taken into account. In these equations the plastic moment is equal to:

$$M_p = \frac{1}{4} f_{y,0} t_0^{\ 2} B_e \tag{9.14}$$

The three moment equilibrium equation that are used to solve the unknowns, are stated in (9.15). In these equations the factor f is used, which is a function of the angle φ_i at which the plastic hinge is formed.

$$\begin{aligned} M_p &= M_A + N_A \frac{d_0}{2}\left(1-\cos(\varphi_1)\right) + F\frac{d_0}{2} f(\varphi_1) \\ -M_p &= M_A + N_A \frac{d_0}{2}\left(1-\cos(\varphi_2)\right) + F\frac{d_0}{2}\left(\sin(\varphi_2) - \sin(\varphi_1) + f(\varphi_2)\right) \\ M_p &= M_A + N_A \frac{d_0}{2}\left(1-\cos(\varphi_3)\right) + F\frac{d_0}{2}\left(\sin(\varphi_3) - \sin(\varphi_1) + f(\varphi_3)\right) \\ f(\varphi_i) &= \frac{2}{\pi}\left(-\cos(\varphi_i) - \frac{1}{2}\varphi_i \sin(\varphi_i) + 1\right) \end{aligned} \tag{9.15}$$

In the model there are three unknowns, which are stated in the three equilibrium equations. With these equations the unknowns stated in M_A, N_A and F can be solved. When calculated, these can be substituted in the equilibrium equation at the location of the second hinge φ_2, leaving this location as the only unknown variable. By rewriting this equilibrium equation, the strength of the joint can be obtained:

$$\frac{F_{1,y}}{f_{y,0} t_0^{\ 2}\left(\dfrac{B_e}{d_0}\right)} = \frac{2\left(1+\sqrt{1-\beta^2}\right)}{\left(1-\dfrac{\varphi_2}{\pi}\right)\sin(\varphi_2)\left(1+\sqrt{1-\beta^2}\right) - \left(1-\dfrac{\arcsin(\beta)}{\pi}\right)\beta\left(1+\cos(\varphi)\right)} \tag{9.16}$$

The model used to derive this equation is a simplified model, in which the interaction between the normal force N, shear force V and bending moment M is not taken into account. This basic model can be turned into an 'exact' model by applying additional expressions of the normal force and shear force to the previous model. Because of the interaction between the forces, the Von Mises yield criterion has to be used in order to obtain the locations of the plastic hinges. Deriving this 'exact' model the following equation is obtained:

$$\frac{F_{1,y}}{f_{y,0}t_0^{\,2}\left(\frac{B_e}{d_0}\right)} = \frac{2\left(1+\sqrt{1-\beta^2}\right)}{\left(1-\frac{\varphi_2}{\pi}\right)\sin\left(\varphi_2\right)\left(1+\sqrt{1-\beta^2}\right)-\left(1-\frac{\arcsin\left(\beta\right)}{\pi}\right)\beta\left(1+\cos\left(\varphi\right)\right)+\frac{0.7}{\gamma^2}} \tag{9.17}$$

$$\varphi_2 = 1.2 + 0.8\beta^2$$

In order to determine the load capacity of a T-joint plate-to-CHS connection, the model used for the CHS-to-CHS connection has to be adapted. The plate-to-CHS ring connection can be simplified to a CHS-to-CHS connection with a very small diameter ratio β (d_1/d_0). Due to the small plate diameter hinge 1 will be located near the upper support of the ring. With this assumption, an analytical model which can that describes the numerical and experimental results. By comparing these results, an equation can be obtained which describes the load capacity of the connection.

In the numerical model used in this research, the T-type plate-to-CHS joint is modelled as a three point bending model supported by a roller at the chord neutral axis (Figure 81). To prevent an unstable condition, lateral restraints were applied at the boundaries. This approach causes a high bending moment in the cross section at the position of the connection, leading to normal stresses in the chord. To remove these chord normal stresses, an opposite in-plane bending moment ($M_{0,end}=N_1l_0/4$) was applied at the boundaries. This end moment ($M_{0,end}$) is a function of the applied normal load on the plate (N_1) and the effective length of the chord length (l_0). As a result large in-plane bending moments occur at both boundaries of the CHS member, for which reinforcement could be needed at an area near the boundaries called ''reinforcement band''. Reinforcement in this band is needed if the stresses at the support exceed the yield stress.

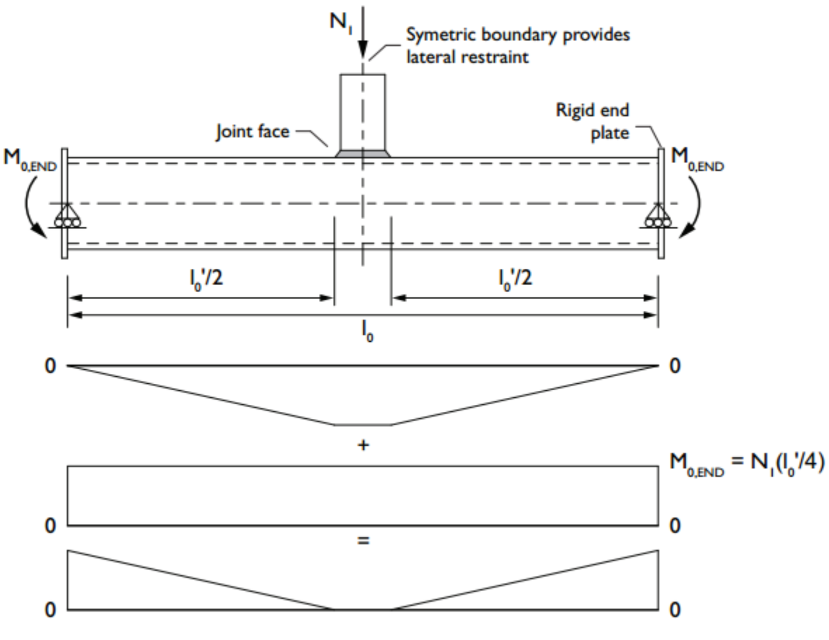

Figure 81: T-type loading to exclude chord axial stress at joint face (Voth, 2010) [1]

In the numerical analysis, a parametric study was conducted with the three-dimensional model described above. The parametric study contains the following variable parameters (shown in Figure 82):

- Effective chord length parameter, $\alpha' = 2l_0'/d_0$
- Nominal plate width ratio, $\beta = b_1/d$
- Nominal plate depth ratio, $\eta = h_1/d$
- Half diameter to thickness ratio, $\gamma = d_0/2t_0$

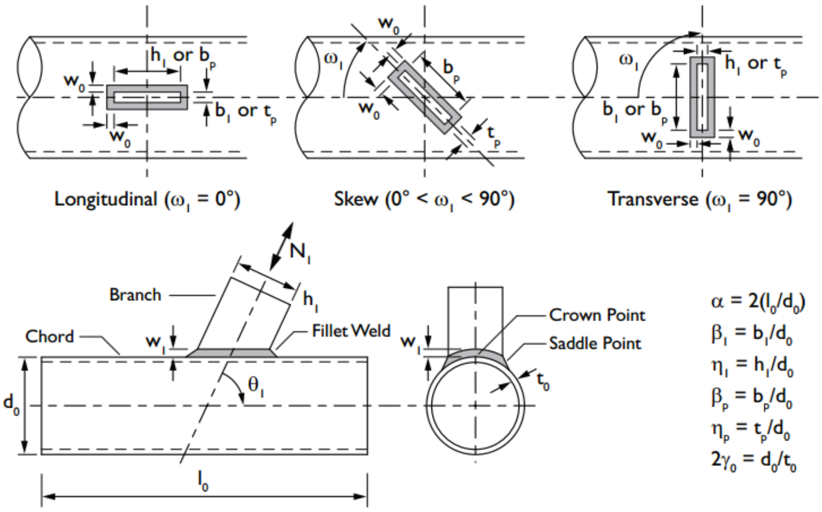

Figure 82: Parameters of T-type plate to CHS joints [2]

From the numerical and experimental analysis it is obtained that the load capacity due to compressive forces is lower than the ultimate load due to tensile forces. Because of this the equations derived from the data are based on the compressive forces and are therefore conservative in the case of tensile forces.

Kurobane et al. (1976) derived an equation of the load capacity for a longitudinal T-type plate-to-CHS connection, which is based on the simplified model. The equation is given below:

$$N_1 = 6.43 f_{y0} t_0^2 \left(1 + \frac{\eta}{2}\right) \tag{9.18}$$

Wardenier (1982) used the simplified ring model and applied the influence of the axial load, which reduces the connection capacity. The equation derived using this model is given in (9.19). The influence is presented in the equation as the addition of the function f(n). This function is the ratio between the normal stress f_0 in the connecting surface due to axial load and bending, and the yield stress f_{y0}.

$$N_1 = f_{y0} t_0^2 \left(4.2 + 3\eta\right) f\left(n\right) \tag{9.19}$$

$$f\left(n\right) = 1.2 - 0.5\left|n\right| \qquad for \;\; n < -0.4$$

$$f\left(n\right) = 1.0 \qquad for \;\; n \geq -0.4$$

$$Where: \;\; n = \frac{f_0}{f_{y0}}$$

After multiple reanalysis of existing numerical and experimental results, a new equation of the capacity of the T-type plate-to-CHS connection is derived by Wardenier et al. [2] (2008, 2009). This equation is given in (9.20). One of the most significant changes is the way the axial load is taken into account. The influence of the axial load is based on numerical analysis and is presented in the chord stress function Q_f. In this function the value C_1 is equal to 0.25 for chord compressive stress ($n < 0$) and equal to 0.20 for chord tension stress ($n \geq 0$).

$$N_1 = 5\left(1+0.4\eta\right)Q_f \frac{f_{y0}t_0^2}{\sin\left(\theta\right)} \tag{9.20}$$

$$Q_f = \left(1-\left|n\right|\right)^{C_1} \quad with: \; n = \frac{N_0}{N_{pl,0}} + \frac{M_0}{M_{pl,0}}$$

Most recently Voth [3] (2010) conducted a research using numerous experimental connections and finite element models, in order to gain a better understanding of branch plate-to-CHS connections and determine the influence of different geometries and loads on the connection capacity. In contrast to the research by Wardenier et al., Voth conducts that the plate thickness is significant for the connection capacity. Therefore the influence of the plate thickness is included in the calculations by Voth. The proposed calculation for chord face plastification is given below:

$$N_1 = 7.6\xi\left(1+\left(\frac{b_1}{d_0}\right)^2\right)\left(1+0.6\frac{h_1}{d_0}\right)\left(\frac{d_0}{2t_0}\right)^{0.1} Q_f \frac{f_{y0}t_0^2}{\sin\left(\theta_1\right)} \qquad \xi = 0.9 \tag{9.21}$$

$$Q_f = \left(1-\left|n\right|\right)^{C_1} \quad with: \; n = \frac{N_0}{N_{pl,0}} + \frac{M_0}{M_{pl,0}}$$

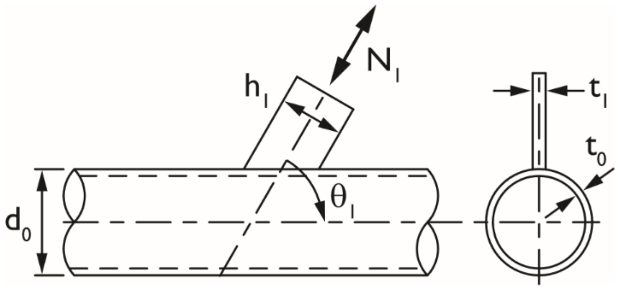

Figure 83: Longitudinal T-type branch plate-to-CHS connection, described in Wardenier [2] et al. and Voth [3]

Besides plastification of the chord, punching shear could also lead to an ultimate load due to failure of the chord. Punching shear occurs by initiation of a crack at a point of high stress concentration in the hollow section chord. When the load on the connection increases, the crack could propagate around the weld perimeter causing punching shear failure. By using the numerical and experimental data, the load capacity can be determined using the limit state criteria that the local maximum stress cannot exceed the punching shear stress. The equation for punching shear failure described by both Wardenier and Voth is given in (9.22). In this equation the normal force and both in-plane and out-of-plane bending moments are taken into account. In case only a normal force under an angle θ_1 is present in the model, the equation can be simplified.

$$\frac{N_1}{A_1} + \frac{M_{ip,1}}{W_{el,ip,1}} \frac{M_{op,1}}{W_{el,op,1}} \leq 1.16 f_{y0} \frac{t_0}{t_1} \quad \rightarrow \quad N_1 \leq 1.16 h_1 \frac{f_{y0}t_0}{\sin^2\left(\theta_1\right)} \tag{9.22}$$

A.1.1 Local load stresses in cylindrical shells at plate clips

In the paper of Dekker and Cuperus [22] the stresses in the shell due to the loaded clip are analysed with a finite element model. In the paper the results from the FEM analysis of the local load stresses in cylindrical shells are presented.

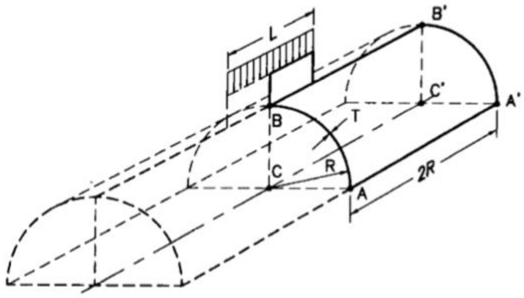

Figure 84: Model of a cylindrical shell loaded by a longitudinal clip [22]

A thin walled shells with a radius over thickness ratio (R/T) equal or larger than 50 are assumed. It is also assumed that thin clips with length L are being used with the same thickness as the shell. The clips are subjected to radial load or in-plane moment load. The dimensions R, T and L are given in the non-dimensional geometry ratios R/T and L/R. R/T gives the relative thickness of the shell and L/R gives the relative size of the clip with respect with to the radius of the cylinder. These ratios are set out against the highest occurring stress intensity according to Von Mises. These stress intensities (SI) found are transformed into a non-dimensional form inspired by the shrink ring method (9.23). From this formula the stress concentration factor (SCF) is back calculated and plotted against the non-dimensional ratios.

$$SI = SCF.\frac{\sqrt{Rt}}{t^2}.Line\ load \tag{9.23}$$

As expected, from this paper it follows that the largest contribution of the maximum stress is from the bending stress. Because of this reason the shrink ring method, which causes mainly longitudinal stresses, does not give a good representation of the ring stresses. From the results it also follows that for the general behaviour of a circular hollow section under a thrust/radial loading, the SCF is linearly ascending with the clip size parameter L/R for a constant relative thickness R/t.

From the outcomes of this paper number of equations are derived to determine the stress concentration factors. For longitudinal clips subjected to radial loading equation (9.24) can be applied, and equation (9.25) can be applied for moment loading. These equations are applicable in the domain given by (9.26). In case both types of loading are applied these stress concentration factors can be added. In this study the shear force is not considered and the influence of the shear stress is therefore neglected.

$$SCF = 1.55\left(\frac{R}{t}\right)^{0.38}\left(\frac{L}{R}+0.125\right) \tag{9.24}$$

$$SCF = 0.23\left(\frac{R}{t}\right)^{0.62}\frac{L}{R} \tag{9.25}$$

$$40 < \frac{R}{t} < 250 \;\; ; \;\; 0.04 < \frac{L}{R} < 0.6 \tag{9.26}$$

A.1.1 Two-dimensional Finite Element Model (FEM)

As an alternative on Roark’s method, Soh et al. [23] derived a two-dimensional model to determine the ring stresses in a circular hollow section under radial loading. The model consisted of a ring supported by springs and subjected to a point load. The spring elements were used to simulate the interaction between the neighbouring cross sections of the CHS. The model consists of 18 curved beam elements, each with six degrees of freedom at every node, and 17 spring elements. To check the model’s reliability it was compared with Roark’s method for a ring under a point load.

The ring with radius R and point load P consists of n segments with length . The spring stiffness in the model is representing the shear force between the ring segments. The spring stiffness (k) and thus the shear force ($F_x^{'}$) acting on this segment is given in equation (9.27). The changes in ring diameter used in this equation (Δ_H, Δ_V) are given in a table for the accompanying load case in the Roark method, where they are denoted as ΔD_H and ΔD_V.

$$k = \frac{F_x^{'}}{u} = \frac{Pl}{\pi R \Delta}\sin\left(\beta\right)$$
$$\Delta = \sqrt{\left(\Delta_x\right)^2 + \left(\Delta_y\right)^2} = \sqrt{\left(\frac{\Delta_H \sin\left(\beta\right)}{2}\right)^2 + \left(\frac{\Delta_V}{2}\left(1+\cos\left(\beta\right)\right)\right)^2} \tag{9.27}$$

Although this two-dimensional model is similar to the Roark method and gives a good representation of the stress distribution in a CHS, it still is too conservative. A possible solution would be to use a reduction of the point load on the flange plate which is integrated in the 2-dimensional finite element model. The reduction factor scales down the point load to account for the effects of bending and tension. The factor is given by the ratio of q/q’, in which q is the force equal P/2Rθ (with θ as the angle) and q’ is the combination from the normal force (q_t) and bending (q_b).

As a final remark it can be found in a second comparison that the use of a simplified model to calculate the ring stiffness has to be chosen properly. For this comparison three models are used, two of which consists of a ring model with a distributed load applied and the third consists of a ring model with the geometry of a stiffener applied at which a point load is active. In the comparison the bending moment distribution along the circumference of the ring. From this it can be seen that there’s a big difference between the models with the distributed load (dotted line) and the one with the applied stiffener geometry (straight line) in Figure 85.

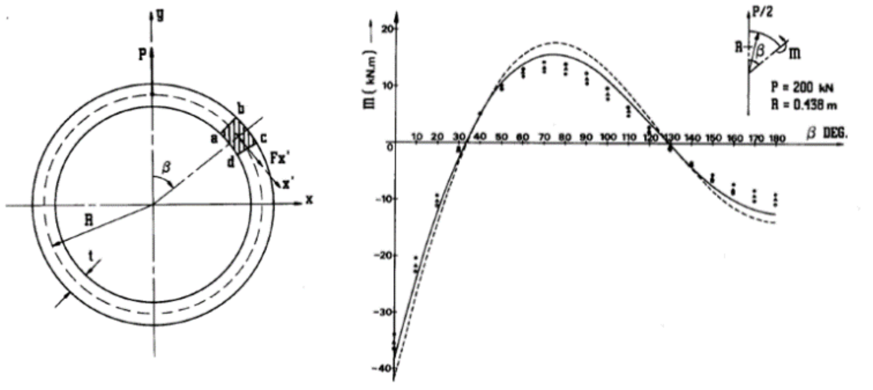

Fig. 8. Moment distributions along the circumference of the ring obtained from the Roark and finite element solutions. Roark’s solution (---). Solution obtained using the first proposed method to estimate spring constants (——). Solutions obtained using the second proposed method to estimate spring constants (△, ⊙, ●) where △ is for Δ = 0·0015 m, ⊙ is for Δ = 0·0025 m and ● is for Δ = 0·0075m.

Figure 85: Comparison of the spring stiffness influence in bending moment distribution of the two dimensional FEM by Soh et al. [23]

In addition to this study, Choo et al. [24] studied the significance of stiffener angles on the strength enhancement in padeye to CHS connections. In this study an alternative indicator βD was used for the stiffening, which consists of the pipe diameter (D) and a parameter (β) found in the relation with the angle (θ) of the stiffener. The value of the parameter is:

$$\sin(\theta) = \beta \tag{9.28}$$

Several connections where investigated, using four different locations A,B,C and D along the main plate at which the stiffeners could be placed (Figure 86). The four locations used where two edge stiffeners and two centre stiffeners, symmetric on both sides from the padeye pinhole. Two types of stiffener where used, namely a profiled and a non-profiled stiffener. The profiled stiffener is commonly used in practice and can be seen as a non-profiled stiffener with some material removed, both are given in Figure 86. With these variations a parametric study was performed.

From the parametric study using nonlinear finite element analysis, it follows that using stiffeners with a stiffening angle θ up to 40˚ gives a significant strength enhancement, and only a minor enhancement for further increase from 40˚ to 90˚. It was also obtained that in case two stiffeners on the outside locations A and D are used, adding two stiffeners gives a 12% increase on the ultimate strength while relocation of the stiffeners to the inner locations B and C only gives a 4% increase.

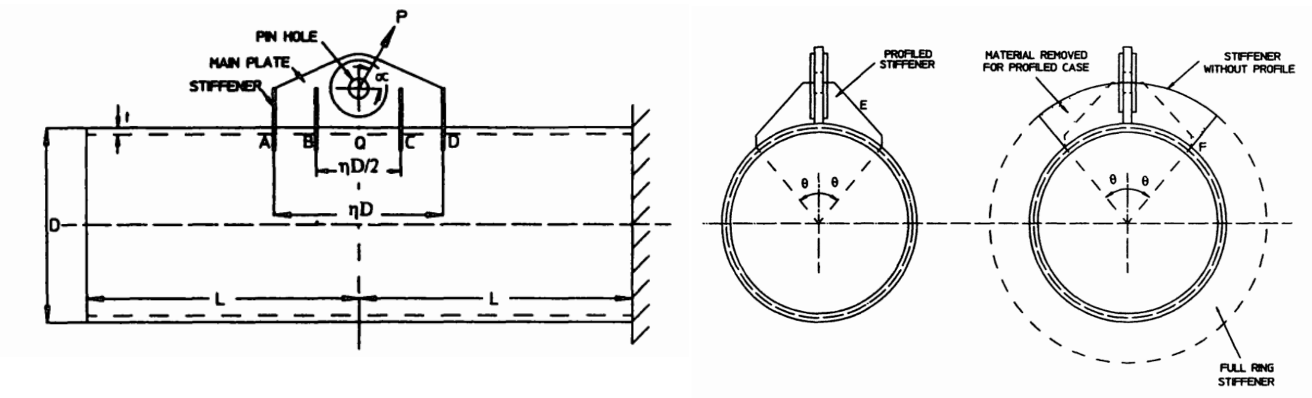

Figure 86: Locations of stiffeners on the CHS, modelled as a cantilever beam (Choo et al.) [24]

A.4 Analytical Models

The analytical modelling can be done in a two-dimensional model using curved beam theory and in a three-dimensional model using shell theory. To determine the static stress distribution, three conditions have to be satisfied: the condition of equilibrium, the stress-strain relations and the compatibility conditions. These conditions are used to describe the equations of elasticity. In the case of a two-dimensional elastic problem eight quantities have to be determined: three stress components, three strain components and two displacement components. For a three-dimensional problem the number of quantities that have to be determined is 15: six stress components, six strain components and three displacement components. The three-dimensional model the number of components that have to be determined is much bigger and therefore more complex. However, the three-dimensional model will be more accurate because it contains the influence of the neighbouring cross-sections, which the two-dimensional model doesn't. For both models the derivation and the assumptions to derive the equations are given in this chapter.

A.4.1 Two-dimensional models

The complex formulation of the three-dimensional shell problem can be greatly simplified into a two-dimensional case by using plane stress or plane strain, as stated in Ugural and Fenster [25]. By using this assumption the two-dimensional problem can be solved using Airy's stress function and Euler-Bernoulli theory for curved beams.

The principle of plane stress can be applied in many problems in practice. This principle can be applied on structures for which the stress vector is zero across a particular surface. This is the case for thin plates/shells which are loaded parallel to its face, for instance a pressure vessel in which the hoop force is much larger than the radial pressure. In the applied load case in this thesis this isn't the case, thus this theory can't be used.

The idea of plain strain is that in a case where one dimension, in most cases the length, of the structure is much greater than the other two dimensions, the strain for this dimension is constrained by nearby material and small compared with the strains for the other two dimensions. This principle can be applied on the applied load case, and will be worked out below. The principle of plain strain states for the strains longitudinal that $\varepsilon_{zz} = \gamma_{rz} = \gamma_{\theta z} = 0$. This gives the stress and strain tensor (9.29) following the standard strain expression and the stress-strain relation, in which a non-zero longitudinal stress σ_{zz} is needed to keep the constraint $\varepsilon_{zz} = 0$. This leads to the same standard expression for the strain as (9.31).

$$\underline{\underline{\varepsilon}} = \begin{bmatrix} \varepsilon_r & \gamma_{r\theta} & 0 \\ \gamma_{r\theta} & \varepsilon_\theta & 0 \\ 0 & 0 & 0 \end{bmatrix}; \underline{\underline{\sigma}} = \begin{bmatrix} \sigma_r & \tau_{r\theta} & 0 \\ \tau_{r\theta} & \sigma_\theta & 0 \\ 0 & 0 & \sigma_{zz} \end{bmatrix} \tag{9.29}$$

A.4.2 Timoshenko and Euler-Bernoulli curved beam theory

For a structural member to be modelled as a beam if the ratio between the thickness (h) and the characteristic length (L) should be relatively small. In comparison with a straight beam, a curved beam must have a small ratio between the thickness (h) and the radius (R). From comparative simulations it follows that this ratio must equal or smaller than 1/10.

In a two-dimensional problem a distinction can be made between thick and thin curved beams. In thin curved beams the transverse shear deflection is neglected, therefore allowing only deformation due to bending. For thin curved beams the Euler-Bernoulli can be applied. For thick beams however the transverse shear deflection has a large influence, therefore the Euler-Bernoulli theory can't be applied. Instead the Timoshenko theory is used. This theory allows a further rotation of the normal which results in a nonzero shearing strain. Because the assumption of a plane section remaining plane leads to a constant shear stress, a shear correction factor is used to obtain the realistic parabolic variation of shear stress.
Gasmi et al. [26] describe the derivation of Timoshenko and Euler-Bernoulli curved beam theory. For the derivation of the Timoshenko curved beam theory the displacement field from (9.30) is assumed, following the sign conventions in Figure 87. In this equation the displacements in transverse ($u_r(\theta)$) and circumferential ($u_{\theta 0}(\theta)$) direction and the cross-section rotation ($\varphi(\theta)$) are given.

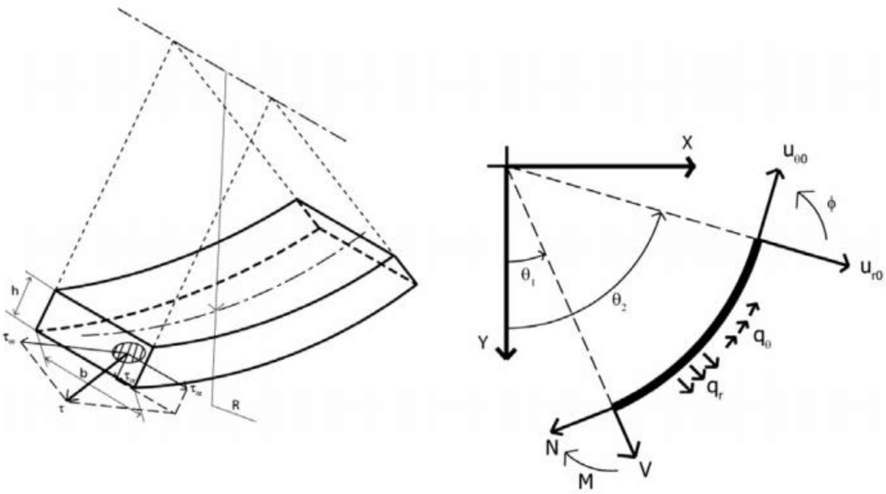

Figure 87: Uniformly curved beam with rectangular cross section in 3D (left) and 1D (right) [26]

Besides this the thickness variable (z) is introduced, which is the difference between the radius of the curve (R) and the distance from the origin to the considered element (r). The substitution of the equation for strain expressed in polar coordinates into (9.30) gives (9.31).

$$\begin{aligned} u_r(z,\theta) &= u_r(\theta) \\ u_\theta(z,\theta) &= u_{\theta 0}(\theta) + z\phi(\theta) \\ With: z &= r - R \end{aligned} \tag{9.30}$$

$$\begin{aligned} \varepsilon_r &= \frac{\partial u_r}{\partial r} = 0 \\ \varepsilon_\theta &= \frac{1}{r}\left(\frac{\partial u_\theta}{\partial \theta} + u_r\right) = \frac{1}{R+z}\left(\frac{du_{\theta 0}}{d\theta} + u_r + z\frac{d\phi}{d\theta}\right) \\ \gamma_{r\theta} &= \frac{1}{r}\frac{\partial u_r}{\partial \theta} + \frac{\partial u_\theta}{\partial r} - \frac{u_\theta}{r} = \frac{1}{R+z}\left(\frac{du_r}{d\theta} - u_{\theta 0} + R\phi\right) \end{aligned} \tag{9.31}$$

The bending moments, axial force and shear force can be expressed in terms of the strains. Given the linear relation between stresses and strains, (9.31) can be substituted into these equation. With this the forces and moment in (9.32) can be given in terms of displacements and rotation.

$$\begin{aligned}
M &= \int_A z\sigma_\theta dA = \int_A zE\varepsilon_\theta dA = \int_A \frac{zE}{R+z}\left(\frac{du_{\theta 0}}{d\theta} + u_r + z\frac{d\phi}{d\theta}\right)dA = \frac{EI}{R}\frac{d\phi}{d\theta} \\
N &= \int_A \sigma_\theta dA = \int_A E\varepsilon_\theta dA = \int_A \frac{E}{R+z}\left(\frac{du_{\theta 0}}{d\theta} + u_r + z\frac{d\phi}{d\theta}\right)dA = \frac{EA}{R}\left(\frac{du_{\theta 0}}{d\theta} + u_r\right) \\
V &= \int_A \tau_{r\theta} dA = \int_A G\gamma_{r\theta} dA = \int_A \frac{G}{R+z}\left(\frac{du_r}{d\theta} - u_{\theta 0} + R\phi\right)dA = \frac{GA}{R}\left(\frac{du_r}{d\theta} - u_{\theta 0} + R\phi\right)
\end{aligned} \tag{9.32}$$

Finally the equilibrium equations (9.33) are determined with the help of the principle of virtual work, consisting of virtual strain energy and virtual potential energy. In the equilibrium the radial and circumferential distributed loads, $q_r(\theta)$ and $q_{\theta 0}(\theta)$ respectively, are considered. These loads are applied at the mid-surface of the beam.

$$\begin{aligned}
&\frac{dN}{d\theta} + V = -Rbq_\theta \\
&N - \frac{dV}{d\theta} = Rbq_r \\
&\frac{dM}{d\theta} - RV = 0
\end{aligned} \tag{9.33}$$

With the equations stated above the governing differential equations can be derived. This is done by substituting (9.32) into (9.33), which gives coupled equations. To be able to solve the equations analytically they have to be uncoupled and expressed in only one unknown. This uncoupling gives three equations in (9.34) which are the equation for the transverse displacement and the relations between the circumferential displacement, cross-section rotation and transverse displacement.

$$\begin{aligned}
&\frac{d^5u_r}{d\theta^5} + 2\frac{d^3u_r}{d\theta^3} + \frac{du_r}{d\theta} = \frac{R^2b\left(R^2EA + EI\right)}{EIEA}\frac{dq_r}{d\theta} - \frac{R^2b}{GA}\frac{d^3q_r}{d\theta^3} + \frac{R^4b}{EI}q_\theta - \frac{R^2b\left(EA+GA\right)}{GAEA}\frac{d^2q_\theta}{d\theta^2} \\
&\frac{du_0}{d\theta} = -P\left(\frac{d^4u_r}{d\theta^4} + \frac{d^2u_r}{d\theta^2}\right) - u_r + \frac{R^2b}{EA}q_r - P\frac{R^2b}{GA}\frac{d^2q_r}{d\theta^2} - P\frac{R^2b\left(EA+GA\right)}{GAEA}\frac{dq_\theta}{d\theta} \\
&\phi = \frac{1}{R}\left(u_{\theta 0} - \left(1 + \frac{EA}{GA}\right)\frac{du_r}{d\theta}\right) - \frac{EA}{RGA}\frac{d^2u_{\theta 0}}{d\theta^2} - \frac{Rb}{GA}q_\theta \\
&With: P = \frac{EIGA}{R^2EAGA + EIGA + EIEA}
\end{aligned}$$

(9.34)

For the derivation of the Euler Bernoulli curved beam theory it is assumed that there is no shear deformation in the cross-section, expressed in (9.35). Following the same procedure as for the Timoshenko curved beam theory this results in the general equation stated in (9.36). It can be seen that in if the shear stiffness (GA), which is the resistance against shear deformation, becomes infinitely large, equation (9.34) becomes the same as (9.36) and therefore the Timoshenko beam will act as a Euler-Bernoulli Beam.

$$\begin{aligned} u_r(z,\theta) &= u_r(\theta) \\ u_\theta(z,\theta) &= u_{\theta 0}(\theta) - \frac{r-R}{R}\left(\frac{du_r}{d\theta} - u_{\theta 0}\right) \end{aligned} \tag{9.35}$$

$$\begin{aligned} &\frac{d^5u_r}{d\theta^5} + 2\frac{d^3u_r}{d\theta^3} + \frac{du_r}{d\theta} = \frac{R^2b\left(R^2EA+EI\right)}{EIEA}\frac{dq_r}{d\theta} + \frac{R^4b}{EI}q_\theta - \frac{R^2b}{EA}\frac{d^2q_\theta}{d\theta^2} \\ &\frac{du_0}{d\theta} = -Q\left(\frac{d^4u_r}{d\theta^4} + \frac{d^2u_r}{d\theta^2}\right) - u_r + \frac{R^2b}{EA}\left(q_r - Q\frac{dq_\theta}{d\theta}\right) \\ &With: Q = \frac{EI}{EI + R^2EA} \end{aligned} \tag{9.36}$$

By using the theory of the Euler-Bernoulli curved beam, the normal force, shear force and bending moment distribution over the circumference of the ring can be determined using equation (9.37).

$$\begin{aligned} N(\theta) &= \frac{EA}{R}\left(\frac{du_{\theta 0}}{d\theta} + u_r\right) \\ M(\theta) &= \frac{EI}{R^2}\left(\frac{d^2u_r}{d\theta^2} - \frac{du_{\theta 0}}{d\theta}\right); \quad \phi(\theta) = \frac{1}{R}\left(-\frac{du_r}{d\theta} + u_{\theta 0}\right) \\ V(\theta) &= \frac{dM}{d\theta} = -\frac{EI}{R^3}\left(\frac{d^3u_r}{d\theta^3} - \frac{d^2u_{\theta 0}}{d\theta^2}\right) \end{aligned} \tag{9.37}$$

Appendix B Padeye comparison table

			Wintershall Noordzee B.V. 27.1920		GFD Suez 27.1726			Chevron A18 27.1692		Ika-JZ 27.1748	Cardon-Perla 27.200	Mean	Min	Max
			Row 1: A1	Row 2: A2		A1	A2	Row A	Row C	B2				
CHS	d_0	[mm]	1219.2	1219.2	1371.6	1066.8	1219.2	1219.2	1219.2	800	1397	1192	800	1397
	t_0	[mm]	57.2	57.2	50.8	57.2	57.2	57.2	57.2	35	63.5	55	35	64
Main plate	b_m	[mm]	2000	2000	1300	1330	1300	1445	1250	1100	1291	1446	1100	2000
	R_m	[mm]	420	420	360	385	375	470	375	275	305	376	275	470
	R_0	[mm]	103	128	105.5	113	111	140	110	92.5	102	112	93	140
	R_c	[mm]	360	360	310	330	325	390	325	225	254	320	225	390
	h_0	[mm]	580	625	400	400	425	500	500	348	318	455	318	625
	t_m	[mm]	80	100	50	70	70	70	65	55	64	69	50	100
	t_c	[mm]	40	65	40	50	50	60	45	30	64	49	30	65
Stiffener	d_{end}	[mm]	280	280	300	300	300	300	300	285	631	331	280	631
	$t_{si,ring}$	[mm]	200	200	300	200	200	200	200	200	-	213	200	300
	h_{s1}	[mm]	520	675	300	300	325	450	450	268	318	401	268	675
	t_{s1}	[mm]	50	50	50	50	50	50	50	30	50.8	48	30	51
	h_{s2}	[mm]	400	400	400	535	490	600	500	268	64	406	64	600
	t_{s2}	[mm]	50	50	50	50	50	50	50	30	-	48	30	50
	h_{sc}	[mm]	670	825	400	625	490	450	450	268	318	500	268	825
	t_{sc}	[mm]	50	50	30	30	30	30	30	30	50.8	37	30	51
	$t_{sc,ring}$	[mm]	100	100	100	100	100	100	100	80	102	98	80	102
	d_{sc}	[mm]	650	650	550	550	500	460	410	445	565	531	410	650
Ratios	γ	[-]	10.7	10.7	13.5	9.3	10.7	10.7	10.7	11.4	11.0	10.9	9.3	13.5
	η	[-]	1.64	1.64	0.95	1.25	1.07	1.19	1.03	1.38	0.92	1.23	0.92	1.64
	β	[-]	0.07	0.08	0.04	0.07	0.06	0.06	0.05	0.07	0.05	0.06	0.04	0.08

Table 11: Comparison of padeyes from projects performed by Seaway Heavy Lifting containing a padeye load case

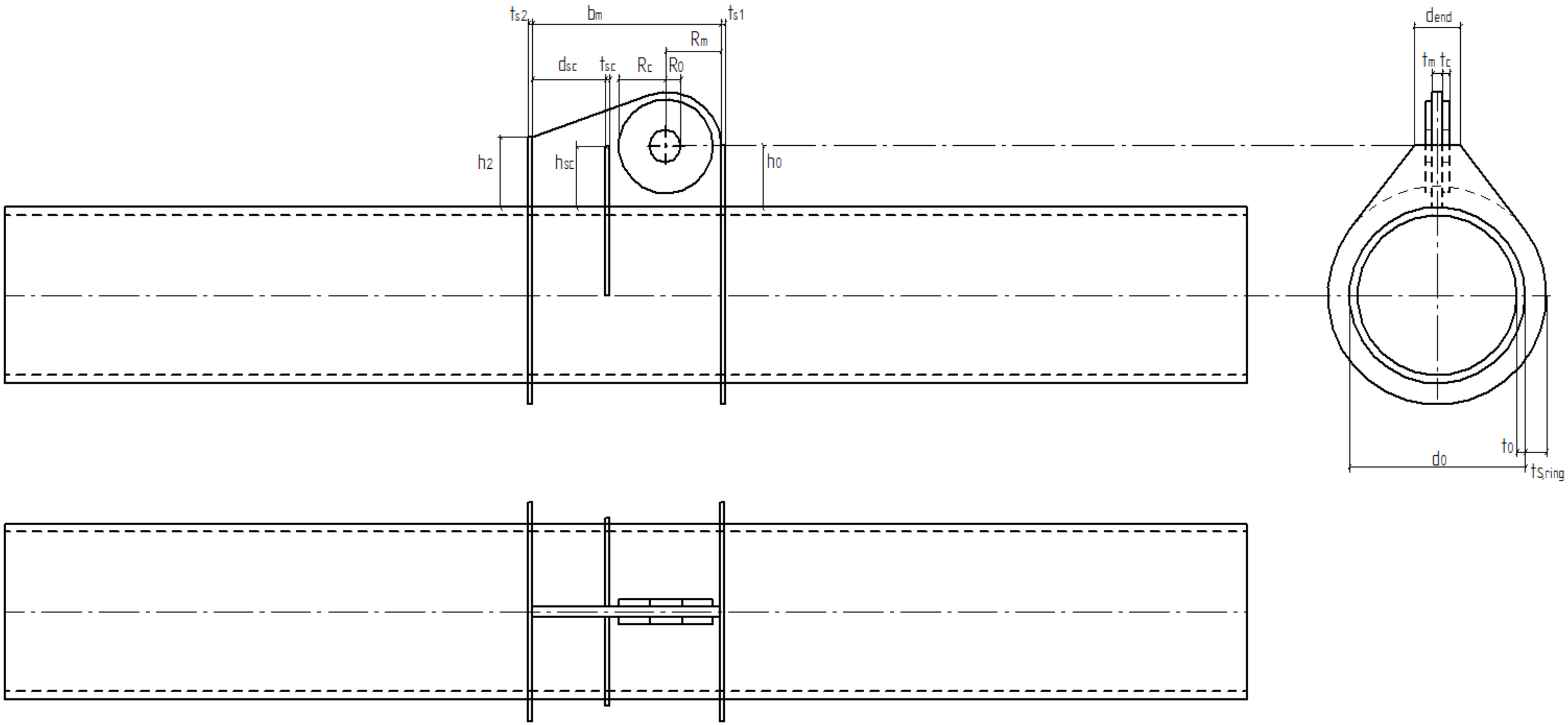

Figure 88: Padeye geometry including additional ring stiffeners

Table 12: Mean relative deviation between individual dimension and mean dimensions of padeyes from projects performed by Seaway Heavy Lifting containing a padeye load case

Project			**Wintershall Noordzee B.V. 27.1920**		**GFD Suez 27.1726**			**Chevron A18 27.1692**		**Ika-JZ 27.1748**	**Cardon-Perla 27.200**
			Row 1: A1	**Row 2: A2**		**A1**	**A2**	**Row A**	**Row C**	**B2**	
Main plate	R_m	[mm]	0.12	0.12	0.04	0.02	0.00	0.25	0.00	0.27	0.19
	R_0	[mm]	0.08	0.15	0.06	0.01	0.01	0.25	0.01	0.17	0.09
	R_c	[mm]	0.13	0.13	0.03	0.03	0.02	0.22	0.02	0.30	0.21
	h_0	[mm]	0.27	0.37	0.12	0.12	0.07	0.10	0.10	0.24	0.30
	t_m	[mm]	0.15	0.44	0.28	0.01	0.01	0.01	0.06	0.21	0.08
	t_c	[mm]	0.19	0.32	0.19	0.01	0.01	0.22	0.09	0.39	0.30
Stiffener	d_{end}	[mm]	0.15	0.15	0.09	0.09	0.09	0.09	0.09	0.14	0.91
	$t_{si,ring}$	[mm]	0.06	0.06	0.41	0.06	0.06	0.06	0.06	0.06	-
	h_{s1}	[mm]	0.30	0.68	0.25	0.25	0.19	0.12	0.12	0.33	0.21
	t_{s1}	[mm]	0.04	0.04	0.04	0.04	0.04	0.04	0.04	0.37	0.06
	h_{s2}	[mm]	0.02	0.02	0.02	0.32	0.21	0.48	0.23	0.34	0.84
	t_{s2}	[mm]	0.05	0.05	0.05	0.05	0.05	0.05	0.05	0.37	-
	h_{sc}	[mm]	0.34	0.65	0.20	0.25	0.02	0.10	0.10	0.46	0.36
	t_{sc}	[mm]	0.36	0.36	0.18	0.18	0.18	0.18	0.18	0.18	0.38
	$t_{sc,ring}$	[mm]	0.02	0.02	0.02	0.02	0.02	0.02	0.02	0.18	0.04
	d_{sc}	[mm]	0.22	0.22	0.04	0.04	0.06	0.13	0.23	0.16	0.06
	MRD		0.16	0.23	0.13	0.10	0.06	0.15	0.09	0.25	0.28

Appendix C Finite Element Modelling

For the choice on element type and the elements size used in the mesh, a mesh convergence study will be performed. The element type and size that is most feasible is determined by using the convergence criterion, which states that the outputs between the different element sizes may not differ more than 5%. The elements used to determine the most feasible element type and size are given in Table 13.

Table 13: Element properties derived from Ansys mechanical APDL

Element	Element type	Nodes	Dof's per node	Geometry	Default int.
Solid 185	3-D linear	8	u_x, u_y, u_z	Hex-,tetrahedral, pyramid, prism	Full integration
Solid 186	3-D quadratic	20	u_x, u_y, u_z	Hex-,tetrahedral, pyramid, prism	Reduced integration
Shell 181	2-D linear	4	u_x, u_y, u_z φ_x, φ_y, φ_z	square, triangular, membrane	Reduced integration
Shell 281	2-D linear	8	u_x, u_y, u_z φ_x, φ_y, φ_z	square, triangular, membrane	Reduced integration
Solid-Shell 190	3-D linear	8	u_x, u_y, u_z	square, triangular	Reduced integration

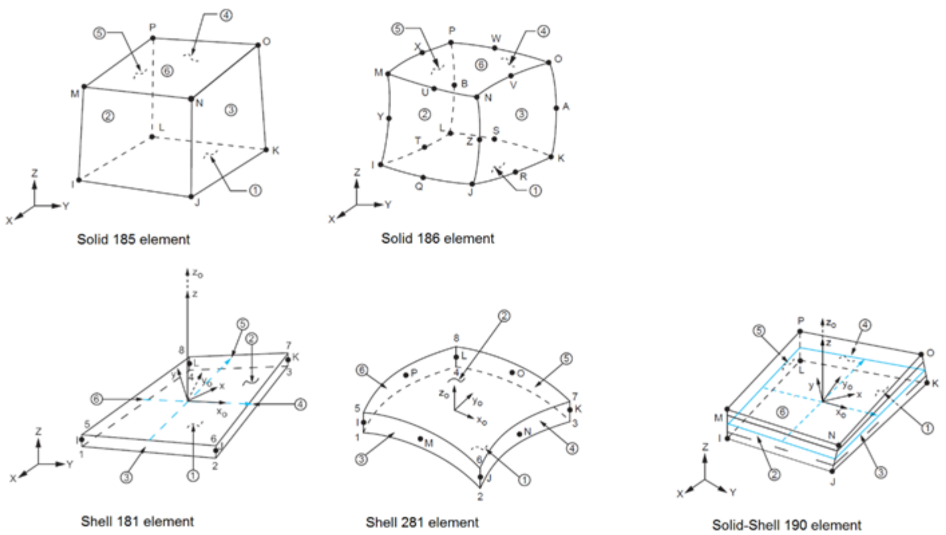

Figure 89:Element types from Ansys mechanical APDL Element Reference [27]

C.1 Element size

For all models the displacement vector (u_{sum}) and the Von Mises equivalent stress (σ_{eqv}) is considered. The displacement vector sum (u_{sum}) in node 1 in the padeye load case is plotted against the element size used in Figure 90. From this figure it can be seen that the shell 181, shell 281 converge at a large element size. For the solid 186 elements this is also true in case the thickness of the CHS is divided into 4 elements. The solid 85 elements converge for an element size smaller than 20 mm, when the thickness of the CHS is divided into 8 elements.

The Von Mises stress (σ_{eqv}) in node 1 in the padeye loadcase is plotted against the element size used in Figure 91. In this figure a similar behaviour can be seen as for the displacement vector in Figure 90, except for the fact that shell 181 element converges at an element size of 20 mm. Still both shell elements and the solid 186 element are more accurate at larger elements size than the solid 185 elements.

Because the shell 281 and the solid 186 elements use mid-size nodes, misalignment could occur in the CHS to main plate connection. This means that the edge nodes could connect with the mid-side nodes which lead to inaccurate solutions. Because of this reason and the fact that the shell 181 elements is nearly as accurate as the shell 281 and solid 186 elements, shell 181 elements are chosen. A governing element size is 20 mm is used from this point onwards.

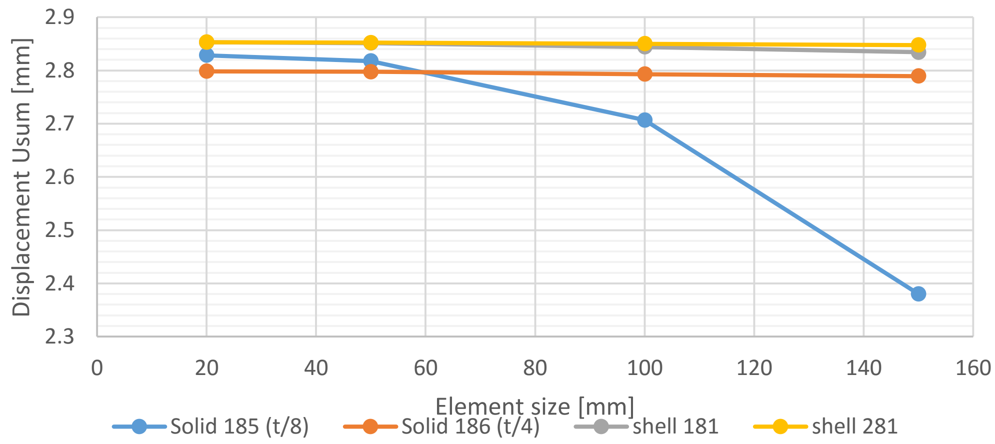

Figure 90: Displacement vector sum (u_{sum}) for multiple element type and size

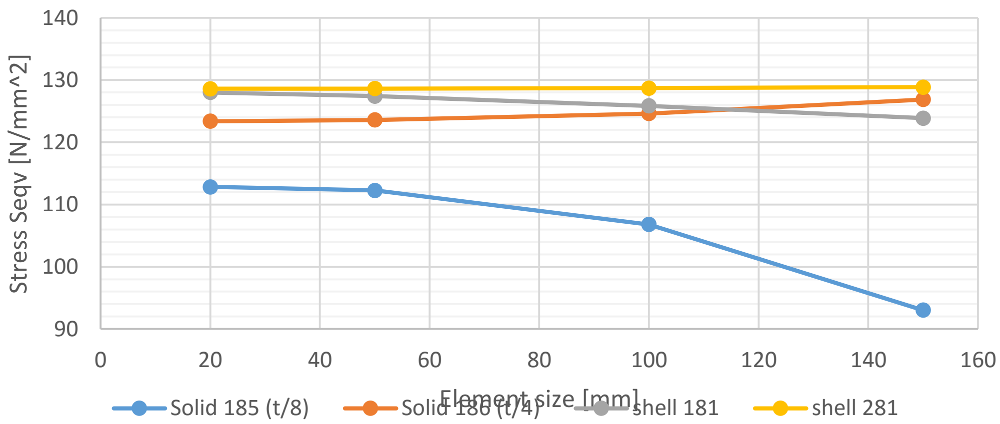

Figure 91: Von Mises stress (σ_{eqv}) for multiple element type and size

C.1.1 Mesh refinement

In order to reduce the computation time of the model using shell 181 elements, the mesh can be refined by using a fine mesh at locations which are of interest and a coarse mesh at locations which are not. This leads to a mid-section (at the padeye connection) with element size n_1 and the end-sections with element size n_2. The length of the mid-section is dependent of the length ΔL on both sides of the padeye. Both the element size n_2 and the length ΔL will be changed while element size N_1 will remain unchanged and equal to the determined 20 mm.

The displacements and stresses are given in Figure 92 and Figure 93. In these graphs the element size $n_2 = 20$ mm is the reference model, in which the complete model will have element size $n_1 = n_2 = 20$ mm. In the graph showing the displacement vector it can be seen that for element size n_2 of 200 mm or smaller, and a length ΔL of 400 mm or larger the model is closest to the reference model.

In the graph showing the Von Mises equivalent stress it can be noted that a similar conclusion can be drawn about the length ΔL. In this graph the model is closest to the reference model for a length ΔL of 400 or larger, but an element size up to 600 mm.

From these two graphs it can be concluded that the model is closest to the reference model for an element size $n_1 = 20$ mm, $n_2 = 200$ mm and length ΔL = 400 mm.

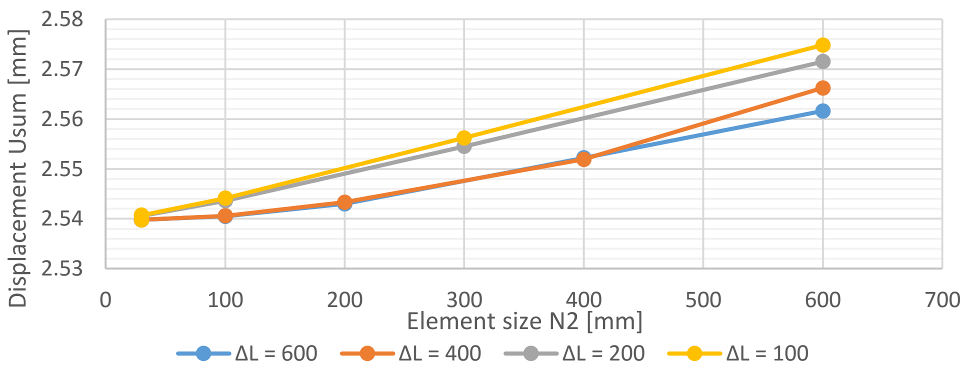

Figure 92: Displacement vector sum (u_{sum}) for multiple lengths ΔL and element size N2 in mesh refinement

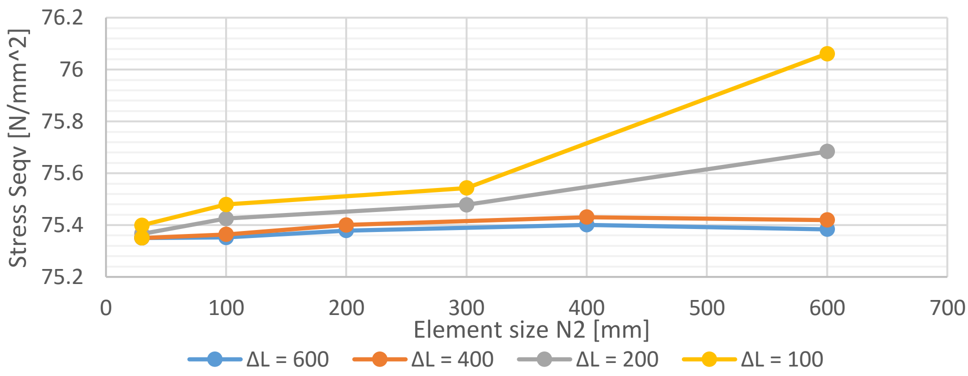

Figure 93: Von Mises stress (σ_{eqv}) for multiple lengths ΔL and element size N2 in mesh refinement

C.2 Reinforcement band

In order to assume that failure of the padeye to CHS connection is governing, a reinforced band has to be applied to the CHS at the supports. This is to prevent plastic failure of the CHS due to the applied bending moment at the support. The reinforced band has a larger yield stress than the rest of the CHS, causing the material in this part to have linear elastic behaviour for high loads. The assumed yield stress of the reinforced band is σ_y = 500 N/mm^2 instead of σ_y = 335 N/mm^2.

Plastic failure of the CHS can only occur when the load capacity of the padeye to CHS connection is larger than the load capacity of the CHS cross-section. This is in the case of a stiff CHS cross-section with a small diameter, causing large normal stresses in the cross-section due to the bending moment. The governing cross-section for this type of failure is the CHS with diameter d_0 = 800 mm. The length of the reinforced band is determined for the governing diameter. In order to determine the length, the load capacity of the padeye model with the governing diameter is obtained from finite element analysis using the 4% plastic strain limit. The results from these analysis are shown in Figure 94, from which it can be seen that the solution converges for a reinforced band length of 800 mm. This means that from a reinforced band length of 800 mm, an increase of the length will have no influence of the load capacity of the padeye load case model.

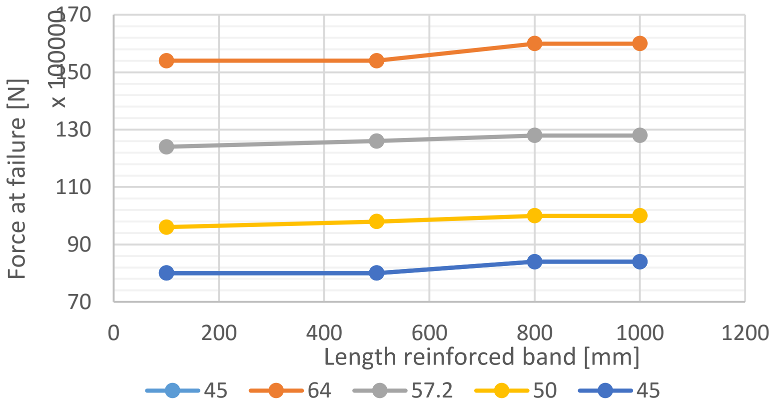

Figure 94: Force at failure for variable reinforced band width

C.3 Analysis

To obtain the stresses from the Finite Element Model, an analysis has to be performed. A distinction can be made between the linear and nonlinear analysis types. In the linear elastic analysis the displacements are assumed small, the strain is proportional to the stress, the loads are independent on displacements and the supports remain unchanged during loading.

The nonlinear analysis can be subdivided in geometrical nonlinearities, material nonlinearities and boundary nonlinearities. The geometrical nonlinearities take into account the effect of large displacements on the overall geometric configuration of the structure. Because of these large displacements the angle of the force on the structure will change during loading, causing the force to change. The material nonlinearities take into account the fact that the material behaviour is not linear. The material models that can be used in this analysis are nonlinear elastic, elastoplastic, viscoelastic and viscoplastic. Finally for the boundary nonlinearities, displacement dependant boundary conditions are taken into account. These nonlinearities are usually found in contact problems, in which a force is modelled that can only have influence on a structure when it has a contact area.

In the analysis the element stiffness matrices have to be integrated over volumes and surfaces and then inverted to solve for the displacements of each element. For this numerical integration of the function in each element, a number of points is calculated and their position is optimised. These points are known as Gaussian co-ordinates or Gauss points. For each of these points the function is multiplied by a weight function and then added together to calculate the integral. The more Gauss points used in the integration, the more accurate the solution will become. But an increase in Gauss points also means an increase in computation time.

Sun [28] described that using full integration can cause a numerical problem called shear locking in first order elements. This is due to the fact that the edges of a first order, linear, element are not able to bend to curves, lacking the ability to assume a curved shape (Figure 95). This causes the strain energy in the element to generate shear deformation instead of bending deformation. The effect of shear locking is that the element becomes very stiff under a bending moment.

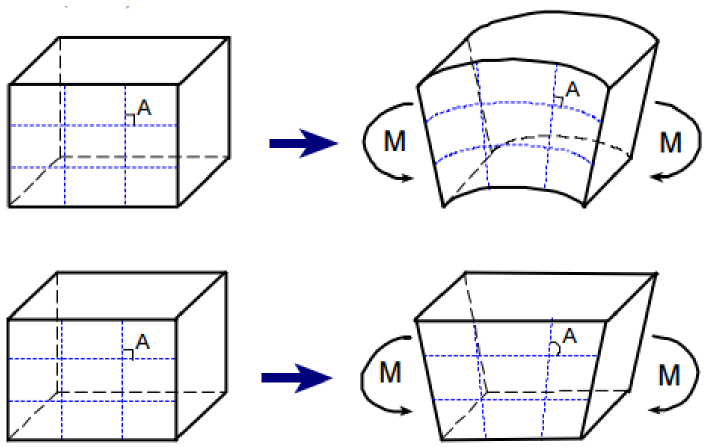

Figure 95: Shear locking of a finite element under bending, caused by the inability of linear elements to curve [28]

In order to prevent locking, higher order elements should be chosen of reduced integration can be applied to solve the problem. Using reduced integration the function will be calculated with less Gauss points, and thus the computation time will be less but the accuracy of the element will be less. In some cases reduced integration can cause instability due to the stiffness matrix being zero, which is known as the hourglass mode [28]. The hourglass mode is caused by a deformed element in which the normal- and shear stresses are zero. This can be seen in Figure 96, in which the lines in the element remain straight and perpendicular to each other and thus having no strain energy. It typically occurs when a single layer of linear elements is used, where individual elements are severely deformed while the overall mesh is section is undeformed. A way to prevent this from happening is using two or more layers of higher order elements.

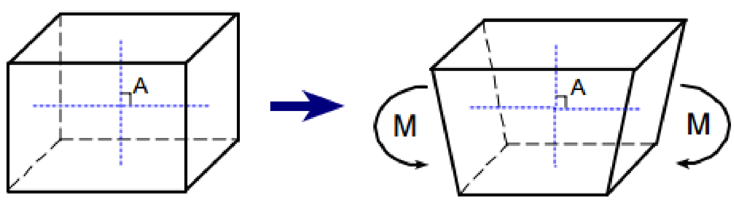

Figure 96: Hourglass mode of a finite element under bending, caused by deformation in for which stresses remain zero [11]

C.4 Ansys Mechanical APDL macro

C.4.1 Plate load case

```
!Variables
bm = 1300                     !Base width padeye main plate [mm]
d00 = 800
Rt = 0.5*d00                  !Radius CHS                   [mm]
t = 64
dt = 64
L = 6*d00                     !Length CHS                   [mm]

!Constants
pi=ACOS(-1)
tm = bm/18.6                  !Thickness main plate         [mm]
h0 = bm/3.06                  !Height center hole=bm/3.05   [mm]

!Mesh
N1 = 20                       !Element size  [mm]
N2 = 300
dL = 400
dl2 = 500

! Force
aaa=60
alfa = (aaa)*pi/180           !Force angle   [radians]
FP = 20E+6                    !Force         [N]
tsteps = 50

!------------------------------------------------------------------------------------------
!------------------------------------------------------------------------------------------

/PREP7                        !Preprocessor
ET,1,SHELL181                 !Element: 8 node solid
ET,2,SHELL181
ET,3,SHELL181
ET,4,MASS21
ET,5,SHELL181

       MP,EX,1,210000                 !Youngs modulus
       MP,PRXY,1,.3           !Poisson's Ratio
       tb,plastic,1,1,3,miso
       tbtemp,0
       tbpt,defi,0.004,335    !Plastic yield and stress
       tbpt,defi,0.02,338.4
       tbpt,defi,0.15,450

       MP,EX,2,210000
       MP,PRXY,2,.3
       tb,plastic,2,1,3,miso
       tbtemp,0
       tbpt,defi,0.004,335    !Plastic yield and stress
       tbpt,defi,0.02,338.4
       tbpt,defi,0.15,450

       MP,EX,3,210000
       MP,PRXY,3,.3
       tb,plastic,3,1,3,miso
       tbtemp,0
       tbpt,defi,0.004,335    !Plastic yield and stress
       tbpt,defi,0.02,338.4
       tbpt,defi,0.15,450

       keyopt,4,3,0
       r,4,0.001,0.001,0.001,0.001,0.001,0.001

       MP,EX,5,210000
       MP,PRXY,5,.3
       tb,plastic,5,1,1,miso
       tbtemp,0
       tbpt,defi,0.004,500    !Plastic yield and stress
       tbpt,defi,0.02,505
       tbpt,defi,0.15,600
SECTYPE,1,SHELL                       !Padeye main plate
SECDATA,tm,,,9                !Thickness and number of integration points
SECTYPE,2,SHELL                       !Cheekplates
```

```
SECDATA,tm+2*tc,,,9
SECTYPE,3,SHELL                      !Tubular
SECDATA,t,,,9
SECTYPE,5,SHELL                      !Tubular
SECDATA,t,,,9

!PADEYE
k,0,0,0,0
k,0,0,h0+t/2,0
k,0,-bm/2,h0+t/2,0
k,0,bm/2,h0+t/2

k,0,-L/2-bm/2,-Rt+t/2,0              !Circle center -L/2
k,0,-L/2-bm/2,-Rt+t/2,-50
k,0,-L/2-bm/2,-Rt+t/2+50,0

k,0,-L/2-bm/2+dl2,-Rt+t/2,0          !Circle center reinf.
k,0,-L/2-bm/2+dl2,-Rt+t/2,-50
k,0,-L/2-bm/2+dl2,-Rt+t/2+50,0

k,0,-bm/2-dL,-Rt+t/2,0
k,0,-bm/2-dL,-Rt+t/2,-50
k,0,-bm/2-dL,-Rt+t/2+50,0

k,0,-bm/2,-Rt+t/2,0           !Circle center bottom main plate
k,0,-bm/2,-Rt+t/2,-50
k,0,-bm/2,-Rt+t/2+50,0

k,0,0,-Rt+t/2,0
k,0,0,-Rt+t/2,-50
k,0,0,-Rt+t/2+50,0

k,0,bm/2,-Rt+t/2,0            !Circle center top main plate
k,0,bm/2,-Rt+t/2,-50
k,0,bm/2,-Rt+t/2+50,0

k,0,bm/2+dL,-Rt+t/2,0
k,0,bm/2+dL,-Rt+t/2,-50
k,0,bm/2+dL,-Rt+t/2+50,0

k,0,L/2+bm/2-dl2,-Rt+t/2,0           !Circle center reinf.
k,0,L/2+bm/2-dl2,-Rt+t/2,-50
k,0,L/2+bm/2-dl2,-Rt+t/2+50,0

k,0,bm/2+L/2,-Rt+t/2,0        !Circle center L/2
k,0,bm/2+L/2,-Rt+t/2,-50
k,0,bm/2+L/2,-Rt+t/2+50,0

               !Create circles
kbegin=5
kend=31
*do,_i,kbegin,kend,3
       cskp,11,0,_i,_i + 1,_i + 2
       csys,11
       wpcsys,-1
       pcirc,Rt-t/2,,0,360
       adele,1
*enddo

CSYS,0                        !Change active CS to global CS
WPCSYS,-1                     !Working Plane location

_kpbegin=32                   !Creating lines between circles
_kpend=63
*do,_i,_kpbegin,_kpend,1
       lstr,_i,_i + 4
*enddo

_lbegin=1                     !Creating area's between lines
_lend=32
*do,_i,_lbegin,_lend,1
       *if,_i,eq,4,then
       al,_i,_i + 4, _i + 36, _i + 33
       *elseif,_i,eq,8
       al,_i,_i + 4, _i + 36, _i + 33
       *elseif,_i,eq,12
       al,_i,_i + 4, _i + 36, _i + 33
```

```
        *elseif,_i,eq,16
        al,_i,_i + 4, _i + 36, _i + 33
        *elseif,_i,eq,20
        al,_i,_i + 4, _i + 36, _i + 33
        *elseif,_i,eq,24
        al,_i,_i + 4, _i + 36, _i + 33
        *elseif,_i,eq,28
        al,_i,_i + 4, _i + 36, _i + 33
        *elseif,_i,eq,32
        al,_i,_i + 4, _i + 36, _i + 33
        *else
        al,_i,_i + 4, _i + 36, _i + 37
        *endif
*enddo

k,0,-bm/2,n1,0
k,0,0,n1,0                          !Cross-section for Nodal Forces
k,0,bm/2,n1,0

lstr,2,3
lstr,3,68
lstr,68,45
lstr,45,49
lstr,49,53
lstr,53,70
lstr,70,4
lstr,2,4
lstr,2,69
lstr,69,49
lstr,68,69
lstr,69,70

al,69,70,75,77
al,73,74,75,78
al,50,71,76,77
al,54,72,76,78

lsel,s,line,,1,36,1
lesize,all,,,(d00*pi)/(4*30)
allsel

asel,s,loc,y,0,h0                   !Adding material prop. to areas
aatt,1,1,1,,1
asel,s,loc,y,0,-2*Rt
asel,r,loc,x,-L/2+dl2,L/2-dl2
AATT,3,3,3,,3
asel,s,loc,x,-L/2-bm/2+dl2,-L/2-bm/2
asel,a,loc,x,L/2+bm/2,L/2+bm/2-dl2
aatt,5,5,5,,5
ALLSEL

 !MESH
MSHAPE,0,2-D
ESIZE,N2
asel,s,loc,x,-bm/2-dL,-bm/2-L/2
asel,a,loc,x,bm/2+dL,bm/2+L/2
amesh,all
allsel
ESIZE,N1
asel,s,loc,x,-bm/2-dL,bm/2+dL
amesh,all
allsel

        ! Nodes for BC's and Force
n,,L/2+bm/2,-Rt+t/2,0        !Nodes for BC's L/2
nodex1=NODE(L/2+bm/2,-Rt+t/2,0)              !master node
lsel,s,loc,x,L/2+bm/2               !slave nodes
nsll,s,1
cm,compx1,node
nsel,a,node,,nodex1
cerig,nodex1,all,all
allsel

n,,-L/2-bm/2,-Rt+t/2,0       !Nodes for BC's -L/2
nodex2=NODE(-L/2-bm/2,-Rt+t/2,0)      !master node
lsel,s,loc,x,-L/2-bm/2              !slave nodes
nsll,s,1
```

```
cm,compx2,node
nsel,a,node,,nodex2
cerig,nodex2,all,all
allsel

type,4                        !Adding mass elements to master nodes
mat,4
real,4
secnum,4
e,nodex1
e,nodex2
allsel

*get,_wallasol,active,,time,wall
FINISH
!---------------------------------------------------------------------------------------------
/SOL                          !Solution

esel,s,cent,y,h0-n1,h0+t/2
nsle,s,1
nsel,r,loc,y,h0+t/2
cm,fnodes,node
allsel

F,fnodes,Fy,(Fp*n1/bm)*sin(alfa)
F,fnodes,Fx,(Fp*n1/bm)*cos(alfa)
F,nodex1,Mz,0.25*Fp*(L)*sin(alfa)
F,nodex2,Mz,-0.25*Fp*(L)*sin(alfa)

D,nodex1,ux,0,,,,uy,uz,rotx,roty      !BC's -L/2
D,nodex2,uy,0,,,,uz,rotx,roty         !BC's L/2
allsel

!Nonlinear analysis
        NLGEOM,OFF
        NSUBST,tsteps  !,1000,1               !nr. of substeps, max nr., min nr.
        OUTRES,ALL,ALL
        AUTOTS,OFF
        LNSRCH,ON
        NEQIT,1000
        !CUTCONTROL,PLSLIMIT,0.04

ANTYPE,0                      !Analysis type:static
SOLVE                         !Solve problem

*get,_wallbsol,active,,time,wall
FINISH
!---------------------------------------------------------------------------------------------
```

C.4.2 Padeye load case

```
!Variables
bm = 1300                     !Base width padeye main plate [mm]
d00 = 1219.2                  !Diameter CHS                 [mm]
Rt = 0.5*d00                  !Radius CHS                   [mm]
t = 57.2                             !Thickness CHS                [mm]
dt = 57.2
L = 6*d00                     !Length CHS                   [mm]

!Constants
pi=ACOS(-1)
tm = bm/18.6                  !Thickness main plate;        bm/18.6 [mm]
tc = bm/26                    !Thickness cheek plate; bm/26 [mm]
h0 = bm/3.06                  !Height center hole;   bm/3.06 [mm]
h2 = bm/2.65                  !Height padeye bottom;        bm/2.65 [mm]
R0 = bm/11.7                  !Radius pinhole;       bm/11.7 [mm]
Rc = bm/4                     !Radius cheek plate;   bm/4    [mm]
Rm = bm/3.47                  !Radius main plate;    bm/3.47 [mm]
a = atan((h0+Rm-h2)/(bm-1.5*Rm))!Angle main plate

!Mesh
N1 = 20                       !Element size 1                      [mm]
N2 = 300                      !Element size 2               [mm]
dL = 400                      !Length intermediate          [mm]
dl2 = 800                     !Length support                      [mm]

! Force
aaa = 40
alfa = (aaa)*pi/180           !Force angle                  [radians]
FP = 20E+6                    !Force                        [N]
tsteps = 100

!------------------------------------------------------------------------------------------
!------------------------------------------------------------------------------------------

/PREP7                        !Preprocessor
ET,1,SHELL181                 !Element: 4 node shell
ET,2,SHELL181
ET,3,SHELL181
ET,4,MASS21                   !Mass element bc
ET,5,SHELL181


       MP,EX,1,210000                !Youngs modulus
       MP,PRXY,1,.3           !Poisson's Ratio
       tb,plastic,1,1,3,miso  !plastic material behaviour
       tbtemp,0
       tbpt,defi,0.004,335    !Yield strain
       tbpt,defi,0.02,338.4   !Yield plateau
       tbpt,defi,0.15,450     !Ultimate strain

       MP,EX,2,210000
       MP,PRXY,2,.3
       tb,plastic,2,1,3,miso
       tbtemp,0
       tbpt,defi,0.004,335
       tbpt,defi,0.02,338.4
       tbpt,defi,0.15,450

       MP,EX,3,210000
       MP,PRXY,3,.3
       tb,plastic,3,1,3,miso
       tbtemp,0
       tbpt,defi,0.004,335
       tbpt,defi,0.02,338.4
       tbpt,defi,0.15,450

       keyopt,4,3,0
       r,4,0.001,0.001,0.001,0.001,0.001,0.001

       MP,EX,5,210000
       MP,PRXY,5,.3
       tb,plastic,5,1,1,miso
       tbtemp,0
       tbpt,defi,0.004,500
```

```
        tbpt,defi,0.02,505
        tbpt,defi,0.15,600

SECTYPE,1,SHELL                       !Padeye main plate
SECDATA,tm,,,9                !Thickness and number of integration points
SECTYPE,2,SHELL                       !Cheekplates
SECDATA,tm+2*tc,,,9
SECTYPE,3,SHELL                       !Tubular
SECDATA,dt,,,9
SECTYPE,5,SHELL                       !Tubular
SECDATA,dt,,,9

!PADEYE
k,0,0,h0+t/2,0                !Keypoints
k,0,50,h0+t/2,0
k,0,0,h0+t/2+50,0
k,0,-bm+Rm,h2+t/2,0
k,0,-L/2-bm+Rm,-Rt+t/2,0      !Circle center -L/2
k,0,-L/2-bm+Rm,-Rt+t/2,-50
k,0,-L/2-bm+Rm,-Rt+t/2+50,0
k,0,-bm+Rm-L/2+dl2,-Rt+t/2,0  !Circle center reinf.
k,0,-bm+Rm-L/2+dl2,-Rt+t/2,-50
k,0,-bm+Rm-L/2+dl2,-Rt+t/2+50,0
k,0,-bm+Rm-dL,-Rt+t/2,0               !Circle N2
k,0,-bm+Rm-dL,-Rt+t/2,-50
k,0,-bm+Rm-dL,-Rt+t/2+50,0
k,0,-bm+Rm,-Rt+t/2,0          !Circle center bottom main plate
k,0,-bm+Rm,-Rt+t/2,-50
k,0,-bm+Rm,-Rt+t/2+50,0
k,0,Rm,-Rt+t/2,0              !Circle center top main plate
k,0,Rm,-Rt+t/2,-50
k,0,Rm,-Rt+t/2+50,0
k,0,Rm+dL,-Rt+t/2,0           !Circle N2
k,0,Rm+dL,-Rt+t/2,-50
k,0,Rm+dL,-Rt+t/2+50,0
k,0,Rm+L/2-dL2,-Rt+t/2,0      !Circle center reinf.
k,0,Rm+L/2-dL2,-Rt+t/2,-50
k,0,Rm+L/2-dL2,-Rt+t/2+50,0
k,0,Rm+L/2,-Rt+t/2,0          !Circle center L/2
k,0,Rm+L/2,-Rt+t/2,-50
k,0,Rm+L/2,-Rt+t/2+50,0

CSKP,11,0,1,2,3                       !Local Coordinate System, number 11, keypoints 3,4,1
CSYS,11                       !Activates local CS 11
WPCSYS,-1                     !Working Plane location

pcirc,Rm,,0,90+(a*180/pi)     !Circle around WP axis
pcirc,R0,Rc,0,360             !Circle for cheekplate

CSYS,0                        !Change active CS to global CS
WPCSYS,-1                     !Working Plane location

adele,1                       !Delete area of circle
allsel
               !Create circles
kbegin=5
kend=26
*do,_i,kbegin,kend,3
        cskp,11,0,_i,_i + 1,_i + 2
        csys,11
        wpcsys,-1
        pcirc,Rt-t/2,,0,360
        adele,1
*enddo
CSYS,0                        !Change active CS to global CS
WPCSYS,-1                     !Working Plane location

_kpbegin=40                   !Creating lines between circles
_kpend=67
*do,_i,_kpbegin,_kpend,1
        lstr,_i,_i + 4
*enddo
ldele,2,3,,1                  !Creating lines padeye
lstr,53,4
lstr,4,30
lstr,29,57
```

```
_lbegin=12                    !Creating area's between lines
_lend=39
*do,_i,_lbegin,_lend,1
       *if,_i,eq,15,then
       al,_i,_i + 4, _i + 29, _i + 32
       *elseif,_i,eq,19
       al,_i,_i + 4, _i + 29, _i + 32
       *elseif,_i,eq,23
       al,_i,_i + 4, _i + 29, _i + 32
       *elseif,_i,eq,27
       al,_i,_i + 4, _i + 29, _i + 32
       *elseif,_i,eq,31
       al,_i,_i + 4, _i + 29, _i + 32
       *elseif,_i,eq,35
       al,_i,_i + 4, _i + 29, _i + 32
       *elseif,_i,eq,39
       al,_i,_i + 4, _i + 29, _i + 32
       *else
       al,_i,_i + 4, _i + 32, _i + 33
       *endif
*enddo

lsel,s,line,,1,3,1            !Creating padeye area
lsel,a,line,,57
lsel,a,line,,72
al,all
allsel
aptn,30,2
adele,31
allsel
lsel,s,line,,8,11,1           !Dividing unmeshed line by 10
lesize,all,,,10
allsel

lsel,s,line,,12,43,1
lesize,all,,,(d00*pi)/(4*30)
allsel
!------------------------------
CSKP,11,0,1,2,3                       !Local Coordinate System, number 11, keypoints 3,4,1
CSYS,11                       !Activates local CS 11
WPCSYS,-1                     !Working Plane location
pcirc,Rc,Rm,0,360
aovlap,30,32
aglue,2,33
CSYS,0                        !Change active CS to global CS
WPCSYS,-1                     !Working Plane location
!-------------------------------
k,0,-bm+Rm,2*n1,0             !Cross-section for Nodal Forces
k,0,Rm,2*n1,0
lstr,29,75
asbl,31,1

ASEL,S,AREA,,32,33
asel,a,area,,30                       !Adding material prop. to areas
AATT,1,1,1,,1
ASEL,S,AREA,,2
AATT,2,2,2,,2
ASEL,S,AREA,,6,25,1
AATT,3,3,3,,3
ASEL,S,AREA,,3,5,1
asel,a,area,,1
asel,a,area,,26,29
AATT,5,5,5,,5
ALLSEL

 !MESH
MSHAPE,0,2-D
ESIZE,N2
asel,s,loc,x,-bm+Rm-dL,-L
asel,a,loc,x,Rm+dL,+L
amesh,all
allsel
ESIZE,N1
asel,s,loc,x,-bm+Rm-dL,Rm+dL
amesh,all
allsel
```

```
! Nodes for BC's and Force
n,,L/2+Rm,-Rt+t/2,0            !Nodes for BC's L/2
nodex1=NODE(L/2+Rm,-Rt+t/2,0)         !master node
lsel,s,loc,x,L/2+Rm                   !slave nodes
nsll,s,1
cm,compx1,node
nsel,a,node,,nodex1
cerig,nodex1,all,all
allsel

n,,-L/2-bm+Rm,-Rt+t/2,0               !Nodes for BC's -L/2
nodex2=NODE(-L/2-bm+Rm,-Rt+t/2,0)     !master node
lsel,s,loc,x,-L/2-bm+Rm                      !slave nodes
nsll,s,1
cm,compx2,node
nsel,a,node,,nodex2
cerig,nodex2,all,all
allsel

type,4                         !Adding mass elements to master nodes
mat,4
real,4
secnum,4
e,nodex1
e,nodex2
allsel

n,,0,h0+t/2,0                  !Creating cartwheel
cnode=node(0,h0+t/2,0)
cartwheel,2*R0,tm+2*tc,cnode,,1
allsel

*get,_wallasol,active,,time,wall
FINISH
!---------------------------------------------------------------------------------------------
/SOL                           !Solution
F,cnode,Fy,Fp*sin(alfa)
F,cnode,Fx,Fp*cos(alfa)
F,nodex1,Mz,0.25*Fp*sin(alfa)*L
F,nodex2,Mz,-0.25*Fp*sin(alfa)*L
D,nodex1,ux,0,,,,uy,uz,rotx,roty      !BC's -L/2
D,nodex2,uy,0,,,,uz,rotx,roty         !BC's L/2
allsel
!Nonlinear analysis
       NLGEOM,OFF
       NSUBST,tsteps  !,1000,1              !nr. of substeps, max nr., min nr.
       OUTRES,ALL,ALL
       AUTOTS,OFF
       LNSRCH,ON
       NEQIT,1000
       !CUTCONTROL,PLSLIMIT,0.04

ANTYPE,0                       !Analysis type:static
SOLVE                          !Solve problem

*get,_wallbsol,active,,time,wall
FINISH
!---------------------------------------------------------------------------------------------
```

Appendix D Analytical model

D.1 Euler Bernoulli curved beam theory

In order to derive an equation that describes the load capacity of the padeye and plate load case, both load case have to be simplified. This can be done by translating the three-dimensional plate-to-CHS model into a two-dimensional ring model. In this ring model, a ring is subjected to a point load, which is supported by a transverse shear force. Due to symmetry only half of the ring has to be considered, leaving a curved beam on two fixed supports. This model is shown in Figure 97, and can be solved using the Euler-Bernoulli theory for curved beams.

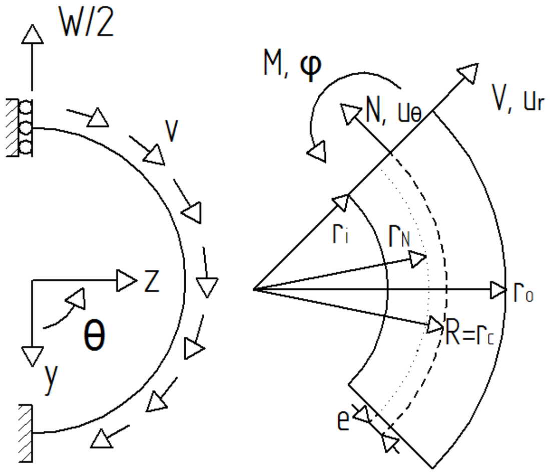

Figure 97: geometry of the Euler-Bernoulli curved beam model

The shear force v is assumed to be distributed constant over the total length of the ring, and can be separated into a component in z- and y-direction. From this it can be noticed that the summation of the shear force component in z-direction is zero, and the summation of the component in y-direction is equal to point load W. From this the load v can be determined, which is shown in equation (12.1).

$$
\begin{aligned}
&v_y = v\sin(\theta) \\
&\int\int v_y dA = \int_0^b\int_0^\pi v\sin(\theta)Rd\theta db = -\frac{W}{2} \\
&v = q_\theta = -\frac{W}{4bR}
\end{aligned}
\tag{12.1}
$$

With the distributed shear force v known, the uncoupled differential equations following the Euler-Bernoulli curved beam theory can be solved. By substituting the shear force v into equation (9.36), two separated differential equations are obtained which are stated in (12.2). The first differential equation with unknown radial deformation u_r is a fifth order equation, while the second differential equation with unknown lateral deformation u_θ is a first order equation. Because a distributed force is present, the solution of the fifth order equation is divided into a homogeneous and a particular solution.

$$\begin{aligned}
&\frac{d^5u_r}{d\theta^5}+2\frac{d^3u_r}{d\theta^3}+\frac{du_r}{d\theta}=-\frac{R^4b}{EI}\frac{W}{4bR}\\
&\frac{du_\theta}{d\theta}=-\left(\frac{EI}{EI+EAR^2}\right)\left(\frac{d^4u_r}{d\theta^4}+\frac{d^2u_r}{d\theta^2}\right)-u_r
\end{aligned} \tag{12.2}$$

To solve the homogeneous solution, a trial solution is substituted in the differential equation, which is stated in equation (12.3). Because the first differential equation is of the fifth order, five solutions can be found for unknown r in the trial solution. One of these solutions is the trivial solution, while the other four are equal to ± i. From this the homogeneous solution is obtained.

$$\begin{aligned}
&u_{r,H}=\sum_{n=1}^{5}u_{r,\mathrm{n}}=\sum_{n=1}^{5}e^{\mathrm{r}_n\theta}\\
&r^5+2r^3+r=(r^2+1)(r^2+1)r=0\\
&r_1=0\quad r_{2,3,4,5}=\pm i\\
&u_{r,H}=C_1\cos(\theta)+C_2\sin(\theta)+C_3\theta\cos(\theta)+C_4\theta\sin(\theta)+\mathrm{C}_5
\end{aligned} \tag{12.3}$$

In order to solve the particular solution, a trial solution is used as well. This trial solution has the same form as the distributed load, which is constant. Because a constant (C_5) is already used in the homogeneous solution, the trial solution has to be multiplied by the variable angle θ. By doing this the particular solution can be obtained from equation (12.4). With both the homogeneous and the particular solution of the radial deformation known, the total solution can be obtained:

$$\begin{aligned}
&u_{r,P}=C_6\theta^2+C_7\theta\\
&u_{r,P}=0+-\frac{WR^3}{4EI}\theta
\end{aligned} \tag{12.4}$$

$$u_r=u_{r,H}+u_{r,P}=C_1\cos(\theta)+C_2\sin(\theta)+C_3\theta\cos(\theta)+C_4\theta\sin(\theta)+\mathrm{C}_5-\frac{WR^3}{4EI}\theta \tag{12.5}$$

The differential equation describing lateral deformation is a first order equation. By substituting the total solution for the radial displacement in equation (12.2), the equation can be solved by performing a single integration. The equations of the radial and lateral deformation has to be substituted into the equations in (12.6) to calculate the rotation, the bending moment, the shear force and the normal force.

$$\begin{aligned}
&\phi(\theta_i)=\frac{1}{R}\left(-\frac{du_r}{d\theta}+u_{\theta0}\right)\quad ;M(\theta_i)=-\frac{EI}{R^2}\left(\frac{d^2u_r}{d\theta^2}-\frac{du_{\theta0}}{d\theta}\right)\\
&u_r(\theta_i)\quad ;V(\theta_i)=\frac{dM}{d\theta}=-\frac{EI}{R^3}\left(\frac{d^3u_r}{d\theta^3}-\frac{d^2u_{\theta0}}{d\theta^2}\right)\\
&u_{\theta0}(\theta_i)\quad ;N(\theta_i)=\frac{EA}{R}\left(\frac{du_{\theta0}}{d\theta}+u_r\right)
\end{aligned} \tag{12.6}$$

The unknown constant C_1 till C_7 which are still present in these equations, can be solved by substituting the boundary conditions. In these conditions the rotation (ϕ), deformations (u_r, u_θ) and the shear force (V) are used to restrain the ring model. With these boundary conditions, given in equation (12.7), the unknown constants can be solved and the displacements and rotations are solved. These displacements and rotations are given in equation (12.8).

$$\theta_i = 0 \begin{cases} u_r(0) = 0 \\ u_{\theta 0}(0) = 0 \\ \phi(0) = 0 \end{cases} \qquad \theta_i = \pi \begin{cases} u_{\theta 0}(\pi) = 0 \\ \phi(\pi) = 0 \\ V(\pi) = \dfrac{W}{2} \end{cases} \tag{12.7}$$

$$\begin{aligned} u_\theta &= \frac{1}{8}\frac{WR^3}{\pi EI}\left[\left(\pi^2 - 8Q + \frac{\pi\theta}{1-Q}\right)\sin(\theta) + 4(\pi-\theta)(\cos(\theta)-1) + \theta^2\pi - \theta\pi^2\right] \\ u_r &= -\frac{1}{8}\frac{WR^3}{\pi EI}\left[\left(4\theta - 3\pi - \frac{\pi EI}{EAR^2}\right)\sin(\theta) + \left((\pi^2-4) + \frac{\pi\theta}{1-Q}\right)\cos(\theta) + 2\theta\pi - \pi^2 + 4\right] \\ \phi &= \frac{WR^2}{\pi EI}\left[(1-Q)\sin(\theta) + \frac{\pi}{4}\cos(\theta) + \frac{1}{8}\left(\theta^2\pi - \pi^2\theta + 4\theta - 2\pi\right)\right] \\ with \quad Q &= \frac{EI}{EAR^2 + EI} \end{aligned} \tag{12.8}$$

The normal force, shear force and bending moment distribution in the ring circumference can be determined by substituting equation (12.8) into equation (12.6). The resulting force and bending moment distributions are given below:

$$\begin{aligned} N(\theta) &= \frac{W}{\pi}\left(\frac{\pi}{4}\sin(\theta) - \xi\cos(\theta)\right) \\ V(\theta) &= -\frac{W}{\pi}\left(\frac{\pi}{4}(\cos(\theta)-1) + \xi\sin(\theta)\right) \\ \mathrm{M}(\theta) &= \frac{WR}{\pi}\left(\frac{1}{4}\pi(\theta - \sin(\theta)) + \xi\cos(\theta) - \frac{\pi^2}{8} + \frac{1}{2}\right) \quad with \quad \xi = \frac{AR^2}{AR^2 + I} \end{aligned} \tag{12.9}$$

With the values from equation (12.9) known, the Von Mises equivalent stress distribution can be obtained using equation (12.10). In this equation the transverse stress due to a bending moment is determined in a different way for the curved beam as would be the case for a straight beam [19]. In case of a straight beam, the curvature at both sides is equal and therefore the strain due to a bending moment is equal as well. In the case of a curved beam, the outside and the inside of the ring have a different initial curvature due to the different radius. Therefore the strain at both sides of the curved beam due to a bending moment is different.

$$\begin{aligned} &\sigma_{eqv} = \sqrt{\left(\left(\sigma_{\theta,N} + \sigma_{\theta,M}\right)^2 + 3\tau_{r\theta}^2\right)} \\ &\sigma_{\theta,N} = \frac{N}{b_{eff}t_0}; \quad \tau_{r\theta} = \frac{V}{b_{eff}t_0}; \quad \sigma_{\theta,M} = \frac{M\left(A - rA_m\right)}{Ar\left(RA_m - A\right)} \end{aligned} \tag{12.10}$$

In the calculation of the transverse stress for a curved beam, the eccentricity between the neutral axis and the central axis of the cross-section is taken into account. The dimensions used in the equation of the transverse stress are stated in equation (12.11) and shown in Figure 97. By substituting these dimensions into equation (12.10) an eccentricity factor e can be obtained, which is given in (12.12).

$$
\begin{aligned}
&A_m = b\ln\left(\frac{r_o}{r_i}\right); \quad A = bt_0; \quad I = \frac{1}{12}bt_0^{\ 3} \\
&r = r_o = \frac{d_o}{2}; \quad r_i = \frac{d_o}{2} - t_0; \quad R = \frac{1}{2}(d_o - t_0)
\end{aligned} \tag{12.11}
$$

By performing this substitution a large equation is obtained, which is a function of the diameter d_0 and the thickness t_0 of the CHS. By using the formula for these CHS diameter and thickness within the considered geometric range, Figure 98 can be obtained. In this graph it can be seen that the relation between the eccentricity factor and the diameter over thickness ratio is linear. The dimensionless eccentricity factor, obtained from Figure 98, will be used from this point onwards.

$$
\sigma_{\theta,M} = \frac{Me}{\frac{1}{4}b_{eff}t_0 d_o}; \quad with \quad e = -\frac{\left(1 - \frac{d_o}{2t_0}\ln\left(\frac{d_o}{(d_o - 2t_0)}\right)\right)}{\left(\left(\frac{d_o}{t_0} - 1\right)\ln\left(\frac{d_o}{(d_o - 2t_0)}\right) - 2\right)} \simeq 3\frac{d_o}{2t_0} - 1.0 \tag{12.12}
$$

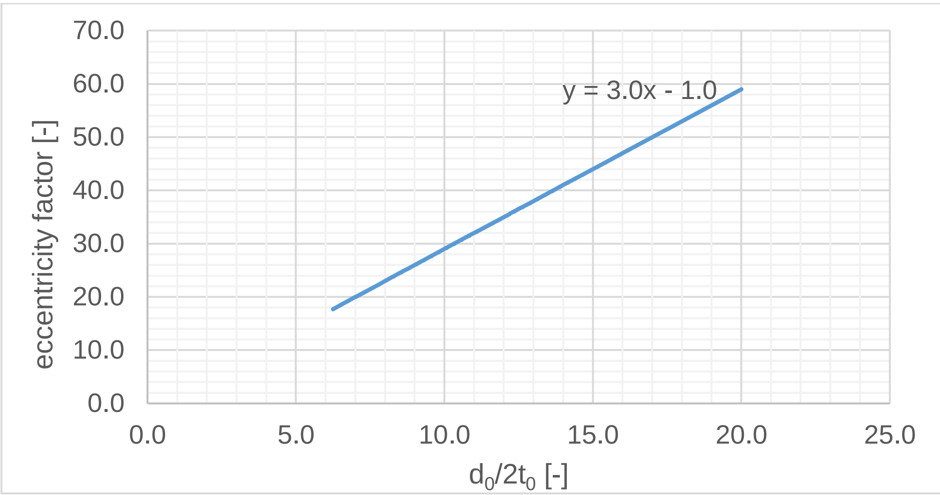

Figure 98: Eccentricity factor in the CHS cross-section, due to eccentricity between the neutral axis and the centroid axis

By substituting equation (12.11) into equation (12.9), the stress equations can be expressed as a function of the CHS dimensions. This leads to the factor ξ as described below. With the diameter d_0 being at least 10 times larger than the thickness t_0, the factor $(d_0\text{-}t_0)^2/t_0^2$ is much larger than 1/3. Therefore the constant 1/3 can be neglected, leaving the factor ξ to become equal to 1. With the value of the eccentricity factor and the factor ξ known, the stress components of the Von Mises stress can be obtained. These are given in equation (12.13)

$$
\xi = \frac{AR^2}{AR^2 + I} = \frac{(d_o - t)^2}{t^2\left(\frac{(d_o - t)^2}{t^2} + \frac{1}{3}\right)} \approx 1
$$

$$
\begin{aligned}
\sigma_{\theta,N}(\theta) &= \frac{N}{bt_0} = \frac{W}{\pi b_{eff} t_0}\left(\frac{\pi}{4}\sin(\theta) - \cos(\theta)\right) \\
\tau_{r\theta}(\theta) &= \frac{V}{bt_0} = -\frac{W}{\pi b_{eff} t_0}\left(\frac{\pi}{4}\left(\cos(\theta) - 1\right) + \sin(\theta)\right) \\
\sigma_{\theta,M}(\theta) &= \frac{Me}{\frac{1}{4}bt_0 d_0} = \frac{We}{2\pi b_{eff} t_0}\left(\pi\left(\theta - \sin(\theta)\right) + 4\cos(\theta) - \frac{\pi^2}{2} + 2\right)
\end{aligned}
\tag{12.13}
$$

These stress distributions can be plotted for the mean geometry of the padeye load case. The result is shown in Figure 99, in which the Von Mises stress distribution is compared for both theory used by Roark and the Euler-Bernoulli curved beam theory. For the Euler-Bernoulli theory the different stress components are shown; the transverse stress due to normal force and bending moment and the shear stress due to the shear force.

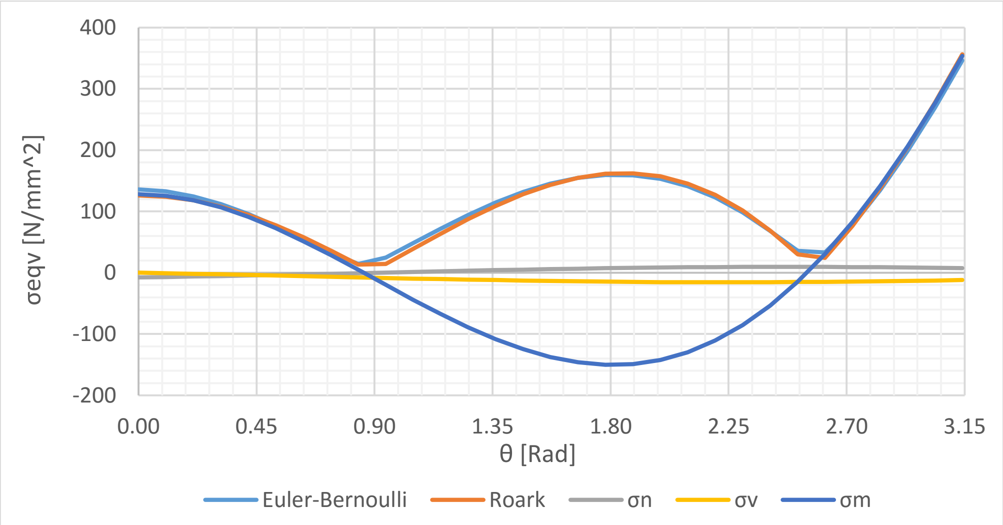

Figure 99: Von Mises stress distribution following Roark and Euler-Bernoulli curved beam theory for the mean CHS geometry, and the different stress components in Euler-Bernoulli curved beam theory.

From Figure 99 it can be noted that the Von Mises stress according to the Euler-Bernoulli theory is largely dependent of the transverse bending moment stress. Because of this it is assumed that the Von Mises stress is equal to the absolute value of the transverse bending moment stress. The maximal Von Mises stress occurs at the top of the ring (θ = π), at which the force is applied. In order to determine the load capacity, the stress at this location will be considered as governing stress from this point onwards. Due to the use of linear elastic theory, the stress at the governing location cannot exceed the yield stress. By applying these assumptions, the stress equation becomes the following:

$$
\sigma_{eqv}(\pi) = \sqrt{\sigma_{\theta,M}(\pi)^2} = \frac{W}{\pi b_{eff} t_0}\left(3\frac{d_0}{2t_0} - 1\right)\left(\frac{\pi^2}{4} + 1\right) \leq f_y
\tag{12.14}
$$

This equation is, amongst others, dependent of the force W on the ring. This force follows from the force N_1 which is applied on the padeye/plate, which causes a vertical force and a bending moment. The vertical force is due to the vertical force component, while the bending moment is due to the horizontal force component. The relation between the force W on the ring and the force N_1 on the padeye/plate is given below:

$$W = \left(\frac{N_1 \sin(\alpha)}{b_m} + \frac{h_0 N_1 \cos(\alpha)}{\frac{1}{6} b_m^{\ 2}} \right) b_{eff} = \frac{N_1 b_{eff}}{b_m} \left(\sin(\alpha) + 1.96 \cos(\alpha) \right) \qquad (12.15)$$

When substituting (12.15) into (12.14) and rewriting this equation, an equation can be obtained that describes the load capacity of the padeye/plate-to-CHS connection as a function of the geometry. This equation is described below:

$$N_1 = \frac{\pi b_m}{\left(3 \frac{d_0}{2t_0} - 1 \right) \left(\frac{\pi^2}{4} + 1 \right)} \frac{f_y t_0}{\sin(\alpha) + 1.96 \cos(\alpha)} \qquad (12.16)$$

This equation can be described as a normalised load. This normalised load is dimensionless and is a function of the dimensionless ratio's $\gamma = d_0/2t_0$ and $\eta = b_m/d_0$. Because the equation stated in (12.16) is only dependent of the ratio γ, this equation has to be altered. This can be obtained in two different ways: by multiplying the equation with γ/γ or multiplying with η/η. The first multiplication leads to the normalised load stated in (12.17), while the second is stated in (12.18). Both equations have to be compared using the results following the FEA, in order to determine which described the results in the best way.

$$\begin{aligned} N_1 &= 0.91 \frac{\gamma}{\gamma} \frac{b_m}{(3\gamma - 1)} \frac{f_{y0} t_0}{\sin(\alpha) + 1.96 \cos(\alpha)} \\ \frac{N_1}{f_{y0} t_0^{\ 2}} &= \frac{\eta \gamma}{(3\gamma - 1)} \frac{1.81}{\sin(\alpha) + 1.96 \cos(\alpha)} \end{aligned} \qquad (12.17)$$

$$\begin{aligned} N_1 &= 0.91 \frac{\eta}{\eta} \frac{b_m}{(3\gamma - 1)} \frac{f_{y0} t_0}{\sin(\alpha) + 1.96 \cos(\alpha)} \\ \frac{N_1}{f_{y0} t_0 d_0} &= \frac{\eta}{(3\gamma - 1)} \frac{0.91}{\sin(\alpha) + 1.96 \cos(\alpha)} \end{aligned} \qquad (12.18)$$

Besides the ring model using the Euler-Bernoulli curved beam theory, the ring model can be derived using other theories. Plastic theory is used in the ring model derived by Togo (Figure 100), which describes the load capacity of a T-type CHS-to-CHS connection. In this model it is assumed that plastic hinges are formed in the ring in case the plastic moment is reached at this location. The locations of the plastic hinges are unknown. To determine the load capacity of the model, the locations of the plastic hinges have to be determined at which the lowest load capacity is reached. This leads to an equation of the load capacity given in (5.13).

$$N_1 = \frac{2 f_{y,0} t_0^{\,2} \left(\frac{B_e}{d_0}\right)\left(1+\sqrt{1-\beta^2}\right)}{\left(1-\frac{\varphi_2}{\pi}\right)\sin\left(\varphi_2\right)\left(1+\sqrt{1-\beta^2}\right)-\beta\left(1-\frac{\arcsin\left(\beta\right)}{\pi}\right)\left(1+\cos\left(\varphi_2\right)\right)+\frac{0.7}{\gamma^2}} \tag{12.19}$$

$$\varphi_2 = 1.2 + 0.8\beta^2$$

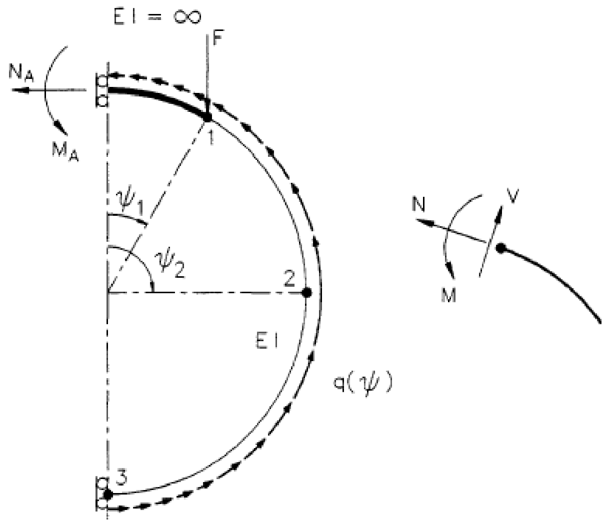

Figure 100: Ring model derived by Togo using plastic theory

This is however the case for a T-type CHS-to-CHS connection. In the case of a plate-to-CHS connection, the angle at which hinge number 1 is formed will be close to zero due to the small plate width. Therefore the β ratio ($\beta = b_1/d_0$) will be close to zero. By substituting this into (12.19) , the following equation can be obtained:

$$N_1 = 5.7\frac{B_e}{d_0}\frac{\gamma^2}{1.64\gamma^2+1} f_{y,0} t_0^{\,2} \tag{12.20}$$

In this equation B_e is the the effective connection length of the CHS. In case the effective length is equal to the plate length, B_e/d_0 becomes equal to $b_m/d_0 = \eta$. The equation can be rewritten into equation (5.14). When comparing the equation from both the model using Euler-Bernoulli curved beam theory and the plastic ring model derived by Togo, it can be seen that both equations are dependent of the yield stress, CHS thickness and dimensionless ratio's η and γ. The difference in both equations is the power of the ratio γ that is used, which is a power 2 in the model by Togo and a power 1 in the model using Euler-Bernoulli, while in both cases the power of the ratio η remains 1.

$$N_1 = 5.7\frac{\eta\gamma^2}{1.64\gamma^2+1} f_{y,0} t_0^{\,2} \tag{12.21}$$

Appendix E FEA Results

E.1 Plate load case

E.1.1 Force angle α_{ip} = 90˚

Table 14: Ultimate load from FEA analysis in the plate load case α_{ip} = 90˚ for d_0 = 800

d_0 [mm]	b_m [mm]	t_0 [mm]	$N_{1,4\%}$ [N]	ε_{max}	$\gamma = d_0/2t_0$	$\eta = b_m/d_0$	$N_{1,4\%}/f_y d_0 t_0$
800	1100	64.0	1.32E+07	4.68E-02	6.25	1.38	0.770
		57.2	1.08E+07	4.94E-02	6.99	1.38	0.705
		50.0	8.25E+06	4.50E-02	8.00	1.38	0.616
		45.0	6.82E+06	4.63E-02	8.89	1.38	0.566
		40.0	5.50E+06	4.72E-02	10.0	1.38	0.513
		35.0	4.30E+06	4.73E-02	11.4	1.38	0.458
	1300	64.0	1.46E+07	4.83E-02	6.25	1.63	0.851
		57.2	1.18E+07	4.76E-02	6.99	1.63	0.770
		50.0	9.12E+06	4.66E-02	8.00	1.63	0.681
		45.0	7.48E+06	4.66E-02	8.89	1.63	0.620
		40.0	6.00E+06	4.69E-02	10.0	1.63	0.560
		35.0	4.70E+06	4.73E-02	11.4	1.63	0.501
	1600	64.0	1.72E+07	5.07E-02	6.25	2.00	1.003
		57.2	1.40E+07	5.05E-02	6.99	2.00	0.913
		50.0	1.10E+07	4.95E-02	8.00	2.00	0.817
		45.0	9.02E+06	4.79E-02	8.89	2.00	0.748
		40.0	7.40E+06	4.88E-02	10.0	2.00	0.690
		35.0	5.90E+06	4.78E-02	11.4	2.00	0.629

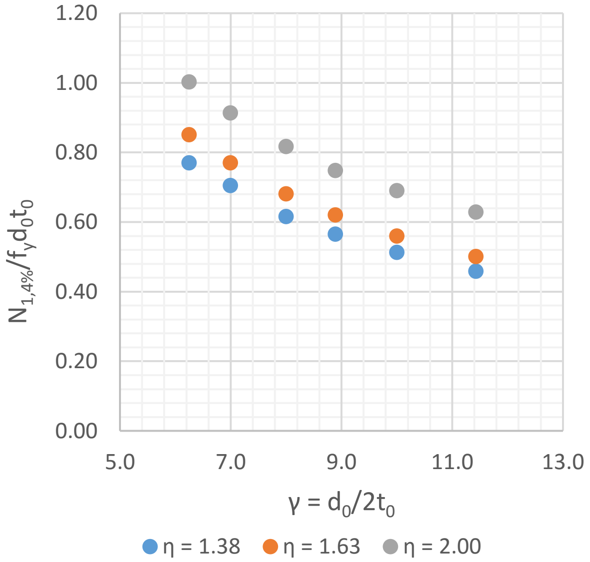

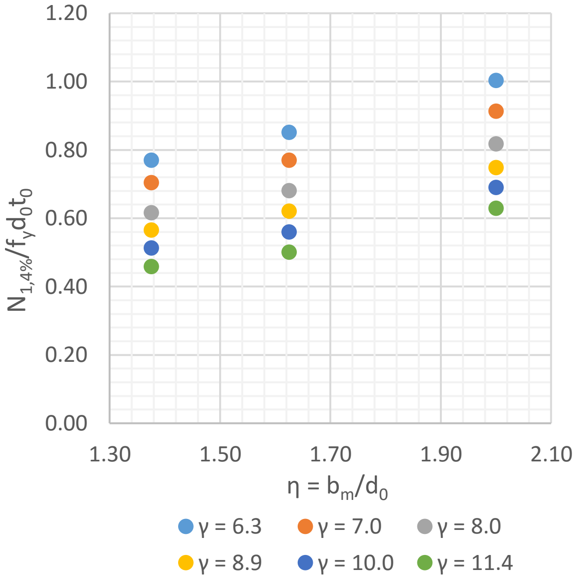

Figure 101: Ultimate load from FEA analysis in the plate load case α_{ip} = 90˚ for d_0 = 800

Table 15: Ultimate load from FEA analysis in the plate load case α_{ip} = 90˚ for d_0 = 900

d_0 [mm]	b_m [mm]	t_0 [mm]	$N_{1,4\%}$ [N]	ε_{max}	$\gamma = d_0/2t_0$	$\eta = b_m/d_0$	$N_{1,4\%}/f_yd_0t_0$
900	1100	64.0	1.24E+07	4.80E-02	7.0	1.22	0.643
		57.2	1.01E+07	4.83E-02	7.9	1.22	0.583
		50.0	7.80E+06	4.82E-02	9.0	1.22	0.517
		45.0	6.40E+06	4.81E-02	10.0	1.22	0.472
		40.0	5.04E+06	4.49E-02	11.3	1.22	0.418
		35.0	3.96E+06	4.56E-02	12.9	1.22	0.375
	1300	64.0	1.36E+07	4.79E-02	7.0	1.44	0.705
		57.2	1.10E+07	4.74E-02	7.9	1.44	0.635
		50.0	8.55E+06	4.92E-02	9.0	1.44	0.567
		45.0	7.00E+06	4.90E-02	10.0	1.44	0.516
		40.0	5.52E+06	4.60E-02	11.3	1.44	0.458
		35.0	4.32E+06	4.60E-02	12.9	1.44	0.409
	1600	64.0	1.54E+07	4.72E-02	7.0	1.78	0.798
		57.2	1.25E+07	4.75E-02	7.9	1.78	0.722
		50.0	9.75E+06	5.06E-02	9.0	1.78	0.647
		45.0	7.90E+06	4.86E-02	10.0	1.78	0.582
		40.0	6.32E+06	4.80E-02	11.3	1.78	0.524
		35.0	4.86E+06	4.54E-02	12.9	1.78	0.461
	1800	64.0	1.66E+07	4.93E-02	7.0	2.00	0.860
		57.2	1.34E+07	4.87E-02	7.9	2.00	0.774
		50.0	1.04E+07	4.97E-02	9.0	2.00	0.687
		45.0	8.50E+06	5.02E-02	10.0	2.00	0.626
		40.0	6.72E+06	4.75E-02	11.3	2.00	0.557
		35.0	5.18E+06	4.57E-02	12.9	2.00	0.491
	2000	64.0	1.96E+07	4.77E-02	7.0	2.22	1.016
		57.2	1.49E+07	4.91E-02	7.9	2.22	0.861
		50.0	1.17E+07	4.99E-02	9.0	2.22	0.776
		45.0	9.72E+06	4.95E-02	10.0	2.22	0.716
		40.0	7.90E+06	4.82E-02	11.3	2.22	0.655
		35.0	6.24E+06	4.58E-02	12.9	2.22	0.591

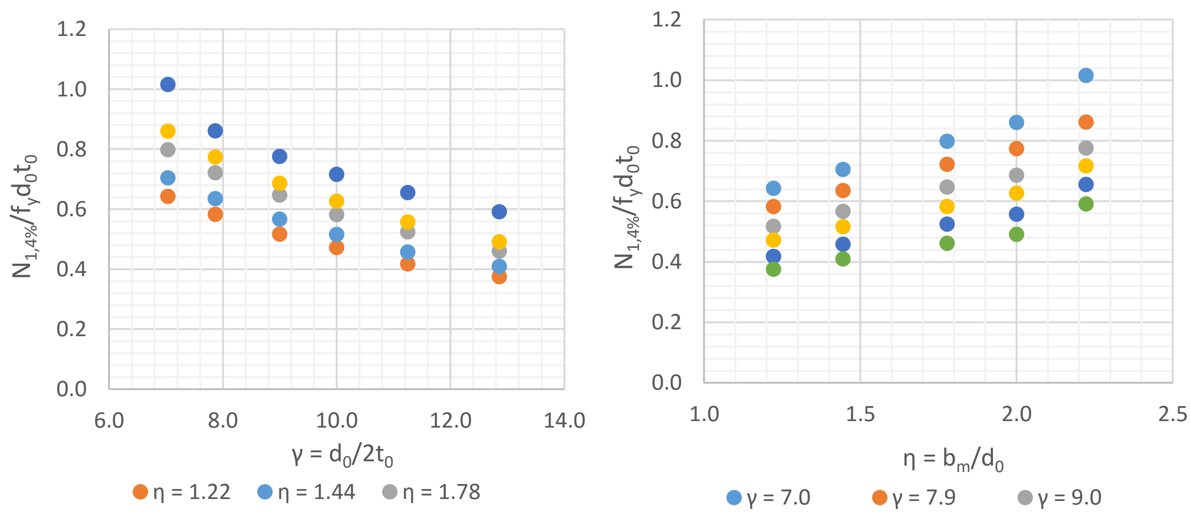

Figure 102: Ultimate load from FEA analysis in the plate load case α_{ip} = 90˚ for d_0 = 900

Table 16: Ultimate load from FEA analysis in the plate load case α_{ip} = 90˚ for d_0 = 1100

d_0 [mm]	b_m [mm]	t_0 [mm]	$N_{1,4\%}$ [N]	ε_{max}	$\gamma = d_0/2t_0$	$\eta = b_m/d_0$	$N_{1,4\%}/f_yd_0t_0$

1100	1100	64.0	1.11E+07	4.77E-02	8.59	1.00	0.471
		57.2	8.85E+06	4.59E-02	9.62	1.00	0.420
		50.0	6.90E+06	4.69E-02	11.00	1.00	0.374
		45.0	5.70E+06	4.80E-02	12.22	1.00	0.344
		40.0	4.56E+06	4.74E-02	13.75	1.00	0.309
		35.0	3.55E+06	4.64E-02	15.71	1.00	0.275
	1300	64.0	1.20E+07	4.71E-02	8.59	1.18	0.509
		57.2	9.75E+06	4.87E-02	9.62	1.18	0.463
		50.0	7.50E+06	4.76E-02	11.00	1.18	0.407
		45.0	6.20E+06	4.90E-02	12.22	1.18	0.374
		40.0	4.88E+06	4.60E-02	13.75	1.18	0.331
		35.0	3.80E+06	4.51E-02	15.71	1.18	0.295
	1600	64.0	1.37E+07	4.92E-02	8.59	1.45	0.579
		57.2	1.10E+07	4.86E-02	9.62	1.45	0.519
		50.0	8.47E+06	4.89E-02	11.00	1.45	0.460
		45.0	6.90E+06	4.79E-02	12.22	1.45	0.416
		40.0	5.52E+06	4.73E-02	13.75	1.45	0.374
		35.0	4.25E+06	4.52E-02	15.71	1.45	0.330
	1800	64.0	1.46E+07	4.98E-02	8.59	1.64	0.617
		57.2	1.17E+07	4.99E-02	9.62	1.64	0.555
		50.0	9.02E+06	4.96E-02	11.00	1.64	0.490
		45.0	7.40E+06	4.97E-02	12.22	1.64	0.446
		40.0	5.84E+06	4.72E-02	13.75	1.64	0.396
		35.0	4.44E+06	4.36E-02	15.71	1.64	0.344
	2000	64.0	1.55E+07	5.10E-02	8.59	1.82	0.656
		57.2	1.25E+07	5.13E-02	9.62	1.82	0.591
		50.0	9.60E+06	5.08E-02	11.00	1.82	0.521
		45.0	7.80E+06	4.94E-02	12.22	1.82	0.470
		40.0	6.09E+06	4.56E-02	13.75	1.82	0.413
		35.0	4.68E+06	4.36E-02	15.71	1.82	0.363

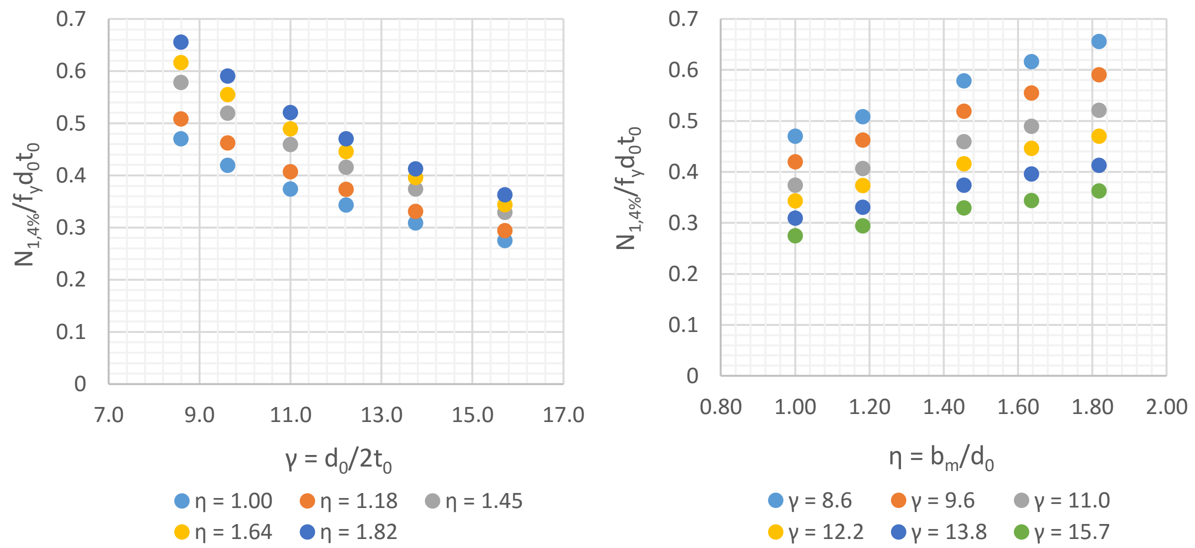

Figure 103: Ultimate load from FEA analysis in the plate load case α_{ip} = 90˚ for d_0 = 1100

Table 17: Ultimate load from FEA analysis in the plate load case α_{ip} = 90˚ for d_0 = 1219.2

d_0 [mm]	b_m [mm]	t_0 [mm]	$N_{1,4\%}$ [N]	ε_{max}	$\gamma = d_0/2t_0$	$\eta = b_m/d_0$	$N_{1,4\%}/f_y d_0 t_0$
1219.2	1100	64.0	1.04E+07	4.59E-02	9.53	0.90	0.396

		57.2	8.40E+06	4.70E-02	10.66	0.90	0.360
		50.0	6.50E+06	4.69E-02	12.19	0.90	0.318
		45.0	5.36E+06	4.77E-02	13.55	0.90	0.292
		40.0	4.26E+06	4.62E-02	15.24	0.90	0.261
		35.0	3.35E+06	4.64E-02	17.42	0.90	0.234
	1300	64.0	1.13E+07	4.69E-02	9.53	1.07	0.430
		57.2	9.12E+06	4.79E-02	10.66	1.07	0.390
		50.0	7.10E+06	4.89E-02	12.19	1.07	0.348
		45.0	5.76E+06	4.75E-02	13.55	1.07	0.313
		40.0	4.62E+06	4.70E-02	15.24	1.07	0.283
		35.0	3.60E+06	4.60E-02	17.42	1.07	0.252
	1600	64.0	1.28E+07	4.90E-02	9.53	1.31	0.488
		57.2	1.03E+07	4.99E-02	10.66	1.31	0.442
		50.0	7.90E+06	4.86E-02	12.19	1.31	0.387
		45.0	6.48E+06	4.86E-02	13.55	1.31	0.353
		40.0	5.16E+06	4.71E-02	15.24	1.31	0.316
		35.0	3.95E+06	4.42E-02	17.42	1.31	0.276
	1800	64.0	1.35E+07	4.90E-02	9.53	1.48	0.516
		57.2	1.10E+07	5.05E-02	10.66	1.48	0.469
		50.0	8.40E+06	4.95E-02	12.19	1.48	0.411
		45.0	6.86E+06	4.87E-02	13.55	1.48	0.373
		40.0	5.39E+06	4.57E-02	15.24	1.48	0.330
		35.0	4.14E+06	4.34E-02	17.42	1.48	0.290
	2000	64.0	1.43E+07	4.93E-02	9.53	1.64	0.545
		57.2	1.16E+07	5.09E-02	10.66	1.64	0.494
		50.0	8.91E+06	5.05E-02	12.19	1.64	0.436
		45.0	7.20E+06	4.83E-02	13.55	1.64	0.392
		40.0	5.67E+06	4.57E-02	15.24	1.64	0.347
		35.0	4.32E+06	4.26E-02	17.42	1.64	0.302

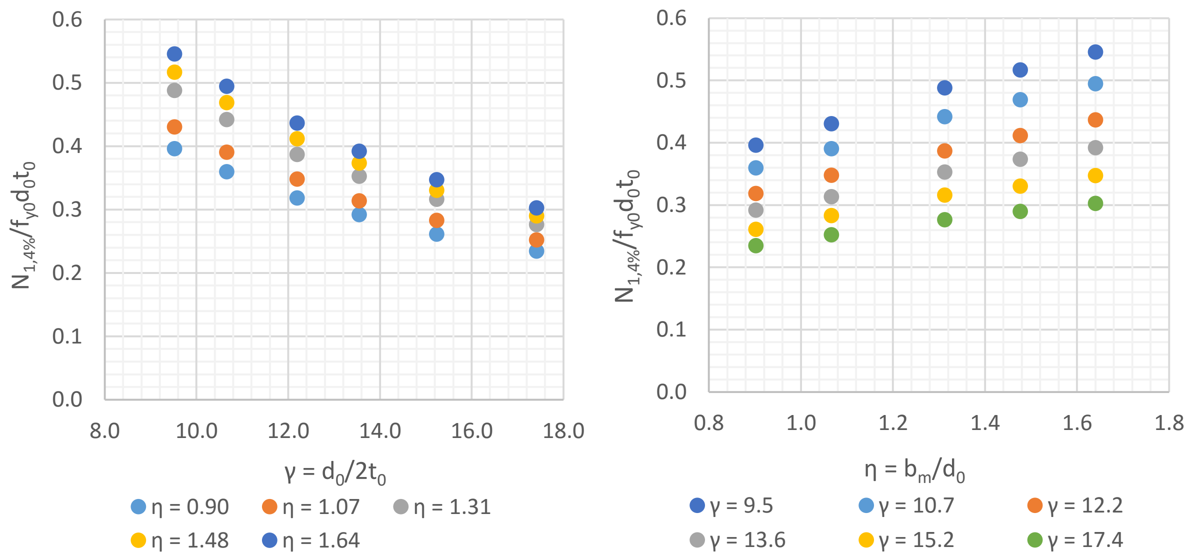

Figure 104: Ultimate load from FEA analysis in the plate load case α_{ip} = 90˚ for d_0 = 1219.2

Table 18: Ultimate load from FEA analysis in the plate load case α_{ip} = 90˚ for d_0 = 1400

d_0 [mm]	b_m [mm]	t_0 [mm]	$N_{1,4\%}$ [N]	ε_{max}	$\gamma = d_0/2t_0$	$\eta = b_m/d_0$	$N_{1,4\%}/f_y d_0 t_0$
1400	1100	64.0	9.60E+06	4.70E-02	10.94	0.79	0.320
		57.2	7.80E+06	4.83E-02	12.24	0.79	0.291
		50.0	6.00E+06	4.74E-02	14.00	0.79	0.256

	45.0	4.90E+06	4.68E-02	15.56	0.79	0.232
	40.0	3.90E+06	4.55E-02	17.50	0.79	0.208
	35.0	3.05E+06	4.67E-02	20.00	0.79	0.186
1300	64.0	1.04E+07	4.76E-02	10.94	0.93	0.345
	57.2	8.40E+06	4.88E-02	12.24	0.93	0.313
	50.0	6.50E+06	4.87E-02	14.00	0.93	0.277
	45.0	5.30E+06	4.79E-02	15.56	0.93	0.251
	40.0	4.26E+06	4.75E-02	17.50	0.93	0.227
	35.0	3.30E+06	4.55E-02	20.00	0.93	0.201
1600	64.0	1.16E+07	4.83E-02	10.94	1.14	0.385
	57.2	9.45E+06	5.08E-02	12.24	1.14	0.352
	50.0	7.30E+06	5.04E-02	14.00	1.14	0.311
	45.0	5.95E+06	4.92E-02	15.56	1.14	0.282
	40.0	4.70E+06	4.66E-02	17.50	1.14	0.251
	35.0	3.60E+06	4.36E-02	20.00	1.14	0.219
1800	64.0	1.23E+07	4.97E-02	10.94	1.29	0.410
	57.2	9.90E+06	5.00E-02	12.24	1.29	0.369
	50.0	7.70E+06	5.06E-02	14.00	1.29	0.328
	45.0	6.23E+06	4.84E-02	15.56	1.29	0.295
	40.0	4.92E+06	4.59E-02	17.50	1.29	0.262
	35.0	3.77E+06	4.40E-02	20.00	1.29	0.230
2000	64.0	1.31E+07	5.14E-02	10.94	1.43	0.435
	57.2	1.05E+07	5.08E-02	12.24	1.43	0.390
	50.0	8.00E+06	4.91E-02	14.00	1.43	0.341
	45.0	6.51E+06	4.78E-02	15.56	1.43	0.308
	40.0	5.10E+06	4.45E-02	17.50	1.43	0.272
	35.0	3.95E+06	4.30E-02	20.00	1.43	0.241

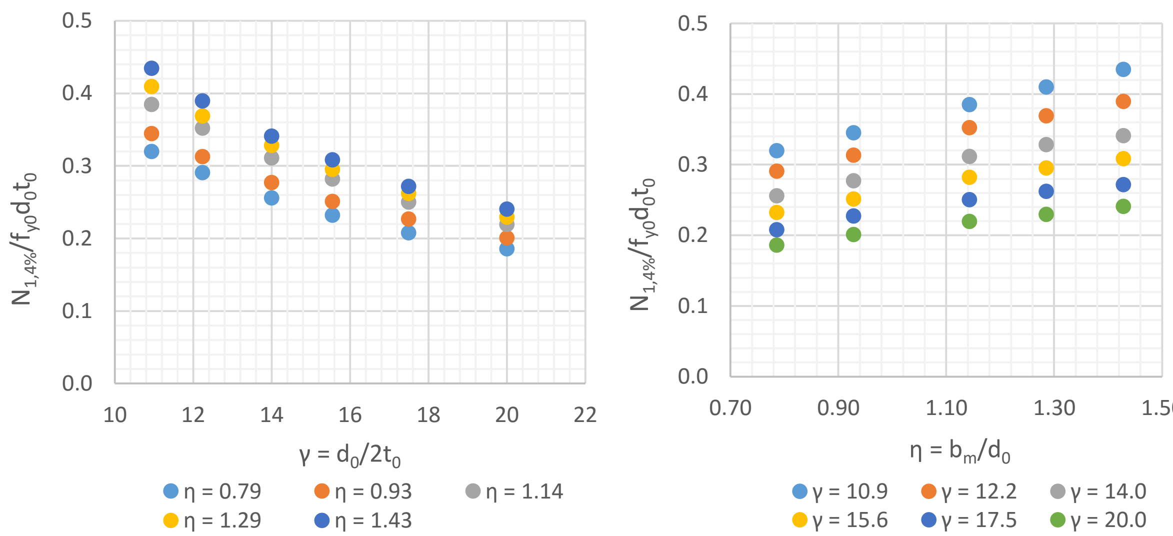

Figure 105: Ultimate load from FEA analysis in the plate load case α_{ip} = 90˚ for d_0 = 1400

A.1.1 Force angle $\alpha_{ip} = 60^\circ$

Table 19: Ultimate load from FEA analysis in the plate load case $\alpha_{ip} = 60^\circ$ for $d_0 = 800$

d_0 [mm]	b_m [mm]	t_0 [mm]	$N_{1,4\%}$ [N]	ε_{max}	$\gamma = d_0/2t_0$	$\eta = b_m/d_0$	$N_{1,4\%}/f_y d_0 t_0$
800	1100	64.0	1.10E+07	4.93E-02	6.3	1.38	0.638
		57.2	8.64E+06	4.53E-02	7.0	1.38	0.564
		50.0	6.70E+06	4.60E-02	8.0	1.38	0.500
		45.0	5.46E+06	4.52E-02	8.9	1.38	0.453
		40.0	4.38E+06	4.52E-02	10.0	1.38	0.409
		35.0	3.40E+06	4.43E-02	11.4	1.38	0.362
	1300	64.0	1.17E+07	4.70E-02	6.3	1.63	0.682
		57.2	9.36E+06	4.64E-02	7.0	1.63	0.611
		50.0	7.20E+06	4.59E-02	8.0	1.63	0.537
		45.0	5.92E+06	4.64E-02	8.9	1.63	0.491
		40.0	4.74E+06	4.62E-02	10.0	1.63	0.442
		35.0	3.70E+06	4.57E-02	11.4	1.63	0.394
	1600	64.0	1.32E+07	4.78E-02	6.3	2.00	0.770
		57.2	1.07E+07	4.78E-02	7.0	2.00	0.695
		50.0	8.30E+06	4.75E-02	8.0	2.00	0.619
		45.0	6.93E+06	4.91E-02	8.9	2.00	0.575
		40.0	5.60E+06	4.79E-02	10.0	2.00	0.522
		35.0	4.44E+06	4.67E-02	11.4	2.00	0.473
	1800	64.0	1.39E+07	4.84E-02	6.3	2.25	0.812
		57.2	1.12E+07	4.75E-02	7.0	2.25	0.731
		50.0	8.91E+06	5.05E-02	8.0	2.25	0.665
		45.0	7.29E+06	4.87E-02	8.9	2.25	0.604
		40.0	5.92E+06	4.79E-02	10.0	2.25	0.552
		35.0	4.68E+06	4.64E-02	11.4	2.25	0.499
	2000	64.0	1.45E+07	4.77E-02	6.3	2.50	0.842
		57.2	1.19E+07	5.02E-02	7.0	2.50	0.776
		50.0	9.35E+06	5.09E-02	8.0	2.50	0.698
		45.0	7.70E+06	4.97E-02	8.9	2.50	0.638
		40.0	6.24E+06	4.85E-02	10.0	2.50	0.582
		35.0	4.90E+06	4.62E-02	11.4	2.50	0.522

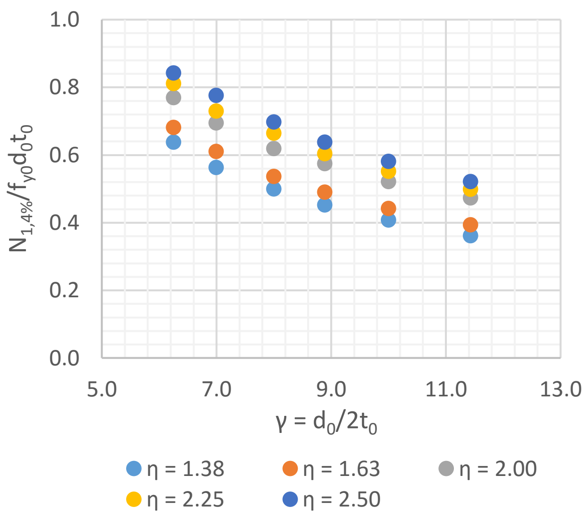

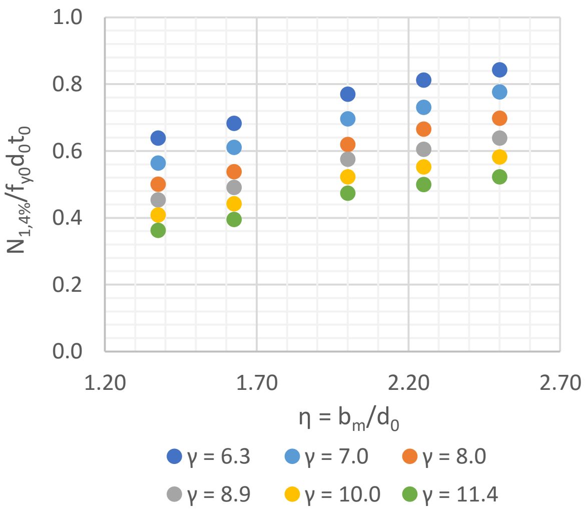

Figure 106: Ultimate load from FEA analysis in the plate load case $\alpha_{ip} = 60^\circ$ for $d_0 = 800$

Table 20: Ultimate load from FEA analysis in the plate load case α_{ip} = 60˚ for d_0 = 900

d_0 [mm]	b_m [mm]	t_0 [mm]	$N_{1,4\%}$ [N]	ε_{max}	$\gamma = d_0/2t_0$	$\eta = b_m/d_0$	$N_{1,4\%}/f_y d_0 t_0$
900	1100	64.0	1.02E+07	4.84E-02	7.9	1.22	0.529
		57.2	8.10E+06	4.62E-02	9.0	1.22	0.470
		50.0	6.20E+06	4.51E-02	10.0	1.22	0.411
		45.0	5.11E+06	4.59E-02	11.3	1.22	0.377
		40.0	4.08E+06	4.52E-02	12.9	1.22	0.338
		35.0	3.20E+06	4.57E-02	7.0	1.22	0.303
	1300	64.0	1.10E+07	4.79E-02	7.9	1.44	0.567
		57.2	8.76E+06	4.75E-02	9.0	1.44	0.508
		50.0	6.70E+06	4.62E-02	10.0	1.44	0.444
		45.0	5.53E+06	4.72E-02	11.3	1.44	0.408
		40.0	4.38E+06	4.55E-02	12.9	1.44	0.363
		35.0	3.45E+06	4.61E-02	7.0	1.44	0.327
	1600	64.0	1.22E+07	4.84E-02	7.9	1.78	0.630
		57.2	9.72E+06	4.79E-02	9.0	1.78	0.564
		50.0	7.60E+06	4.96E-02	10.0	1.78	0.504
		45.0	6.16E+06	4.80E-02	11.3	1.78	0.454
		40.0	4.92E+06	4.69E-02	12.9	1.78	0.408
		35.0	3.85E+06	4.65E-02	7.0	1.78	0.365
	1800	64.0	1.28E+07	4.84E-02	7.9	2.00	0.661
		57.2	1.03E+07	4.95E-02	9.0	2.00	0.598
		50.0	8.00E+06	4.99E-02	10.0	2.00	0.531
		45.0	6.56E+06	4.97E-02	11.3	2.00	0.484
		40.0	5.25E+06	4.86E-02	12.9	2.00	0.435
		35.0	4.02E+06	4.53E-02	7.0	2.00	0.381
	2000	64.0	1.37E+07	4.90E-02	7.9	2.22	0.707
		57.2	1.11E+07	4.93E-02	9.0	2.22	0.644
		50.0	8.80E+06	5.11E-02	10.0	2.22	0.584
		45.0	7.29E+06	5.03E-02	11.3	2.22	0.537
		40.0	5.92E+06	4.89E-02	12.9	2.22	0.491
		35.0	4.68E+06	4.69E-02	7.9	2.22	0.443

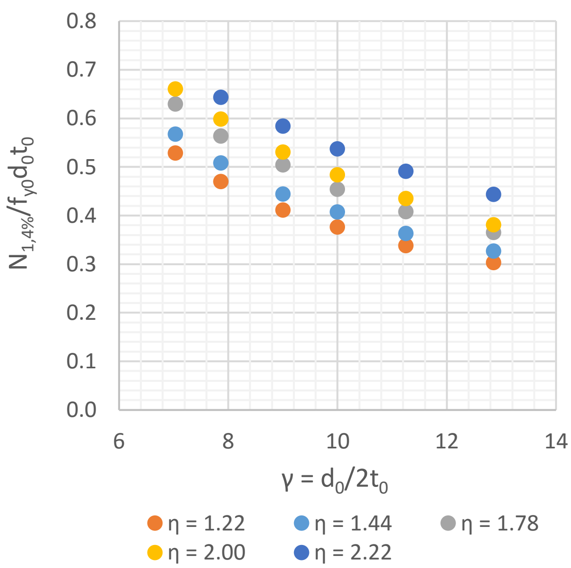

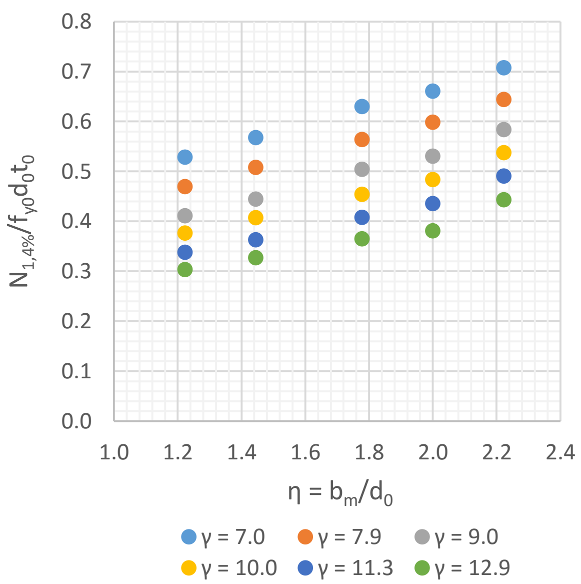

Figure 107: Ultimate load from FEA analysis in the plate load case α_{ip} = 60˚ for d_0 = 900

Table 21: Ultimate load from FEA analysis in the plate load case α_{ip} = 60˚ for d_0 = 1100

d_0 [mm]	b_m [mm]	t_0 [mm]	$N_{1,4\%}$ [N]	ε_{max}	$\gamma = d_0/2t_0$	$\eta = b_m/d_0$	$N_{1,4\%}/f_y d_0 t_0$
1100	1100	64.0	9.15E+06	4.85E-02	8.6	1.00	0.388
		57.2	7.28E+06	4.70E-02	9.6	1.00	0.345
		50.0	5.60E+06	4.64E-02	11.0	1.00	0.304
		45.0	4.62E+06	4.71E-02	12.2	1.00	0.279
		40.0	3.65E+06	4.50E-02	13.8	1.00	0.248
		35.0	2.90E+06	4.68E-02	15.7	1.00	0.225
	1300	64.0	9.75E+06	4.81E-02	8.6	1.18	0.413
		57.2	7.80E+06	4.76E-02	9.6	1.18	0.370
		50.0	6.00E+06	4.69E-02	11.0	1.18	0.326
		45.0	4.92E+06	4.68E-02	12.2	1.18	0.297
		40.0	3.95E+06	4.67E-02	13.8	1.18	0.268
		35.0	3.10E+06	4.65E-02	15.7	1.18	0.240
	1600	64.0	1.07E+07	4.72E-02	8.6	1.45	0.452
		57.2	8.70E+06	4.95E-02	9.6	1.45	0.413
		50.0	6.70E+06	4.88E-02	11.0	1.45	0.364
		45.0	5.53E+06	4.96E-02	12.2	1.45	0.333
		40.0	4.38E+06	4.70E-02	13.8	1.45	0.297
		35.0	3.40E+06	4.54E-02	15.7	1.45	0.264
	1800	64.0	1.13E+07	4.85E-02	8.6	1.64	0.477
		57.2	9.15E+06	5.00E-02	9.6	1.64	0.434
		50.0	7.10E+06	5.03E-02	11.0	1.64	0.385
		45.0	5.84E+06	5.03E-02	12.2	1.64	0.352
		40.0	4.62E+06	4.75E-02	13.8	1.64	0.313
		35.0	3.55E+06	4.47E-02	15.7	1.64	0.275
	2000	64.0	1.19E+07	4.99E-02	8.6	1.82	0.502
		57.2	9.57E+06	5.02E-02	9.6	1.82	0.454
		50.0	7.40E+06	4.99E-02	11.0	1.82	0.402
		45.0	6.08E+06	4.95E-02	12.2	1.82	0.367
		40.0	4.80E+06	4.66E-02	13.8	1.82	0.326
		35.0	3.70E+06	4.43E-02	15.7	1.82	0.287

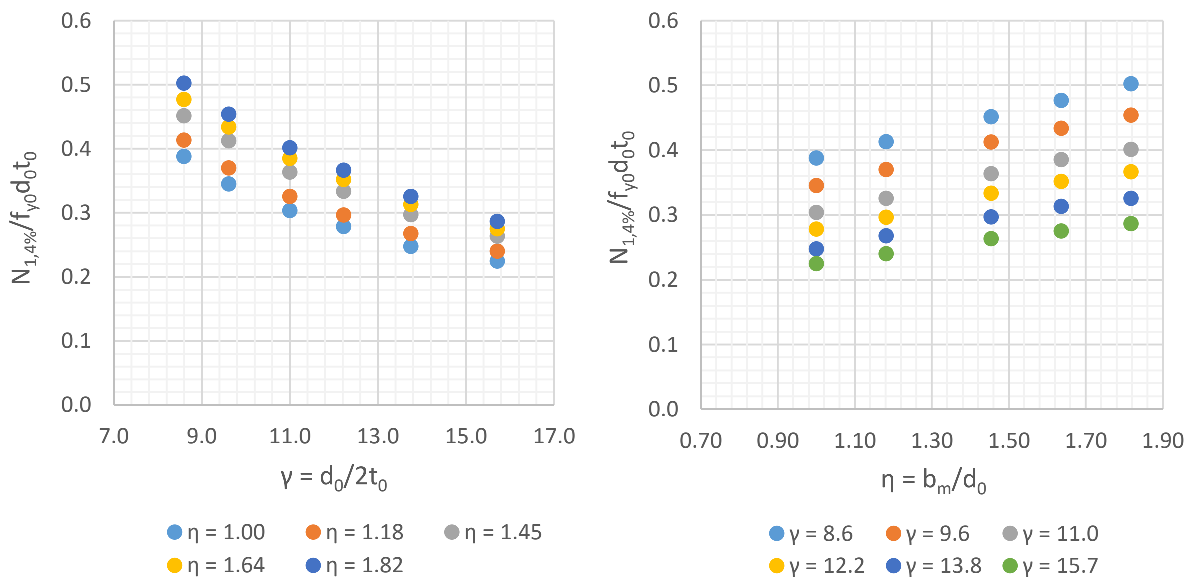

Figure 108: Ultimate load from FEA analysis in the plate load case α_{ip} = 60˚ for d_0 = 1100

Table 22: Ultimate load from FEA analysis in the plate load case α_{ip} = 60˚ for d_0 = 1219.2

d_0 [mm]	b_m [mm]	t_0 [mm]	$N_{1,4\%}$ [N]	ε_{max}	$\gamma = d_0/2t_0$	$\eta = b_m/d_0$	$N_{1,4\%}/f_y d_0 t_0$
1219.2	1100	64.0	8.55E+06	4.70E-02	9.5	0.90	0.327
		57.2	6.90E+06	4.74E-02	10.7	0.90	0.295
		50.0	5.30E+06	4.66E-02	12.2	0.90	0.260
		45.0	4.38E+06	4.74E-02	13.5	0.90	0.238
		40.0	3.45E+06	4.48E-02	15.2	0.90	0.211
		35.0	2.75E+06	4.67E-02	17.4	0.90	0.192
	1300	64.0	9.15E+06	4.75E-02	9.5	1.07	0.350
		57.2	7.30E+06	4.67E-02	10.7	1.07	0.312
		50.0	5.70E+06	4.78E-02	12.2	1.07	0.279
		45.0	4.68E+06	4.78E-02	13.5	1.07	0.255
		40.0	3.75E+06	4.72E-02	15.2	1.07	0.230
		35.0	2.95E+06	4.71E-02	17.4	1.07	0.206
	1600	64.0	1.01E+07	4.79E-02	9.5	1.31	0.384
		57.2	8.20E+06	4.97E-02	10.7	1.31	0.351
		50.0	6.30E+06	4.86E-02	12.2	1.31	0.308
		45.0	5.16E+06	4.81E-02	13.5	1.31	0.281
		40.0	4.15E+06	4.76E-02	15.2	1.31	0.254
		35.0	3.20E+06	4.49E-02	17.4	1.31	0.224
	1800	64.0	1.07E+07	4.97E-02	9.5	1.48	0.407
		57.2	8.60E+06	5.01E-02	10.7	1.48	0.368
		50.0	6.70E+06	5.08E-02	12.2	1.48	0.328
		45.0	5.46E+06	4.93E-02	13.5	1.48	0.297
		40.0	4.32E+06	4.65E-02	15.2	1.48	0.264
		35.0	3.35E+06	4.47E-02	17.4	1.48	0.234
	2000	64.0	1.11E+07	4.97E-02	9.5	1.64	0.425
		57.2	9.02E+06	5.09E-02	10.7	1.64	0.386
		50.0	7.00E+06	5.09E-02	12.2	1.64	0.343
		45.0	5.67E+06	4.84E-02	13.5	1.64	0.308
		40.0	4.50E+06	4.61E-02	15.2	1.64	0.275
		35.0	3.45E+06	4.29E-02	17.4	1.64	0.241

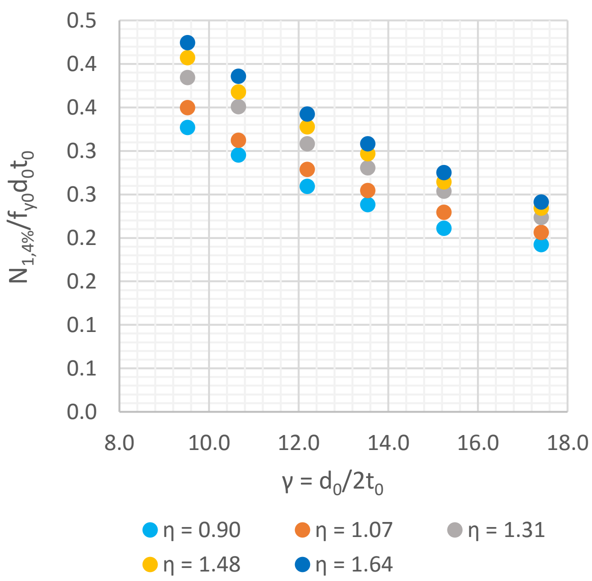

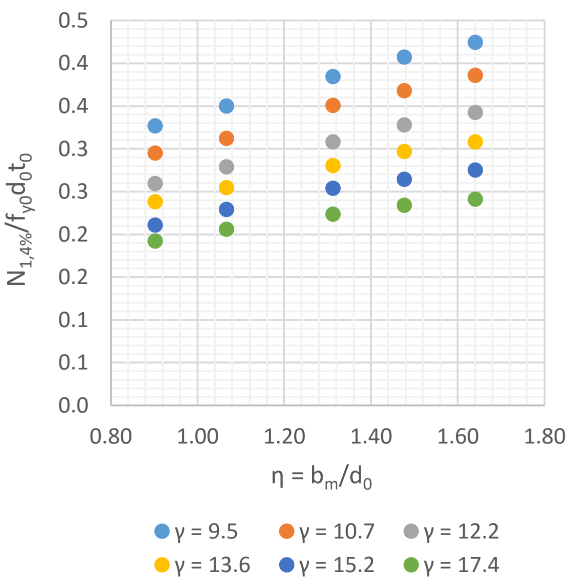

Figure 109: Ultimate load from FEA analysis in the plate load case α_{ip} = 60˚ for d_0 = 1219.2

Table 23: Ultimate load from FEA analysis in the plate load case α_{ip} = 60˚ for d_0 = 1400

d_0 [mm]	b_m [mm]	t_0 [mm]	$N_{1,4\%}$ [N]	ε_{max}	$\gamma = d_0/2t_0$	$\eta = b_m/d_0$	$N_{1,4\%}/f_y d_0 t_0$
1400	1100	64.0	7.95E+06	4.77E-02	10.9	0.79	0.265
		57.2	6.40E+06	4.78E-02	12.2	0.79	0.239
		50.0	4.90E+06	4.62E-02	14.0	0.79	0.209
		45.0	4.08E+06	4.78E-02	15.6	0.79	0.193
		40.0	3.25E+06	4.64E-02	17.5	0.79	0.173
		35.0	2.55E+06	4.61E-02	20.0	0.79	0.155
	1300	64.0	8.40E+06	4.70E-02	10.9	0.93	0.280
		57.2	6.80E+06	4.78E-02	12.2	0.93	0.253
		50.0	5.32E+06	4.89E-02	14.0	0.93	0.227
		45.0	4.32E+06	4.73E-02	15.6	0.93	0.205
		40.0	3.50E+06	4.80E-02	17.5	0.93	0.187
		35.0	2.75E+06	4.73E-02	20.0	0.93	0.168
	1600	64.0	9.30E+06	4.88E-02	10.9	1.14	0.310
		57.2	7.50E+06	4.89E-02	12.2	1.14	0.280
		50.0	5.88E+06	5.03E-02	14.0	1.14	0.251
		45.0	4.80E+06	4.91E-02	15.6	1.14	0.227
		40.0	3.85E+06	4.78E-02	17.5	1.14	0.205
		35.0	2.95E+06	4.41E-02	20.0	1.14	0.180
	1800	64.0	9.75E+06	4.94E-02	10.9	1.29	0.325
		57.2	7.90E+06	5.00E-02	12.2	1.29	0.294
		50.0	6.16E+06	5.06E-02	14.0	1.29	0.263
		45.0	5.04E+06	4.94E-02	15.6	1.29	0.239
		40.0	4.00E+06	4.67E-02	17.5	1.29	0.213
		35.0	3.10E+06	4.45E-02	20.0	1.29	0.189
	2000	64.0	1.02E+07	5.02E-02	10.9	1.43	0.340
		57.2	8.30E+06	5.13E-02	12.2	1.43	0.309
		50.0	6.40E+06	5.00E-02	14.0	1.43	0.273
		45.0	5.25E+06	4.91E-02	15.6	1.43	0.249
		40.0	4.15E+06	4.60E-02	17.5	1.43	0.221
		35.0	3.20E+06	4.33E-02	20.0	1.43	0.195

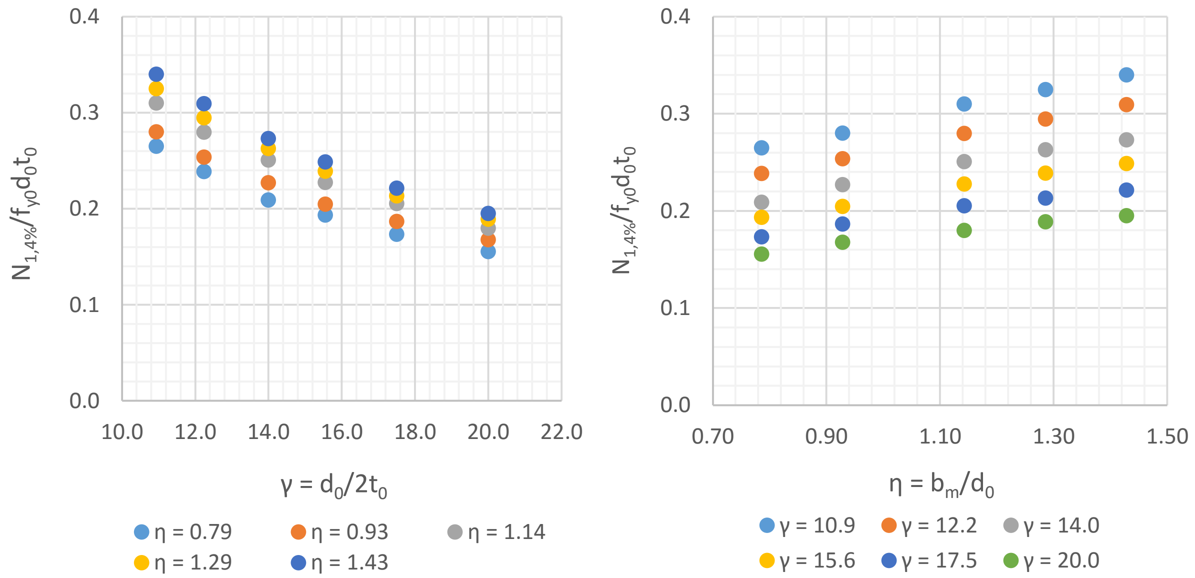

Figure 110: Ultimate load from FEA analysis in the plate load case α_{ip} = 60˚ for d_0 = 1400

E.2 Padeye load case

E.2.1 Constant padeye geometry

Table 24: Ultimate load from FEA analysis in the padeye load case with constant geometry, for $d_0 = 800$

d_0 [mm]	b_m [mm]	t_0 [mm]	$N_{1,4\%}$ [N]	ε_{max}	$\gamma = d_0/2t_0$	$\eta = b_m/d_0$	$N_{1,4\%}/f_y d_0 t_0$
800	1100	64.0	1.56E+07	5.31E-02	6.3	1.38	0.91
		57.2	1.26E+07	4.78E-02	7.0	1.38	0.82
		50.0	9.75E+06	4.55E-02	8.0	1.38	0.73
		45.0	8.16E+06	4.90E-02	8.9	1.38	0.68
		40.0	6.50E+06	4.62E-02	10.0	1.38	0.61
		35.0	5.12E+06	4.69E-02	11.4	1.38	0.55
	1300	64.0	1.70E+07	4.85E-02	6.3	1.63	0.99
		57.2	1.38E+07	4.76E-02	7.0	1.63	0.90
		50.0	1.08E+07	4.85E-02	8.0	1.63	0.81
		45.0	8.88E+06	4.80E-02	8.9	1.63	0.74
		40.0	7.10E+06	4.65E-02	10.0	1.63	0.66
		35.0	5.60E+06	4.73E-02	11.4	1.63	0.60
	1600	64.0	1.92E+07	4.85E-02	6.3	2.00	1.12
		57.2	1.56E+07	4.96E-02	7.0	2.00	1.02
		50.0	1.22E+07	4.83E-02	8.0	2.00	0.91
		45.0	9.96E+06	4.76E-02	8.9	2.00	0.83
		40.0	8.00E+06	4.70E-02	10.0	2.00	0.75
		35.0	6.16E+06	4.38E-02	11.4	2.00	0.66

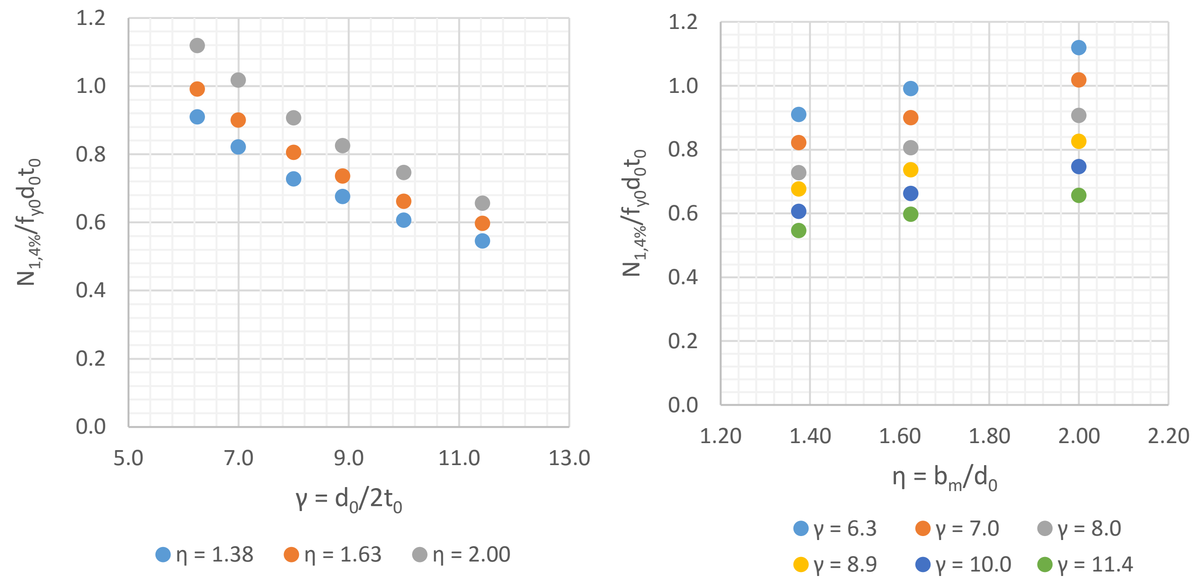

Figure 111: Ultimate load from FEA analysis in the padeye load case with constant geometry, for $d_0 = 800$

Table 25: Ultimate load from FEA analysis in the padeye load case with constant geometry, for d_0 = 900

d_0 [mm]	b_m [mm]	t_0 [mm]	$N_{1,4\%}$ [N]	ε_{max}	$\gamma = d_0/2t_0$	$\eta = b_m/d_0$	$N_{1,4\%}/f_y d_0 t_0$
900	1100	64.0	1.46E+07	4.90E-02	7.0	1.22	0.75
		57.2	1.19E+07	4.86E-02	7.9	1.22	0.69
		50.0	9.15E+06	4.66E-02	9.0	1.22	0.61
		45.0	7.60E+06	4.84E-02	10.0	1.22	0.56
		40.0	6.10E+06	4.77E-02	11.3	1.22	0.51
		35.0	4.80E+06	4.80E-02	12.9	1.22	0.45
	1300	64.0	1.60E+07	4.94E-02	7.0	1.44	0.83
		57.2	1.28E+07	4.65E-02	7.9	1.44	0.74
		50.0	1.01E+07	4.85E-02	9.0	1.44	0.67
		45.0	8.20E+06	4.70E-02	10.0	1.44	0.60
		40.0	6.60E+06	4.70E-02	11.3	1.44	0.55
		35.0	5.12E+06	4.48E-02	12.9	1.44	0.49
	1600	64.0	1.78E+07	4.79E-02	7.0	1.78	0.92
		57.2	1.46E+07	5.07E-02	7.9	1.78	0.85
		50.0	1.13E+07	4.89E-02	9.0	1.78	0.75
		45.0	9.30E+06	5.02E-02	10.0	1.78	0.69
		40.0	7.30E+06	4.53E-02	11.3	1.78	0.61
		35.0	5.68E+06	4.42E-02	12.9	1.78	0.54
	1800	64.0	1.92E+07	5.03E-02	7.0	2.00	1.00
		57.2	1.56E+07	5.04E-02	7.9	2.00	0.90
		50.0	1.21E+07	4.97E-02	9.0	2.00	0.80
		45.0	9.75E+06	4.62E-02	10.0	2.00	0.72
		40.0	7.80E+06	4.53E-02	11.3	2.00	0.65
		35.0	6.00E+06	4.28E-02	12.9	2.00	0.57
	2000	64.0	2.02E+07	4.76E-02	7.0	2.22	1.05
		57.2	1.64E+07	4.80E-02	7.9	2.22	0.95
		50.0	1.28E+07	4.79E-02	9.0	2.22	0.85
		45.0	1.04E+07	4.57E-02	10.0	2.22	0.76
		40.0	8.20E+06	4.34E-02	11.3	2.22	0.68
		35.0	6.32E+06	4.17E-02	12.9	2.22	0.60

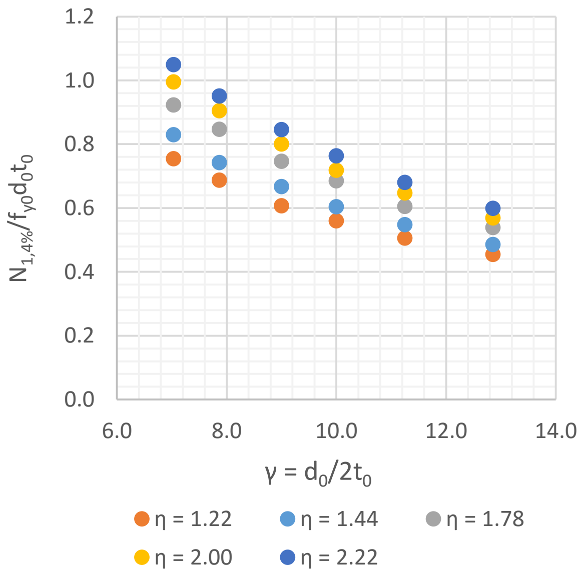

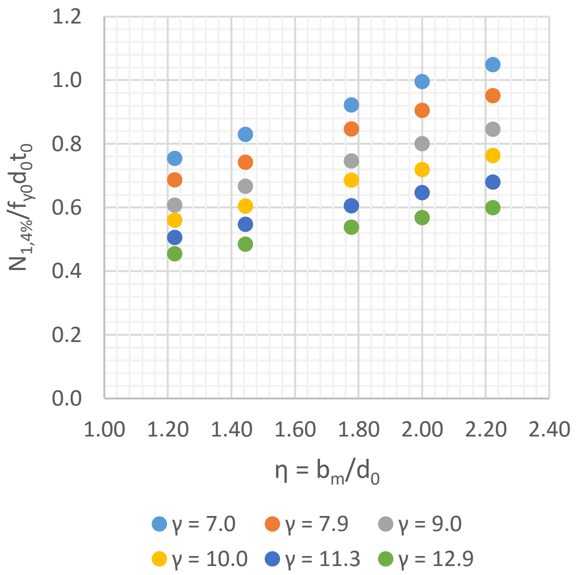

Figure 112: Ultimate load from FEA analysis in the padeye load case with constant geometry, for d_0 = 900

Table 26: Ultimate load from FEA analysis in the padeye load case with constant geometry, for d_0 = 1100

d_0 [mm]	b_m [mm]	t_0 [mm]	$N_{1,4\%}$ [N]	ε_{max}	$\gamma = d_0/2t_0$	$\eta = b_m/d_0$	$N_{1,4\%}/f_y d_0 t_0$
1100	1100	64.0	1.32E+07	4.98E-02	8.6	1.00	0.56
		57.2	1.06E+07	4.82E-02	9.6	1.00	0.50
		50.0	8.25E+06	4.82E-02	11.0	1.00	0.45
		45.0	6.80E+06	4.83E-02	12.2	1.00	0.41
		40.0	5.40E+06	4.61E-02	13.8	1.00	0.37
		35.0	4.27E+06	4.67E-02	15.7	1.00	0.33
	1300	64.0	1.42E+07	4.84E-02	8.6	1.18	0.60
		57.2	1.14E+07	4.72E-02	9.6	1.18	0.54
		50.0	9.00E+06	4.99E-02	11.0	1.18	0.49
		45.0	7.30E+06	4.75E-02	12.2	1.18	0.44
		40.0	5.90E+06	4.79E-02	13.8	1.18	0.40
		35.0	4.55E+06	4.49E-02	15.7	1.18	0.35
	1600	64.0	1.58E+07	4.91E-02	8.6	1.45	0.67
		57.2	1.28E+07	4.97E-02	9.6	1.45	0.61
		50.0	9.90E+06	4.91E-02	11.0	1.45	0.54
		45.0	8.10E+06	4.81E-02	12.2	1.45	0.49
		40.0	6.40E+06	4.51E-02	13.8	1.45	0.43
		35.0	4.90E+06	4.20E-02	15.7	1.45	0.38
	1800	64.0	1.68E+07	4.90E-02	8.6	1.64	0.71
		57.2	1.37E+07	5.03E-02	9.6	1.64	0.65
		50.0	1.05E+07	4.88E-02	11.0	1.64	0.57
		45.0	8.60E+06	4.79E-02	12.2	1.64	0.52
		40.0	6.80E+06	4.53E-02	13.8	1.64	0.46
		35.0	5.18E+06	4.17E-02	15.7	1.64	0.40
	2000	64.0	1.78E+07	4.91E-02	8.6	1.82	0.75
		57.2	1.44E+07	4.97E-02	9.6	1.82	0.68
		50.0	1.11E+07	4.85E-02	11.0	1.82	0.60
		45.0	9.02E+06	4.67E-02	12.2	1.82	0.54
		40.0	7.10E+06	4.37E-02	13.8	1.82	0.48
		35.0	5.39E+06	4.00E-02	15.7	1.82	0.42

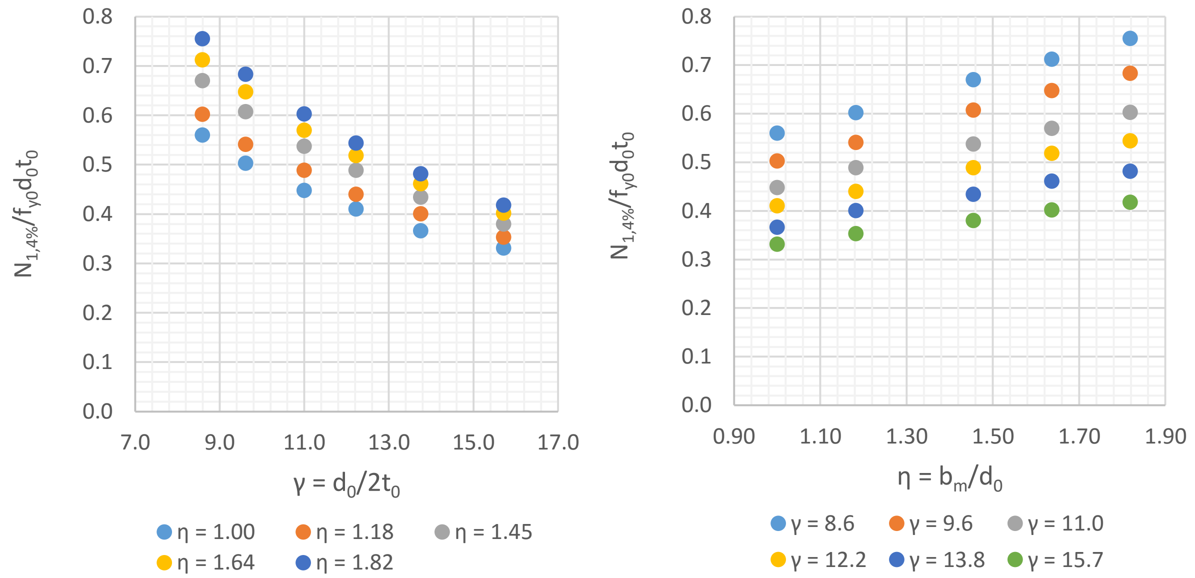

Figure 113: Ultimate load from FEA analysis in the padeye load case with constant geometry, for d_0 = 1100

Table 27: Ultimate load from FEA analysis in the padeye load case with constant geometry, for d_0 = 1219.2

d_0 [mm]	b_m [mm]	t_0 [mm]	$N_{1,4\%}$ [N]	ε_{max}	$\gamma = d_0/2t_0$	$\eta = b_m/d_0$	$N_{1,4\%}/f_y d_0 t_0$
1219.2	1100	64.0	1.23E+07	4.71E-02	9.5	0.90	0.47
		57.2	9.90E+06	4.64E-02	10.7	0.90	0.42
		50.0	7.80E+06	4.83E-02	12.2	0.90	0.38
		45.0	6.40E+06	4.79E-02	13.5	0.90	0.35
		40.0	5.10E+06	4.62E-02	15.2	0.90	0.31
		35.0	3.99E+06	4.51E-02	17.4	0.90	0.28
	1300	64.0	1.34E+07	4.82E-02	9.5	1.07	0.51
		57.2	1.08E+07	4.83E-02	10.7	1.07	0.46
		50.0	8.40E+06	4.84E-02	12.2	1.07	0.41
		45.0	6.90E+06	4.82E-02	13.5	1.07	0.38
		40.0	5.50E+06	4.64E-02	15.2	1.07	0.34
		35.0	4.27E+06	4.44E-02	17.4	1.07	0.30
	1600	64.0	1.48E+07	4.91E-02	9.5	1.31	0.57
		57.2	1.20E+07	4.97E-02	10.7	1.31	0.51
		50.0	9.36E+06	5.05E-02	12.2	1.31	0.46
		45.0	7.60E+06	4.83E-02	13.5	1.31	0.41
		40.0	6.00E+06	4.52E-02	15.2	1.31	0.37
		35.0	4.62E+06	4.27E-02	17.4	1.31	0.32
	1800	64.0	1.58E+07	5.03E-02	9.5	1.48	0.60
		57.2	1.28E+07	5.02E-02	10.7	1.48	0.55
		50.0	9.90E+06	5.03E-02	12.2	1.48	0.48
		45.0	8.00E+06	4.74E-02	13.5	1.48	0.44
		40.0	6.30E+06	4.42E-02	15.2	1.48	0.39
		35.0	4.83E+06	4.14E-02	17.4	1.48	0.34
	2000	64.0	1.66E+07	4.94E-02	9.5	1.64	0.64
		57.2	1.34E+07	5.00E-02	10.7	1.64	0.57
		50.0	1.04E+07	4.88E-02	12.2	1.64	0.51
		45.0	8.40E+06	4.67E-02	13.5	1.64	0.46
		40.0	6.60E+06	4.36E-02	15.2	1.64	0.40
		35.0	5.04E+06	4.04E-02	17.4	1.64	0.35

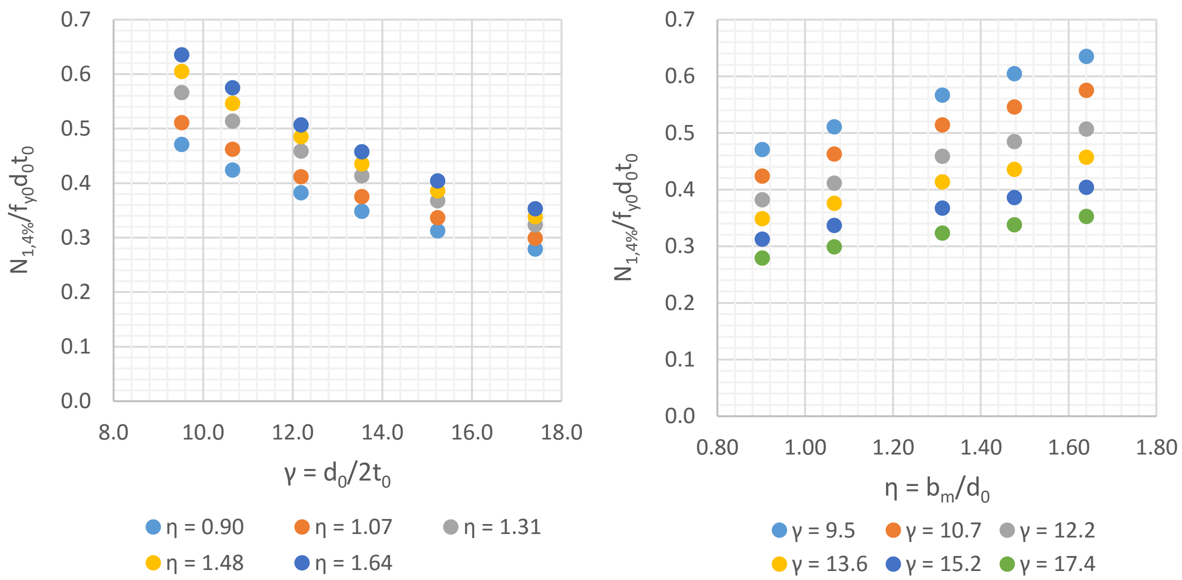

Figure 114: Ultimate load from FEA analysis in the padeye load case with constant geometry, for d_0 = 1219.2

Table 28: Ultimate load from FEA analysis in the padeye load case with constant geometry, for d_0 = 1400

d_0 [mm]	b_m [mm]	t_0 [mm]	$N_{1,4\%}$ [N]	ε_{max}	$\gamma = d_0/2t_0$	$\eta = b_m/d_0$	$N_{1,4\%}/f_y d_0 t_0$
1219.2	1100	64.0	1.14E+07	4.77E-02	10.9	0.79	0.38
		57.2	9.15E+06	4.68E-02	12.2	0.79	0.34
		50.0	7.20E+06	4.84E-02	14.0	0.79	0.31
		45.0	5.90E+06	4.76E-02	15.6	0.79	0.28
		40.0	4.72E+06	4.64E-02	17.5	0.79	0.25
		35.0	3.66E+06	4.41E-02	20.0	0.79	0.22
	1300	64.0	1.22E+07	4.74E-02	10.9	0.93	0.41
		57.2	9.90E+06	4.80E-02	12.2	0.93	0.37
		50.0	7.80E+06	4.99E-02	14.0	0.93	0.33
		45.0	6.30E+06	4.72E-02	15.6	0.93	0.30
		40.0	5.04E+06	4.57E-02	17.5	0.93	0.27
		35.0	3.90E+06	4.33E-02	20.0	0.93	0.24
	1600	64.0	1.36E+07	4.99E-02	10.9	1.14	0.45
		57.2	1.10E+07	4.95E-02	12.2	1.14	0.41
		50.0	8.55E+06	5.02E-02	14.0	1.14	0.36
		45.0	6.90E+06	4.71E-02	15.6	1.14	0.33
		40.0	5.44E+06	4.39E-02	17.5	1.14	0.29
		35.0	4.20E+06	4.16E-02	20.0	1.14	0.26
	1800	64.0	1.44E+07	5.05E-02	10.9	1.29	0.48
		57.2	1.16E+07	4.95E-02	12.2	1.29	0.43
		50.0	9.00E+06	4.97E-02	14.0	1.29	0.38
		45.0	7.30E+06	4.74E-02	15.6	1.29	0.35
		40.0	5.68E+06	4.28E-02	17.5	1.29	0.30
		35.0	4.38E+06	4.04E-02	20.0	1.29	0.27
	2000	64.0	1.52E+07	5.11E-02	10.9	1.43	0.51
		57.2	1.22E+07	4.96E-02	12.2	1.43	0.45
		50.0	9.30E+06	4.72E-02	14.0	1.43	0.40
		45.0	7.60E+06	4.61E-02	15.6	1.43	0.36
		40.0	5.92E+06	4.19E-02	17.5	1.43	0.32
		35.0	4.56E+06	3.94E-02	20.0	1.43	0.28

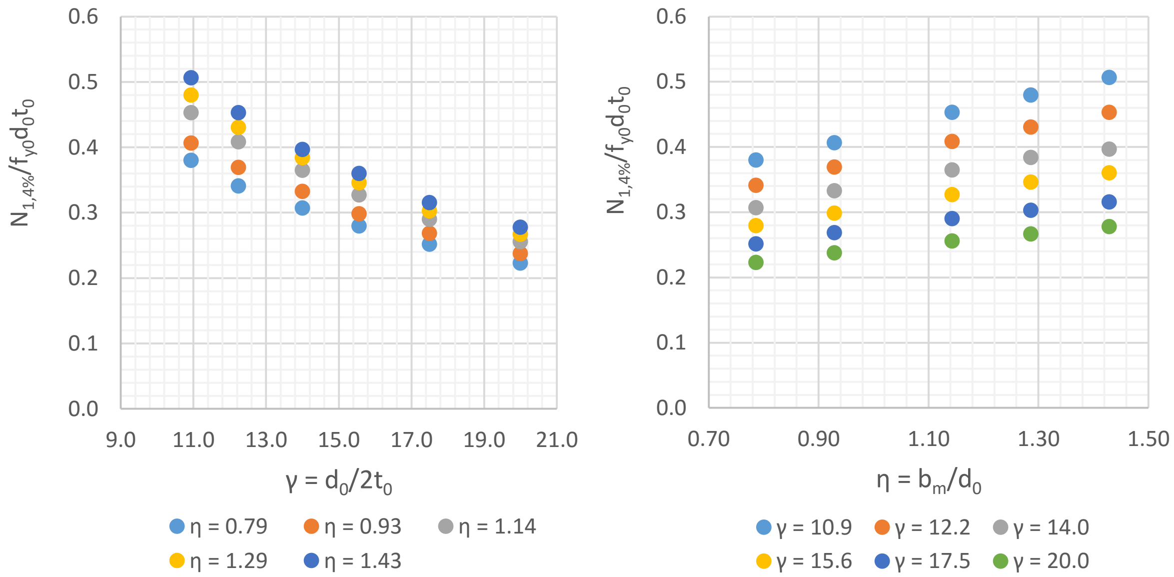

Figure 115: Ultimate load from FEA analysis in the padeye load case with constant geometry, for d_0 = 1400

E.2.2 Variable padeye geometry

Table 29: Ultimate load from FEA analysis in the padeye load case with variable geometry, for $d_0 = 800$

d_0 [mm]	b_m [mm]	t_0 [mm]	$N_{1,4\%}$ [N]	$\gamma=d_0/2t_0$ [-]	$\eta=b_m/d_0$ [-]	$\lambda=b_m/(R_m+h_0)$ [-]	$N_{1,4\%}/f_y d_0 t_0$ [-]
800	1100	64.0	1.38E+07	6.3	1.38	1.38	0.80
		57.2	1.10E+07	7.0	1.38	1.38	0.72
		50.0	8.40E+06	8.0	1.38	1.38	0.63
		45.0	7.00E+06	8.9	1.38	1.38	0.58
		40.0	5.60E+06	10.0	1.38	1.38	0.52
		35.0	4.40E+06	11.4	1.38	1.38	0.47
	1300	64.0	1.70E+07	6.3	1.63	1.63	0.99
		57.2	1.38E+07	7.0	1.63	1.63	0.90
		50.0	1.08E+07	8.0	1.63	1.63	0.81
		45.0	9.00E+06	8.9	1.63	1.63	0.75
		40.0	7.20E+06	10.0	1.63	1.63	0.67
		35.0	5.60E+06	11.4	1.63	1.63	0.60
	1600	64.0	1.66E+07	6.3	2.00	2.00	0.97
		57.2	1.34E+07	7.0	2.00	2.00	0.87
		50.0	1.04E+07	8.0	2.00	2.00	0.78
		45.0	8.40E+06	8.9	2.00	2.00	0.70
		40.0	6.80E+06	10.0	2.00	2.00	0.63
		35.0	5.20E+06	11.4	2.00	2.00	0.55

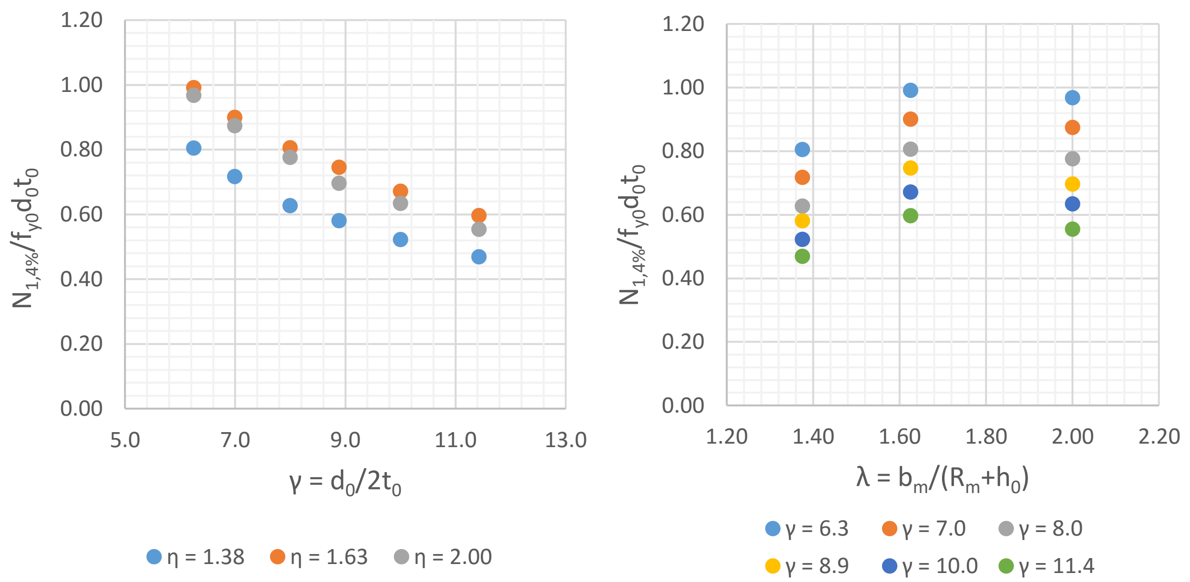

Figure 116: Ultimate load from FEA analysis in the padeye load case with variable geometry, for d0 = 800

Table 30: Ultimate load from FEA analysis in the padeye load case with variable geometry, for d_0 = 900

d_0 [mm]	b_m [mm]	t_0 [mm]	$N_{1,4\%}$ [N]	$\gamma=d_0/2t_0$ [-]	$\eta=b_m/d_0$ [-]	$\lambda=b_m/(R_m+h_0)$ [-]	$N_{1,4\%}/f_y d_0 t_0$ [-]
900	1100	64.0	1.28E+07	7.0	1.22	1.38	0.66
		57.2	1.02E+07	7.9	1.22	1.38	0.59
		50.0	8.00E+06	9.0	1.22	1.38	0.53
		45.0	6.60E+06	10.0	1.22	1.38	0.49
		40.0	5.20E+06	11.3	1.22	1.38	0.43
		35.0	4.20E+06	12.9	1.22	1.38	0.40
	1300	64.0	1.60E+07	7.0	1.44	1.63	0.83
		57.2	1.28E+07	7.9	1.44	1.63	0.74
		50.0	1.00E+07	9.0	1.44	1.63	0.66
		45.0	8.20E+06	10.0	1.44	1.63	0.60
		40.0	6.60E+06	11.3	1.44	1.63	0.55
		35.0	5.20E+06	12.9	1.44	1.63	0.49
	1600	64.0	1.54E+07	7.0	1.78	2.00	0.80
		57.2	1.24E+07	7.9	1.78	2.00	0.72
		50.0	9.60E+06	9.0	1.78	2.00	0.64
		45.0	7.80E+06	10.0	1.78	2.00	0.57
		40.0	6.20E+06	11.3	1.78	2.00	0.51
		35.0	4.80E+06	12.9	1.78	2.00	0.45
	1800	64.0	1.50E+07	7.0	2.00	2.25	0.78
		57.2	1.20E+07	7.9	2.00	2.25	0.70
		50.0	9.40E+06	9.0	2.00	2.25	0.62
		45.0	7.60E+06	10.0	2.00	2.25	0.56
		40.0	6.00E+06	11.3	2.00	2.25	0.50
		35.0	4.60E+06	12.9	2.00	2.25	0.44
	2000	64.0	1.48E+07	7.0	2.22	2.50	0.77
		57.2	1.20E+07	7.9	2.22	2.50	0.70
		50.0	9.20E+06	9.0	2.22	2.50	0.61
		45.0	7.40E+06	10.0	2.22	2.50	0.55
		40.0	6.00E+06	11.3	2.22	2.50	0.50
		35.0	4.60E+06	12.9	2.22	2.50	0.44

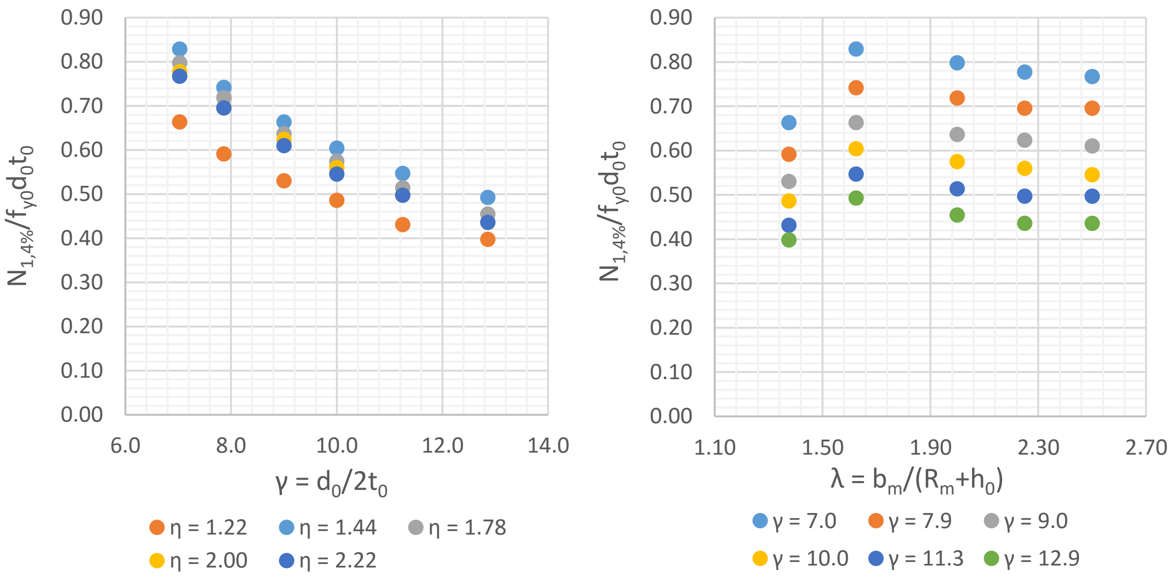

Figure 117: Ultimate load from FEA analysis in the padeye load case with variable geometry, for d0 = 900

Table 31: Ultimate load from FEA analysis in the padeye load case with variable geometry, for d_0 = 1100

d_0 [mm]	b_m [mm]	t_0 [mm]	$N_{1,4\%}$ [N]	$\gamma=d_0/2t_0$ [-]	$\eta=b_m/d_0$ [-]	$\lambda=b_m/(R_m+h_0)$ [-]	$N_{1,4\%}/f_y d_0 t_0$ [-]
1100	1100	64.0	1.14E+07	8.6	1.00	1.38	0.48
		57.2	9.00E+06	9.6	1.00	1.38	0.43
		50.0	7.00E+06	11.0	1.00	1.38	0.38
		45.0	5.80E+06	12.2	1.00	1.38	0.35
		40.0	4.60E+06	13.8	1.00	1.38	0.31
		35.0	3.60E+06	15.7	1.00	1.38	0.28
	1300	64.0	1.42E+07	8.6	1.18	1.63	0.60
		57.2	1.14E+07	9.6	1.18	1.63	0.54
		50.0	9.00E+06	11.0	1.18	1.63	0.49
		45.0	7.40E+06	12.2	1.18	1.63	0.45
		40.0	6.00E+06	13.8	1.18	1.63	0.41
		35.0	4.60E+06	15.7	1.18	1.63	0.36
	1600	64.0	1.36E+07	8.6	1.45	2.00	0.58
		57.2	1.08E+07	9.6	1.45	2.00	0.51
		50.0	8.40E+06	11.0	1.45	2.00	0.46
		45.0	6.80E+06	12.2	1.45	2.00	0.41
		40.0	5.40E+06	13.8	1.45	2.00	0.37
		35.0	4.20E+06	15.7	1.45	2.00	0.33
	1800	64.0	1.32E+07	8.6	1.64	2.25	0.56
		57.2	1.06E+07	9.6	1.64	2.25	0.50
		50.0	8.20E+06	11.0	1.64	2.25	0.45
		45.0	6.60E+06	12.2	1.64	2.25	0.40
		40.0	5.20E+06	13.8	1.64	2.25	0.35
		35.0	4.00E+06	15.7	1.64	2.25	0.31
	2000	64.0	1.30E+07	8.6	1.82	2.50	0.55
		57.2	1.04E+07	9.6	1.82	2.50	0.49
		50.0	8.00E+06	11.0	1.82	2.50	0.43
		45.0	6.60E+06	12.2	1.82	2.50	0.40
		40.0	5.20E+06	13.8	1.82	2.50	0.35
		35.0	4.00E+06	15.7	1.82	2.50	0.31

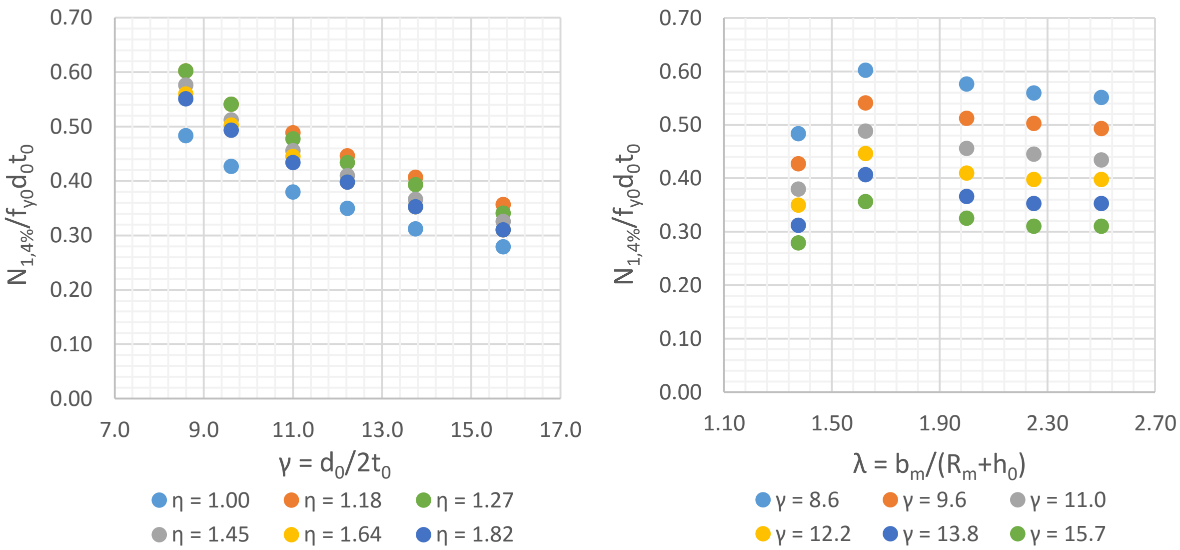

Figure 118: Ultimate load from FEA analysis in the padeye load case with variable geometry, for d0 = 1100

Table 32: Ultimate load from FEA analysis in the padeye load case with variable geometry, for d_0 = 1219.2

d_0 [mm]	b_m [mm]	t_0 [mm]	$N_{1,4\%}$ [N]	$\gamma=d_0/2t_0$ [-]	$\eta=b_m/d_0$ [-]	$\lambda=b_m/(R_m+h_0)$ [-]	$N_{1,4\%}/f_y d_0 t_0$ [-]
1219.2	1100	64.0	1.06E+07	9.5	0.90	1.38	0.41
		57.2	8.60E+06	10.7	0.90	1.38	0.37
		50.0	6.60E+06	12.2	0.90	1.38	0.32
		45.0	5.40E+06	13.5	0.90	1.38	0.29
		40.0	4.40E+06	15.2	0.90	1.38	0.27
		35.0	3.40E+06	17.4	0.90	1.38	0.24
	1300	64.0	1.34E+07	9.5	1.07	1.63	0.51
		57.2	1.08E+07	10.7	1.07	1.63	0.46
		50.0	8.40E+06	12.2	1.07	1.63	0.41
		45.0	7.00E+06	13.5	1.07	1.63	0.38
		40.0	5.60E+06	15.2	1.07	1.63	0.34
		35.0	4.40E+06	17.4	1.07	1.63	0.31
	1600	64.0	1.26E+07	9.5	1.31	2.00	0.48
		57.2	1.02E+07	10.7	1.31	2.00	0.44
		50.0	7.80E+06	12.2	1.31	2.00	0.38
		45.0	6.40E+06	13.5	1.31	2.00	0.35
		40.0	5.20E+06	15.2	1.31	2.00	0.32
		35.0	4.00E+06	17.4	1.31	2.00	0.28
	1800	64.0	1.22E+07	9.5	1.48	2.25	0.47
		57.2	1.00E+07	10.7	1.48	2.25	0.43
		50.0	7.60E+06	12.2	1.48	2.25	0.37
		45.0	6.20E+06	13.5	1.48	2.25	0.34
		40.0	5.00E+06	15.2	1.48	2.25	0.31
		35.0	3.80E+06	17.4	1.48	2.25	0.27
	2000	64.0	1.22E+07	9.5	1.64	2.50	0.47
		57.2	9.80E+06	10.7	1.64	2.50	0.42
		50.0	7.60E+06	12.2	1.64	2.50	0.37
		45.0	6.20E+06	13.5	1.64	2.50	0.34
		40.0	4.80E+06	15.2	1.64	2.50	0.29
		35.0	3.80E+06	17.4	1.64	2.50	0.27

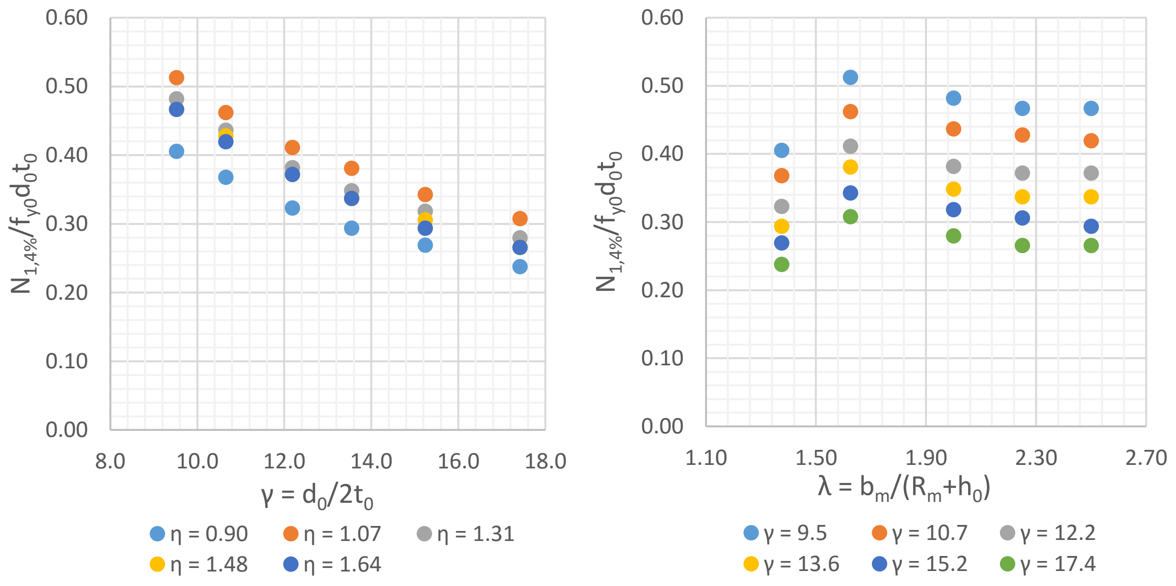

Figure 119: Ultimate load from FEA analysis in the padeye load case with variable geometry, for d0 = 1219.2

Table 33: Ultimate load from FEA analysis in the padeye load case with variable geometry, for d_0 = 1400

d_0 [mm]	b_m [mm]	t_0 [mm]	$N_{1,4\%}$ [N]	$\gamma=d_0/2t_0$ [-]	$\eta=b_m/d_0$ [-]	$\lambda=b_m/(R_m+h_0)$ [-]	$N_{1,4\%}/f_y d_0 t_0$ [-]
1400	1100	64.0	9.80E+06	10.9	0.79	1.38	0.33
		57.2	8.00E+06	12.2	0.79	1.38	0.30
		50.0	6.20E+06	14.0	0.79	1.38	0.26
		45.0	5.00E+06	15.6	0.79	1.38	0.24
		40.0	4.00E+06	17.5	0.79	1.38	0.21
		35.0	3.20E+06	20.0	0.79	1.38	0.19
	1300	64.0	1.22E+07	10.9	0.93	1.63	0.41
		57.2	1.00E+07	12.2	0.93	1.63	0.37
		50.0	7.80E+06	14.0	0.93	1.63	0.33
		45.0	6.40E+06	15.6	0.93	1.63	0.30
		40.0	5.20E+06	17.5	0.93	1.63	0.28
		35.0	4.00E+06	20.0	0.93	1.63	0.24
	1600	64.0	1.16E+07	10.9	1.14	2.00	0.39
		57.2	9.20E+06	12.2	1.14	2.00	0.34
		50.0	7.20E+06	14.0	1.14	2.00	0.31
		45.0	5.80E+06	15.6	1.14	2.00	0.27
		40.0	4.60E+06	17.5	1.14	2.00	0.25
		35.0	3.60E+06	20.0	1.14	2.00	0.22
	1800	64.0	1.12E+07	10.9	1.29	2.25	0.37
		57.2	9.00E+06	12.2	1.29	2.25	0.34
		50.0	7.00E+06	14.0	1.29	2.25	0.30
		45.0	5.80E+06	15.6	1.29	2.25	0.27
		40.0	4.60E+06	17.5	1.29	2.25	0.25
		35.0	3.60E+06	20.0	1.29	2.25	0.22
	2000	64.0	1.10E+07	10.9	1.43	2.50	0.37
		57.2	9.00E+06	12.2	1.43	2.50	0.34
		50.0	7.00E+06	14.0	1.43	2.50	0.30
		45.0	5.60E+06	15.6	1.43	2.50	0.27
		40.0	4.40E+06	17.5	1.43	2.50	0.23
		35.0	3.40E+06	20.0	1.43	2.50	0.21

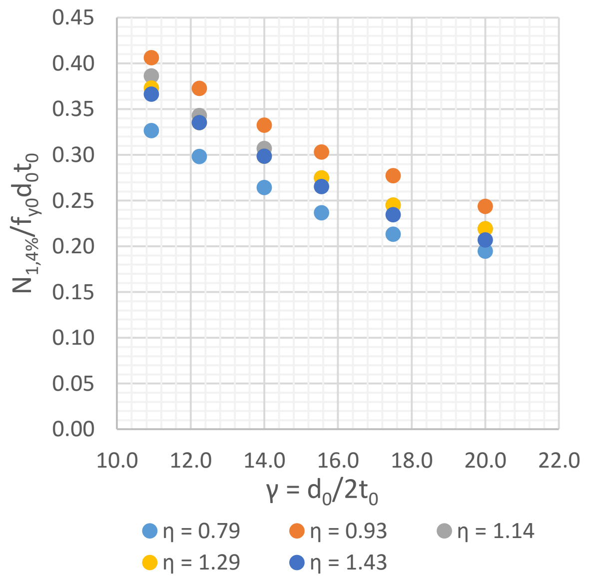

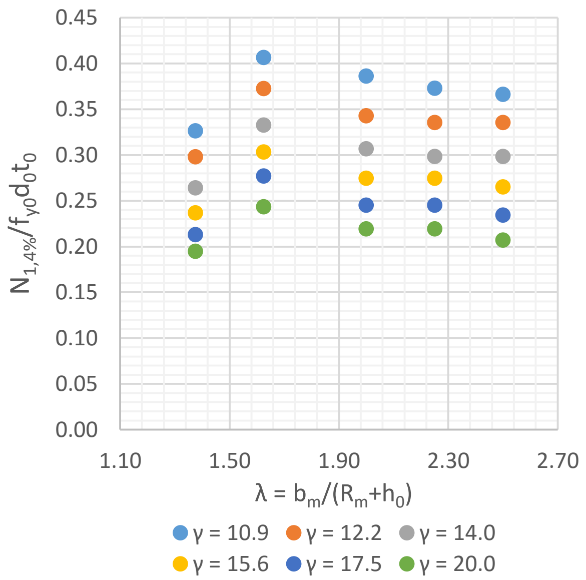

Figure 120: Ultimate load from FEA analysis in the padeye load case with variable geometry, for d0 = 1400

Appendix F Post-processing FEA results

F.1 Matlab curve fitting tool

In order to determine an equation that described the data, Matlab curve fitting uses the coefficient of determination. This coefficient, denoted as R^2, is a number that indicates how well the statistical model fits the data. The value of R^2 varies between 0 and 1, where 0 indicates that the data is not fit at all and 1 indicates that the data is fit perfectly. The equation of R^2 is given in (13.1). In this equation, y_i is the observed data at point i and f_i is the determined data at point i from the curve. The value ẏ is the mean value following the data.

$$R^2 = 1 - \frac{SS_{res}}{SS_{tot}} = 1 - \frac{\sum_i (y_i - f_i)^2}{\sum_i (y_i - \bar{y})^2}; \quad with: \bar{y} = \frac{1}{n}\sum_{i=1}^{n} y_i \tag{13.1}$$

The deviation of the curve with respect to the data is denoted as the Root Mean Squared Error (RMSE). This RMSE is given below:

$$RMSE = \sqrt{\frac{1}{n}\sum_{i=1}^{n}(y_i - f_i)^2} \tag{13.2}$$

```
A=importdata('Results.txt');
gamma = A(:,1);
eta = A(:,2);
Force = A(:,3);

plot3(gamma,eta,Force,'.-')

tri = delaunay(gamma,eta);
plot(gamma,eta,'.-')

[r,c] = size(tri);
disp(r)

h = trisurf(tri,gamma,eta,Force);
axis vis3d
%axis off
l = light('Position',[-50 -15 29]);
%set(gca,'CameraPosition',[208 -50 7687])
lighting phong
shading interp
colorbar EastOutside

cftool
```

Figure 121: Matlab script of the curve fitting tool

F.2 Plate load case

F.2.1 Force angle $\alpha_{ip} = 90^{\circ}$

Table 34: Comparison between FEA data and engineering tool in the plate load case ($\alpha_{ip} = 90^{\circ}$) for $d_0 = 800$

d_0 [mm]	b_m [mm]	t_0 [mm]	$\gamma = d_0/2t_0$ [-]	$\eta = b_m/d_0$ [-]	$N_{1,4\%}$ [N] FEM	$N_{1,4\%}$ [N] Eng. tool	Difference [%]
800	1100	64.0	6.25	1.38	1.32E+07	1.30E+07	1.4
		57.2	6.99	1.38	1.08E+07	1.04E+07	3.5
		50.0	8.00	1.38	8.25E+06	7.98E+06	3.3
		45.0	8.89	1.38	6.82E+06	6.47E+06	5.1
		40.0	10.00	1.38	5.50E+06	5.12E+06	6.9
		35.0	11.43	1.38	4.30E+06	3.93E+06	8.7
	1300	64.0	6.25	1.63	1.46E+07	1.44E+07	1.4
		57.2	6.99	1.63	1.18E+07	1.15E+07	2.4
		50.0	8.00	1.63	9.12E+06	8.82E+06	3.3
		45.0	8.89	1.63	7.48E+06	7.15E+06	4.4
		40.0	10.00	1.63	6.00E+06	5.66E+06	5.6
		35.0	11.43	1.63	4.70E+06	4.34E+06	7.6
	1600	64.0	6.25	2.00	1.72E+07	1.64E+07	4.4
		57.2	6.99	2.00	1.40E+07	1.32E+07	6.0
		50.0	8.00	2.00	1.10E+07	1.01E+07	8.0
		45.0	8.89	2.00	9.02E+06	8.18E+06	9.4
		40.0	10.00	2.00	7.40E+06	6.47E+06	12.6
		35.0	11.43	2.00	5.90E+06	4.96E+06	15.9

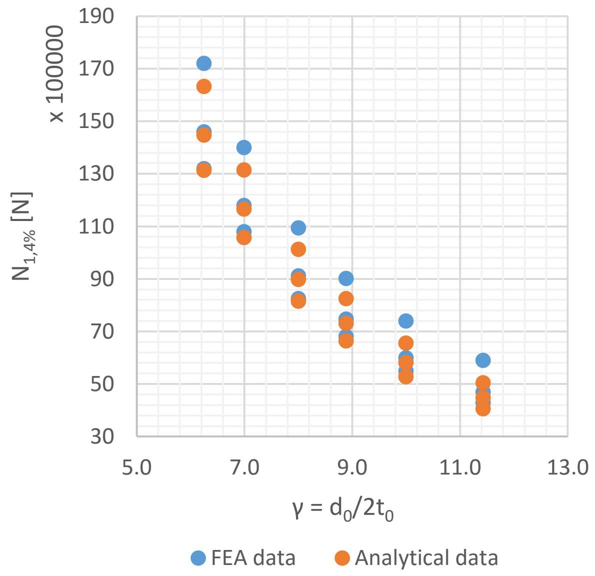

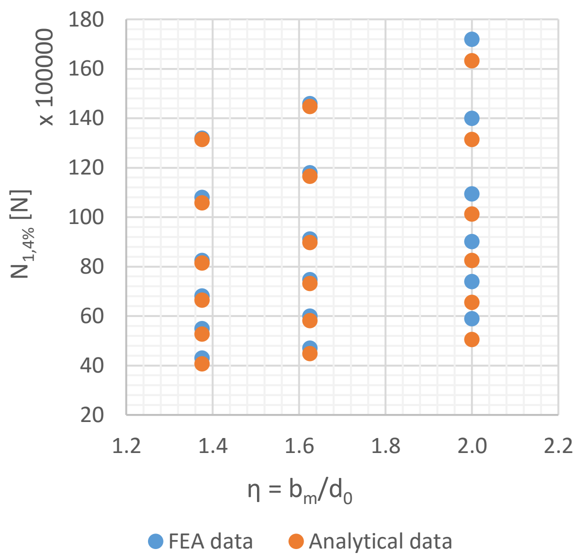

Figure 122: Comparison between FEA data and engineering tool in the plate load case ($\alpha_{ip} = 90^{\circ}$) for $d_0 = 800$

Table 35: Comparison between FEA data and engineering tool in the plate load case (α_{ip} = 90˚) for d_0 = 900

d_0 [mm]	b_m [mm]	t_0 [mm]	$\gamma = d_0/2t_0$ [-]	$\eta = b_m/d_0$ [-]	$N_{1,4\%}$ [N] FEM	$N_{1,4\%}$ [N] Eng. tool	Difference [%]
900	1100	64.0	7.03	1.22	1.24E+07	1.22E+07	1.5
		57.2	7.87	1.22	1.01E+07	9.77E+06	2.8
		50.0	9.00	1.22	7.80E+06	7.48E+06	4.1
		45.0	10.00	1.22	6.40E+06	6.07E+06	5.2
		40.0	11.25	1.22	5.04E+06	4.80E+06	4.8
		35.0	12.86	1.22	3.96E+06	3.68E+06	7.1
	1300	64.0	7.03	1.44	1.36E+07	1.34E+07	1.3
		57.2	7.87	1.44	1.10E+07	1.07E+07	1.9
		50.0	9.00	1.44	8.55E+06	8.23E+06	3.8
		45.0	10.00	1.44	7.00E+06	6.67E+06	4.7
		40.0	11.25	1.44	5.52E+06	5.28E+06	4.4
		35.0	12.86	1.44	4.32E+06	4.05E+06	6.3
	1600	64.0	7.03	1.78	1.54E+07	1.53E+07	0.9
		57.2	7.87	1.78	1.25E+07	1.22E+07	1.9
		50.0	9.00	1.78	9.75E+06	9.35E+06	4.1
		45.0	10.00	1.78	7.90E+06	7.58E+06	4.0
		40.0	11.25	1.78	6.32E+06	6.00E+06	5.1
		35.0	12.86	1.78	4.86E+06	4.60E+06	5.4
	1800	64.0	7.03	2.00	1.66E+07	1.65E+07	0.7
		57.2	7.87	2.00	1.34E+07	1.32E+07	1.2
		50.0	9.00	2.00	1.04E+07	1.01E+07	2.5
		45.0	10.00	2.00	8.50E+06	8.19E+06	3.7
		40.0	11.25	2.00	6.72E+06	6.48E+06	3.6
		35.0	12.86	2.00	5.18E+06	4.97E+06	4.1
	2000	64.0	7.03	2.22	1.96E+07	1.77E+07	9.7
		57.2	7.87	2.22	1.49E+07	1.42E+07	4.6
		50.0	9.00	2.22	1.17E+07	1.08E+07	7.3
		45.0	10.00	2.22	9.72E+06	8.79E+06	9.5
		40.0	11.25	2.22	7.90E+06	6.96E+06	11.9
		35.0	12.86	2.22	6.24E+06	5.33E+06	14.5

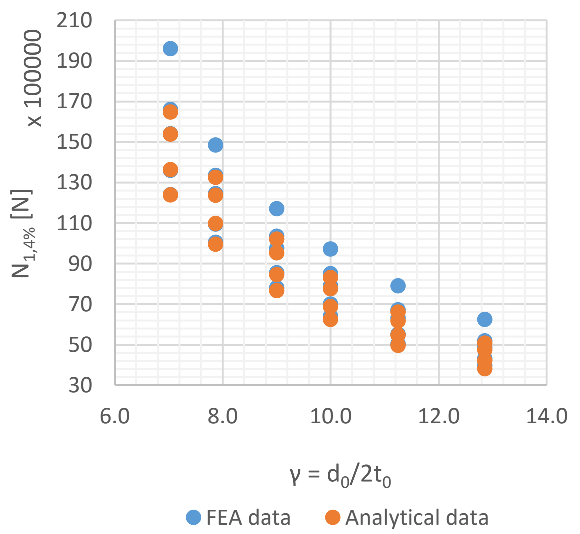

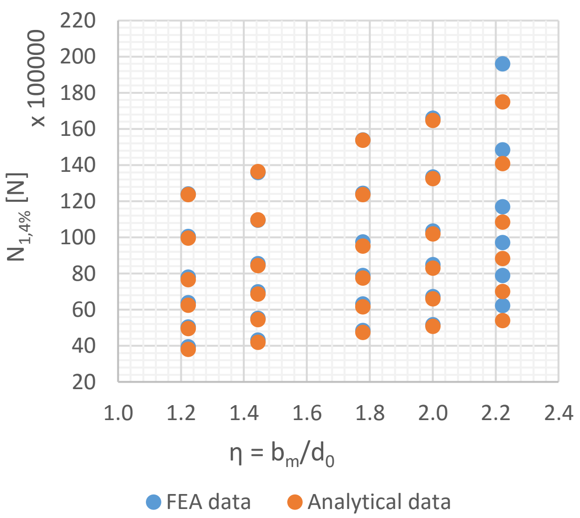

Figure 123: Comparison between FEA data and engineering tool in the plate load case (α_{ip} = 90˚) for d_0 = 900

Table 36: Comparison between FEA data and engineering tool in the plate load case (α_{ip} = 90˚) for d_0 = 1100

d_0 [mm]	b_m [mm]	t_0 [mm]	$\gamma = d_0/2t_0$ [-]	$\eta = b_m/d_0$ [-]	$N_{1,4\%}$ [N] FEM	$N_{1,4\%}$ [N] Eng. tool	Difference [%]
1100	1100	64.0	8.6	1.00	1.11E+07	1.10E+07	0.7
		57.2	9.6	1.00	8.85E+06	8.82E+06	0.4
		50.0	11.0	1.00	6.90E+06	6.75E+06	2.2
		45.0	12.2	1.00	5.70E+06	5.47E+06	4.0
		40.0	13.8	1.00	4.56E+06	4.33E+06	5.1
		35.0	15.7	1.00	3.55E+06	3.32E+06	6.6
	1300	64.0	8.6	1.18	1.20E+07	1.20E+07	-0.2
		57.2	9.6	1.18	9.75E+06	9.62E+06	1.4
		50.0	11.0	1.18	7.50E+06	7.36E+06	1.9
		45.0	12.2	1.18	6.20E+06	5.97E+06	3.7
		40.0	13.8	1.18	4.88E+06	4.72E+06	3.3
		35.0	15.7	1.18	3.80E+06	3.62E+06	4.8
	1600	64.0	8.6	1.45	1.37E+07	1.35E+07	0.9
		57.2	9.6	1.45	1.10E+07	1.08E+07	1.2
		50.0	11.0	1.45	8.47E+06	8.28E+06	2.2
		45.0	12.2	1.45	6.90E+06	6.71E+06	2.7
		40.0	13.8	1.45	5.52E+06	5.31E+06	3.8
		35.0	15.7	1.45	4.25E+06	4.07E+06	4.2
	1800	64.0	8.6	1.64	1.46E+07	1.45E+07	0.2
		57.2	9.6	1.64	1.17E+07	1.16E+07	0.7
		50.0	11.0	1.64	9.02E+06	8.89E+06	1.4
		45.0	12.2	1.64	7.40E+06	7.21E+06	2.6
		40.0	13.8	1.64	5.84E+06	5.70E+06	2.3
		35.0	15.7	1.64	4.44E+06	4.37E+06	1.5
	2000	64.0	8.6	1.82	1.55E+07	1.55E+07	-0.4
		57.2	9.6	1.82	1.25E+07	1.24E+07	0.2
		50.0	11.0	1.82	9.60E+06	9.51E+06	1.0
		45.0	12.2	1.82	7.80E+06	7.71E+06	1.2
		40.0	13.8	1.82	6.09E+06	6.10E+06	-0.1
		35.0	15.7	1.82	4.68E+06	4.67E+06	0.1

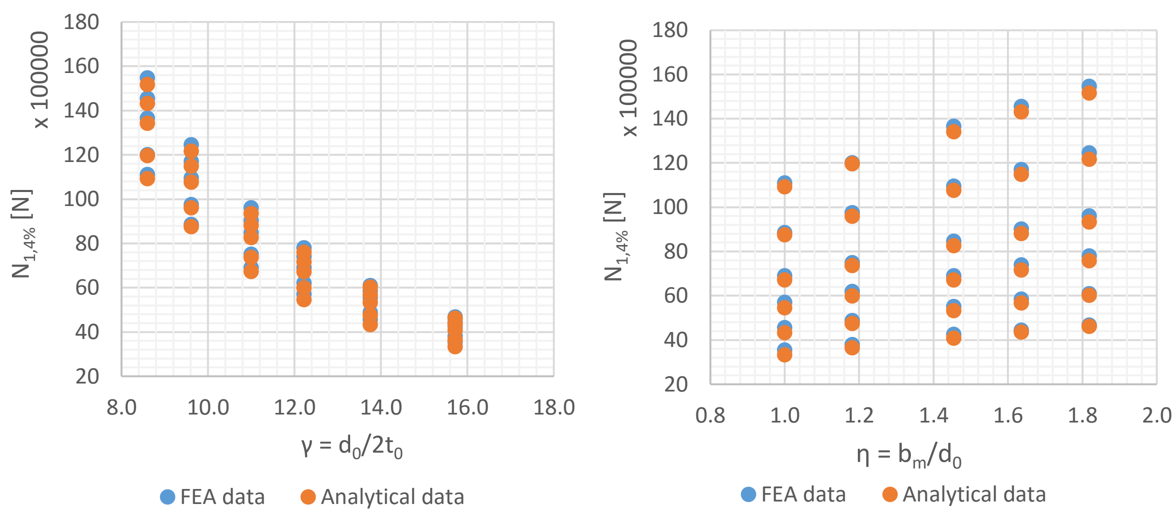

Figure 124: Comparison between FEA data and engineering tool in the plate load case (α_{ip} = 90˚) for d_0 = 1100

Table 37: Comparison between FEA data and engineering tool in the plate load case (α_{ip} = 90˚) for d_0 = 1219.2

d_0 [mm]	b_m [mm]	t_0 [mm]	$\gamma = d_0/2t_0$ [-]	$\eta = b_m/d_0$ [-]	$N_{1,4\%}$ [N] FEM	$N_{1,4\%}$ [N] Eng. tool	Difference [%]
1219.2	1100	64.0	9.53	0.90	1.04E+07	1.05E+07	-1.4
		57.2	10.66	0.90	8.40E+06	8.40E+06	0.1
		50.0	12.19	0.90	6.50E+06	6.42E+06	1.2
		45.0	13.55	0.90	5.36E+06	5.21E+06	2.8
		40.0	15.24	0.90	4.26E+06	4.12E+06	3.3
		35.0	17.42	0.90	3.35E+06	3.16E+06	5.8
	1300	64.0	9.53	1.07	1.13E+07	1.14E+07	-1.3
		57.2	10.66	1.07	9.12E+06	9.12E+06	0.0
		50.0	12.19	1.07	7.10E+06	6.98E+06	1.7
		45.0	13.55	1.07	5.76E+06	5.66E+06	1.8
		40.0	15.24	1.07	4.62E+06	4.47E+06	3.2
		35.0	17.42	1.07	3.60E+06	3.43E+06	4.8
	1600	64.0	9.53	1.31	1.28E+07	1.28E+07	-0.1
		57.2	10.66	1.31	1.03E+07	1.02E+07	1.1
		50.0	12.19	1.31	7.90E+06	7.81E+06	1.2
		45.0	13.55	1.31	6.48E+06	6.33E+06	2.3
		40.0	15.24	1.31	5.16E+06	5.01E+06	3.0
		35.0	17.42	1.31	3.95E+06	3.84E+06	2.9
	1800	64.0	9.53	1.48	1.35E+07	1.37E+07	-1.2
		57.2	10.66	1.48	1.10E+07	1.09E+07	0.2
		50.0	12.19	1.48	8.40E+06	8.36E+06	0.4
		45.0	13.55	1.48	6.86E+06	6.78E+06	1.2
		40.0	15.24	1.48	5.39E+06	5.36E+06	0.5
		35.0	17.42	1.48	4.14E+06	4.11E+06	0.7
	2000	64.0	9.53	1.64	1.43E+07	1.46E+07	-2.2
		57.2	10.66	1.64	1.16E+07	1.17E+07	-0.9
		50.0	12.19	1.64	8.91E+06	8.92E+06	-0.1
		45.0	13.55	1.64	7.20E+06	7.23E+06	-0.4
		40.0	15.24	1.64	5.67E+06	5.72E+06	-0.8
		35.0	17.42	1.64	4.32E+06	4.38E+06	-1.4

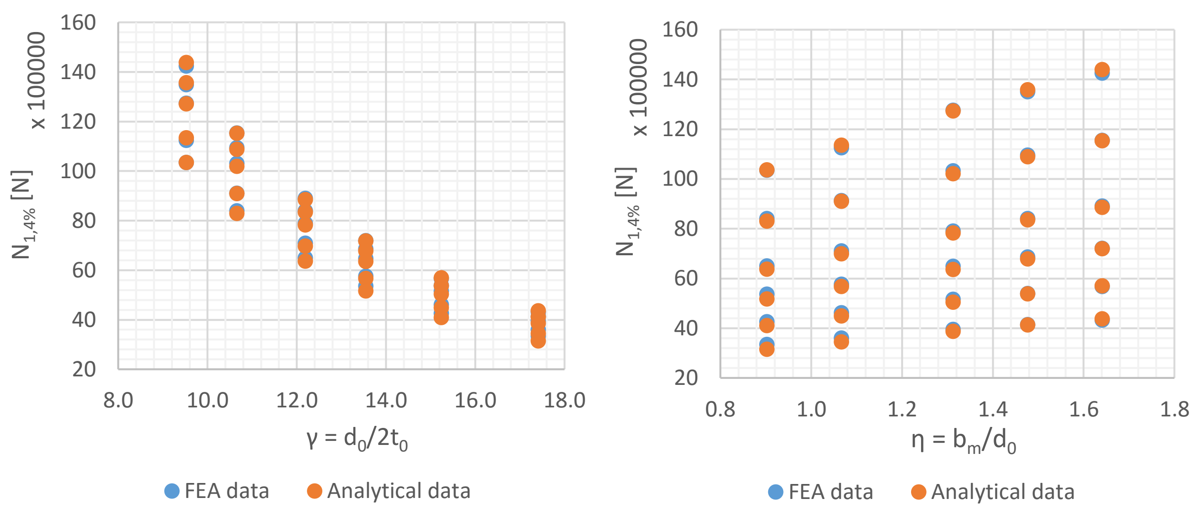

Figure 125: Comparison between FEA data and engineering tool in the plate load case (α_{ip} = 90˚) for d_0 = 1219.2

Table 38: Comparison between FEA data and engineering tool in the plate load case (α_{ip} = 90˚) for d_0 = 1400

d_0 [mm]	b_m [mm]	t_0 [mm]	$\gamma = d_0/2t_0$ [-]	$\eta = b_m/d_0$ [-]	$N_{1,4\%}$ [N] FEM	$N_{1,4\%}$ [N] Eng. tool	Difference [%]
1400	1100	64.0	10.9	0.79	9.60E+06	9.87E+06	-2.8
		57.2	12.2	0.79	7.80E+06	7.89E+06	-1.2
		50.0	14.0	0.79	6.00E+06	6.04E+06	-0.6
		45.0	15.6	0.79	4.90E+06	4.89E+06	0.1
		40.0	17.5	0.79	3.90E+06	3.87E+06	0.8
		35.0	20.0	0.79	3.05E+06	2.97E+06	2.8
	1300	64.0	10.9	0.93	1.04E+07	1.07E+07	-3.0
		57.2	12.2	0.93	8.40E+06	8.52E+06	-1.5
		50.0	14.0	0.93	6.50E+06	6.52E+06	-0.3
		45.0	15.6	0.93	5.30E+06	5.29E+06	0.3
		40.0	17.5	0.93	4.26E+06	4.18E+06	1.9
		35.0	20.0	0.93	3.30E+06	3.20E+06	2.9
	1600	64.0	10.9	1.14	1.16E+07	1.18E+07	-2.5
		57.2	12.2	1.14	9.45E+06	9.47E+06	-0.2
		50.0	14.0	1.14	7.30E+06	7.25E+06	0.8
		45.0	15.6	1.14	5.95E+06	5.87E+06	1.3
		40.0	17.5	1.14	4.70E+06	4.64E+06	1.2
		35.0	20.0	1.14	3.60E+06	3.56E+06	1.1
	1800	64.0	10.9	1.29	1.23E+07	1.26E+07	-2.7
		57.2	12.2	1.29	9.90E+06	1.01E+07	-2.0
		50.0	14.0	1.29	7.70E+06	7.73E+06	-0.4
		45.0	15.6	1.29	6.23E+06	6.27E+06	-0.6
		40.0	17.5	1.29	4.92E+06	4.95E+06	-0.7
		35.0	20.0	1.29	3.77E+06	3.80E+06	-0.7
	2000	64.0	10.9	1.43	1.31E+07	1.34E+07	-2.8
		57.2	12.2	1.43	1.05E+07	1.07E+07	-2.7
		50.0	14.0	1.43	8.00E+06	8.21E+06	-2.6
		45.0	15.6	1.43	6.51E+06	6.66E+06	-2.3
		40.0	17.5	1.43	5.10E+06	5.26E+06	-3.2
		35.0	20.0	1.43	3.95E+06	4.03E+06	-2.1

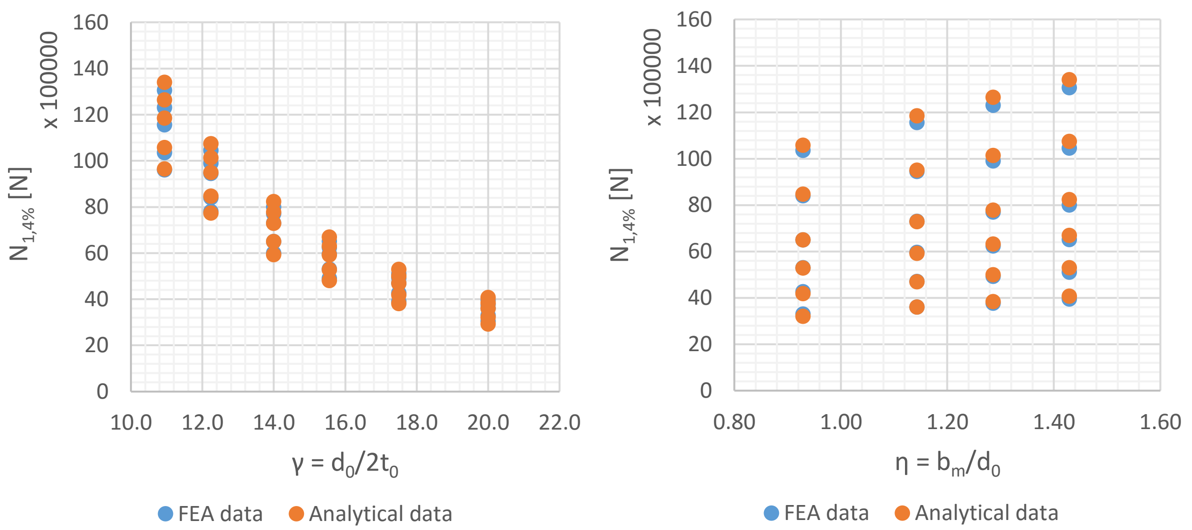

Figure 126: Comparison between FEA data and engineering tool in the plate load case (α_{ip} = 90˚) for d_0 = 1400

F.2.2 Force angle α = 60˚

Table 39: Comparison between FEA data and engineering tool in the plate load case (α_{ip} = 60˚) for d_0 = 800

d_0 [mm]	b_m [mm]	t_0 [mm]	$\gamma = d_0/2t_0$ [-]	$\eta = b_m/d_0$ [-]	$N_{1,4\%}$ [N] FEM	$N_{1,4\%}$ [N] Eng. tool	Difference [%]
800	1100	64.0	6.3	1.38	1.10E+07	1.05E+07	4.2
		57.2	7.0	1.38	8.64E+06	8.40E+06	2.8
		50.0	8.0	1.38	6.70E+06	6.43E+06	4.0
		45.0	8.9	1.38	5.46E+06	5.22E+06	4.5
		40.0	10.0	1.38	4.38E+06	4.13E+06	5.8
		35.0	11.4	1.38	3.40E+06	3.16E+06	6.9
	1300	64.0	6.3	1.63	1.17E+07	1.16E+07	0.9
		57.2	7.0	1.63	9.36E+06	9.28E+06	0.8
		50.0	8.0	1.63	7.20E+06	7.11E+06	1.3
		45.0	8.9	1.63	5.92E+06	5.76E+06	2.6
		40.0	10.0	1.63	4.74E+06	4.56E+06	3.8
		35.0	11.4	1.63	3.70E+06	3.50E+06	5.5
	1600	64.0	6.3	2.00	1.32E+07	1.33E+07	-0.4
		57.2	7.0	2.00	1.07E+07	1.06E+07	0.5
		50.0	8.0	2.00	8.30E+06	8.12E+06	2.1
		45.0	8.9	2.00	6.93E+06	6.59E+06	4.9
		40.0	10.0	2.00	5.60E+06	5.21E+06	6.9
		35.0	11.4	2.00	4.44E+06	4.00E+06	10.0
	1800	64.0	6.3	2.25	1.39E+07	1.44E+07	-3.1
		57.2	7.0	2.25	1.12E+07	1.15E+07	-2.6
		50.0	8.0	2.25	8.91E+06	8.80E+06	1.2
		45.0	8.9	2.25	7.29E+06	7.14E+06	2.1
		40.0	10.0	2.25	5.92E+06	5.65E+06	4.6
		35.0	11.4	2.25	4.68E+06	4.33E+06	7.5
	2000	64.0	6.3	2.50	1.45E+07	1.55E+07	-7.0
		57.2	7.0	2.50	1.19E+07	1.24E+07	-4.0
		50.0	8.0	2.50	9.35E+06	9.48E+06	-1.3
		45.0	8.9	2.50	7.70E+06	7.69E+06	0.2
		40.0	10.0	2.50	6.24E+06	6.08E+06	2.5
		35.0	11.4	2.50	4.90E+06	4.66E+06	4.8

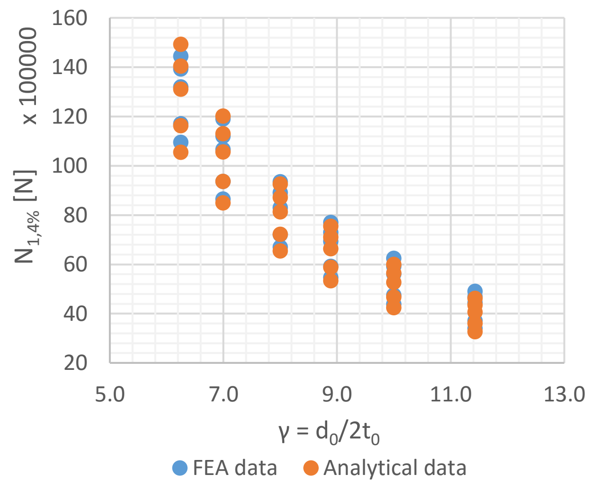

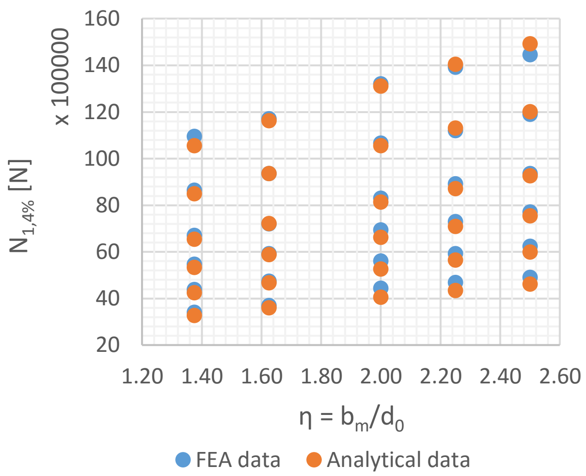

Figure 127: Comparison between FEA data and engineering tool in the plate load case (α_{ip} = 60˚) for d_0 = 800

Table 40: Comparison between FEA data and engineering tool in the plate load case (α_{ip} = 60˚) for d_0 = 900

d_0 [mm]	**b_m [mm]**	**t_0 [mm]**	**$\gamma = d_0/2t_0$ [-]**	**$\eta = b_m/d_0$ [-]**	**$N_{1,4\%}$ [N] FEM**	**$N_{1,4\%}$ [N] Eng. tool**	**Difference [%]**
900	1100	64.0	7.0	1.22	1.02E+07	9.84E+06	3.6
		57.2	7.9	1.22	8.10E+06	7.87E+06	2.8
		50.0	9.0	1.22	6.20E+06	6.03E+06	2.8
		45.0	10.0	1.22	5.11E+06	4.89E+06	4.4
		40.0	11.3	1.22	4.08E+06	3.87E+06	5.2
		35.0	12.9	1.22	3.20E+06	2.96E+06	7.4
	1300	64.0	7.0	1.44	1.10E+07	1.08E+07	1.2
		57.2	7.9	1.44	8.76E+06	8.66E+06	1.2
		50.0	9.0	1.44	6.70E+06	6.63E+06	1.1
		45.0	10.0	1.44	5.53E+06	5.38E+06	2.8
		40.0	11.3	1.44	4.38E+06	4.25E+06	2.9
		35.0	12.9	1.44	3.45E+06	3.26E+06	5.5
	1600	64.0	7.0	1.78	1.22E+07	1.23E+07	-1.2
		57.2	7.9	1.78	9.72E+06	9.84E+06	-1.2
		50.0	9.0	1.78	7.60E+06	7.53E+06	0.9
		45.0	10.0	1.78	6.16E+06	6.11E+06	0.8
		40.0	11.3	1.78	4.92E+06	4.83E+06	1.8
		35.0	12.9	1.78	3.85E+06	3.71E+06	3.8
	1800	64.0	7.0	2.00	1.28E+07	1.33E+07	-4.2
		57.2	7.9	2.00	1.03E+07	1.06E+07	-3.0
		50.0	9.0	2.00	8.00E+06	8.14E+06	-1.7
		45.0	10.0	2.00	6.56E+06	6.60E+06	-0.6
		40.0	11.3	2.00	5.25E+06	5.22E+06	0.6
		35.0	12.9	2.00	4.02E+06	4.00E+06	0.5
	2000	64.0	7.0	2.22	1.37E+07	1.43E+07	-4.5
		57.2	7.9	2.22	1.11E+07	1.14E+07	-2.8
		50.0	9.0	2.22	8.80E+06	8.74E+06	0.7
		45.0	10.0	2.22	7.29E+06	7.09E+06	2.8
		40.0	11.3	2.22	5.92E+06	5.61E+06	5.3
		35.0	12.9	2.22	4.68E+06	4.30E+06	8.2

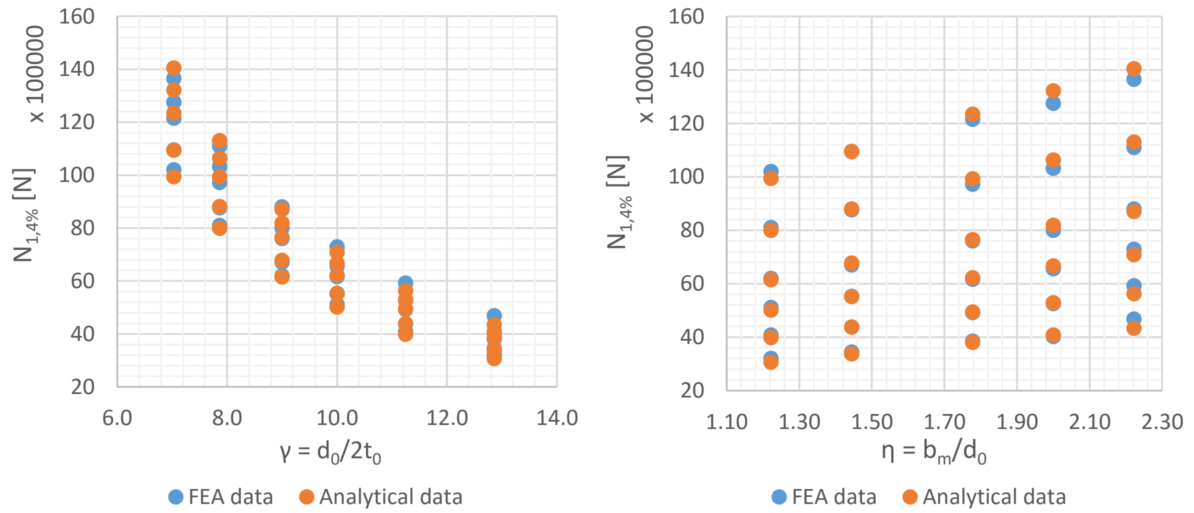

Figure 128: Comparison between FEA data and engineering tool in the plate load case (α_{ip} = 60˚) for d_0 = 900

Table 41: Comparison between FEA data and engineering tool in the plate load case (α_{ip} = 60˚) for d_0 = 1100

d_0 [mm]	b_m [mm]	t_0 [mm]	$\gamma = d_0/2t_0$ [-]	$\eta = b_m/d_0$ [-]	$N_{1,4\%}$ [N] FEM	$N_{1,4\%}$ [N] Eng. tool	Difference [%]
1100	1100	64.0	8.6	1.00	9.15E+06	8.88E+06	2.9
		57.2	9.6	1.00	7.28E+06	7.10E+06	2.4
		50.0	11.0	1.00	5.60E+06	5.44E+06	2.9
		45.0	12.2	1.00	4.62E+06	4.41E+06	4.6
		40.0	13.8	1.00	3.65E+06	3.49E+06	4.5
		35.0	15.7	1.00	2.90E+06	2.67E+06	7.8
	1300	64.0	8.6	1.18	9.75E+06	9.69E+06	0.6
		57.2	9.6	1.18	7.80E+06	7.75E+06	0.6
		50.0	11.0	1.18	6.00E+06	5.93E+06	1.2
		45.0	12.2	1.18	4.92E+06	4.81E+06	2.3
		40.0	13.8	1.18	3.95E+06	3.80E+06	3.7
		35.0	15.7	1.18	3.10E+06	2.92E+06	6.0
	1600	64.0	8.6	1.45	1.07E+07	1.09E+07	-2.3
		57.2	9.6	1.45	8.70E+06	8.72E+06	-0.2
		50.0	11.0	1.45	6.70E+06	6.67E+06	0.4
		45.0	12.2	1.45	5.53E+06	5.41E+06	2.2
		40.0	13.8	1.45	4.38E+06	4.28E+06	2.3
		35.0	15.7	1.45	3.40E+06	3.28E+06	3.5
	1800	64.0	8.6	1.64	1.13E+07	1.17E+07	-4.1
		57.2	9.6	1.64	9.15E+06	9.36E+06	-2.3
		50.0	11.0	1.64	7.10E+06	7.17E+06	-0.9
		45.0	12.2	1.64	5.84E+06	5.81E+06	0.5
		40.0	13.8	1.64	4.62E+06	4.60E+06	0.5
		35.0	15.7	1.64	3.55E+06	3.52E+06	0.8
	2000	64.0	8.6	1.82	1.19E+07	1.25E+07	-5.6
		57.2	9.6	1.82	9.57E+06	1.00E+07	-4.6
		50.0	11.0	1.82	7.40E+06	7.66E+06	-3.5
		45.0	12.2	1.82	6.08E+06	6.21E+06	-2.2
		40.0	13.8	1.82	4.80E+06	4.91E+06	-2.4
		35.0	15.7	1.82	9.15E+06	3.77E+06	-1.8

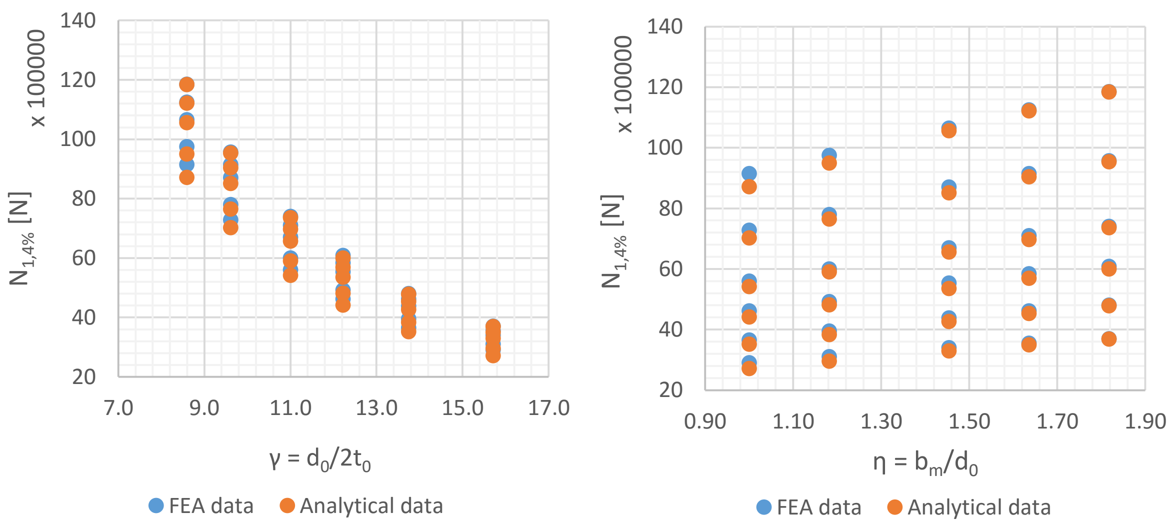

Figure 129: Comparison between FEA data and engineering tool in the plate load case (α_{ip} = 60˚) for d_0 = 1100

Table 42: Comparison between FEA data and engineering tool in the plate load case (α_{ip} = 60˚) for d_0 = 1219.2

d_0 [mm]	b_m [mm]	t_0 [mm]	$\gamma = d_0/2t_0$ [-]	$\eta = b_m/d_0$ [-]	$N_{1,4\%}$ [N] FEM	$N_{1,4\%}$ [N] Eng. tool	Difference [%]

1219.2	1100	64.0	9.5	0.90	8.55E+06	8.46E+06	1.1
		57.2	10.7	0.90	6.90E+06	6.76E+06	2.0
		50.0	12.2	0.90	5.30E+06	5.18E+06	2.3
		45.0	13.5	0.90	4.38E+06	4.20E+06	4.2
		40.0	15.2	0.90	3.45E+06	3.32E+06	3.8
		35.0	17.4	0.90	2.75E+06	2.54E+06	7.5
	1300	64.0	9.5	1.07	9.15E+06	9.19E+06	-0.4
		57.2	10.7	1.07	7.30E+06	7.35E+06	-0.7
		50.0	12.2	1.07	5.70E+06	5.62E+06	1.4
		45.0	13.5	1.07	4.68E+06	4.56E+06	2.6
		40.0	15.2	1.07	3.75E+06	3.61E+06	3.9
		35.0	17.4	1.07	2.95E+06	2.76E+06	6.3
	1600	64.0	9.5	1.31	1.01E+07	1.03E+07	-2.3
		57.2	10.7	1.31	8.20E+06	8.22E+06	-0.3
		50.0	12.2	1.31	6.30E+06	6.29E+06	0.1
		45.0	13.5	1.31	5.16E+06	5.10E+06	1.1
		40.0	15.2	1.31	4.15E+06	4.03E+06	2.8
		35.0	17.4	1.31	3.20E+06	3.09E+06	3.4
	1800	64.0	9.5	1.48	1.07E+07	1.10E+07	-3.4
		57.2	10.7	1.48	8.60E+06	8.81E+06	-2.4
		50.0	12.2	1.48	6.70E+06	6.74E+06	-0.6
		45.0	13.5	1.48	5.46E+06	5.46E+06	-0.1
		40.0	15.2	1.48	4.32E+06	4.32E+06	0.0
		35.0	17.4	1.48	3.35E+06	3.31E+06	1.2
	2000	64.0	9.5	1.64	1.11E+07	1.17E+07	-5.8
		57.2	10.7	1.64	9.02E+06	9.39E+06	-4.1
		50.0	12.2	1.64	7.00E+06	7.18E+06	-2.6
		45.0	13.5	1.64	5.67E+06	5.83E+06	-2.7
		40.0	15.2	1.64	4.50E+06	4.61E+06	-2.4
		35.0	17.4	1.64	3.45E+06	3.53E+06	-2.3

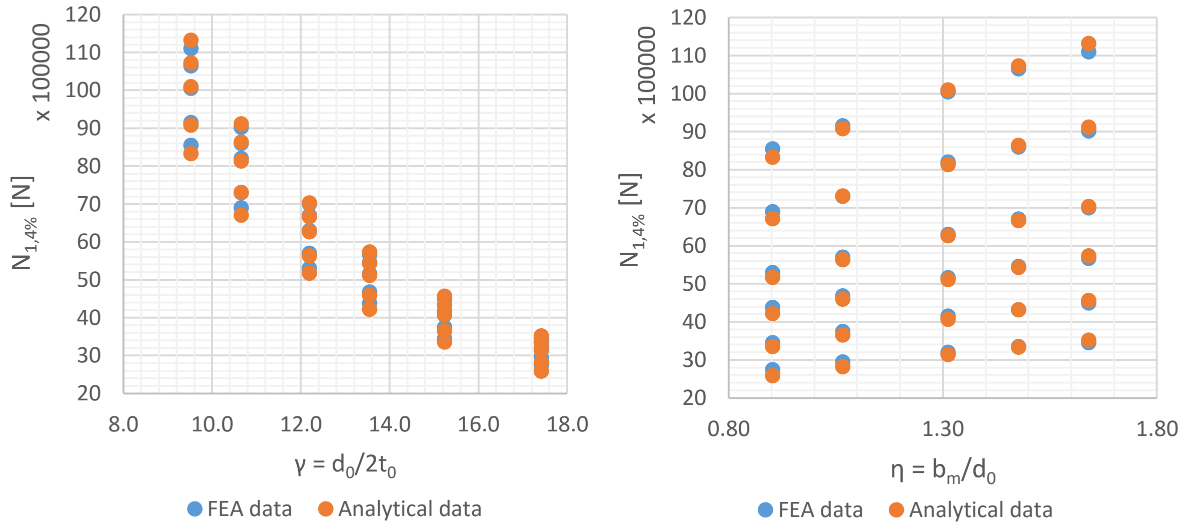

Figure 130: Comparison between FEA data and engineering tool in the plate load case (α_{ip} = 60˚) for d_0 = 1219.2

Table 43: Comparison between FEA data and engineering tool in the plate load case (α_{ip} = 60˚) for d_0 = 1400

d_0 [mm]	b_m [mm]	t_0 [mm]	$\gamma = d_0/2t_0$ [-]	$\eta = b_m/d_0$ [-]	$N_{1,4\%}$ [N] FEM	$N_{1,4\%}$ [N] Eng. tool	Difference [%]
1400	1100	64.0	10.9	0.79	7.95E+06	7.95E+06	0.0

		57.2	12.2	0.79	6.40E+06	6.36E+06	0.6
		50.0	14.0	0.79	4.90E+06	4.87E+06	0.7
		45.0	15.6	0.79	4.08E+06	3.94E+06	3.3
		40.0	17.5	0.79	3.25E+06	3.12E+06	4.0
		35.0	20.0	0.79	2.55E+06	2.39E+06	6.3
	1300	64.0	10.9	0.93	8.40E+06	8.59E+06	-2.2
		57.2	12.2	0.93	6.80E+06	6.87E+06	-1.0
		50.0	14.0	0.93	5.32E+06	5.25E+06	1.2
		45.0	15.6	0.93	4.32E+06	4.26E+06	1.4
		40.0	17.5	0.93	3.50E+06	3.37E+06	3.8
		35.0	20.0	0.93	2.75E+06	2.58E+06	6.1
	1600	64.0	10.9	1.14	9.30E+06	9.54E+06	-2.6
		57.2	12.2	1.14	7.50E+06	7.63E+06	-1.7
		50.0	14.0	1.14	5.88E+06	5.84E+06	0.7
		45.0	15.6	1.14	4.80E+06	4.73E+06	1.4
		40.0	17.5	1.14	3.85E+06	3.74E+06	2.8
		35.0	20.0	1.14	2.95E+06	2.87E+06	2.8
	1800	64.0	10.9	1.29	9.75E+06	1.02E+07	-4.4
		57.2	12.2	1.29	7.90E+06	8.14E+06	-3.0
		50.0	14.0	1.29	6.16E+06	6.23E+06	-1.1
		45.0	15.6	1.29	5.04E+06	5.05E+06	-0.2
		40.0	17.5	1.29	4.00E+06	3.99E+06	0.2
		35.0	20.0	1.29	3.10E+06	3.06E+06	1.3
	2000	64.0	10.9	1.43	1.02E+07	1.08E+07	-6.0
		57.2	12.2	1.43	8.30E+06	8.65E+06	-4.2
		50.0	14.0	1.43	6.40E+06	6.62E+06	-3.4
		45.0	15.6	1.43	5.25E+06	5.36E+06	-2.2
		40.0	17.5	1.43	4.15E+06	4.24E+06	-2.2
		35.0	20.0	1.43	3.20E+06	3.25E+06	-1.6

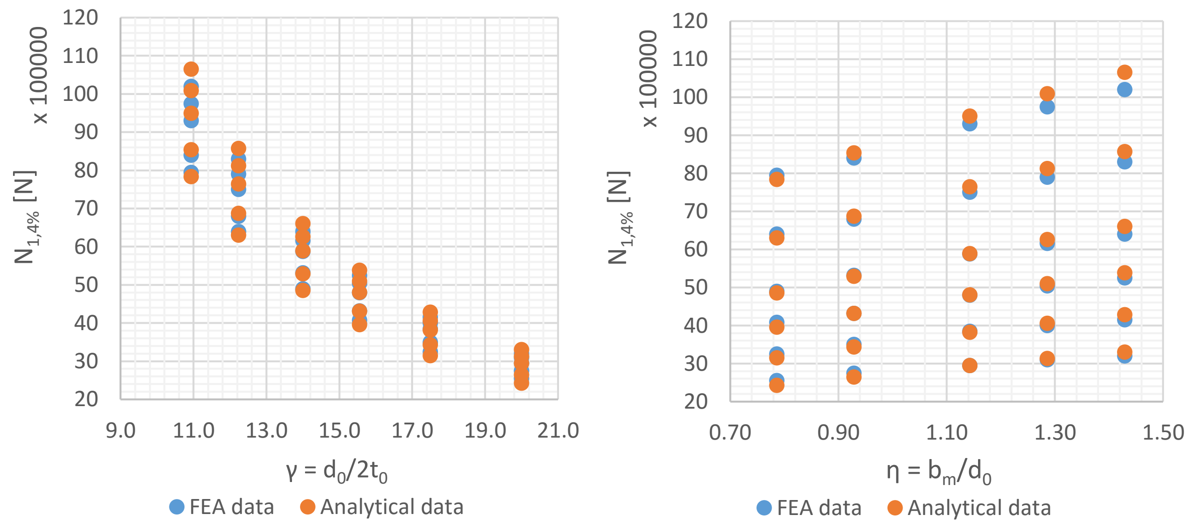

Figure 131: Comparison between FEA data and engineering tool in the plate load case (α_{ip} = 60˚) for d_0 = 1400

F.3 Padeye load case

F.3.1 Constant padeye geometry

Table 44: Comparison between FEA data and engineering tool in the padeye load case with constant geometry, $d_0 = 800$

d_0 [mm]	b_m [mm]	t_0 [mm]	$\gamma = d_0/2t_0$ [-]	$\eta = b_m/d_0$ [-]	$N_{1,4\%}$ [N] FEM	$N_{1,4\%}$ [N] Eng. tool	Difference [%]
800	1100	64.0	6.3	1.38	1.56E+07	1.51E+07	3.0
		57.2	7.0	1.38	1.26E+07	1.21E+07	3.6
		50.0	8.0	1.38	9.75E+06	9.33E+06	4.3
		45.0	8.9	1.38	8.16E+06	7.58E+06	7.1
		40.0	10.0	1.38	6.50E+06	6.01E+06	7.5
		35.0	11.4	1.38	5.12E+06	4.62E+06	9.8
	1300	64.0	6.3	1.63	1.70E+07	1.67E+07	1.6
		57.2	7.0	1.63	1.38E+07	1.34E+07	2.7
		50.0	8.0	1.63	1.08E+07	1.03E+07	4.5
		45.0	8.9	1.63	8.88E+06	8.38E+06	5.6
		40.0	10.0	1.63	7.10E+06	6.64E+06	6.4
		35.0	11.4	1.63	5.60E+06	5.10E+06	8.8
	1600	64.0	6.3	2.00	1.92E+07	1.91E+07	0.4
		57.2	7.0	2.00	1.56E+07	1.53E+07	1.6
		50.0	8.0	2.00	1.22E+07	1.18E+07	3.0
		45.0	8.9	2.00	9.96E+06	9.58E+06	3.8
		40.0	10.0	2.00	8.00E+06	7.59E+06	5.1
		35.0	11.4	2.00	6.16E+06	5.83E+06	5.3

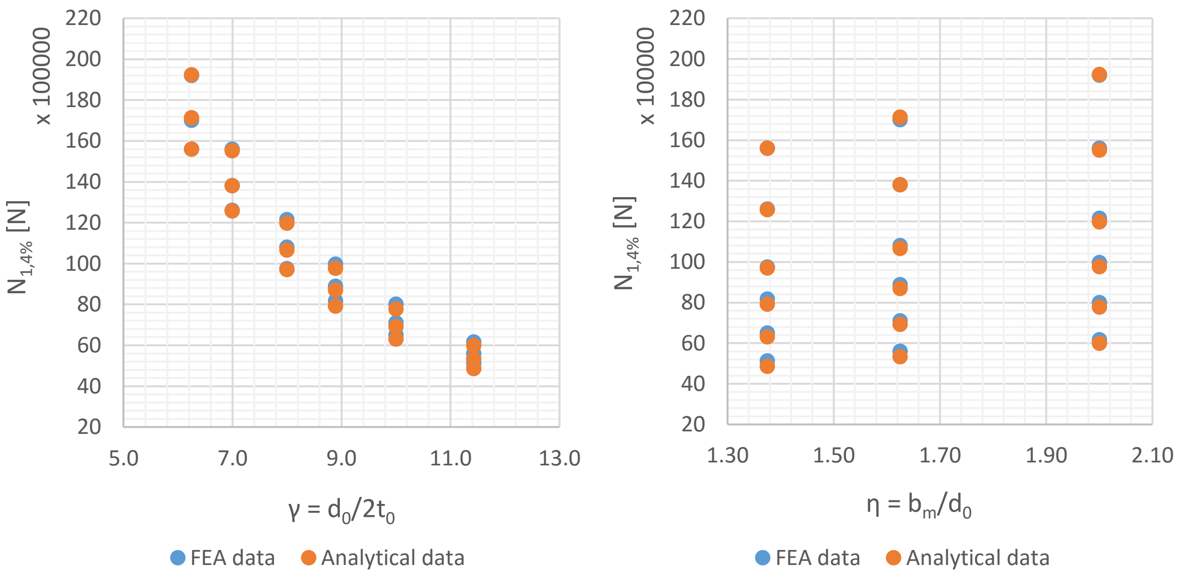

Figure 132: Comparison between FEA data and engineering tool in the padeye load case with constant geometry, $d_0 = 800$

Table 45: Comparison between FEA data and engineering tool in the padeye load case with constant geometry, $d_0 = 900$

d_0 [mm]	b_m [mm]	t_0 [mm]	$\gamma = d_0/2t_0$ [-]	$\eta = b_m/d_0$ [-]	$N_{1,4\%}$ [N] FEM	$N_{1,4\%}$ [N] Eng. tool	Difference [%]
900	1100	64.0	7.0	1.22	1.46E+07	1.42E+07	2.2
		57.2	7.9	1.22	1.19E+07	1.14E+07	3.7
		50.0	9.0	1.22	9.15E+06	8.76E+06	4.2
		45.0	10.0	1.22	7.60E+06	7.12E+06	6.3
		40.0	11.3	1.22	6.10E+06	5.64E+06	7.5
		35.0	12.9	1.22	4.80E+06	4.33E+06	9.7
	1300	64.0	7.0	1.44	1.60E+07	1.57E+07	2.2
		57.2	7.9	1.44	1.28E+07	1.26E+07	1.9
		50.0	9.0	1.44	1.01E+07	9.64E+06	4.1
		45.0	10.0	1.44	8.20E+06	7.83E+06	4.5
		40.0	11.3	1.44	6.60E+06	6.21E+06	6.0
		35.0	12.9	1.44	5.12E+06	4.77E+06	6.9
	1600	64.0	7.0	1.78	1.78E+07	1.78E+07	0.1
		57.2	7.9	1.78	1.46E+07	1.43E+07	2.3
		50.0	9.0	1.78	1.13E+07	1.10E+07	2.6
		45.0	10.0	1.78	9.30E+06	8.90E+06	4.3
		40.0	11.3	1.78	7.30E+06	7.05E+06	3.4
		35.0	12.9	1.78	5.68E+06	5.42E+06	4.6
	1800	64.0	7.0	2.00	1.92E+07	1.92E+07	-0.1
		57.2	7.9	2.00	1.56E+07	1.54E+07	1.2
		50.0	9.0	2.00	1.21E+07	1.18E+07	2.0
		45.0	10.0	2.00	9.75E+06	9.61E+06	1.4
		40.0	11.3	2.00	7.80E+06	7.62E+06	2.3
		35.0	12.9	2.00	6.00E+06	5.85E+06	2.5
	2000	64.0	7.0	2.22	2.02E+07	2.06E+07	-2.0
		57.2	7.9	2.22	1.64E+07	1.66E+07	-0.9
		50.0	9.0	2.22	1.28E+07	1.27E+07	0.4
		45.0	10.0	2.22	1.04E+07	1.03E+07	0.3
		40.0	11.3	2.22	8.20E+06	8.18E+06	0.2
		35.0	12.9	2.22	6.32E+06	6.28E+06	0.6

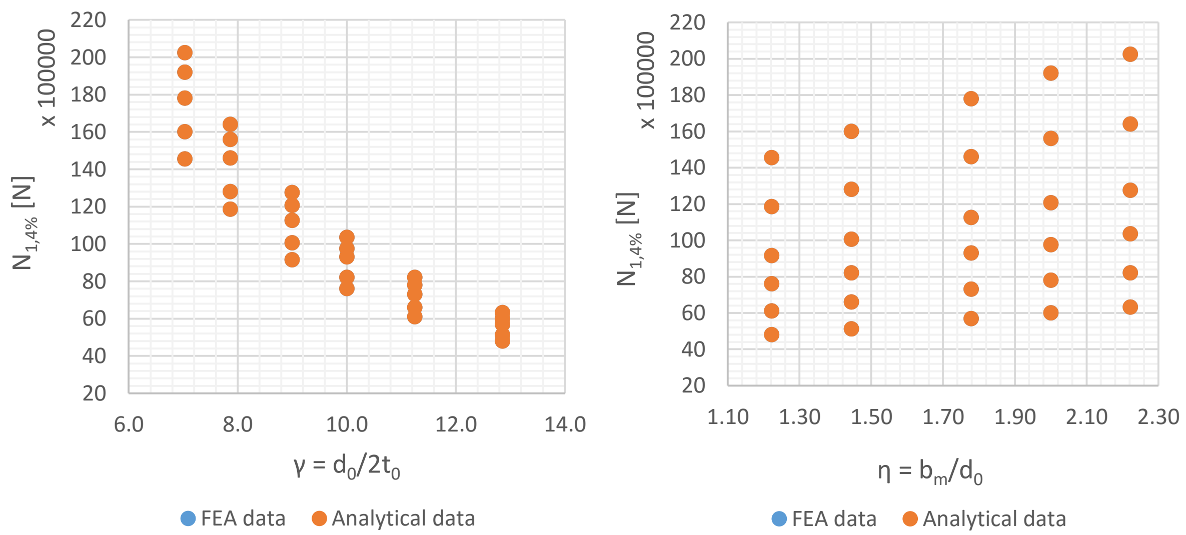

Figure 133: Comparison between FEA data and engineering tool in the padeye load case with constant geometry, $d_0 = 900$

Table 46: Comparison between FEA data and engineering tool in the padeye load case with constant geometry, d_0 = 1100

d_0 [mm]	b_m [mm]	t_0 [mm]	$\gamma = d_0/2t_0$ [-]	$\eta = b_m/d_0$ [-]	$N_{1,4\%}$ [N] FEM	$N_{1,4\%}$ [N] Eng. tool	Difference [%]
1100	1100	64.0	8.6	1.00	1.32E+07	1.29E+07	2.3
		57.2	9.6	1.00	1.06E+07	1.03E+07	2.5
		50.0	11.0	1.00	8.25E+06	7.93E+06	3.9
		45.0	12.2	1.00	6.80E+06	6.44E+06	5.3
		40.0	13.8	1.00	5.40E+06	5.10E+06	5.5
		35.0	15.7	1.00	4.27E+06	3.92E+06	8.3
	1300	64.0	8.6	1.18	1.42E+07	1.41E+07	0.9
		57.2	9.6	1.18	1.14E+07	1.13E+07	1.1
		50.0	11.0	1.18	9.00E+06	8.65E+06	3.9
		45.0	12.2	1.18	7.30E+06	7.02E+06	3.8
		40.0	13.8	1.18	5.90E+06	5.56E+06	5.7
		35.0	15.7	1.18	4.55E+06	4.27E+06	6.1
	1600	64.0	8.6	1.45	1.58E+07	1.58E+07	-0.2
		57.2	9.6	1.45	1.28E+07	1.27E+07	0.9
		50.0	11.0	1.45	9.90E+06	9.73E+06	1.7
		45.0	12.2	1.45	8.10E+06	7.90E+06	2.4
		40.0	13.8	1.45	6.40E+06	6.26E+06	2.2
		35.0	15.7	1.45	4.90E+06	4.81E+06	1.9
	1800	64.0	8.6	1.64	1.68E+07	1.70E+07	-1.2
		57.2	9.6	1.64	1.37E+07	1.36E+07	0.1
		50.0	11.0	1.64	1.05E+07	1.05E+07	0.4
		45.0	12.2	1.64	8.60E+06	8.49E+06	1.3
		40.0	13.8	1.64	6.80E+06	6.72E+06	1.1
		35.0	15.7	1.64	5.18E+06	5.16E+06	0.4
	2000	64.0	8.6	1.82	1.78E+07	1.82E+07	-2.1
		57.2	9.6	1.82	1.44E+07	1.46E+07	-1.2
		50.0	11.0	1.82	1.11E+07	1.12E+07	-0.7
		45.0	12.2	1.82	9.02E+06	9.07E+06	-0.6
		40.0	13.8	1.82	7.10E+06	7.19E+06	-1.2
		35.0	15.7	1.82	5.39E+06	5.52E+06	-2.4

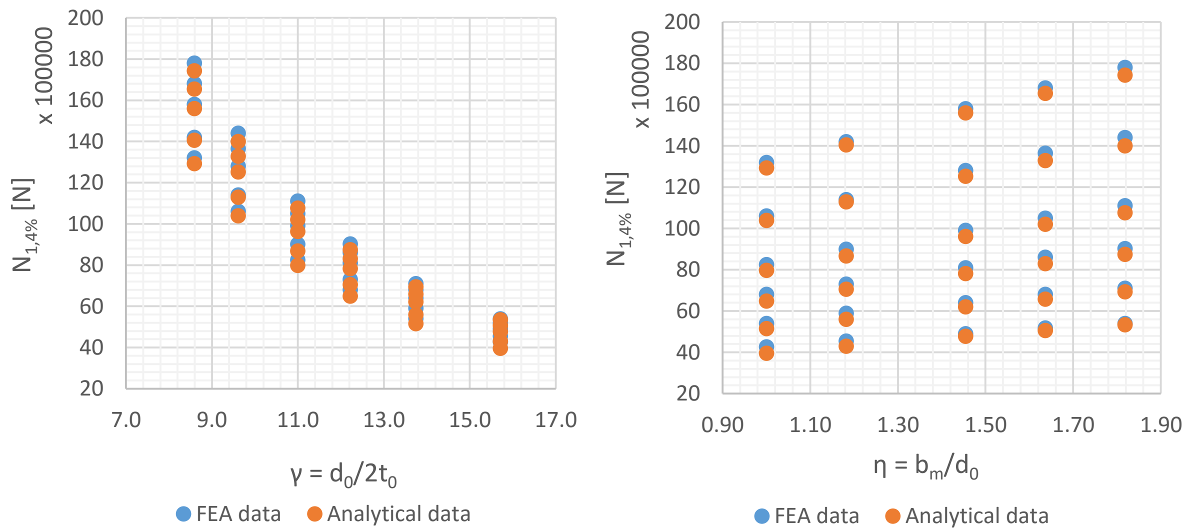

Figure 134: Comparison between FEA data and engineering tool in the padeye load case with constant geometry, d_0 = 1100

Table 47: Comparison between FEA data and engineering tool in the padeye load case with constant geometry, $d_0 = 1219.2$

d_0 [mm]	b_m [mm]	t_0 [mm]	$\gamma = d_0/2t_0$ [-]	$\eta = b_m/d_0$ [-]	$N_{1,4\%}$ [N] FEM	$N_{1,4\%}$ [N] Eng. tool	Difference [%]
1219.2	1100	64.0	9.5	0.90	1.23E+07	1.23E+07	-0.1
		57.2	10.7	0.90	9.90E+06	9.86E+06	0.4
		50.0	12.2	0.90	7.80E+06	7.56E+06	3.1
		45.0	13.5	0.90	6.40E+06	6.14E+06	4.1
		40.0	15.2	0.90	5.10E+06	4.86E+06	4.7
		35.0	17.4	0.90	3.99E+06	3.73E+06	6.5
	1300	64.0	9.5	1.07	1.34E+07	1.34E+07	-0.2
		57.2	10.7	1.07	1.08E+07	1.07E+07	0.8
		50.0	12.2	1.07	8.40E+06	8.21E+06	2.2
		45.0	13.5	1.07	6.90E+06	6.67E+06	3.4
		40.0	15.2	1.07	5.50E+06	5.28E+06	4.0
		35.0	17.4	1.07	4.27E+06	4.05E+06	5.1
	1600	64.0	9.5	1.31	1.48E+07	1.50E+07	-1.1
		57.2	10.7	1.31	1.20E+07	1.20E+07	0.1
		50.0	12.2	1.31	9.36E+06	9.19E+06	1.8
		45.0	13.5	1.31	7.60E+06	7.46E+06	1.8
		40.0	15.2	1.31	6.00E+06	5.91E+06	1.5
		35.0	17.4	1.31	4.62E+06	4.53E+06	1.8
	1800	64.0	9.5	1.48	1.58E+07	1.60E+07	-1.4
		57.2	10.7	1.48	1.28E+07	1.28E+07	-0.7
		50.0	12.2	1.48	9.90E+06	9.84E+06	0.6
		45.0	13.5	1.48	8.00E+06	7.99E+06	0.1
		40.0	15.2	1.48	6.30E+06	6.33E+06	-0.5
		35.0	17.4	1.48	4.83E+06	4.86E+06	-0.5
	2000	64.0	9.5	1.64	1.66E+07	1.71E+07	-2.9
		57.2	10.7	1.64	1.34E+07	1.37E+07	-1.9
		50.0	12.2	1.64	1.04E+07	1.05E+07	-1.4
		45.0	13.5	1.64	8.40E+06	8.52E+06	-1.4
		40.0	15.2	1.64	6.60E+06	6.75E+06	-2.2
		35.0	17.4	1.64	5.04E+06	5.18E+06	-2.7

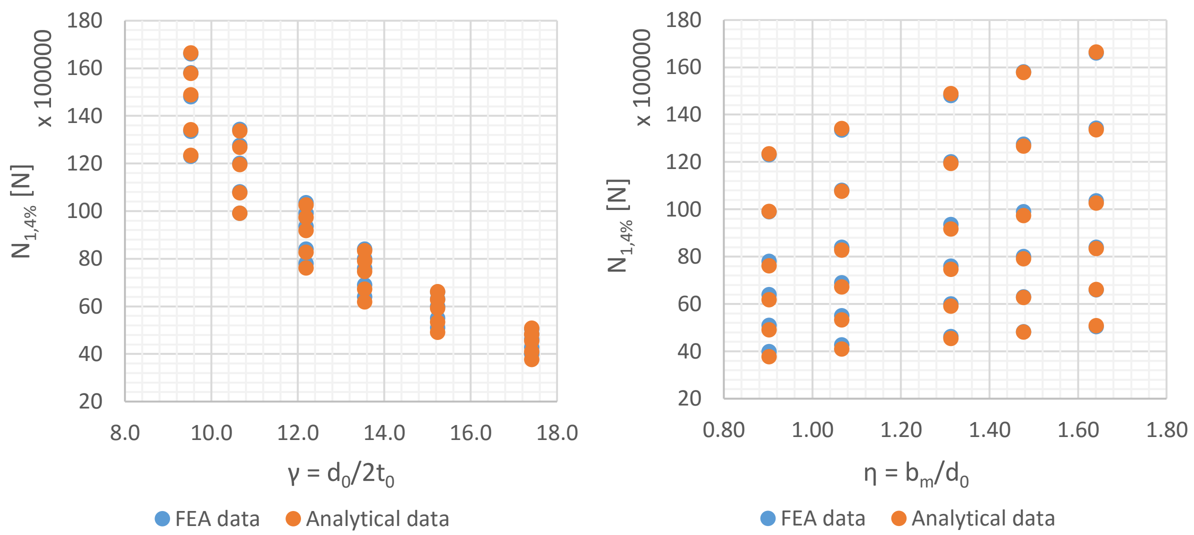

Figure 135: Comparison between FEA data and engineering tool in the padeye load case with constant geometry, $d_0 = 1219.2$

Table 48: Comparison between FEA data and engineering tool in the padeye load case with constant geometry, d_0 = 1400

d_0 [mm]	b_m [mm]	t_0 [mm]	$\gamma = d_0/2t_0$ [-]	$\eta = b_m/d_0$ [-]	$N_{1,4\%}$ [N] FEM	$N_{1,4\%}$ [N] Eng. tool	Difference [%]
1400	1100	64.0	10.9	0.79	1.14E+07	1.16E+07	-1.7
		57.2	12.2	0.79	9.15E+06	9.29E+06	-1.5
		50.0	14.0	0.79	7.20E+06	7.12E+06	1.1
		45.0	15.6	0.79	5.90E+06	5.78E+06	2.1
		40.0	17.5	0.79	4.72E+06	4.57E+06	3.1
		35.0	20.0	0.79	3.66E+06	3.51E+06	4.1
	1300	64.0	10.9	0.93	1.22E+07	1.25E+07	-2.7
		57.2	12.2	0.93	9.90E+06	1.00E+07	-1.3
		50.0	14.0	0.93	7.80E+06	7.69E+06	1.4
		45.0	15.6	0.93	6.30E+06	6.24E+06	1.0
		40.0	17.5	0.93	5.04E+06	4.94E+06	2.0
		35.0	20.0	0.93	3.90E+06	3.79E+06	2.8
	1600	64.0	10.9	1.14	1.36E+07	1.39E+07	-2.3
		57.2	12.2	1.14	1.10E+07	1.11E+07	-1.8
		50.0	14.0	1.14	8.55E+06	8.54E+06	0.1
		45.0	15.6	1.14	6.90E+06	6.93E+06	-0.5
		40.0	17.5	1.14	5.44E+06	5.49E+06	-0.9
		35.0	20.0	1.14	4.20E+06	4.21E+06	-0.3
	1800	64.0	10.9	1.29	1.44E+07	1.48E+07	-3.1
		57.2	12.2	1.29	1.16E+07	1.19E+07	-3.0
		50.0	14.0	1.29	9.00E+06	9.11E+06	-1.2
		45.0	15.6	1.29	7.30E+06	7.40E+06	-1.3
		40.0	17.5	1.29	5.68E+06	5.86E+06	-3.1
		35.0	20.0	1.29	4.38E+06	4.49E+06	-2.6
	2000	64.0	10.9	1.43	1.52E+07	1.58E+07	-3.8
		57.2	12.2	1.43	1.22E+07	1.26E+07	-4.0
		50.0	14.0	1.43	9.30E+06	9.68E+06	-4.1
		45.0	15.6	1.43	7.60E+06	7.86E+06	-3.4
		40.0	17.5	1.43	5.92E+06	6.22E+06	-5.1
		35.0	20.0	1.43	4.56E+06	4.77E+06	-4.7

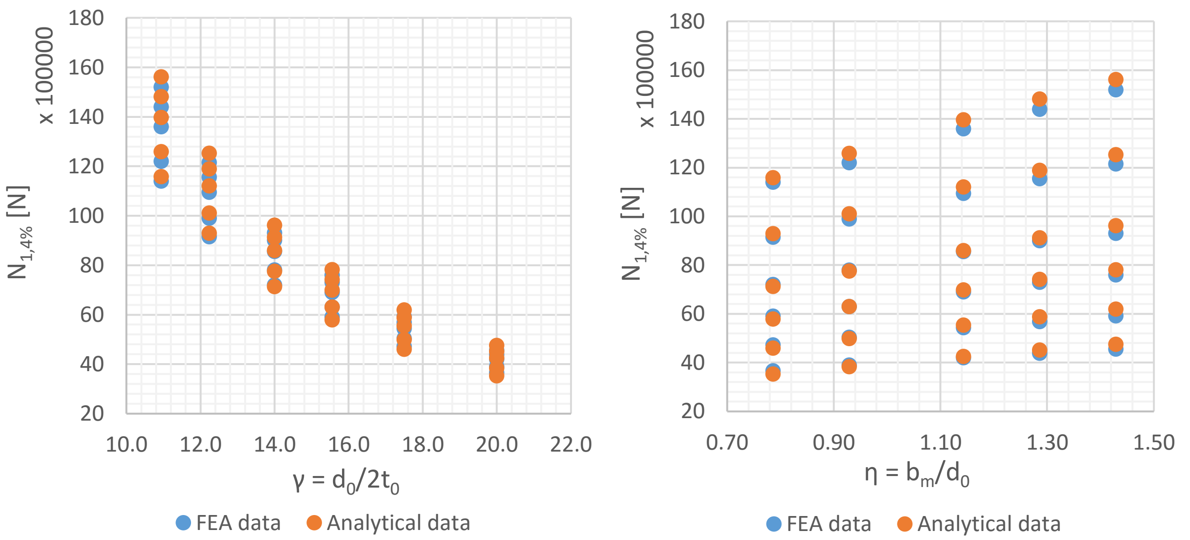

Figure 136: Comparison between FEA data and engineering tool in the padeye load case with constant geometry, d_0 = 1400

F.3.2 Variable padeye geometry

Table 49: Comparison between FEA data and engineering tool in the padeye load case with variable geometry, $d_0 = 800$

d_0 [mm]	b_m [mm]	t_0 [mm]	$\gamma = d_0/2t_0$ [-]	$\eta = b_m/d_0$ [-]	$\lambda = b_m/(R_m+h_0)$ [-]	$N_{1,4\%}$ [N] FEM	$N_{1,4\%}$ [N] Eng. tool	Difference [%]
800	1100	64.0	6.3	1.38	1.38	1.38E+07	1.32E+07	4.6
		57.2	7.0	1.38	1.38	1.10E+07	1.06E+07	3.9
		50.0	8.0	1.38	1.38	8.40E+06	8.11E+06	3.4
		45.0	8.9	1.38	1.38	7.00E+06	6.60E+06	5.8
		40.0	10.0	1.38	1.38	5.60E+06	5.23E+06	6.6
		35.0	11.4	1.38	1.38	4.40E+06	4.02E+06	8.7
	1300	64.0	6.3	1.63	1.63	1.70E+07	1.68E+07	0.9
		57.2	7.0	1.63	1.63	1.38E+07	1.35E+07	2.1
		50.0	8.0	1.63	1.63	1.08E+07	1.04E+07	3.9
		45.0	8.9	1.63	1.63	9.00E+06	8.44E+06	6.3
		40.0	10.0	1.63	1.63	7.20E+06	6.69E+06	7.1
		35.0	11.4	1.63	1.63	5.60E+06	5.14E+06	8.2
	1600	64.0	6.3	2.00	2.00	1.66E+07	1.63E+07	1.8
		57.2	7.0	2.00	2.00	1.34E+07	1.31E+07	2.3
		50.0	8.0	2.00	2.00	1.04E+07	1.01E+07	3.4
		45.0	8.9	2.00	2.00	8.40E+06	8.17E+06	2.8
		40.0	10.0	2.00	2.00	6.80E+06	6.48E+06	4.8
		35.0	11.4	2.00	2.00	5.20E+06	4.98E+06	4.3

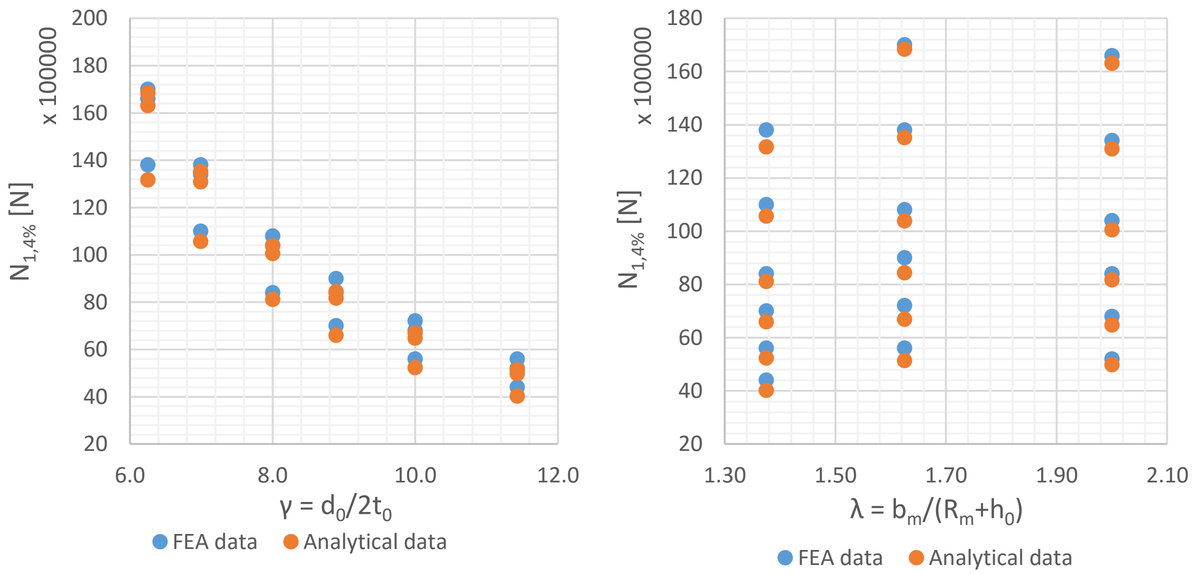

Figure 137: Comparison between FEA data and engineering tool in the padeye load case with variable geometry, $d_0 = 800$

Table 50: Comparison between FEA data and engineering tool in the padeye load case with variable geometry, d_0 = 900

d_0 [mm]	b_m [mm]	t_0 [mm]	$\gamma = d_0/2t_0$ [-]	$\eta = b_m/d_0$ [-]	$\lambda = b_m/(R_m+h_0)$ [-]	$N_{1,4\%}$ [N] FEM	$N_{1,4\%}$ [N] Eng. tool	Difference [%]
900	1100	64.0	7.0	1.22	1.38	1.28E+07	1.24E+07	3.3
		57.2	7.9	1.22	1.38	1.02E+07	9.93E+06	2.6
		50.0	9.0	1.22	1.38	8.00E+06	7.62E+06	4.7
		45.0	10.0	1.22	1.38	6.60E+06	6.19E+06	6.2
		40.0	11.3	1.22	1.38	5.20E+06	4.91E+06	5.6
		35.0	12.9	1.22	1.38	4.20E+06	3.77E+06	10.3
	1300	64.0	7.0	1.44	1.63	1.60E+07	1.58E+07	1.5
		57.2	7.9	1.44	1.63	1.28E+07	1.26E+07	1.2
		50.0	9.0	1.44	1.63	1.00E+07	9.70E+06	3.0
		45.0	10.0	1.44	1.63	8.20E+06	7.88E+06	3.9
		40.0	11.3	1.44	1.63	6.60E+06	6.25E+06	5.3
		35.0	12.9	1.44	1.63	5.20E+06	4.80E+06	7.7
	1600	64.0	7.0	1.78	2.00	1.54E+07	1.52E+07	1.5
		57.2	7.9	1.78	2.00	1.24E+07	1.22E+07	1.8
		50.0	9.0	1.78	2.00	9.60E+06	9.34E+06	2.7
		45.0	10.0	1.78	2.00	7.80E+06	7.59E+06	2.7
		40.0	11.3	1.78	2.00	6.20E+06	6.02E+06	3.0
		35.0	12.9	1.78	2.00	4.80E+06	4.62E+06	3.8
	1800	64.0	7.0	2.00	2.25	1.50E+07	1.48E+07	1.2
		57.2	7.9	2.00	2.25	1.20E+07	1.19E+07	0.9
		50.0	9.0	2.00	2.25	9.40E+06	9.12E+06	3.0
		45.0	10.0	2.00	2.25	7.60E+06	7.41E+06	2.5
		40.0	11.3	2.00	2.25	6.00E+06	5.87E+06	2.1
		35.0	12.9	2.00	2.25	4.60E+06	4.51E+06	1.9
	2000	64.0	7.0	2.22	2.50	1.48E+07	1.46E+07	1.6
		57.2	7.9	2.22	2.50	1.20E+07	1.17E+07	2.6
		50.0	9.0	2.22	2.50	9.20E+06	8.97E+06	2.5
		45.0	10.0	2.22	2.50	7.40E+06	7.29E+06	1.5
		40.0	11.3	2.22	2.50	6.00E+06	5.77E+06	3.8
		35.0	12.9	2.22	2.50	4.60E+06	4.44E+06	3.6

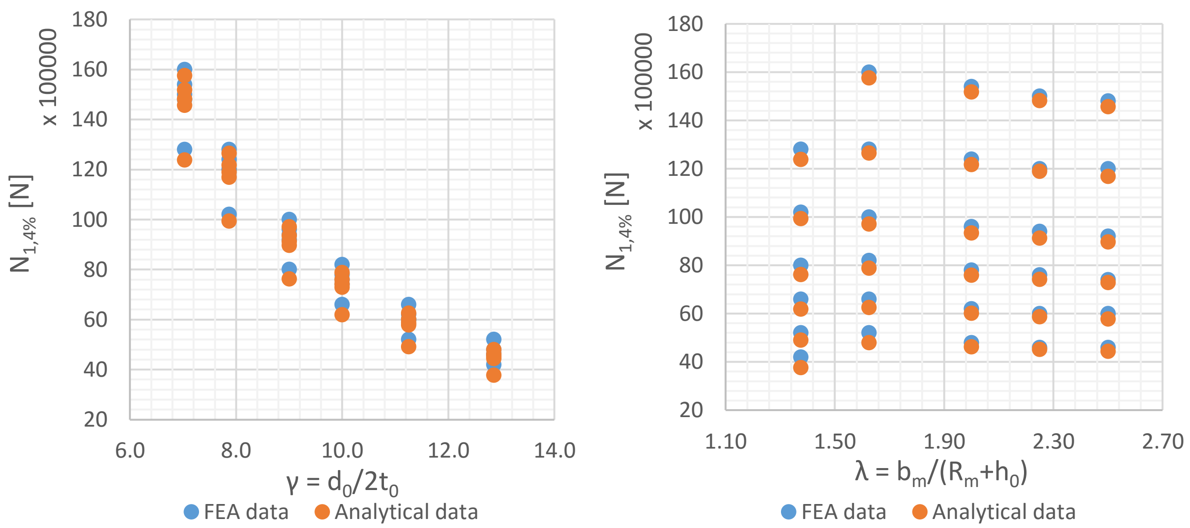

Figure 138: Comparison between FEA data and engineering tool in the padeye load case with variable geometry, d_0 = 900

Table 51: Comparison between FEA data and engineering tool in the padeye load case with variable geometry, d_0 = 1100

d_0 [mm]	b_m [mm]	t_0 [mm]	$\gamma = d_0/2t_0$ [-]	$\eta = b_m/d_0$ [-]	$\lambda = b_m/(R_m+h_0)$ [-]	$N_{1,4\%}$ [N] FEM	$N_{1,4\%}$ [N] Eng. tool	Difference [%]
1100	1100	64.0	8.6	1.00	1.38	1.14E+07	1.12E+07	1.6
		57.2	9.6	1.00	1.38	9.00E+06	8.99E+06	0.1
		50.0	11.0	1.00	1.38	7.00E+06	6.90E+06	1.5
		45.0	12.2	1.00	1.38	5.80E+06	5.60E+06	3.4
		40.0	13.8	1.00	1.38	4.60E+06	4.44E+06	3.5
		35.0	15.7	1.00	1.38	3.60E+06	3.41E+06	5.4
	1300	64.0	8.6	1.18	1.63	1.42E+07	1.42E+07	0.2
		57.2	9.6	1.18	1.63	1.14E+07	1.14E+07	0.4
		50.0	11.0	1.18	1.63	9.00E+06	8.71E+06	3.2
		45.0	12.2	1.18	1.63	7.40E+06	7.07E+06	4.4
		40.0	13.8	1.18	1.63	6.00E+06	5.60E+06	6.6
		35.0	15.7	1.18	1.63	4.60E+06	4.30E+06	6.5
	1600	64.0	8.6	1.27	1.75	1.42E+07	1.40E+07	1.1
		57.2	9.6	1.27	1.75	1.14E+07	1.13E+07	1.3
		50.0	11.0	1.27	1.75	8.80E+06	8.63E+06	1.9
		45.0	12.2	1.27	1.75	7.20E+06	7.01E+06	2.6
		40.0	13.8	1.27	1.75	5.80E+06	5.55E+06	4.3
		35.0	15.7	1.27	1.75	4.40E+06	4.26E+06	3.1
	1800	64.0	8.6	1.45	2.00	1.36E+07	1.35E+07	0.7
		57.2	9.6	1.45	2.00	1.08E+07	1.08E+07	-0.2
		50.0	11.0	1.45	2.00	8.40E+06	8.30E+06	1.2
		45.0	12.2	1.45	2.00	6.80E+06	6.74E+06	0.9
		40.0	13.8	1.45	2.00	5.40E+06	5.34E+06	1.1
		35.0	15.7	1.45	2.00	4.20E+06	4.10E+06	2.4
	2000	64.0	8.6	1.64	2.25	1.32E+07	1.31E+07	0.6
		57.2	9.6	1.64	2.25	1.06E+07	1.05E+07	0.8
		50.0	11.0	1.64	2.25	8.20E+06	8.06E+06	1.7
		45.0	12.2	1.64	2.25	6.60E+06	6.55E+06	0.8
		40.0	13.8	1.64	2.25	5.20E+06	5.19E+06	0.3
		35.0	15.7	1.64	2.25	4.00E+06	3.98E+06	0.5

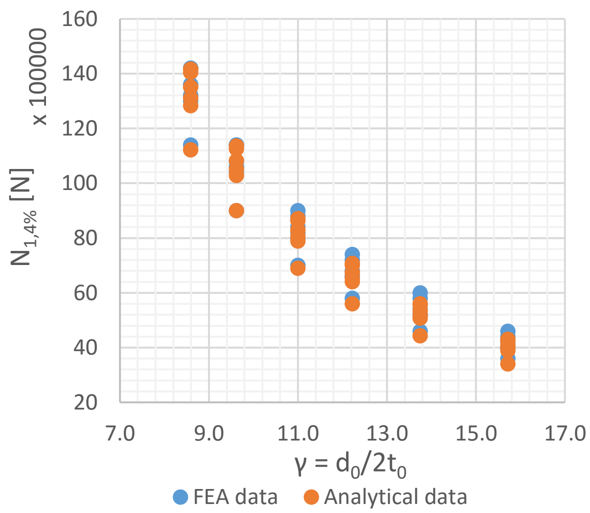

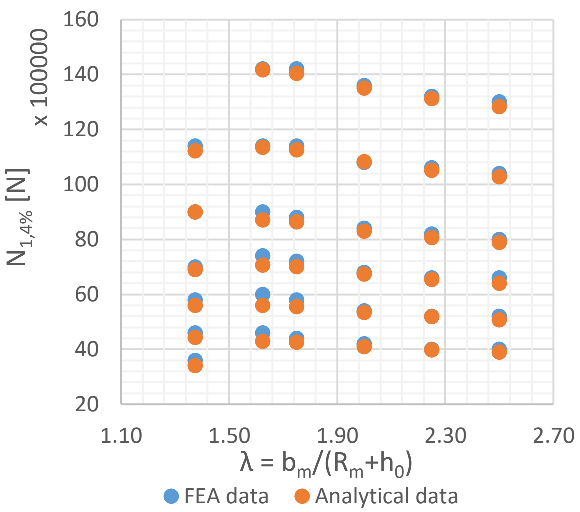

Figure 139: Comparison between FEA data and engineering tool in the padeye load case with variable geometry, d_0 = 1100

Table 52: Comparison between FEA data and engineering tool in the padeye load case with variable geometry, d_0 = 1219.2

d_0 [mm]	b_m [mm]	t_0 [mm]	$\gamma = d_0/2t_0$ [-]	$\eta = b_m/d_0$ [-]	$\lambda = b_m/(R_m+h_0)$ [-]	$N_{1,4\%}$ [N] FEM	$N_{1,4\%}$ [N] Eng. tool	Difference [%]
1219.2	1100	64.0	9.5	0.90	1.38	1.06E+07	1.07E+07	-1.0
		57.2	10.7	0.90	1.38	8.60E+06	8.58E+06	0.2
		50.0	12.2	0.90	1.38	6.60E+06	6.58E+06	0.4
		45.0	13.5	0.90	1.38	5.40E+06	5.34E+06	1.1
		40.0	15.2	0.90	1.38	4.40E+06	4.23E+06	3.9
		35.0	17.4	0.90	1.38	3.40E+06	3.24E+06	4.6
	1300	64.0	9.5	1.07	1.63	1.34E+07	1.35E+07	-0.4
		57.2	10.7	1.07	1.63	1.08E+07	1.08E+07	0.1
		50.0	12.2	1.07	1.63	8.40E+06	8.27E+06	1.6
		45.0	13.5	1.07	1.63	7.00E+06	6.71E+06	4.1
		40.0	15.2	1.07	1.63	5.60E+06	5.32E+06	5.1
		35.0	17.4	1.07	1.63	4.40E+06	4.08E+06	7.3
	1600	64.0	9.5	1.31	2.00	1.26E+07	1.28E+07	-1.3
		57.2	10.7	1.31	2.00	1.02E+07	1.02E+07	-0.3
		50.0	12.2	1.31	2.00	7.80E+06	7.84E+06	-0.5
		45.0	13.5	1.31	2.00	6.40E+06	6.36E+06	0.6
		40.0	15.2	1.31	2.00	5.20E+06	5.04E+06	3.1
		35.0	17.4	1.31	2.00	4.00E+06	3.87E+06	3.3
	1800	64.0	9.5	1.48	2.25	1.22E+07	1.24E+07	-1.3
		57.2	10.7	1.48	2.25	1.00E+07	9.90E+06	1.0
		50.0	12.2	1.48	2.25	7.60E+06	7.59E+06	0.1
		45.0	13.5	1.48	2.25	6.20E+06	6.16E+06	0.6
		40.0	15.2	1.48	2.25	5.00E+06	4.88E+06	2.4
		35.0	17.4	1.48	2.25	3.80E+06	3.75E+06	1.4
	2000	64.0	9.5	1.64	2.50	1.22E+07	1.21E+07	1.1
		57.2	10.7	1.64	2.50	9.80E+06	9.66E+06	1.4
		50.0	12.2	1.64	2.50	7.60E+06	7.41E+06	2.5
		45.0	13.5	1.64	2.50	6.20E+06	6.01E+06	3.0
		40.0	15.2	1.64	2.50	4.80E+06	4.76E+06	0.8
		35.0	17.4	1.64	2.50	3.80E+06	3.66E+06	3.8

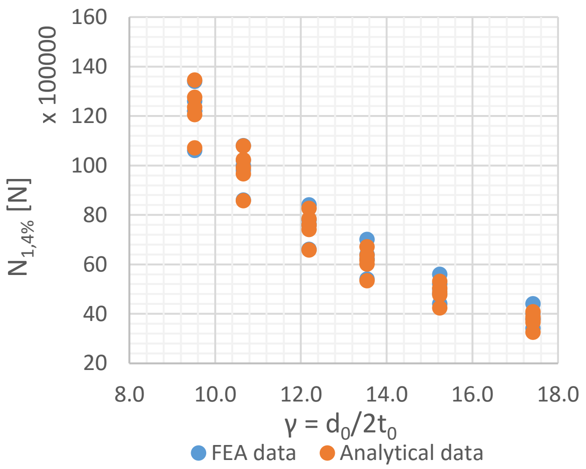

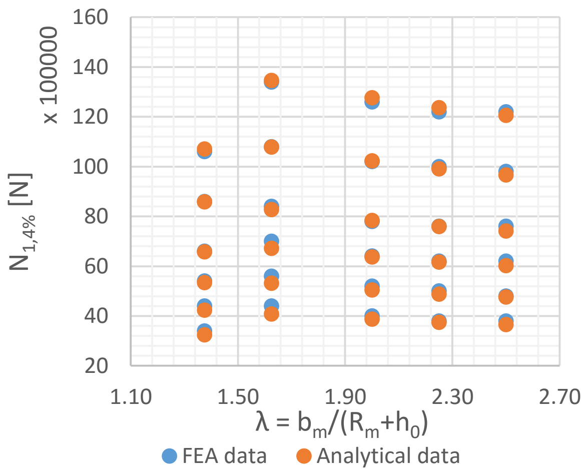

Figure 140: Comparison between FEA data and engineering tool in the padeye load case with variable geometry, d_0 = 1219.2

Table 53: Comparison between FEA data and engineering tool in the padeye load case with variable geometry, d_0 = 1400

d_0 [mm]	b_m [mm]	t_0 [mm]	$\gamma = d_0/2t_0$ [-]	$\eta = b_m/d_0$ [-]	$\lambda = b_m/(R_m+h_0)$ [-]	$N_{1,4\%}$ [N] FEM	$N_{1,4\%}$ [N] Eng. tool	Difference [%]
1400	1100	64.0	10.9	0.79	1.38	9.80E+06	1.01E+07	-2.9
		57.2	12.2	0.79	1.38	8.00E+06	8.08E+06	-1.0
		50.0	14.0	0.79	1.38	6.20E+06	6.19E+06	0.1
		45.0	15.6	0.79	1.38	5.00E+06	5.03E+06	-0.5
		40.0	17.5	0.79	1.38	4.00E+06	3.98E+06	0.5
		35.0	20.0	0.79	1.38	3.20E+06	3.05E+06	4.6
	1300	64.0	10.9	0.93	1.63	1.22E+07	1.26E+07	-3.4
		57.2	12.2	0.93	1.63	1.00E+07	1.01E+07	-1.0
		50.0	14.0	0.93	1.63	7.80E+06	7.74E+06	0.8
		45.0	15.6	0.93	1.63	6.40E+06	6.28E+06	1.9
		40.0	17.5	0.93	1.63	5.20E+06	4.97E+06	4.4
		35.0	20.0	0.93	1.63	4.00E+06	3.82E+06	4.6
	1600	64.0	10.9	1.14	2.00	1.16E+07	1.19E+07	-2.3
		57.2	12.2	1.14	2.00	9.20E+06	9.51E+06	-3.4
		50.0	14.0	1.14	2.00	7.20E+06	7.29E+06	-1.2
		45.0	15.6	1.14	2.00	5.80E+06	5.91E+06	-2.0
		40.0	17.5	1.14	2.00	4.60E+06	4.68E+06	-1.8
		35.0	20.0	1.14	2.00	3.60E+06	3.59E+06	0.2
	1800	64.0	10.9	1.29	2.25	1.12E+07	1.14E+07	-2.2
		57.2	12.2	1.29	2.25	9.00E+06	9.17E+06	-1.9
		50.0	14.0	1.29	2.25	7.00E+06	7.03E+06	-0.4
		45.0	15.6	1.29	2.25	5.80E+06	5.70E+06	1.7
		40.0	17.5	1.29	2.25	4.60E+06	4.52E+06	1.8
		35.0	20.0	1.29	2.25	3.60E+06	3.46E+06	3.8
	2000	64.0	10.9	1.43	2.50	1.10E+07	1.11E+07	-1.2
		57.2	12.2	1.43	2.50	9.00E+06	8.92E+06	0.9
		50.0	14.0	1.43	2.50	7.00E+06	6.83E+06	2.4
		45.0	15.6	1.43	2.50	5.60E+06	5.55E+06	1.0
		40.0	17.5	1.43	2.50	4.40E+06	4.39E+06	0.2
		35.0	20.0	1.43	2.50	3.40E+06	3.37E+06	0.9

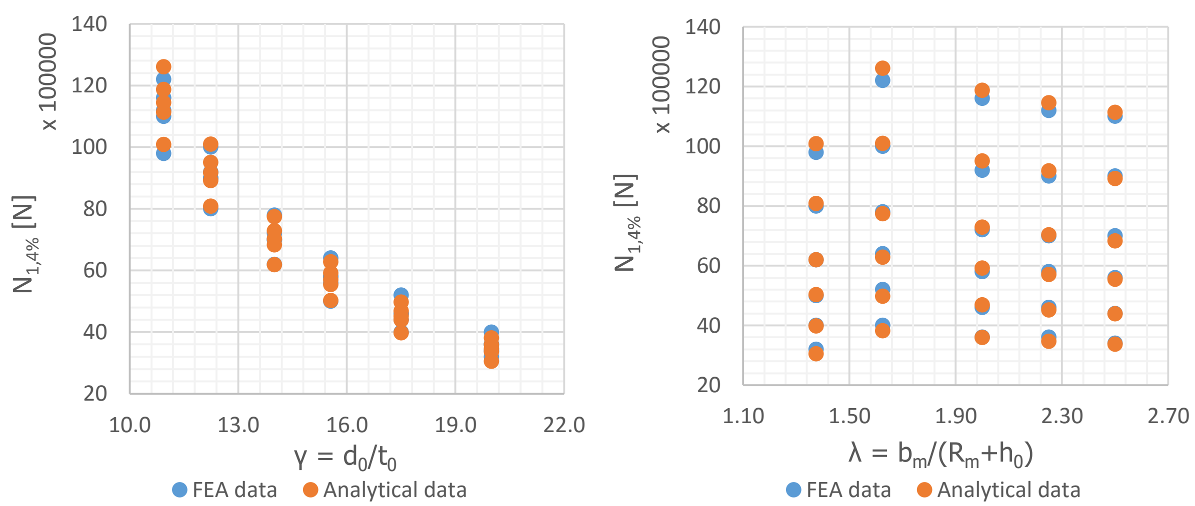

Figure 141: Comparison between FEA data and engineering tool in the padeye load case with variable geometry, d_0 = 1400